Technische Universität München

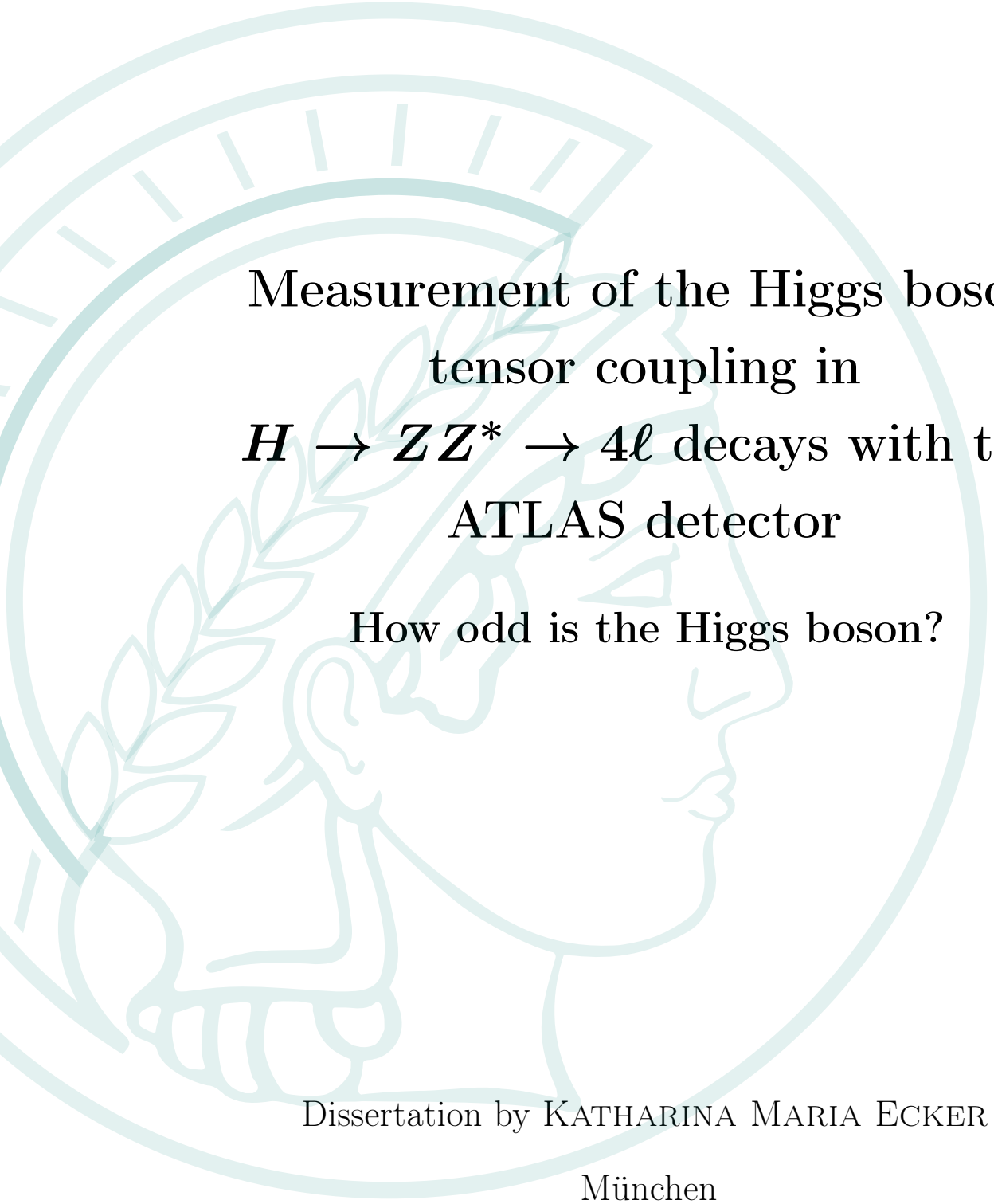

Measurement of the Higgs boson tensor coupling in $H \to ZZ^* \to 4\ell$ decays with the ATLAS detector

How odd is the Higgs boson?

Dissertation by Katharina Maria Ecker

München

April 2018

Fakultät für Physik der

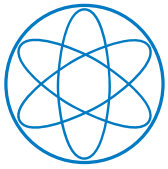

Technischen Universität München

Max-Planck-Institut für Physik
(Werner-Heisenberg-Institut)

Measurement of the Higgs boson tensor coupling in $H \to ZZ^* \to 4\ell$ decays with the ATLAS detector

How odd is the Higgs boson?

Katharina Maria Ecker

Vollständiger Abdruck der von der Fakultät für Physik der Technischen Universität München zur Erlangung des akademischen Grades eines

Doktors der Naturwissenschaften (Dr. rer. nat.)

genehmigten Dissertation.

Vorsitzender:	apl. Prof. Dr. Norbert Kaiser
Prüfende der Dissertation:	
	1. apl. Prof. Dr. Hubert Kroha
	2. Prof. Dr. Lothar Oberauer

Die Dissertation wurde am 05.04.2018 bei der Technischen Universität München eingereicht und durch die Fakultät für Physik am 14.05.2018 angenommen.

Für meine Eltern
Anna & Sebastian Ecker

Abstract

The tensor structure of the Higgs boson couplings to gluons and heavy weak gauge bosons has been probed for small admixtures of non-Standard Model CP-odd and, only for heavy vector bosons, CP-even couplings to the CP-even Standard Model coupling. The Higgs boson candidates are reconstructed in the $H \to ZZ^* \to 4\ell$ ($\ell \equiv e, \mu$) decay channel using proton-proton collision data recorded by the ATLAS detector at the Large Hadron Collider (LHC) in 2011 and 2012 at centre-of-mass energies of $\sqrt{s} = 7$ and 8 TeV corresponding to an integrated luminosity of $24.8\,\text{fb}^{-1}$ and in 2015 and 2016 at $\sqrt{s} = 13$ TeV corresponding to $36.1\,\text{fb}^{-1}$.

The non-Standard Model coupling parameters are defined within an effective field theory, the so-called Higgs characterisation framework. The relative contributions of the CP-even and CP-odd terms are described by the CP mixing angle α. The parameter κ_{Agg} denotes the CP-odd non-Standard Model coupling at the Higgs to gluon interaction vertex and κ_{HVV} and κ_{AVV} the CP-even and CP-odd non-Standard Model couplings of the Higgs boson to weak gauge bosons, respectively. The observable coupling parameters are the product of the coupling strengths κ and the sine or cosine of the CP mixing angle α, $c_\alpha \equiv \cos\alpha$ and $s_\alpha \equiv \sin\alpha$.

Two complementary methods have been used for the measurement. One is solely based on kinematic variables of the four-lepton final state which are sensitive to the presence of non-Standard Model couplings. Constraints on non-Standard Model contributions to the Higgs to Z-boson coupling have been obtained with this approach from the Run-1 data set. A combination with an analogous measurement for $H \to WW^* \to e\nu\mu\nu$ decays has also been performed. The second approach combines the information on the CP structure of the Higgs boson from final state kinematic observables and from the Higgs boson production rate using part of the Run-2 data set. The first constraints on a CP-odd contribution to Higgs boson production in gluon fusion have been derived. All results are in agreement with the Standard Model predictions. The most stringent constraints have been obtained from the production rate with $-0.6 \leq c_\alpha\kappa_{\text{HVV}} \leq 4.2$, $-4.4 \leq s_\alpha\kappa_{\text{AVV}} \leq 4.4$ and $-0.68 \leq s_\alpha\kappa_{\text{Agg}} \leq 0.68$ at 95 % CL.

Contents

Introduction

The Higgs boson discovery in proton-proton collisions at the Large Hadron Collider (LHC) by the ATLAS[1] and CMS[2] experiments [1, 2] in 2012 completed the Standard Model of particle physics and opened a new window to physics beyond the Standard Model as well as for precision tests of the Standard Model. The LHC is located at the international research centre for particle physics CERN[3] near Geneva.

For a long time, the Higgs boson was the last missing piece of the Standard Model [3–6] which describes all known elementary particles and their interactions very successfully. It includes the Higgs mechanism [7–12] introduced in the 1960s for the generation of particle masses without violating the local gauge symmetry of the electroweak interaction. The Higgs mechanism predicts a neutral CP-even scalar field, the Higgs field. Spontaneous breaking of the electroweak gauge symmetry due to a non-vanishing vacuum expectation value of the Higgs field leads to masses of the elementary particles coupling to the Higgs field. The mass of the Higgs boson is not predicted by the Standard Model. It took nearly 50 years to find it at a mass of about 125 GeV [1, 2] in decays into photon, W and Z-boson pairs. In 2013, Peter Higgs and François Englert were rewarded the Noble Prize for physics for the introduction of the Higgs mechanism in relativistic gauge field theories and the prediction of the Higgs boson.

The discovery of the Higgs boson started a new era of precision tests of the Standard Model. The predicted quantum numbers and couplings to other Standard Model particles have to be tested opening a new window for the search for new physics. The Standard Model incorporates the simplest implementation of the Higgs mechanism. However, more complicated realisations with more than one Higgs boson are possible including admixtures of CP-odd states like in supersymmetric extensions of the Standard Model. The CP-odd contribution may also lead to new sources for the violation of the

[1] A Toroidal LHC ApparatuS
[2] Compact Muon Solenoid
[3] Conseil Européen pour la Recherche Nucléaire

CP symmetry. The CP symmetry has to be violated in the early universe in order to generate an excess of matter over antimatter in the universe [13].

So far, all measurements of Higgs boson properties agree with the Standard Model [14–16]. While a pure pseudoscalar state with CP-odd eigenvalue is excluded by the LHC data, it is still possible that CP-even and CP-odd admixtures from non-Standard Model sources are present. CP-odd admixtures can lead to CP violation in the Higgs boson sector. This is especially interesting as the CP violation in the Standard Model is not strong enough to explain the observed asymmetry between matter and antimatter. In this thesis, two methods have been applied for probing the CP nature of the Higgs boson in interactions with gauge bosons using proton-proton collision data recorded by the ATLAS experiment at the LHC at centre-of-mass-energies of 7, 8 and 13 TeV.

The Higgs CP quantum numbers are accessible by studying the tensor structure of the Higgs boson couplings. Two CP-sensitive measurements can be distinguished: the Higgs boson production rate with potential contributions from couplings beyond the Standard Model (BSM), called rate information, and distributions of kinematic variables related to Higgs boson production and decay, referred to as shape information. Two complementary analyses have been performed, one solely based on the shape information, the shape-based analysis, and the other one combining rate and shape information, the rate-based approach since the rate information dominates the sensitivity.

The analyses have been performed for Higgs boson decays via $H \to ZZ^* \to 4\ell$ ($\ell \equiv e, \mu$). LHC Run-1 data taken in 2011 and 2012 at $\sqrt{s} = 7$ and 8 TeV with an integrated luminosity of $24.8\,\text{fb}^{-1}$ and Run-2 data recorded in 2015 and 2016 at $\sqrt{s} = 13$ TeV with $36.1\,\text{fb}^{-1}$ have been analysed. The four-lepton decay is one of the Higgs boson discovery channels. Despite its small branching ratio below 1 %, it provides high sensitivity because of high signal-to-background ratio and since the final state leptons are fully reconstructed with high momentum resolution. This is also very beneficial for the measurement of the tensor structure of the HZZ tensor coupling.

The shape-based analysis is solely based on distributions of CP-sensitive variables of the four-lepton final state. In this analysis, CP-even and CP-odd deviations from the Standard Model can be distinguished and CP violation in the Higgs sector detected. However, the sensitivity is lower than in the rate-based approach. Constraints on additional CP-even and CP-odd couplings in Higgs to vector boson decays have been derived for the full LHC Run-1 data set at $\sqrt{s} = 7$ and 8 TeV combining the

$H \to ZZ^* \to 4\ell$ analysis with a similar one for $H \to WW^* \to e\nu\mu\nu$ decays.

For the rate-based analysis of the 2015 and 2016 Run-2 data at $\sqrt{s} = 13$ TeV, it is necessary to distinguish the Higgs boson production mechanisms to disentangle Standard Model and beyond-Standard Model contributions. This is achieved by event categorisation exploiting production mode topologies and final state kinematics in cross sections templates in addition to the inclusive $H \to ZZ^* \to 4\ell$ reconstruction. CP-odd couplings are probed in the gluon fusion production and additional CP-even and CP-odd couplings are probed in the Higgs to vector boson coupling in production and decay. In order to efficiently model expected changes of rate and shape within this framework, a new method has been developed in this thesis: the so-called morphing method.

The thesis is structured as follows: In Chapter 1 the Standard Model of particle physics is introduced as well as Higgs boson production and decays in proton-proton collisions at the LHC. Extensions of the Standard Model which affect the Higgs boson couplings and model-independent parametrisations of such deviations from the Standard Model are discussed, followed by an overview of the current status of Higgs boson measurements by the ATLAS and CMS experiments. An overview of the ATLAS detector is given in Chapter 2. Particle reconstruction in the ATLAS detector is explained in Chapter 3. The selection of Higgs boson candidates in the four-lepton decay channel is described in Chapter 4 followed by the discussion of the shape- and rate-based tensor structure measurements of the Higgs boson coupling to gauge bosons in Chapter 5 which are compared with each other and with measurements of the CMS experiment. Finally, the results of the analyses are summarised and future improvements are discussed. Methods to model discriminants as a function of interesting parameters including the morphing method, which has been developed for this thesis, are introduced in Chapter 6.

Chapter 1

Theory

In this chapter, the theoretical framework is introduced and the current status of Higgs boson measurements summarised. In Section 1.1, the Standard Model (SM) of particle physics is described with emphasis on the Higgs mechanism. The production of the SM Higgs boson in proton-proton collisions at the Large Hadron Collider (LHC) is described in Section 1.2, and the dominant Higgs boson decay channels in Section 1.3. This is followed in Section 1.4 by a short overview of extensions of the Standard Model and of schemes for model-independent parametrisations including the effective field theory approach and an introduction to the implementation used for the analysis, the so-called Higgs characterisation framework. Finally in Section 1.5, an overview of the current status of Higgs boson property measurements is given.

In this thesis, natural units ($\hbar = c = 1$) are used.

1.1 The Standard Model

1.1.1 Gauge symmetries, interactions and fundamental particles

The SM of particle physics is a renormalisable quantum field theory that describes all known elementary particles and their interactions except gravity: electromagnetism, the weak interaction, for example responsible for radioactive β-decay, and the strong interaction binding quarks together in hadrons. So far all experimental tests of the SM confirm its predictions with high accuracy.

The SM is a gauge theory, i.e. the associated Lagrangian describing the physical state is invariant under local gauge transformations. The gauge symmetry group of the SM

is a product of the three simplest unitary Lie groups,

$$\underbrace{U(1)_Y \times SU(2)_L}_{\text{electroweak}} \underbrace{\times SU(3)_c}_{\text{strong}}. \tag{1.1}$$

The electroweak interaction unifying electromagnetism and the weak force is described by the $U(1)_Y \times SU(2)_L$ group. The $SU(2)_L$ group acts on left-handed (index L) particles. $U(1)_Y$ is the symmetry group of the weak hypercharge Y. The electroweak symmetry is spontaneously broken via the Higgs mechanism. The $SU(3)_c$ symmetry defines the strong interaction that acts on all particles with colour (index c).
Each gauge symmetry group requires the introduction of new vector fields, the gauge fields, whose quanta are the gauge bosons, which mediate the interactions. The particles of the SM are summarised in Figure 1.1. There are two types, fermions and bosons:

- **Fermions:** The Spin $\frac{1}{2}$ particles are grouped into leptons and quarks which are distinguished by flavour quantum numbers. There are three generations of leptons and quarks which share the same interactions, but differ mass. The second and third generations are heavier copies of the first generation, from which ordinary matter is built. Each lepton generation consists of a negatively charged massive fermion together with a very light and electrically neutral neutrino. Each quark generation consists of a pair of massive quarks with electrical charge quantum numbers $+\frac{2}{3}$ and $-\frac{1}{3}$. Quarks carry colour quantum numbers $c = r, g$ or b and therefore are also subject to the strong interaction, while leptons without colour only interact weakly and, in the case of the charged leptons, electromagnetically. For each fermion there is a corresponding anti-fermion with the mass and lifetime but opposite-sign quantum numbers.

- **Vector bosons:** The vector bosons act as mediators of the interactions. The electromagnetic force is carried by the photon that is electrically neutral and massless. The massive gauge bosons of the weak interaction are the electrically charged $W^{\pm}$-bosons and the neutral Z-boson. Gluons are the massless force-carriers of the strong interaction. There are eight types of gluons carrying different combinations of colour charges.

- **Higgs boson:** The electrically and colour neutral, massive Higgs boson is the only observed fundamental scalar particle, i.e. with Spin 0 and CP-eigenvalue +1 (CP-even). The CP symmetry changes particles into their antiparticles (charge

conjugation C) and inverts the sign of all spatial coordinates (parity P). The Higgs boson is a consequence of the Higgs mechanism, which leads to the spontaneous breaking of the electroweak gauge symmetry and gives mass to the weak gauge bosons and the fermions.

Electroweak interaction and the Higgs mechanism

The electromagnetic and weak interactions are unified within the Glashow-Salam-Weinberg [4, 5, 17] theory, a local $U(1)_Y \times SU(2)_L$ gauge theory. The $U(1)_Y$ symmetry corresponds to the weak hypercharge Y, while $SU(2)_L$ is the symmetry group of the weak isospin. The weak isospin interaction couples only to left-handed particles and right-handed antiparticles corresponding to the observed maximum parity violation in the weak charged current interaction.

All SM gauge bosons and fermions are massless as required by the local gauge symmetries and by the combination of global $SU(2)_L$ symmetry and parity violation respectively, which is in contradiction to the observations. This can be solved with the Higgs mechanism [7–12], that breaks the electroweak gauge symmetry spontaneously leaving only the electromagnetic abelian gauge symmetry $U(1)_Q$ with electric charge operator Q unbroken:

$$U(1)_Y \times SU(2)_L \to U(1)_Q. \tag{1.2}$$

The electromagnetic interaction is described by quantum electrodynamics (QED). The weak gauge bosons and fermions acquire their masses via the Higgs mechanism. The Higgs boson is a massive excitation of the Higgs field from the ground state after symmetry breaking.

Quantum chromodynamics

The strong interaction which binds quarks together in baryons and mesons (collectively called hadrons) is described by the $SU(3)_c$ gauge theory of quantum chromodynamics (QCD). Fermions with colour charges (quarks) interact strongly by exchanging the $SU(3)_c$ gauge bosons (gluons). Important characteristics of QCD are *asymptotic freedom* and *confinement*. The strong gauge coupling constant diverges at energies below the confinement scale Λ_{QCD} leading to the breakdown of perturbation theory.

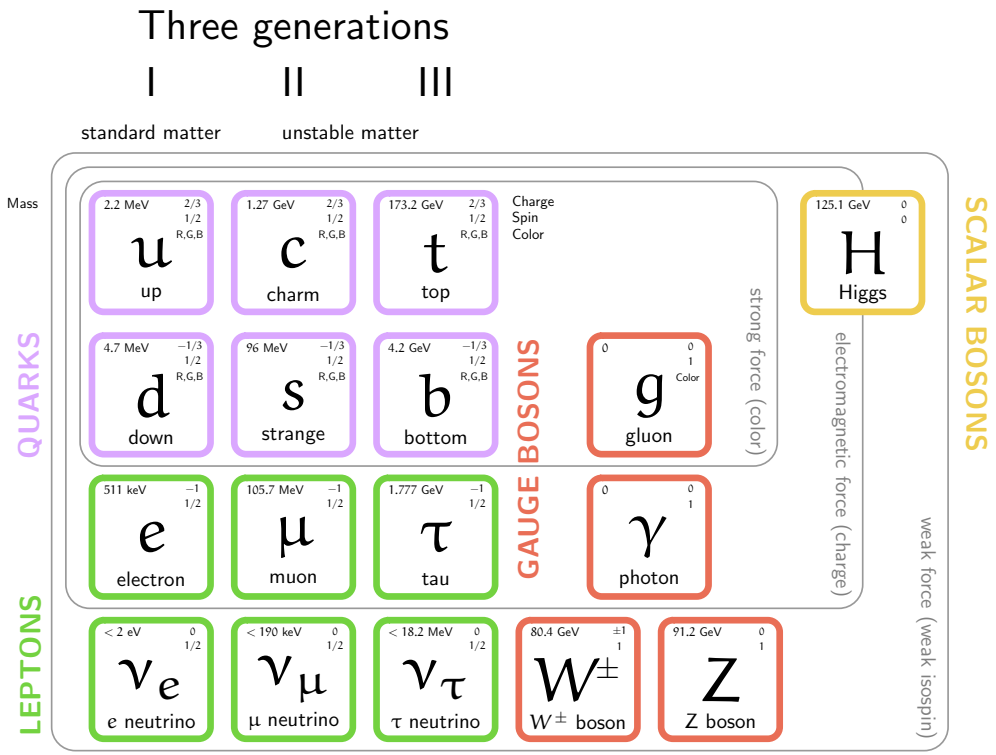

Figure 1.1: Particle content of the SM of particle physics.

At energies above Λ_{QCD}, i.e. smaller distances, the QCD coupling decreases such that the hadron constituents approximately behave as free particles (*asymptotic freedom*), and perturbation theory is applicable.

1.1.2 Mathematical formulation

Detailed introductions to the SM can be found in text books and published lectures [18, 19].

The Lagrangian $\mathscr{L}_{\mathrm{SM}}$ describing all SM particles and their interactions can be written as a sum of a gauge boson kinetic term $\mathscr{L}_B$, a term $\mathscr{L}_F$ describing fermion-gauge boson interactions and a term $\mathscr{L}_H$ describing fermion and gauge boson interactions with the

Higgs field:

$$\mathscr{L}_{\mathrm{SM}} = \mathscr{L}_B + \mathscr{L}_F + \mathscr{L}_H. \tag{1.3}$$

In the following, $\mathscr{L}_B$ and $\mathscr{L}_F$ before electroweak symmetry breaking are introduced to explain the fermion-gauge boson interactions in the SM. The Higgs mechanism is explained by a walkthrough of $\mathscr{L}_H$ before and after the electroweak symmetry is broken.

Gauge boson kinetic terms

The kinetic terms of the gauge fields in the Lagrangian are given by

$$\mathscr{L}_B = -\frac{1}{4} G^a_{\mu\nu} G^{a\mu\nu} - \frac{1}{4} W^a_{\mu\nu} W^{a\mu\nu} - \frac{1}{4} B_{\mu\nu} B^{\mu\nu}, \tag{1.4}$$

with the field strength tensors $G^a_{\mu\nu}$, $W^a_{\mu\nu}$ and $B_{\mu\nu}$ of the $SU(3)_c$, $SU(2)_L$ and $U(1)_Y$ interactions, respectively. The index a runs over the number of gauge fields of each interaction. There are eight gauge fields for strong and three gauge fields for the weak isospin interaction.

For the abelian $U(1)_Y$ gauge interaction, the field strength tensor has the same form as in quantum electrodynamics,

$$B_{\mu\nu} = \partial_\mu B_\nu - \partial_\nu B_\mu, \tag{1.5}$$

with the weak hypercharge gauge field B_μ, which does not interact with itself.

Due to the non-abelian gauge symmetries, the gluon fields G^a_μ and the weak isospin gauge fields W^a_μ have self-interaction corresponding to additional terms in the field strength tensors. For the strong interaction the field strength tensor has the form

$$G^a_{\mu\nu} = \partial_\mu G^a_\nu - \partial_\nu G^a_\mu + g_s f^{abc} G^b_\mu G^c_\nu, \tag{1.6}$$

with the strong coupling constant g_s, $a, b, c = 1, .., 8$, and the $SU(3)$ structure constants f^{abc} defining the anti-commutation rules of the generators t^a:

$$[t^a, t^b] = i f^{abc} t^c. \tag{1.7}$$

The weak isospin field strength tensor is given by

$$W^a_{\mu\nu} = \partial_\mu W^a_\nu - \partial_\nu W^a_\mu + g\epsilon^{abc} W^b_\mu W^c_\nu, \tag{1.8}$$

with the $SU(2)_L$ gauge coupling constant g, $a, b, c = 1, .., 3$ and the $SU(2)$ structure constant ϵ^{abc} in the totally antisymmetric three-index tensor with $\epsilon^{123} = 1$.

Fermion-gauge interaction term

The gauge interactions of the SM fermions are described by

$$\mathscr{L}_F = i\bar{\psi} D_\mu \gamma^\mu \psi. \tag{1.9}$$

with the fermion spinor field ψ, the covariant derivative D_μ and the adjunct spinor $\bar{\psi} = \psi^\dagger \gamma^0$. Which types of interactions the fermions are subject to depend on their charge quantum numbers. The weak hypercharge Y quantum numbers, the third-component of the weak isospin T^3 and the colour quantum numbers c of the first fermion generation of fermions are given in Table 1.1. The couplings of gauge fields and fermions are defined by the gauge covariant derivative

$$D_\mu = \partial_\mu - ig^{'} B_\mu Y - igW^a_\mu T^a - ig_s G^a_\mu t^a, \tag{1.10}$$

with the weak hypercharge coupling strength $g^{'}$ and the generators T^a of the $SU(2)_L$ group. A two-dimensional representation of the weak isospin generators T^a is given by the Pauli spin matrices σ^a, where $T^a = \frac{\sigma^a}{2}$.

Table 1.1: Weak hypercharge Y, weak isospin T^3 and colour c quantum numbers for the each fermion generation of the SM.

Particle type	$(u_L,\, d_L)$	u_R	d_R	$(\nu_L,\, e_L)$	e_R
Y	$\frac{1}{6}$	$\frac{2}{3}$	$-\frac{1}{3}$	$-\frac{1}{2}$	-1
T^3	$\left(+\frac{1}{2}, -\frac{1}{2}\right)$	0	0	$\left(+\frac{1}{2}, -\frac{1}{2}\right)$	0
c	colour-triplet	colour-triplet	colour-triplet	colour-singlet	colour-singlet

Higgs field terms

Explicit gauge boson mass terms $\frac{1}{2}m_B^2 B_\mu B^\mu$ in the Lagrangian violate the local gauge symmetries. Fermion mass terms $-m\bar{\psi}\psi$ together with the maximum parity violation of the weak interaction violate the electroweak gauge symmetry $SU(2)_L$. The explanation of the observed weak gauge boson and the fermion masses requires an additional mechanism. For this purpose, the scalar Higgs field is introduced, which leads to spontaneous $U(1)_Y \times SU(2)_L$ gauge symmetry breaking by assuming a non-zero vacuum. The massless Goldstone modes of the scalar field are absorbed into longitudinal polarisations of the weak gauge bosons, which thus acquire mass. Fermions acquire mass via Yukawa couplings to the Higgs field.

The simplest implementation in the SM is a complex scalar weak isospin doublet with four degrees of freedom,

$$\Phi = \begin{pmatrix} \phi^+ \\ \phi^0 \end{pmatrix}, \tag{1.11}$$

with electrically charged and neutral components ϕ^+ and ϕ^0, respectively. The Lagrangian for the Higgs field and its interactions is given by

$$\mathscr{L}_H = (D_\mu \Phi)^\dagger (D^\mu \Phi) - V(\Phi) - \sum_i \left[y_f \bar{\psi}_{R,f} \bar{\Phi} \psi_{L,f} + h.c. \right], \tag{1.12}$$

with dimensionless Yukawa coupling strength parameter y_f where f runs over the SM fermions. The first term contains the kinetic term of the scalar field Φ and the Higgs-gauge boson interactions, the second term $V(\Phi)$ is the Higgs self-interaction potential, and the third term contains Yukawa couplings of the scalar field Φ to the fermions. The covariant derivative is given by

$$D_\mu = \partial_\mu - i\frac{g'}{2}B_\mu - i\frac{g}{2}W_\mu^a \sigma^a, \tag{1.13}$$

with $Y_\Phi = \frac{1}{2}$ and $T^a = \frac{\sigma^a}{2}$. The minimal version of the gauge invariant Higgs potential allowing to spontaneous symmetry breaking is

$$V(\Phi) = -\mu^2 \Phi^\dagger \Phi + \lambda (\Phi^\dagger \Phi)^2, \tag{1.14}$$

with the Higgs self-interaction constant $\lambda > 0$.

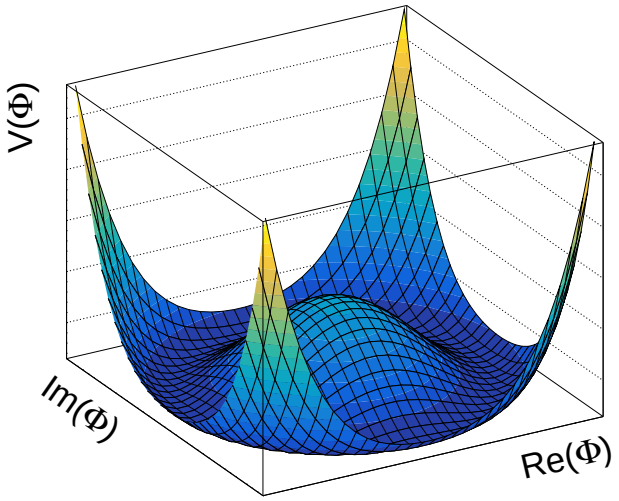

Figure 1.2: Potential $V(\Phi) = -\mu^2\Phi^\dagger\Phi + \lambda(\Phi^\dagger\Phi)^2$ of the complex Higgs field Φ with parameters $-\mu^2 < 0$ and $\lambda > 0$ after spontaneous symmetry breaking.

Depending on the values of the mass parameter μ, two cases can be distinguished:

1. $\mu^2 < 0$: the potential has a minimum at Φ_0. The electroweak symmetry is unbroken.

2. $\mu^2 > 0$: the potential has a minimum for non-zero vacuum expectation value for non-zero vacuum expectation value

$$|\Phi_0| = \sqrt{\frac{\mu^2}{2\lambda}} \equiv \frac{v}{\sqrt{2}} \neq 0, \tag{1.15}$$

(see Figure 1.2).

By selecting a particular ground state, which is not invariant under $U(1)_Y \times SU(2)_L$ transformations, e.g. $\langle\Phi_0\rangle = \frac{1}{\sqrt{2}}\binom{0}{v}$, the $U(1)_Y \times SU(2)_L$ symmetry is spontaneously broken. The field H is a massive radial excitation from the ground state in the spontaneous symmetry breaking phase:

$$\Phi = \frac{1}{\sqrt{2}}\begin{pmatrix} 0 \\ v + H \end{pmatrix}, \tag{1.16}$$

with the three massless excitations longitudinal to the potential minimum (Goldstone modes) have been eliminated in the so-called unitary gauge. They reappear instead as longitudinal polarisation states of the massive weak gauge bosons $W^{\pm}$ and Z. The field quantum of H is the Higgs boson.
The value of the vacuum expectation value v is about 246 GeV [20] determined from the measurement of the Fermi constant $G_F = \frac{1}{\sqrt{2}v^2}$.

By inserting Equation 1.16 into Equation 1.12 with $\mu^2 = \lambda v^2$ (see Equation 1.15), the mass eigenstates of the weak gauge fields, Z_μ and $W^{\pm}_\mu$, and the electromagnetic gauge field A_μ can be identified. The mass terms of the SM particles and the Higgs interaction terms after spontaneous symmetry breaking are contained in

$$\begin{aligned}\mathscr{L}_H =& \frac{1}{2}(\partial_\mu H)(\partial^\mu H) \\ &+ \frac{1}{8}(v+H)^2\left[g^2(W^1_\mu - iW^2_\mu)(W^{1\mu} + iW^{2\mu}) + (-g^{'}B_\mu + gW^3_\mu)^2\right] \\ &- \lambda v^2 H^2 - \lambda v H^3 - \frac{\lambda}{4}H^4 \\ &- \sum_f \left[\frac{y_f}{\sqrt{2}}(v+H)\bar{f}f + h.c.\right]. \end{aligned} \tag{1.17}$$

The first term is the kinetic term of the scalar field H. The second and third terms contain mass terms $m_V^2 V_\mu V^\mu$ and interaction terms $HV_\mu V^\mu$ and $HHV_\mu V^\mu$ of H with the gauge bosons. The weak hypercharge and weak isospin gauge fields mix into mass eigenstates matching the observed $W^{\pm}$ and Z-bosons:

$$W^{\pm}_\mu = \frac{W^1_\mu \mp iW^2_\mu}{\sqrt{2}}, \tag{1.18}$$

$$\begin{pmatrix} Z_\mu \\ A_\mu \end{pmatrix} = \begin{pmatrix} \cos\theta_W & -\sin\theta_W \\ \sin\theta_W & \cos\theta_W \end{pmatrix} \begin{pmatrix} W^3_\mu \\ B_\mu \end{pmatrix}, \tag{1.19}$$

with the Weinberg mixing angle θ_W defined by

$$\cos\theta_W = \frac{g}{\sqrt{g^2 + g'^2}}, \tag{1.20}$$

and the expressions for the gauge boson masses

$$m_W = \frac{g^2 v^2}{4}, \tag{1.21}$$

$$m_Z = \frac{(g^2 + g'^2)v^2}{4}, \tag{1.22}$$

$$m_A = 0. \tag{1.23}$$

The orthogonal state to Z_μ can be associated to the photon field A_μ, which does not couple to the Higgs field and thus does not acquire mass.
The Higgs boson couples to the weak gauge fields $V = W^\pm, Z$ proportional to

$$HW_\mu^+ W_\nu^- \; : \quad i\frac{g^2 v}{2} g_{\mu\nu} = igm_W g_{\mu\nu} = 2i\frac{m_W^2}{v} g_{\mu\nu}, \tag{1.24}$$

$$HHW_\mu^+ W_\nu^- \; : \quad i\frac{g^2}{4} \times 2! g_{\mu\nu} = 2i\frac{m_W^2}{v^2} g_{\mu\nu}, \tag{1.25}$$

$$HZ_\mu Z_\nu \; : \quad i\frac{\left(g^2 + g'^2\right) v}{4} \times 2! g_{\mu\nu} = i\sqrt{g^2 + g'^2} m_Z g_{\mu\nu} = 2i\frac{m_Z^2}{v} g_{\mu\nu}, \tag{1.26}$$

$$HHZ_\mu Z_\nu \; : \quad i\frac{\left(g^2 + g'^2\right)}{8} \times 2! \times 2! g_{\mu\nu} = 2i\frac{m_Z^2}{v^2} g_{\mu\nu}. \tag{1.27}$$

The combinatorial factors 2! account for identical Z-bosons and Higgs bosons.
The Higgs boson mass term $\frac{1}{2} m_H^2 H^2$ as well as triple and quartic self-coupling terms are contained in the third line in Equation 1.17. The Higgs boson mass m_H is given by

$$m_H = \sqrt{2\lambda v^2}, \tag{1.28}$$

and self-coupling strengths are given by

$$HHH \; : \quad -i\lambda v \times 3! = -6i\lambda v = -3i\frac{m_H^2}{v}, \tag{1.29}$$

$$HHHH \; : \quad -i\frac{\lambda}{4} \times 4! = -6i\lambda = -3i\frac{m_H^2}{v^2}, \tag{1.30}$$

with combinatorial factors 3! and 4! to account for three and four identical Higgs bosons.
The Yukawa couplings terms after symmetry breaking (fourth line in Equation 1.17)

contain the fermion mass terms $m_f \bar{f} f$ with

$$m_f = \frac{1}{\sqrt{2}} \lambda v \tag{1.31}$$

and the fermion-Higgs boson interactions $H \bar{f} f$ proportional to

$$Hff : \frac{-iy_f}{\sqrt{2}} = \frac{-im_f}{v}, \tag{1.32}$$

with the Yukawa coupling strengths $y_f = \sqrt{2}\frac{m_f}{v}$.

The Higgs boson couplings to SM particles are proportional to the particle masses. Once the Higgs boson mass is measured (it is a free parameter in the SM), all coupling strengths are predicted in the SM. The Higgs boson couplings are summarised in Figure 1.3[1].

The observed electromagnetic and weak interactions mediated by photon, and weak gauge bosons Z and $W^{\pm}$ are identified by rewriting the covariant derivative of the $U(1)_Y \times SU(2)_L$ theory after electroweak symmetry breaking:

$$D_\mu = \partial_\mu - i\frac{g}{\sqrt{2}} \left(W_\mu^+ T^+ + W_\mu^- T^- \right) - i\frac{e}{\sin\theta_W \cos\theta_W} \left(T^3 - \sin^2\theta_W Q \right) Z_\mu - ieQA_\mu, \tag{1.33}$$

with Equations 1.18 and 1.19 the raising and lowering operators $T^{\pm}$ of $SU(2)_L$, the electromagnetic coupling e and electric charge operator Q with the relations

$$e = \frac{gg'}{\sqrt{g^2 + g'^2}} = g \sin\theta_W = g' \cos\theta_W \quad \text{and} \quad Y = Q - T^3. \tag{1.34}$$

[1]The Feynman diagrams within this thesis are drawn with the TikZ-Feynman [21] package.

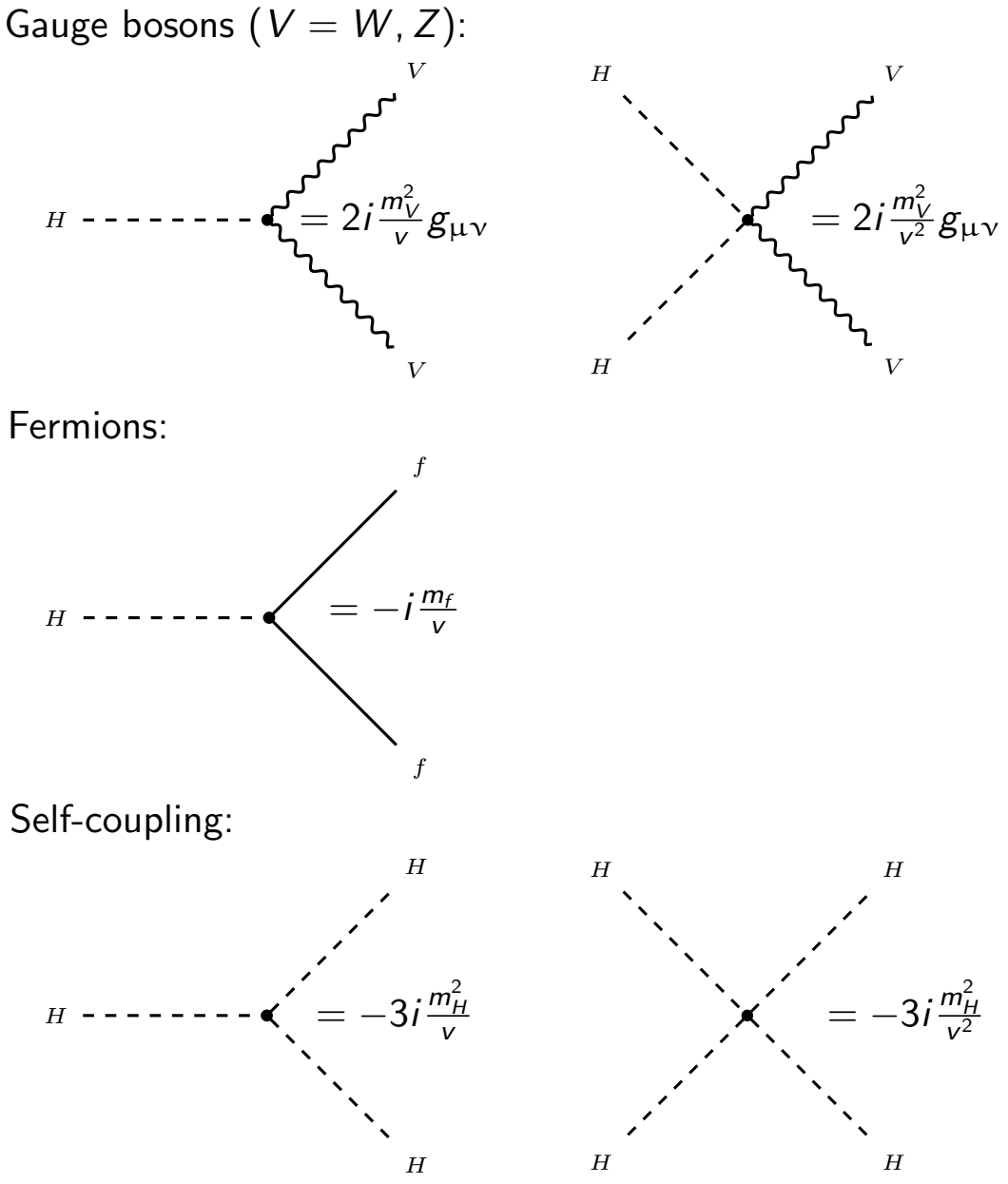

Figure 1.3: Tree-level Feynman diagrams of the Higgs boson couplings to the weak gauge bosons and to fermions, as well as the Higgs boson self-interaction diagrams.

1.1.3 Limitations of the Standard Model

While the predictions of the SM have been verified with very high precision, there are still observations that cannot be explained by the SM [18]. For instance, it does not describe dark matter or dark energy, and the SM neutrinos are predicted to be massless, which is in contradiction to the observation of neutrino flavour oscillations [22–24]. In addition, the CP violation observed in weak decays and described in the SM via the quark mixing matrix, the Cabibbo-Kobayashi-Maskawa matrix (CKM matrix) [25, 26], is too weak to explain the matter-antimatter asymmetry in the universe. Violation of CP symmetry is one of the three Sakharov conditions [13] required for the generation of different amounts of matter and antimatter.

It is thus of interest to search for new sources of CP violation for instance in Higgs boson interactions beyond the SM. The Higgs boson in the SM is a CP-even state and its interactions are predicted to conserve CP symmetry. While the CP = +1 quantum number of the Higgs boson has been experimentally confirmed at the LHC [14–16], CP-odd admixtures predicted by extensions of the SM are still allowed which can lead to additional CP violating effects.

1.2 Production of the Standard Model Higgs boson at the Large Hadron Collider

At the LHC the SM Higgs boson is produced in proton-proton collisions through various production mechanisms. The cross sections of the most dominant production processes are shown as a function of the proton-proton centre-of-mass energy in Figure 1.4. Data sets taken at $\sqrt{s} = 7$ TeV, 8 TeV and 13 TeV have been analysed for this thesis. The cross section values at the LHC energies can be found in Table 1.2. At those centre-of-mass energies, the SM Higgs boson with a mass of about 125 GeV is produced dominantly by gluon fusion (ggF) with a relative contribution of 87% to the total production rate. The corresponding tree-level Feynman diagram is shown in the left side of Figure 1.5. The next important processes are vector boson fusion (VBF), see Figure 1.5 right, with 7 % and associated production with a weak vector boson (VH), see Figure 1.6, with 4 % relative contribution. The associated production with a top or a bottom-quark pair ($t\bar{t}H$ and $b\bar{b}H$), see Figure 1.7, contributes with 1 % each, while the associated production with a single top-quark (tH) (see Figure 1.8) contributes

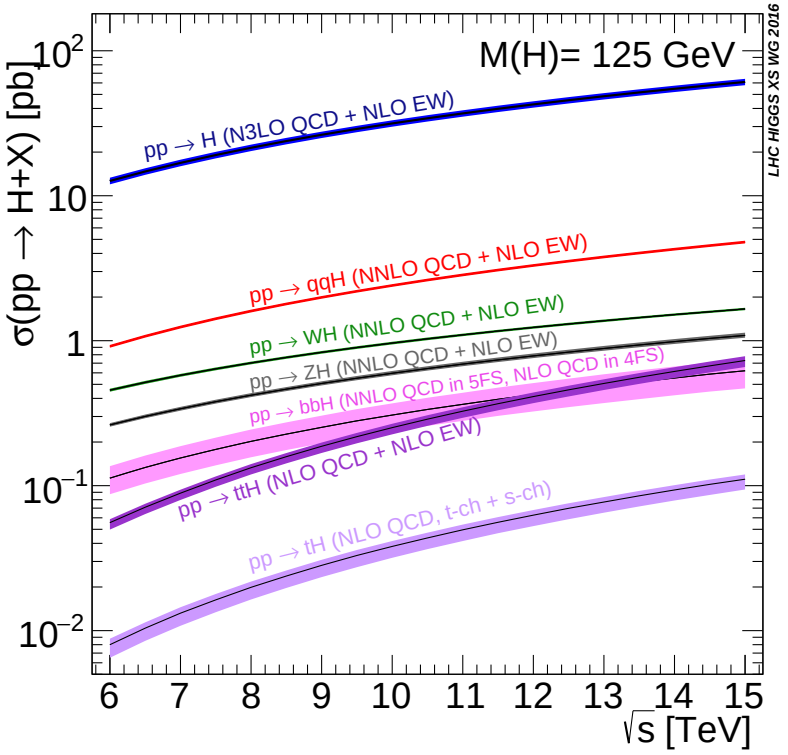

Figure 1.4: Cross sections for the production of the SM Higgs boson with a mass of 125 GeV in proton-proton collisions at centre-of-mass energies from 6 to 15 TeV [27]. Data sets taken at $\sqrt{s} = 7, 8$ and 13 TeV are analysed in this thesis.

with less than 1 % to the total production rate. Experimentally, the different final state signature of the VBF, VH and $t\bar{t}H$ production mechanism can be exploited to improve the discrimination between signal and background processes.

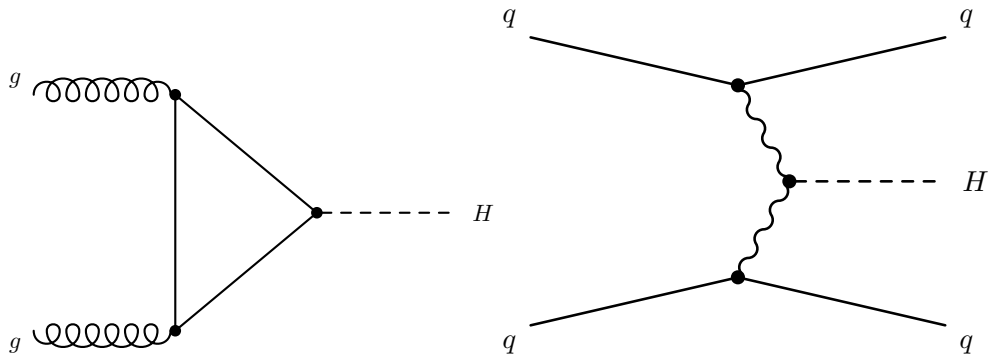

Figure 1.5: Tree-level Feynman diagrams for the SM Higgs boson production processes at the LHC via gluon fusion (ggF, left) and vector boson fusion (VBF, right) [28].

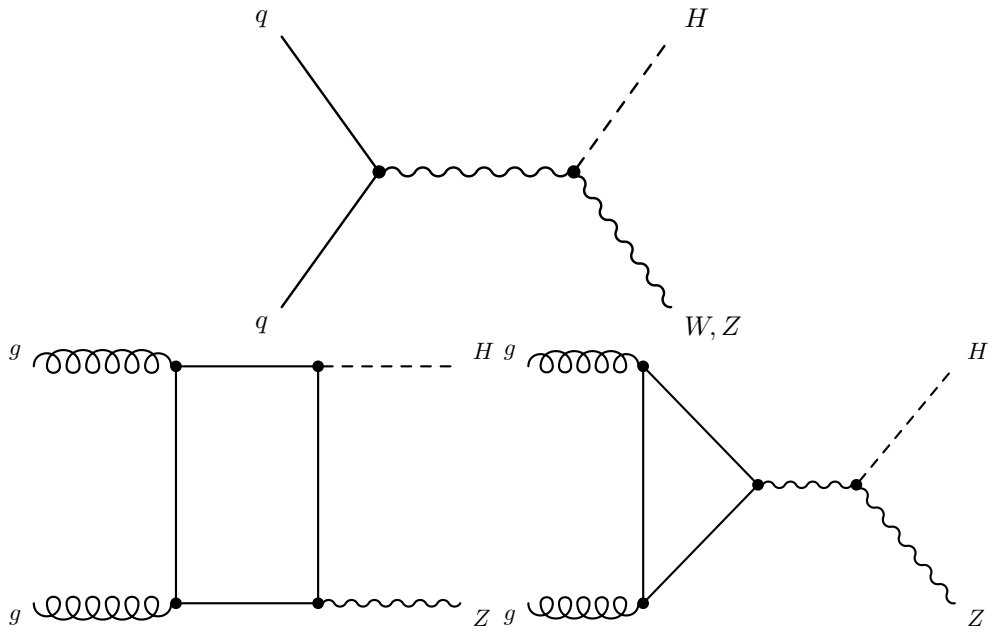

Figure 1.6: Tree-level Feynman diagram for the associated SM Higgs boson production $qq \to VH$ with a weak gauge boson $V = W, Z$ (top) and loop processes for $gg \to ZH$ production (bottom) in proton-proton collisions [28].

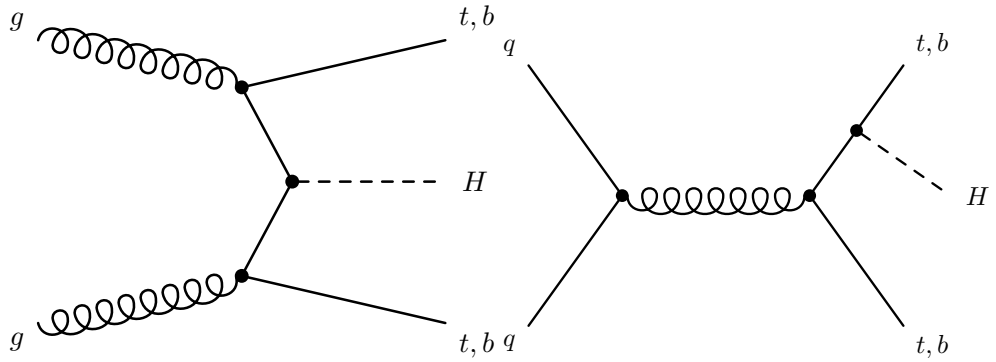

Figure 1.7: Tree-level Feynman diagrams for the SM Higgs boson production in association with a top or a bottom-quark pair ($t\bar{t}H$ and $b\bar{b}H$) [28].

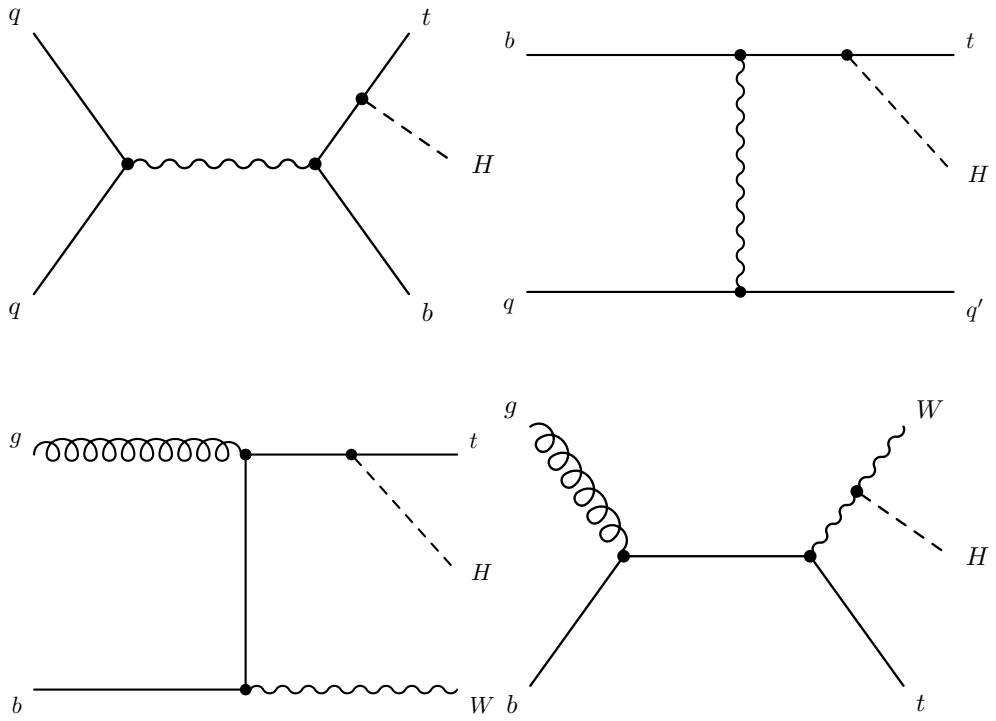

Figure 1.8: Tree-level s-channel and t-channel SM Higgs boson production in association with a top-quark and a quark (top) or a W-boson (bottom) [28].

Table 1.2: SM Higgs boson ($m_H = 125$ GeV) production cross sections for the dominant production processes in proton-proton collisions at the LHC at centre-of-mass energies of $\sqrt{s} = 7$, 8 and 13 TeV [27]. The theoretical errors given are related to uncertainties in the QCD scale, the strong coupling constant α_S and the parton distribution functions (PDF) added in quadrature.

Short name	Production process				cross section [pb]			Feynman-diagram	
					$\sqrt{s} = 7$ TeV	$\sqrt{s} = 8$ TeV	$\sqrt{s} = 13$ TeV		
ggF	gg	$\rightarrow$	H		$16.9 \pm 5.2\%$	$21.4 \pm 5.1\%$	$48.6 \pm 5.0\%$	1.5	
VBF	qq	$\rightarrow$	qqH		$1.24^{+2.2\%}_{-2.2\%}$	$1.60^{+2.2\%}_{-2.2\%}$	$3.78^{+2.1\%}_{-2.1\%}$	1.5	
WH	qq	$\rightarrow$	WH		$0.577^{+2.2\%}_{-2.3\%}$	$0.703^{+2.1\%}_{-2.2\%}$	$1.37^{+1.9\%}_{-2.0\%}$	1.6	
ZH	gg/qq	$\rightarrow$	ZH		$0.339^{+3.1\%}_{-2.9\%}$	$0.421^{+3.4\%}_{-2.9\%}$	$0.88^{+4.1\%}_{-3.5\%}$	1.6	
$t\bar{t}H$	gg/qq	$\rightarrow$	$t\bar{t}H$		$0.089^{+5.6\%}_{-10.2\%}$	$0.133^{+5.9\%}_{-10.2\%}$	$0.51^{+6.8\%}_{-9.9\%}$	1.7	
$b\bar{b}H$	gg/qq	$\rightarrow$	$b\bar{b}H$		$0.16^{+20.7\%}_{-22.4\%}$	$0.20^{+20.7\%}_{-22.3\%}$	$0.49^{+20.2\%}_{-23.9\%}$	1.7	
tH	qq	$\rightarrow$	tHq	(t-ch.)	$0.0123^{+8.8\%}_{-17.9\%}$	$0.0187^{+8.6\%}_{-17.1\%}$	$0.074^{+7.5\%}_{-15.4\%}$	1.8	(top right)
				(s-ch.)	$0.00093^{+4.2\%}_{-3.9\%}$	$0.00121^{+4.0\%}_{-3.7\%}$	$0.00288^{+3.3\%}_{-2.8\%}$	1.8	(top left)
	gq	$\rightarrow$	tHW	(W-ass.)	$0.0022^{+9.4\%}_{-10.0\%}$	$0.0035^{+9.0\%}_{-9.7\%}$	$0.0152^{+8.0\%}_{-9.2\%}$	1.8	(bottom)
Total					$19.3^{+4.5\%}_{-4.5\%}$	$24.5^{+4.5\%}_{-4.5\%}$	$55.7^{+4.4\%}_{-4.4\%}$		

1.3 Decays of the Standard Model Higgs boson

At the measured mass of about 125 GeV, the Higgs boson decays into a large variety of final states (see Figure 1.9). The decay into a bottom-quark pair has the largest branching fraction followed by the decay into a pair of W-bosons. The decays into pairs of gluons, tau leptons and charm-quarks and Z-bosons are the channels with the next highest branching ratios. The Higgs boson decays into pairs of photons and into $Z\gamma$ are at the per mille level, while the decays into $\mu\mu$ are very rare. The branching fraction values are summarised in Table 1.3.

Because of the large QCD background processes in proton-proton collisions, hadronic decay channels are experimentally difficult, like $H \to b\bar{b}$ or not accessible like decays into pairs of gluons and light quarks. Beneficial for suppressing the QCD background are final states with leptons. Thus, the Higgs decays into weak gauge bosons with successive fully leptonic decays of the vector bosons are important for Higgs boson studies. The branching fractions of the currently experimentally accessible decays including the decays into leptonic final states of the weak bosons are shown on the right-hand side of Figure 1.9. The $H \to ZZ^* \to 4\ell$ and $H \to \gamma\gamma$ decays contributed to the Higgs boson discovery [1, 2] as well as the $H \to WW^* \to \ell\nu\ell\nu$ decay channel. $H \to ZZ^* \to 4\ell$ with a branching fraction of the fully leptonic final state of only 0.01 %, and $H \to \gamma\gamma$ suffer from low statistics, but have a very clear signature to distinguish them from the background. All decays depicted on the right-hand side of Figure 1.9 have been observed or there is experimental evidence, except for $H \to \mu\mu$ (see Section 1.5).

Table 1.3: Predicted branching fractions of the SM Higgs boson with a mass of 125 GeV [27]. Uncertainties related to missing higher order corrections and input parameters (α_S, m_c, m_b, m_t) are added linearly.

Decay process			Branching fraction [%]
H	$\to$	$b\bar{b}$	$58.2^{+2.2\%}_{-2.2\%}$
H	$\to$	WW	$21.4^{+2.6\%}_{-2.6\%}$
H	$\to$	gg	$8.2^{+8.2\%}_{-8.2\%}$
H	$\to$	$\tau\tau$	$6.27^{+2.8\%}_{-2.8\%}$
H	$\to$	$c\bar{c}$	$2.89^{+7.7\%}_{-3.4\%}$
H	$\to$	ZZ	$2.62^{+2.6\%}_{-2.6\%}$
H	$\to$	$\gamma\gamma$	$0.227^{+3.3\%}_{-3.3\%}$
H	$\to$	$Z\gamma$	$0.153^{+7.3\%}_{-7.4\%}$
H	$\to$	$\mu\mu$	$0.0218^{+2.8\%}_{-2.9\%}$
H	$\to$	4ℓ $(\ell = e, \mu)$	$0.0124 \pm 2.2\%$
H	$\to$	$\ell\nu\ell\nu$ $(\ell = e, \mu)$	$1.06 \pm 2.2\%$

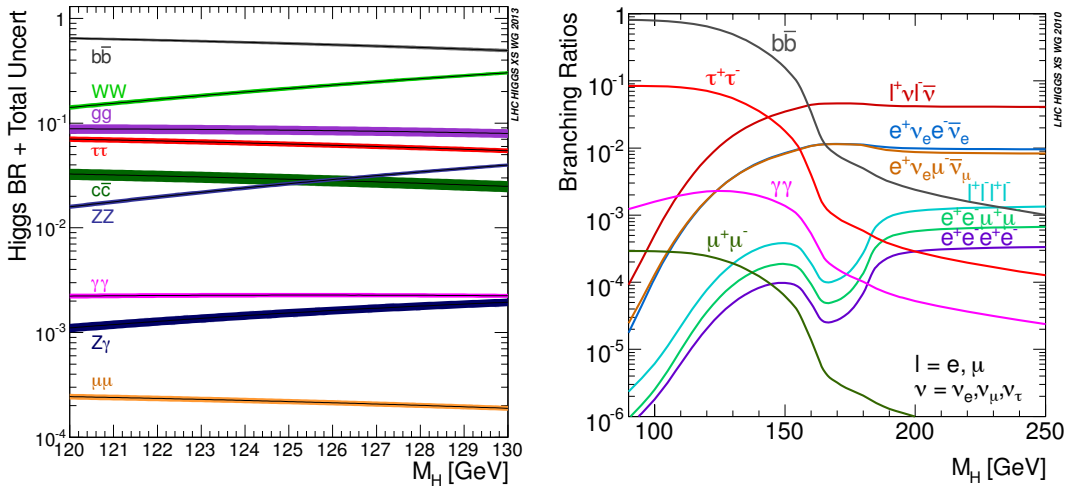

Figure 1.9: Predicted branching fractions of the SM Higgs boson as a function of the Higgs boson mass for all primary decays with branching ratios higher than 10^{-4} (left) and for selected decays into exclusive final states which are experimentally relevant at the LHC (right) [29].

1.4 Higgs boson couplings beyond the Standard Model

The Higgs boson in the SM is a scalar CP-even eigenstate. The ATLAS and CMS experiments have found a scalar resonance with $m_H \approx 125$ GeV. The pure pseudoscalar hypothesis is highly disfavoured by data (see Section 1.5), but it is still possible to have a mostly CP-even scalar with BSM CP-even and CP-odd admixtures, the latter leading to CP violation in the Higgs sector. In this thesis, the hypothesis of a mixed CP state of the discovered scalar boson with $m_H \approx 125$ GeV is tested in the coupling to gauge bosons.

In this section, BSM theories predicting such a resonance are introduced followed by the discussion of approximate descriptions, where the non-SM Higgs boson couplings are parametrised without knowledge of a specific underlying theory. Two approximate descriptions are discussed below: an anomalous couplings approach where the most general production and decay amplitude is derived and an effective field theory where the most general low-energy Lagrangian is written down. In this thesis, an effective theory parametrisation of the non-SM Higgs boson couplings is used, the Higgs characterisation model [30]. No assumption is made on the nature of the underlying theory.

1.4.1 Models beyond the Standard Model

An overview about BSM theories introducing CP violation in the Higgs sector and of possibilities for their detection at the LHC is given in [29] (Section 11.2). In [31] CP violating Higgs boson physics is discussed in great detail.

In general, a pseudoscalar state A couples to gauge bosons via a term

$$\mathscr{L}_{AVV} = \frac{c_V}{\Lambda} A V^{\alpha,\mu\nu} \widetilde{V}^{\alpha}_{\mu\nu}, \tag{1.35}$$

in the Lagrange function, with the gauge boson field strength tensor $V^{\alpha,\mu\nu}$ and its dual tensor $\widetilde{V}^{\alpha}_{\mu\nu} = \frac{1}{2}\epsilon_{\mu\nu\rho\sigma} V^{a,\rho\sigma}$ and with the coupling strength c_V that emerges from new physics at the scale Λ.
Such a term can arise from two classes of theories:

1. Via loop effects in renormalisable weakly-interacting models, for example:

   a) extensions of the Higgs sector or

   b) supersymmetric theories.

2. From non-perturbative extensions of the SM, for example versions of technicolour theories with cut-off scale Λ [32, 33].

Candidates for weakly interacting theories are the Minimal Supersymmetric Standard Model (MSSM), Two-Higgs-Doublet models (2HDM) and Little Higgs models.
Supersymmetry [34–39] is an extension of the SM, where an additional symmetry between bosons and fermions is introduced. Each SM particle has a superpartner whose spin differs by one half. The most intensively investigated supersymmetric theory is the MSSM [40, 41], which comprises a minimum number of new particle states. The MSSM requires two complex Higgs doublets, one for up-type and one for down-type fermion mass terms. In 2HDM models, the SM Higgs boson sector is generally extended by the addition of a second complex Higgs field doublet [42]. There are different types of 2HDM extensions. In type-II models up- and down-type fermions couple to different Higgs doublets like in the MSSM. A consequence of the two doublets are two vacuum expectation values. Their ratio is defined as the parameter $\tan\beta$. In Little Higgs models, the Higgs boson is a pseudo-Goldstone boson arising from the breaking of a global symmetry valid at the higher energy scale.
In weakly interacting models, the pseudoscalar couplings to gauge bosons are introduced

in loops dominated by the top-quark contribution. The pseudoscalar component is heavily suppressed as opposed to the scalar component. Recent studies have shown that the detection of CP violation in the MSSM [43, 44], and in Little Higgs models [45–47] is not feasible at the LHC since small values of $\tan\beta$ are necessary to enhance the pseudoscalar component which are strongly constrained for the MSSM by direct Higgs searches [48]. This restriction does not apply for generic type-II 2HDM models.

In technicolour theories, the Higgs boson is a composite particle. A new strong and confining gauge interaction exists similar to QCD which binds so-called technifermions. Within such theories, pseudoscalar couplings to gauge bosons are possible [43]. Since the new interaction is strong, differences from the SM prediction are much more pronounced and a precision on the order of 10 % on Higgs boson couplings can constrain such models.

1.4.2 Higgs boson tensor coupling parametrisations

There are two options for the model-independent parametrisation of non-SM Higgs boson tensor couplings (see [29], Section 11): either a parametrisation of the scattering amplitude with anomalous couplings or an effective field theory approach. In the anomalous couplings approach, the most general amplitude compatible with Lorentz and gauge invariance is written down, while in an effective theory, the most general effective Lagrangian compatible with Lorentz and gauge invariance is formulated.
The effective Lagrangian approach can be extended with systematic higher order corrections, which is not possible for the anomalous couplings approach. The anomalous couplings approach is, on the other hand, more general since it also describes new light resonances leading to complex coupling strengths, while in the effective theory new physics has to be at higher scales than the measurement.
Under the assumption that the anomalous couplings are constant and real, the anomalous coupling formulation is equivalent to that from an effective field theory. In this thesis, both approaches have been used. The results are presented in the effective field theory formulation, the Higgs characterisation framework [30].
In the following, the Higgs characterisation framework is introduced followed by an overview of the anomalous couplings approach and a translation between both formalisms.

The Higgs characterisation framework

The scope of this thesis is the study of the tensor structure of the Higgs boson coupling to gluons and weak gauge bosons, in particular to ZZ^* in $H \to ZZ^* \to 4\ell$ decays. Potential non-SM couplings of the Higgs boson can be parametrised within an effective field theory approach, the Higgs characterisation framework. An effective theory is a low-energy approximation of the unknown full theory expected to be uncovered only at higher energies. The new physics processes relevant at the higher energy scale are integrated out. With this approach, no specific knowledge of the underlying theory is necessary, i.e. effective theories provide model independent parametrisations of new physics effects. In this thesis, the cut-off energy Λ up to which the effective theory can be applied is assumed to be 1 TeV, as no new particles have been discovered up to this energy scale.

The effective Lagrangian of the Higgs characterisation model describing the interaction of a scalar field H with SM gauge bosons is given by

$$
\begin{aligned}
\mathscr{L}^{V}_{\mathrm{HC}} = & \Bigg\{ c_\alpha \kappa_{\mathrm{SM}} \left[\frac{1}{2} g_{\mathrm{HZZ}} Z_\mu Z^\mu + g_{\mathrm{HWW}} W^+_\mu W^{-\mu} \right] \\
& - \frac{1}{4} \left[c_\alpha \kappa_{\mathrm{H}\gamma\gamma} g_{\mathrm{H}\gamma\gamma} A_{\mu\nu} A^{\mu\nu} + s_\alpha \kappa_{\mathrm{A}\gamma\gamma} g_{\mathrm{A}\gamma\gamma} A_{\mu\nu} \widetilde{A}^{\mu\nu} \right] \\
& - \frac{1}{2} \left[c_\alpha \kappa_{\mathrm{HZ}\gamma} g_{\mathrm{HZ}\gamma} Z_{\mu\nu} A^{\mu\nu} + s_\alpha \kappa_{\mathrm{AZ}\gamma} g_{\mathrm{AZ}\gamma} Z_{\mu\nu} \widetilde{A}^{\mu\nu} \right] \\
& - \frac{1}{4} \left[c_\alpha \kappa_{\mathrm{Hgg}} g_{\mathrm{Hgg}} G^a_{\mu\nu} G^{a,\mu\nu} + s_\alpha \kappa_{\mathrm{Agg}} g_{\mathrm{Agg}} G^a_{\mu\nu} \widetilde{G}^{a,\mu\nu} \right] \\
& - \frac{1}{4} \frac{1}{\Lambda} \left[c_\alpha \kappa_{\mathrm{HZZ}} Z_{\mu\nu} Z^{\mu\nu} + s_\alpha \kappa_{\mathrm{AZZ}} Z_{\mu\nu} \widetilde{Z}^{\mu\nu} \right] \\
& - \frac{1}{2} \frac{1}{\Lambda} \left[c_\alpha \kappa_{\mathrm{HWW}} W^+_{\mu\nu} W^{-\mu\nu} + s_\alpha \kappa_{\mathrm{AWW}} W^+_{\mu\nu} \widetilde{W}^{-\mu\nu} \right] \\
& - \frac{1}{\Lambda} c_\alpha \left[\kappa_{\mathrm{H}\partial\gamma} Z_\nu \partial_\mu A^{\mu\nu} + \kappa_{\mathrm{H}\partial\mathrm{Z}} Z_\nu \partial_\mu Z^{\mu\nu} + \kappa_{\mathrm{H}\partial\mathrm{W}} (W^+_\nu \partial_\mu W^{-\mu\nu} + h.c.) \right] \Bigg\} H.
\end{aligned}
\tag{1.36}
$$

The (reduced) electroweak field strength tensors $V_{\mu\nu}$ and their dual tensors $\widetilde{V}_{\mu\nu}$ in the approximation without self-coupling and the strong field tensors $G^a_{\mu\nu}$ are given

by

$$V_{\mu\nu} = \partial_\mu V_\nu - \partial_\nu V_\mu \qquad (V = A, Z, W^\pm), \tag{1.37}$$

$$\widetilde{V}_{\mu\nu} = \frac{1}{2} \cdot \epsilon_{\mu\nu\rho\sigma} \cdot V^{\rho\sigma}, \tag{1.38}$$

$$G^a_{\mu\nu} = \partial_\mu G^a_\nu - \partial_\nu G^a_\mu + g_s f^{abc} G^b_\mu G^c_\nu. \tag{1.39}$$

The effective Lagrangian for the Higgs coupling to fermions is given in this framework by

$$\mathscr{L}^f_{\mathrm{HC}} = -\sum_{f=t,b,\tau} \left\{ \bar{\psi}_f \left(c_\alpha \kappa_{\mathrm{Hff}} g_{\mathrm{Hff}} + i s_\alpha \kappa_{\mathrm{Aff}} g_{\mathrm{Aff}} \gamma_5 \right) \psi_f \right\} H. \tag{1.40}$$

For simplicity, the first and second-generation fermions are assumed to be massless, such that they do not couple to the Higgs boson.
CP symmetry is not required such that the Higgs particle may not be a CP-eigenstate. The terms in the Lagrangian can be grouped into such with CP-even and CP-odd transformation properties. Parameters of CP-even terms are denoted with index H and those of CP-odd terms with index A indicating the CP-even and CP-odd admixtures H and A of the BSM Higgs boson. The κ parameters are coupling strength parameters. The angle α describes the relative contributions of CP-even and CP-odd terms. The following short notation is used:

$$c_\alpha \equiv \cos\alpha, \qquad s_\alpha \equiv \sin\alpha. \tag{1.41}$$

The first line in Equation 1.36 describes the SM Higgs to weak gauge boson $V = W, Z$ coupling, while the BSM interactions to Z and W-bosons are given in the fifth and sixth lines, respectively. The CP-even and CP-odd terms describing Higgs to $\gamma\gamma$, $Z\gamma$ and gg couplings are described in lines two to four, respectively. In the Higgs characterisation model, these interactions are described by effective couplings, i.e. the interaction is assumed to be point-like. In the SM, the couplings Hgg, $HZ\gamma$ and $H\gamma\gamma$ associated to CP-even terms appear at loop level. In the last line, the so-called derivative operators are described, which can be understood as contact operators $HVff$ [49]. Only CP-even derivative operators are included, the CP-odd analogues vanish [30]. With the exception of $\kappa_{H\partial W}$ all couplings κ are assumed to be real.
The coupling parameters g are defined in [30]. For $\kappa = 1$ they reproduce the SM couplings in case of CP-even terms and the couplings of a 2HDM with $\tan\beta = 1$ in

Table 1.4: Configuration of Higgs characterisation parameters in case of SM and BSM ggF and VBF/VH production with subsequent $H \to VV$ ($V = Z, W$) decays.

	$c_\alpha\kappa_{\mathrm{Hgg}}$	$s_\alpha\kappa_{\mathrm{Agg}}$	$c_\alpha\kappa_{\mathrm{SM}}$	$c_\alpha\kappa_{\mathrm{HVV}}$	$s_\alpha\kappa_{\mathrm{AVV}}$
Standard Model					
ggF	1	0	1	0	0
VBF/VH	0	0	1	0	0
Beyond the Standard Model					
ggF	1	1	1	0	0
VBF/VH	0	0	1	1	1

the CP-odd case. The presence of CP-odd coupling terms with index A leads to CP violating processes.

In this thesis, the BSM CP-even and CP-odd couplings to Z and W-bosons are probed, it is assumed that the BSM couplings are correlated in the same way as in the SM, i.e. $c_\alpha\kappa_{\mathrm{HVV}} = c_\alpha\kappa_{\mathrm{HZZ}} = c_\alpha\kappa_{\mathrm{HWW}}$ and $s_\alpha\kappa_{\mathrm{AVV}} = s_\alpha\kappa_{\mathrm{AZZ}} = s_\alpha\kappa_{\mathrm{AWW}}$. In addition, the effective Higgs to gluon coupling is probed on the presence of CP-odd admixtures, i.e. $s_\alpha\kappa_{\mathrm{Agg}} \neq 0$. Both scenarios are probed independently, all other BSM couplings are assumed to vanish.
The parameter configurations recovering SM and BSM scenarios for ggF and VBF/VH productions with $H \to VV$ ($V = Z, W$) decays are summarised in Table 1.4. In the SM case, the contributions of $HZ\gamma$ and $H\gamma\gamma$ are neglected since they are very small in comparison to tree-level HVV couplings. Two BSM scenarios are given in Table 1.4: the CP violating ggF production due to BSM CP-odd contribution to the Higgs-gluon coupling and BSM contributions to VBF/VH production with higher order CP-even and CP violating CP-odd contributions to HZZ and HWW couplings in production or decay.

Anomalous couplings approach

The anomalous couplings approach is a generic parametrisation of the scattering amplitude. All possible tensor structures that are consistent with gauge and Lorentz

invariance are included into a general scattering amplitude [50]

$$A(X_{J=0} \to VV) = \frac{1}{v}\left(g_1 m_V^2 \epsilon_1^* \epsilon_2^* + g_2 f_{\mu\nu}^{*(1)} f^{*(2),\mu\nu} + g_4 f_{\mu\nu}^{*(1)} \tilde{f}^{*(2),\mu\nu}\right) \tag{1.42}$$

that describes the interactions of a scalar boson with a pair of gauge bosons ($VV = ZZ$, WW, $Z\gamma$, $\gamma\gamma$ and gg) with the gauge boson field strength tensor $f^{i,\mu\nu} = \epsilon_i^\mu q_i^\nu - \epsilon_i^\nu q_i^\mu$ of a gauge boson with momentum vector q_i and polarisation vector ϵ_i and its conjugate $\tilde{f}^{(i),\mu\nu} = \frac{1}{2}\epsilon^{\mu\nu\alpha\beta} f_{\alpha\beta}$ and coupling strengths g_i ($i = 1, 2, 4$) that are momentum dependent form factors. The coupling strengths g_i can in general be complex due to contributions of new light particles. As no new physics has been observed at the LHC, the coupling strengths are assumed to be real and constant. In the SM, the only non-vanishing tree-level coupling is g_1, which corresponds to Higgs to weak gauge boson couplings. The term g_2 is generated in the SM by loop processes and describes the coupling of the Higgs boson with a pair of gauge bosons including processes where at least one is massless, i.e. to $\gamma\gamma$, gg and $Z\gamma$. The term g_4 denotes the pseudoscalar coupling to gauge bosons which is not present in the SM.

The anomalous coupling parametrisation is used in the Monte Carlo event generator JHU [51, 52], which is employed in the shape-based tensor structure analysis described in Section 5.1. In addition, the CMS collaboration has used this parametrisation with the nomenclature $a_1 = g_1$, $a_2 = g_2$ and $a_3 = g_4$ for tensor structure measurements [16, 53–55]. The anomalous coupling and the Higgs characterisation framework formalisms can be translated into each other under the assumption that the couplings g_i are real and constant:

$$\frac{g_2}{g_1} = \widetilde{\kappa}_{\mathrm{HVV}}/\kappa_{\mathrm{SM}} \quad \text{with } \widetilde{\kappa}_{\mathrm{HVV}} = \frac{1}{4}\frac{v}{\Lambda}\kappa_{\mathrm{HVV}}, \tag{1.43}$$

for the CP-even parameters and

$$\frac{g_4}{g_1} = (\widetilde{\kappa}_{\mathrm{AVV}}/\kappa_{\mathrm{SM}}) \cdot \tan\alpha \quad \text{with } \widetilde{\kappa}_{\mathrm{AVV}} = \frac{1}{4}\frac{v}{\Lambda}\kappa_{\mathrm{AVV}}, \tag{1.44}$$

for the CP-odd parameters. The coupling parameters a_1, g_1 and $c_\alpha\kappa_{\mathrm{SM}}$, respectively, correspond to the SM tree-level coupling, a_2, g_2 and $c_\alpha\widetilde{\kappa}_{\mathrm{HVV}}$ to the CP-even BSM term, and a_3, g_4 and $s_\alpha\widetilde{\kappa}_{\mathrm{AVV}}$ to the CP-odd BSM term.

The results of the CMS collaboration are expressed in terms of effective cross sections f_{a_i} with values between 0 and 1, where $f_{a_{2/3}} = 0$ corresponds to the pure SM scalar and $f_{a_{2/3}} = 1$ to the pure BSM CP-even/pseudoscalar state. In [29] (Section 11.4.2)

and in [50] (in Section II) the coupling fractions are defined as follows:

$$\left|\frac{a_i}{a_1}\right| = \sqrt{\frac{f_{a_i}}{f_{a_1}}}\sqrt{\frac{\sigma_1}{\sigma_i}}, \tag{1.45}$$

where $i = 2, 3$ and $f_{a_1} = 1 - \sum_i f_{a_i}$ corresponds to the effective SM tree-level contribution. The effective cross section ratios $\sqrt{\frac{\sigma_1}{\sigma_i}}$ are calculated by computing the cross section for one coupling parameter while all other coupling parameters are set to zero. For the translation between parametrisations in this thesis the cross section values in [53] are used: $\frac{\sigma_1}{\sigma_2} = 2.77$ and $\frac{\sigma_1}{\sigma_3} = 6.53$.

1.5 Status of the Higgs boson measurements

Since the discovery of the Higgs boson in 2012, many measurements have been performed by the ATLAS and CMS collaborations based on data sets taken in the years 2011, 2012, and 2015 to 2017 at centre-of-mass energies of $\sqrt{s} = 7$, 8 TeV and 13 TeV. The LHC data sets are described in Chapter 2. In this section an overview of the current status of the measurements of Higgs boson is given (see also [20]). So far, no significant deviation from the SM prediction has been observed.

Higgs boson mass

The mass of the Higgs boson is a free parameter in the SM. Experimentally, the best mass resolution relative to the Higgs boson mass $m_H \approx 125$ GeV of 1-2 % is obtained in the four-lepton and diphoton final states, which can be fully reconstructed with high precision. In other decay channels, like $H \to WW^* \to \ell\nu\ell\nu$ and $H \to \tau\tau$, only mass resolutions of 20 % and 15 %, respectively, are achieved. The Higgs boson mass resolutions in the main decay channels are summarised in Table 1.5.

A combination of the ATLAS and CMS Higgs boson mass measurements in $H \to \gamma\gamma$ and $H \to ZZ^* \to 4\ell$ decays based on the full Run-1 data sets collected in 2011 and 2012 at centre-of-mass energies of 7 and 8 TeV, gives a Higgs boson mass value of [56]

$$m_H = 125.09 \pm 0.21 \text{ (stat.)} \pm 0.11 \text{ (syst.)} \text{ GeV}. \tag{1.46}$$

Table 1.5: The Higgs boson mass resolutions relative to the Higgs boson mass $m_H \approx 125$ GeV in the main decay channels [20]

Decay channel	Mass resolution
$H \to \gamma\gamma$	1-2 %
$H \to ZZ^* \to 4\ell$	1-2 %
$H \to WW^* \to \ell\nu\ell\nu$	20 %
$H \to b\bar{b}$	10 %
$H \to \tau\tau$	15 %

Since then, ATLAS and CMS published separately results based on Run-2 data [57, 58]. In Figure 1.10 the mass measurements are summarised. Once the Higgs boson mass is determined, its width and the couplings to other SM particles are determined by the theory.

Higgs boson width

The Higgs boson width in the SM of 4 MeV [29] is very small in comparison with the resolution of ATLAS and CMS of 1-2 GeV in the $H \to ZZ^* \to 4\ell$ and $H \to \gamma\gamma$ decay channels. At the LHC, the Higgs boson width can be constrained directly or indirectly. A summary of the Higgs boson width measurements can be found in [20] (Section 11.V.3).

Direct constraints on the width are obtained from the line shape of the Higgs boson mass. Therefore, only upper limits on the Higgs boson width could be derived by ATLAS [60] and CMS [55], which are three orders of magnitude larger than the SM width. A direct lower limit has been obtained by the CMS experiment in $H \to ZZ^* \to 4\ell$ decays from the average lifetime of the Higgs boson determined from the measured displacement of the four-lepton vertex from the primary interaction point, which is compatible with the predicted width [61].

Indirect constraints on the Higgs boson width can be obtained from a mass shift in the diphoton channel [62–64] or from off-shell Higgs boson coupling measurements [65–69]. The latter measurements, performed by ATLAS [70] and CMS [61, 71], are two orders of magnitude more sensitive than the direct ones but rely on additional assumptions. The ATLAS collaboration estimates that the Higgs boson width can be measured

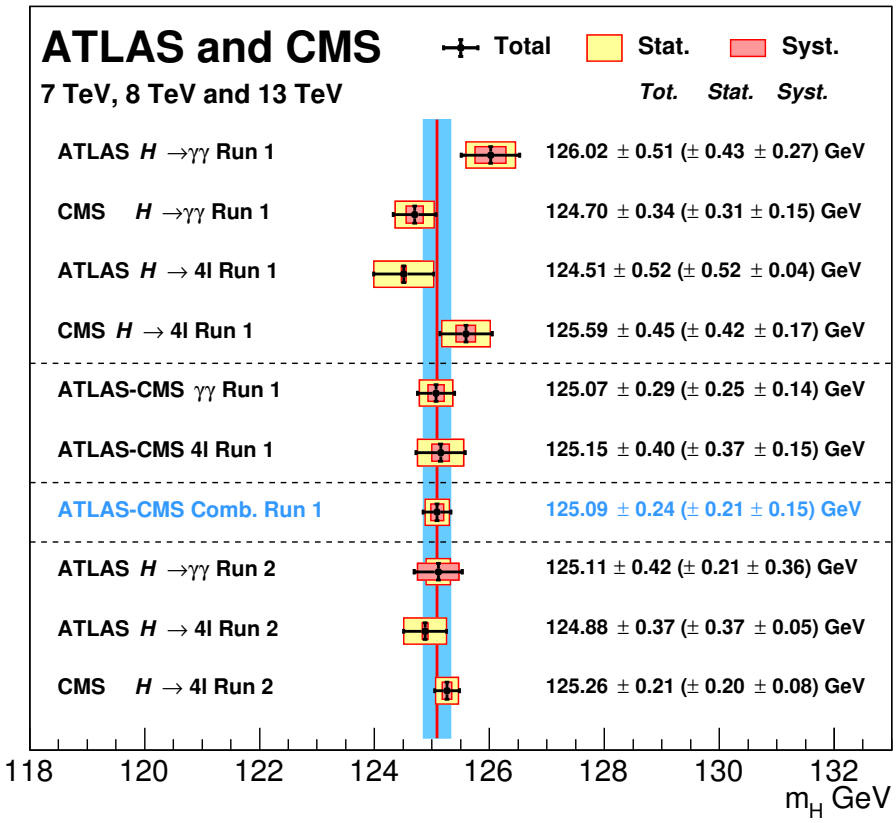

Figure 1.10: Higgs boson mass measurements performed in the four-lepton and diphoton final states by the ATLAS and CMS experiments with Run-1 and Run-2 data [59]. The correct systematic uncertainty of the Run-1 combination of the ATLAS and CMS results is ±0.11 instead of ±0.15 GeV [56].

with a precision of $\Gamma_H = 4.2^{+1.5}_{-2.1}\,\text{MeV}$ from off-shell couplings in $H \to ZZ^* \to 4\ell$ decays with a data set of $3\,\text{ab}^{-1}$ [72] collected at the high-luminosity upgrade of the LHC.

Higgs boson couplings

An essential new test of the SM is provided by the measurements of the Higgs boson couplings to SM particles at the LHC. The most precise coupling measurement comes from the combination of ATLAS and CMS results based on the Run-1 data sets [28]. No significant deviation from SM predictions has been observed. Figure 1.11 shows the expected linear dependence of the coupling strength on the particle mass over a wide mass range.

The main Higgs boson production and decay processes have either been observed with $5\,\sigma$ significance with the Run-1 data or there has been $3\,\sigma$ evidence with the exception of $t\bar{t}H$ production (see Tables 1.6 and 1.7). At the LHC, only the product of production cross section times branching ratio can be measured. The rates of the different Higgs boson production modes have been measured separately for each decay channel.
While the Higgs boson couplings to vector bosons were discovered already with Run-1 data, this was not the case for the coupling to fermions, both in decays ($H \to \tau\tau$ and $H \to b\bar{b}$) and in production ($t\bar{t}H$). The Run-2 data already provided improvements for the Higgs boson to fermion couplings. CMS reported independent observation of $H \to \tau\tau$ decays [73]. Both experiments found evidence for $H \to b\bar{b}$ decays [74, 75] and ATLAS evidence for $t\bar{t}H$ production [76].

Also searches for rare Higgs boson decays, e.g. $H \to \mathsf{Z}\gamma$ and $H \to \mu\mu$, have been performed by ATLAS and CMS [78–81]. Evidence for $H \to \mathsf{Z}\gamma$ and observation of $H \to \mu\mu$ require $3\,\text{ab}^{-1}$ of data to be collected at the high-luminosity upgrade of the LHC (HL-LHC) [82, 83].

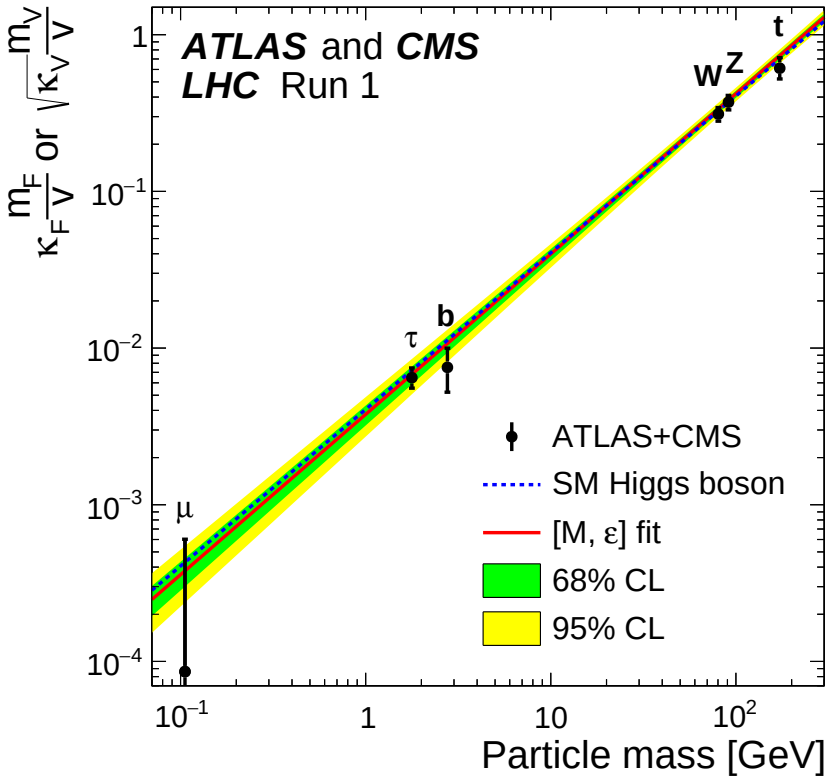

Figure 1.11: The couplings of the Higgs boson to SM particles as a function of the particle mass measured by the ATLAS and CMS experiments with Run-1 data from 2011 and 2012 (black points). The prediction of the SM is indicated by the dashed blue line, while the best linear fit to the data is shown in red with green (yellow) one (two) standard deviation uncertainty bands [28].

Table 1.6: Observed and expected, in parentheses, signal significances for the main Higgs boson production processes from ATLAS and CMS Run-1 data, and ATLAS Run-2 data. The results are not reported by the authors, since the significance exceeds $5\,\sigma$[†].

	ATLAS		CMS		Combined	
	Significance Obs. (Exp.)	Ref.	Significance Obs. (Exp.)	Ref.	Significance Obs. (Exp.)	Ref.
Run-1						
ggF	not reported[†]	[77]	$6.6\,\sigma$ ($7.4\,\sigma$)	[55]	not reported[†]	[28]
VBF	$4.3\,\sigma$ ($3.8\,\sigma$)	[77]	$3.7\,\sigma$ ($3.3\,\sigma$)	[55]	$5.4\,\sigma$ ($4.6\,\sigma$)	[28]
VH ($V = Z, W$)	$2.6\,\sigma$ ($3.1\,\sigma$)	[77]	$2.7\,\sigma$ ($2.9\,\sigma$)	[55]	$3.5\,\sigma$ ($4.2\,\sigma$)	[28]
$t\bar{t}H$	$2.5\,\sigma$ ($1.5\,\sigma$)	[77]	$3.5\,\sigma$ ($1.2\,\sigma$)	[55]	$4.4\,\sigma$ ($2.0\,\sigma$)	[28]
Run-2						
$t\bar{t}H$	$4.2\,\sigma$ ($3.8\,\sigma$)	[76]	–		–	

Table 1.7: Observed and expected, in parentheses, signal significances for the main Higgs boson decay channels from ATLAS and CMS Run-1 and Run-2. The results are not reported by the authors, since the significance exceeds $5\,\sigma$[†].

	ATLAS		CMS		Combined	
	Significance Obs. (Exp.)	Ref.	Significance Obs. (Exp.)	Ref.	Significance Obs. (Exp.)	Ref.
Run-1						
$\gamma\gamma$	$5.2\,\sigma$ $(4.6\,\sigma)$	[77]	$5.6\,\sigma$ $(5.3\,\sigma)$	[55]	not reported[†]	[28]
ZZ	$8.1\,\sigma$ $(6.2\,\sigma)$	[77]	$6.5\,\sigma$ $(6.3\,\sigma)$	[55]	not reported[†]	[28]
WW	$6.5\,\sigma$ $(5.9\,\sigma)$	[77]	$4.7\,\sigma$ $(5.4\,\sigma)$	[55]	not reported[†]	[28]
$\tau\tau$	$4.5\,\sigma$ $(3.4\,\sigma)$	[77]	$3.8\,\sigma$ $(3.9\,\sigma)$	[55]	$5.5\,\sigma$ $(5.0\,\sigma)$	[28]
$b\bar{b}$	$1.4\,\sigma$ $(2.6\,\sigma)$	[77]	$2.0\,\sigma$ $(2.6\,\sigma)$	[55]	$2.6\,\sigma$ $(3.7\,\sigma)$	[28]
Run-2						
$\tau\tau$	–		$4.9\,\sigma$ $(4.7\,\sigma)$	[73]	–	
$b\bar{b}$	$3.5\,\sigma$ $(3.0\,\sigma)$	[74]	$3.3\,\sigma$ $(2.8\,\sigma)$	[75]	–	
Run-1 +Run-2						
$\tau\tau$	–		$5.9\,\sigma$ $(5.9\,\sigma)$	[73]	–	
$b\bar{b}$	–		$3.8\,\sigma$ $(3.8\,\sigma)$	[75]	–	

Higgs boson self coupling

The measurement of the Higgs boson self-coupling is an important probe of the Higgs potential and of the electroweak symmetry breaking mechanism. Studies show that it is very challenging to measure the trilinear coupling and impossible to measure the quartic self-coupling even with the full data set of $3\,\mathrm{ab}^{-1}$ of the high-luminosity upgrade of the LHC (HL-LHC) [20].
The trilinear Higgs boson self-coupling can be measured in Higgs boson pair production. The ATLAS and CMS experiments performed studies of the prospects for measuring the trilinear self-coupling in $HH \to b\bar{b}\gamma\gamma$, $HH \to b\bar{b}\tau\tau$ and $HH \to b\bar{b}WW$ events at the HL-LHC. The most sensitive channel is $HH \to b\bar{b}\gamma\gamma$, for which a signal significances of the trilinear self-coupling measurement of $1.3\,\sigma$ and $1.6\,\sigma$ are expected by the ATLAS [84] and CMS [85] experiments, respectively.

Higgs boson spin and parity

In the SM, the Higgs boson is a scalar particle with even CP quantum number eigenstate. Alternative hypotheses of a pure higher order scalar eigenstate, e.g. HVV interactions with $c_\alpha \kappa_{\mathrm{HVV}} \neq 0$ and $c_\alpha \kappa_{\mathrm{SM}} = 0$, a pure pseudoscalar, vector or pseudovector state, and various spin-2 models have been excluded in favour of the SM expectation both by the ATLAS and the CMS collaboration [14–16]. In the Lagrangian of a pure higher order scalar eigenstate only CP-even terms are included that are of higher order than the SM tree-level term with dimension four. Also the CDF and D0 experiments at the Tevatron found no significant deviations from the SM prediction [86].

The ATLAS and CMS Higgs boson spin and CP measurements have been performed in $H \to ZZ^* \to 4\ell$, $H \to WW^* \to \ell\nu\ell\nu$ and $H \to \gamma\gamma$ decays. Since the decay of a spin-1 particle into two massless vector bosons is forbidden by the Landau-Yang theorem [87, 88], the spin-1 hypothesis is already excluded by the observation of $H \to \gamma\gamma$ decays. The Landau-Yang theorem, however, applies only for an on-shell resonance, i.e. in the narrow-width approximation of the Higgs boson resonance. In addition, it is not excluded that the two reconstructed photons in the $H \to \gamma\gamma$ decays actually are a pair of two collinear photons which cannot be separated experimentally. Therefore, the spin-1 hypothesis has been tested [15].

In Figures 1.12 and 1.13 the distributions of the test statistic for probing the different

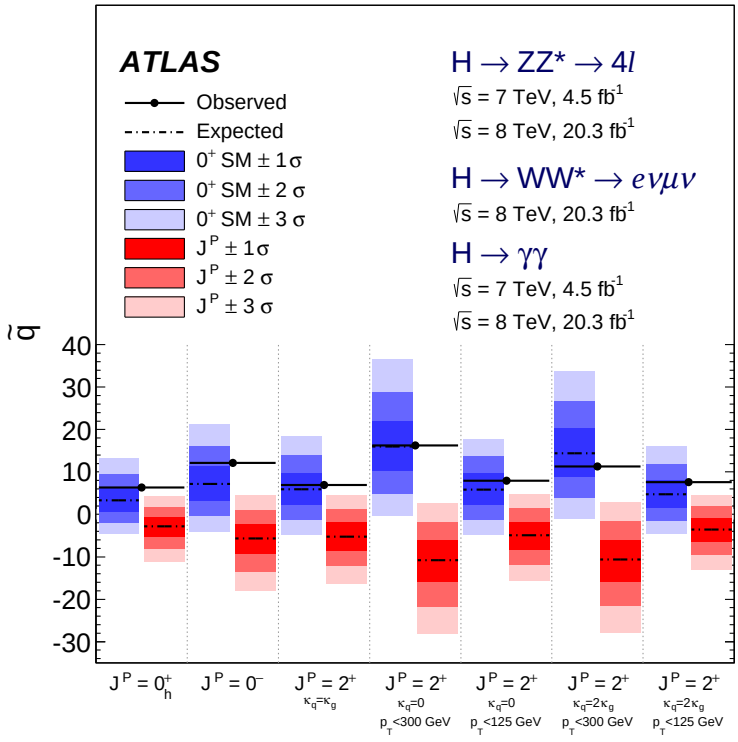

Figure 1.12: Distributions of the test statistics for probing alternative spin-0 and spin-2 hypotheses against the SM prediction of a scalar, CP-even ($J^P = 0^+$) state for the combined $H \to ZZ^* \to 4\ell$ and $H \to WW^* \to \ell\nu\ell\nu$ decays in the full ATLAS Run-1 data set [14]. The distribution for the SM hypothesis is shown in blue and for the alternatives in red.

spin-CP hypotheses against the SM hypothesis, measured by the ATLAS and CMS experiments, are shown. The SM expectation is favoured in all cases. While pure higher order scalar and pseudoscalar states have been ruled out, CP-even and CP-odd admixtures from BSM physics to the predominately SM CP-even Higgs boson state are still possible. This can be probed by measuring the tensor structure of Higgs boson couplings. In this thesis, such measurements have been performed in $H \to ZZ^* \to 4\ell$ decays.

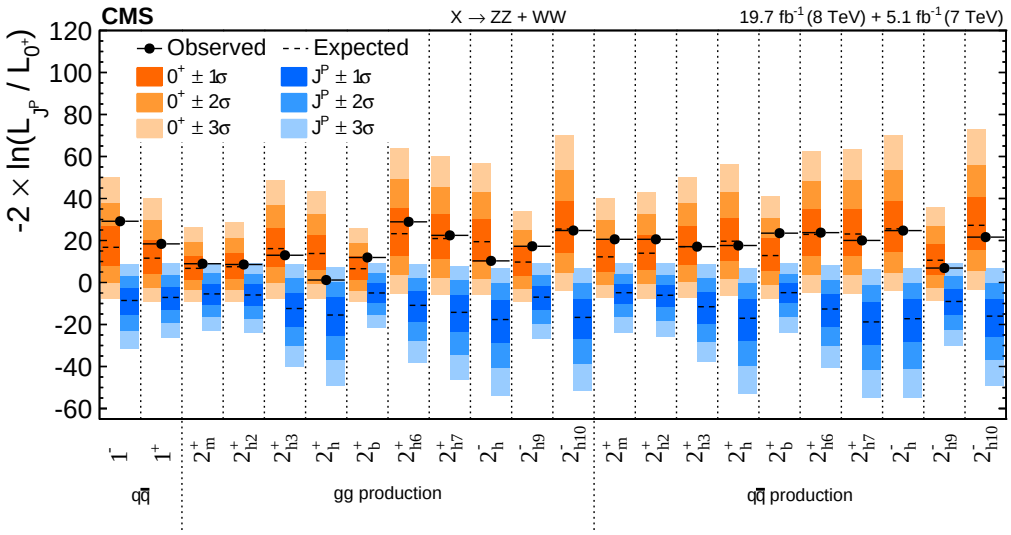

Figure 1.13: Distributions of the test statistics for probing alternative spin-1 and spin-2 hypotheses against the SM prediction of a scalar, CP-even ($J^P = 0^+$) state for the combined $H \to ZZ^* \to 4\ell$ and $H \to WW^* \to \ell\nu\ell\nu$ decays in the full CMS Run-1 data set [16]. The distribution for the SM hypothesis is shown in orange and for the alternatives in blue.

Chapter 2

The ATLAS experiment at the Large Hadron Collider at CERN

In this chapter the ATLAS experiment at the LHC is described. First, the LHC accelerator systems and experiments are introduced together with the CERN research centre. This is followed by an overview of proton-proton collision physics. The ATLAS detector and its subdetectors as well as the data taking conditions are described in the last section.

2.1 The CERN accelerator complex and the experiments at the Large Hadron Collider

CERN (Conseil Européen pour la Recherche Nucléaire) is the european centre for particle physics. It was founded in 1954 and provides infrastructure for fundamental research in the field of particle physics [89]. Located at the border between Switzerland and France, CERN hosts a unique complex of particle accelerators (see Figure 2.1) including the world's largest collider ring, the LHC.

The LHC is 26.7 km in circumference and is located 45 m to 170 m underground [91, 92]. For a large variety of research programs, the LHC collides protons up to energies of 13 TeV and heavy ions, lead nuclei, up to 5.02 TeV per colliding nucleon pair. Before the protons or lead ions reach the LHC ring and are accelerated to their highest energies, they are passing through a series of accelerators summarised in Table 2.1.

First collisions at the LHC took place in 2008. Since then, there have been two very successful periods of data taking referred to as Run-1 and Run-2. Run-1 spanned

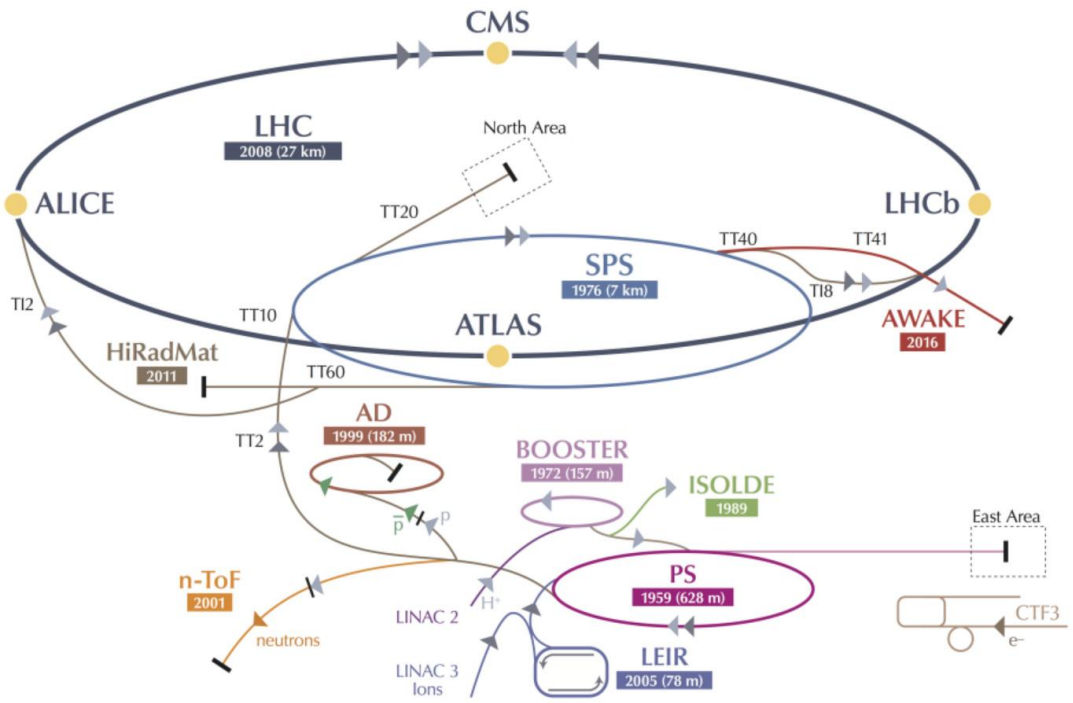

Figure 2.1: Overview of the CERN accelerator complex and experiments [90].

Table 2.1: Summary of the CERN accelerator complex for proton and lead ion collisions at the Large Hadron Collider.

Step	Proton acceleration		Lead ion acceleration	
	Accelerator	Beam energy	Accelerator	Beam energy/nucleon
1.	Linear Accelerator 2 (LINAC2)	50 MeV	Linear Accelerator 3 (LINAC3)	4.2 MeV
2.	Proton Synchrotron Booster (PSB)	1.4 GeV	Low Energy Ion Ring (LEIR)	72 MeV
3.	Proton Synchrotron (PS)	25 GeV	PS	6 GeV
4.	Super Proton Synchrotron (SPS)	450 GeV	SPS	177 GeV
5.	Large Hadron Collider (LHC)	6.5 TeV	LHC	2.5 TeV

the years 2010 to 2012, when proton-proton collisions at energies of $\sqrt{s} = 7$ TeV and $\sqrt{s} = 8$ TeV took place. The second period, Run-2 at a centre-of-mass energy of 13 TeV, is still ongoing. Data taking started in 2015 and will continue until end of 2018. Up to now, the LHC has been running at a maximum centre-of-mass-energy of 13 TeV for proton-proton collisions and of 5.02 TeV per nucleon pair for heavy ion collisions. The design collision energies of 14 TeV and 5.6 TeV, respectively, are expected to be

reached in the next years. More details on Run-1 and Run-2 run conditions and on the data sets recorded by the ATLAS detector can be found in Sections 2.2.1 and 2.3.5, respectively.

In total, seven experiments are located along the LHC ring. ATLAS and CMS are multi-purpose detectors with a large variety of physics topics including the study of the Higgs boson. The ALICE experiment [93] is studying quark-gluon plasma and the LHCb experiment is focusing on b-hadron physics [94]. ATLAS and CMS have specifically been designed for the search for the Higgs boson. On the 4th July 2012, the discovery of a new Higgs-like boson was announced by ATLAS and CMS [1, 2]. Peter Higgs and François Englert were rewarded the Nobel price for physics in 2013 for the formulation of the Higgs mechanism [7–12]. Three smaller experiments are located next to the larger detectors. LHCf [95], next to ATLAS, is studying the forward production of particles in the direction of the beam pipe. MoEDAL [96], next to LHCb, is searching for magnetic monopoles. And TOTEM [97], in the same cavern as CMS, measures the total proton-proton cross section and studies elastic scattering and diffractive processes in forward direction.

In this thesis proton-proton collision data taken with the ATLAS detector are studied.

2.2 Proton-proton collision physics

The number N of events produced by a certain process at a collider, e.g. Higgs boson production, is the product of the cross section σ of the process and of the integrated luminosity:

$$N = L \cdot \sigma. \tag{2.1}$$

While the cross section is specific to the process, the luminosity is solely a property of the collider. In order to probe interesting processes with small cross sections and to find signals over a possibly large background, a large number of events, i.e. high luminosity, are beneficial.

2.2.1 Luminosity

The instantaneous luminosity measures the number of proton-proton interactions per unit cross section and time [98] and is given by

$$L_{inst} = \frac{f\, n_b\, N_1\, N_2}{\Sigma_x\, \Sigma_y} \qquad \left[\frac{1}{\mathrm{s\ cm^2}}\right]. \tag{2.2}$$

It is proportional to the bunch collision frequency f, the number of bunches per beam n_b and the number of protons per bunch N_i $(i = 1, 2)$. The widths of the horizontal and vertical beam profiles at the point of collision are Σ_x and Σ_y, respectively. For high instantaneous luminosities highly focused beams, e.g. small $\Sigma_{x/y}$, are necessary.

The run conditions for the LHC in the data taking period from 2010 to June 2016 are summarised in Table 2.2. For this thesis data from 2011 until December 2016 are used. The LHC is designed for $n_b = 2808$, a bunch frequency of $f = 25\,\mathrm{ns}$ and $N = 1.15 \cdot 10^{11}$ protons per bunch. Design instantaneous luminosities of the LHC are 10^{34} $\mathrm{cm^{-2}s^{-1}}$ for proton-proton collisions and 10^{27} $\mathrm{cm^{-2}s^{-1}}$ for heavy ion collisions [91]. Both values have been reached in 2016 [99].

Table 2.2: Overview of the LHC run conditions [100].

Parameter	Run-1			Run-2		Design
	2010	2011	2012	2015	2016 (until June)	value
Beam energy	3.5	3.5	4.0	6.5	6.5	7.0
Maximum number of bunches n_b	368	1380	1380	2244	2076	2808
Minimum bunch spacing $1/f$ [ns]	150	50	50	25	25	25
Protons per bunch N [10^{11} protons] (average at start of collisions)	1.0	1.3	1.5	1.1	1.1	1.15
Peak inst. luminosity L_{inst} [10^{34} $\mathrm{cm^{-2}s^{-1}}$]	0.021	0.35	0.77	0.51	1.01	1.0
Integrated luminosity delivered L [$\mathrm{fb^{-1}}$]	0.048	5.5	22.8	4.2	8.1	–

The number of collision events available for analysis is determined by the integrated luminosity L, which is the time integral of the instantaneous luminosity:

$$L = \int L_{inst}\, \mathrm{d}t \qquad \left[\frac{1}{\mathrm{cm^2}}\right]. \tag{2.3}$$

The integrated luminosities delivered by the LHC in the years 2010 to June 2016 are also listed in Table 2.2.

2.2.2 Proton-proton collision cross section and parton distribution functions

At the LHC protons are collided, which are bound states of three valence quarks (uud), sea quark-antiquark pairs and gluons. Quarks and gluons are subject to the strong interaction described by QCD (see Section 1.1). The hard-scattering process in proton-proton collisions at high energies takes place between the proton constituents, quarks and gluons or partons, and can be described by QCD perturbation theory.

Each parton carries a fraction x of the total proton momentum. The parton distribution function (PDF) $f(x)$ is the probability density distribution of the momentum fraction of each particle type. At leading-order (LO) in QCD, the total proton-proton cross section is given by

$$\sigma_{tot} = \int_0^1 \mathrm{d}x_1 \int_0^1 \mathrm{d}x_2 \sum_{ij} f_i(x_1) f_j(x_2)\, \widehat{\sigma}_{ij}(x_1 x_2 s) \tag{2.4}$$

with the parton distribution functions $f_i(x_1)$ and $f_j(x_2)$ of the colliding partons i and j, the LHC centre-of-mass energy $\sqrt{s}$, and the cross section $\widehat{\sigma}$ of the parton interaction taking place at energy $\sqrt{x_1 x_2 s}$. The parton distribution functions cannot be calculated perturbatively. Instead they have to be determined from deep inelastic electron/neutrino-proton scattering and proton-(anti)proton collider data, e.g. from Drell-Yan gauge boson and inclusive jet production measurements.

The parton distribution functions measured at a certain energy scale Q are extrapolated to the LHC energies using the DGLAP evolution equations [101–103] at a certain order of QCD correction. Parton distribution functions are provided by dedicated groups as so-called PDF sets, which are for instance CT [104], MMHT [105] and NNPDF [106, 107]. For the LHC measurements, the available PDF sets are combined to the so-called PDF4LHC set [108]. In Figure 2.2, the proton PDFs are shown for energies of $s = Q^2 = 10\ \mathrm{GeV}^2$ and $10^4\ \mathrm{GeV}^2$. The main fraction of the proton energy is carried by gluons, followed by sea and valence quarks. The gluon and sea quark PDFs increase rapidly towards small x, while the valence quark PDFs peak at a momentum fraction of about $x = 0.1$. The gluon and sea quark PDFs have a large uncertainty

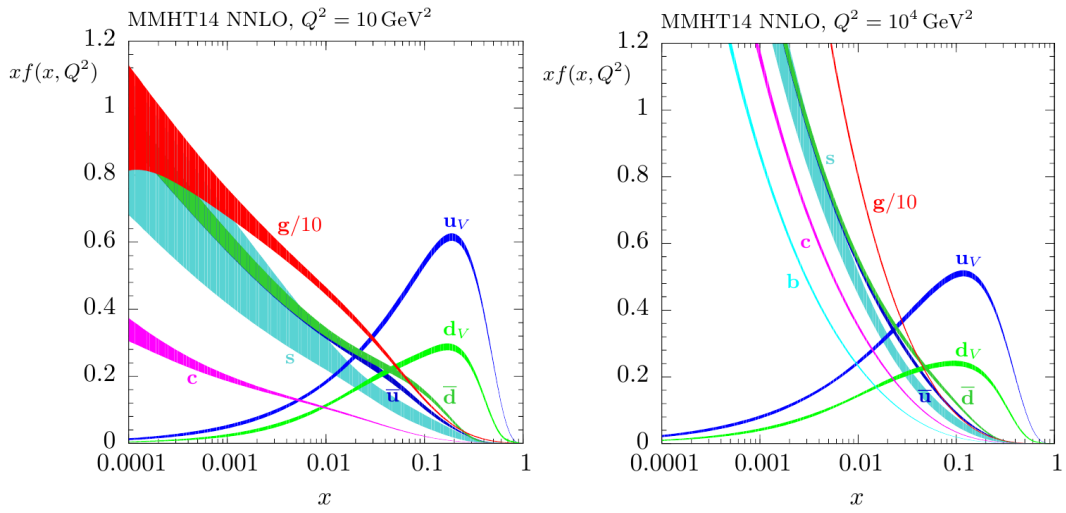

Figure 2.2: The MMHT2014 PDF sets at next-to-next-to-leading-order (NNLO) QCD at centre-of-mass-energies $s = Q^2 = 10$ GeV^2 (left) and 10^4 GeV^2 (right) with 68 % confidence level uncertainty bands [105].

especially at small x. At LHC energies, momentum fractions of the colliding partons in the range $x = 10^{-3} - 10^{-1}$ are most relevant. Therefore, production processes are often dominated by gluon fusion.

In Figure 2.3 cross sections of different processes produced in proton-(anti)proton collisions are shown over a wide range of centre-of-mass energies. Interesting processes, such as Higgs boson production, are many orders of magnitude below the total proton-(anti)proton cross section. Therefore, high-collision rates and a selective trigger system are needed in order to sort out interesting events from the large QCD background (see Sections 2.3.2 and 2.3.5).

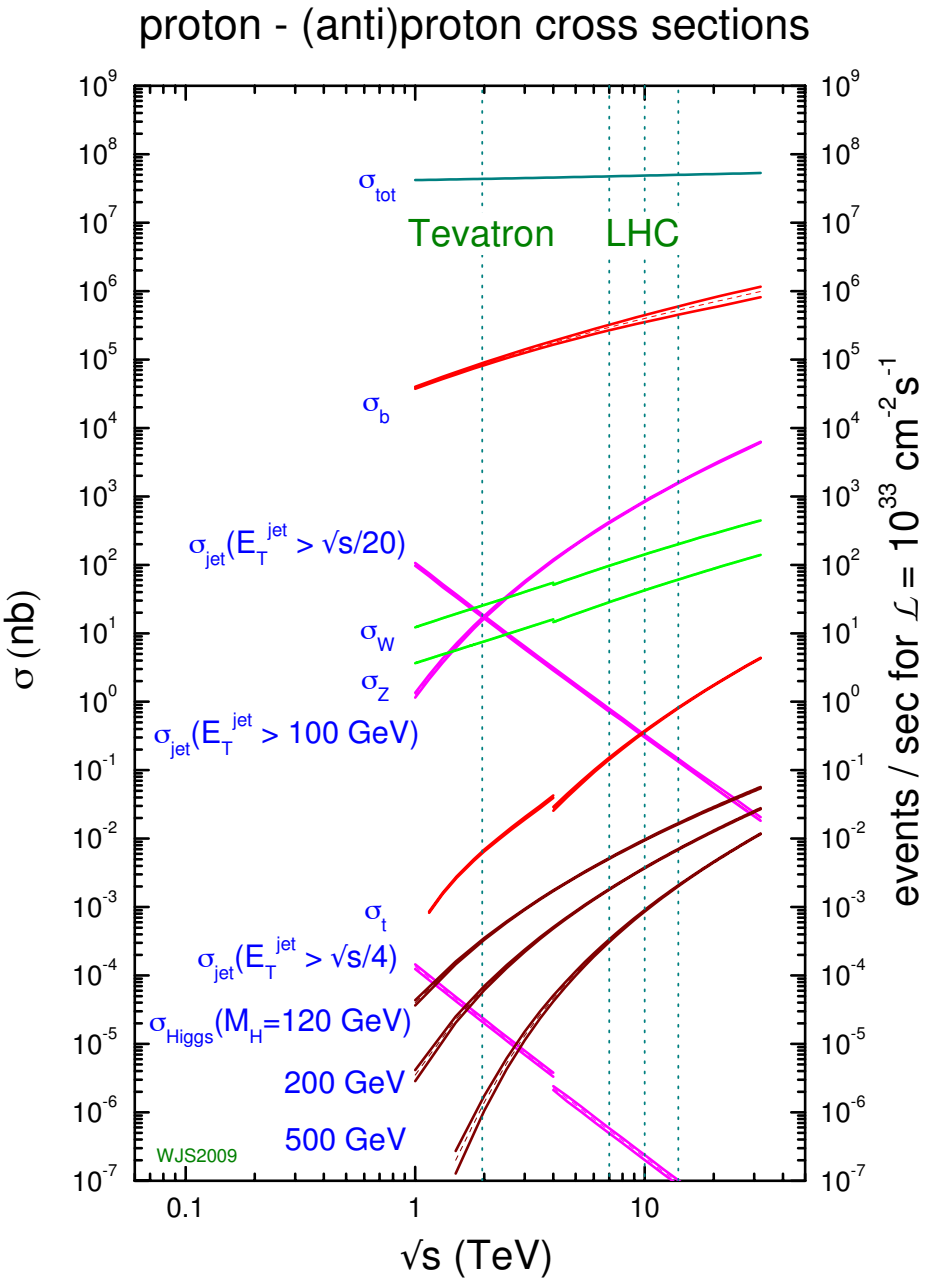

Figure 2.3: Cross sections of selected processes (left y-axis) and corresponding event rates at an instantaneous luminosity of $L_{inst} = 10^{33}$ cm^{-2} s^{-1} (right y-axis) as a function of the centre-of-mass energy at hadron colliders [109]. The break in the cross section curves is at the transition from proton-antiproton (at the Tevatron) to proton-proton collisions (at the LHC).

2.3 The ATLAS detector

The ATLAS detector [94] is a multi-purpose detector for high-energy physics at the LHC. The main goal of the ATLAS experiment was to find the Higgs boson in proton-proton collisions at the LHC, which was achieved in 2012. Other motivations for the experiment are SM precision measurements and the search for physics beyond the Standard Model (BSM). Also studies of heavy ion collisions at the LHC are performed. The components of the ATLAS detector are described after the introduction of the ATLAS coordinate system and nomenclature. The particle reconstruction in the ATLAS experiment is discussed in Chapter 3.

2.3.1 Nomenclature

ATLAS coordinate system

The nominal proton-proton interaction point is the origin of the coordinate system (see Figure 2.4). The z-axis is pointing along the beam direction and the x-y plane is transverse to it with the positive x-axis pointing towards the centre of the LHC ring and the positive y-axis pointing upwards. The azimuthal angle ϕ is measured around the beam axis and the polar angle θ from the beam axis as shown in Figure 2.4. The transverse momentum p_{T} and the transverse energy E_{T} are the projections of the momentum $\vec{p}$ and energy $\vec{E}$ vectors in the transverse plane:

$$p_{\mathrm{T}} = |\vec{p}| \cdot \sin\theta, \tag{2.5}$$

$$E_{\mathrm{T}} = |\vec{E}| \cdot \sin\theta. \tag{2.6}$$

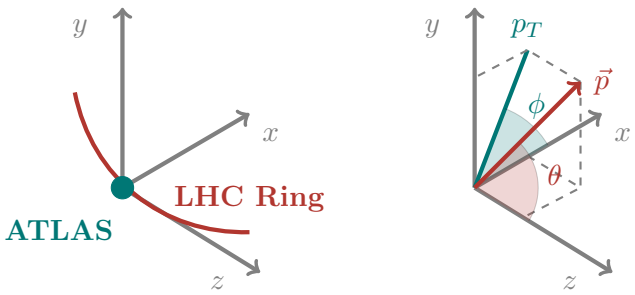

Figure 2.4: Illustration of the ATLAS coordinate system in Cartesian (left) and polar coordinates (right) [110].

Pseudorapidity and rapidity

Instead of the polar angle θ, the pseudorapidity

$$\eta = -\ln \tan\left(\frac{\theta}{2}\right) \tag{2.7}$$

illustrated in Figure 2.5 is frequently used which is defined symmetric with respect to the transverse plane. Large values of $|\eta|$ correspond to small angles to the beam, while $\eta \approx 0$ is close to the transverse plane. For massive objects, in particular for jets, the rapidity is used:

$$y = \frac{1}{2} \ln \frac{E + p_z}{E - p_z}. \tag{2.8}$$

For massless objects η becomes equal to the rapidity y.

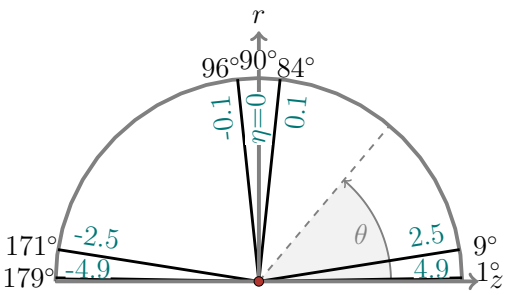

Figure 2.5: Illustration of relation between polar angle θ and pseudorapidity η where $r = \sqrt{x^2 + y^2}$ is the radius parameter in the transverse plane.

Angular distance

The angular distance between two objects is given by

$$\Delta R = \sqrt{\Delta\eta^2 + \Delta\phi^2}, \tag{2.9}$$

with the distances $\Delta\eta = (\eta_1 - \eta_2)$ and $\Delta\phi = (\phi_1 - \phi_2)$ in pseudorapidity and azimuthal angle.

Impact parameter

A measure for the association of tracks to the primary, hard-scattering vertex and to secondary vertices displaced from the primary vertex are the transverse and longitudinal impact parameters illustrated in Figure 2.6. The transverse impact parameter d_0 is defined as the distance of closest approach to the beam axis, while the longitudinal impact parameter z_0 is the z-coordinate of the point of closest approach.

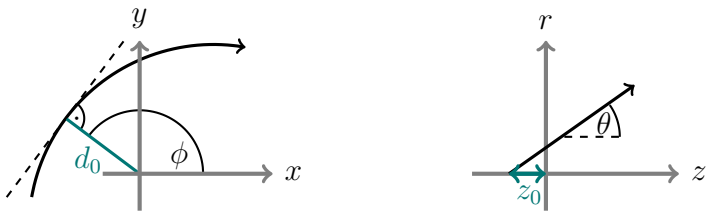

Figure 2.6: Illustration of transverse (left) and longitudinal (right) track impact parameters.

Energy-momentum conservation in the transverse plane

At hadron colliders, e.g. the LHC, composite particles collide. The longitudinal momenta of the incoming partons in the hard-scattering process are unknown and the fragmentation products of the partons not participating in the hard-scattering process leave the interaction region undetected in the direction of the beam pipe. Thus, energy-momentum conservation can only be employed in the transverse plane. The sum of the transverse momenta of all final state objects has to be zero,

$$\sum_{\substack{\text{final state} \\ \text{objects}}} \vec{p}_{\mathrm{T},j} = \vec{0}, \tag{2.10}$$

because the incoming partons in the collisions have no transverse momenta. This is helpful for the reconstruction of neutrinos or new particles, which leave the detector undetected. They can be detected due to the imbalance in the transverse momentum and energy. The missing transverse energy corresponding to the energy of undetected

particles is given by

$$E_T^{miss} = -\left| \sum_{\substack{\text{final state} \\ \text{objects}}} \vec{p}_{\mathrm{T},j} \right| . \tag{2.11}$$

Parameters in the transverse (x-y) plane are therefore an important quantity for physics analysis.

2.3.2 Detector components

An overview of the ATLAS detector is shown in Figure 2.7. With a length of about 44 m and a diameter of 25 m it is the largest collider detector built so far. The detector covers almost the full solid angle and is forward-backward symmetric with respect to the beam direction.
The inner tracking detector is closest to the beam line, followed by the electromagnetic and hadronic calorimeters which measure the energies of electromagnetically and hadronically interacting particles. The muon spectrometer which determines the size of the ATLAS detector surrounds the calorimeters. The magnet system of the ATLAS detector consists of two superconducting magnets, a solenoid and a toroid magnet. The first one surrounds the inner detector, while the second belongs to the muon spectrometer.
In the following, all ATLAS subdetector systems and the trigger and data acquisition system are explained. The detector stayed mostly the same during the two LHC runs, except that a new innermost pixel detector layer, the Insertable B-Layer, and additional muon chambers were inserted during the 2013-2014 shut down when the LHC was upgraded from $\sqrt{s} = 8$ to 13 TeV.

Magnet system

A special feature of the ATLAS detector are the two superconducting magnet systems. A thin solenoid magnet surrounds the inner detector producing a magnetic field strength of 2 T. The second one is part of the muon detector and consists of three air-core toroid magnets with eight coils each one in the barrel and one in each endcap region (see Figures 2.7 and 2.8). They provide a magnetic field with a bending power of ~ 2.5 Tm in the barrel region ($|\eta| < 1.05$) of the muon spectrometer and of up to 6 Tm

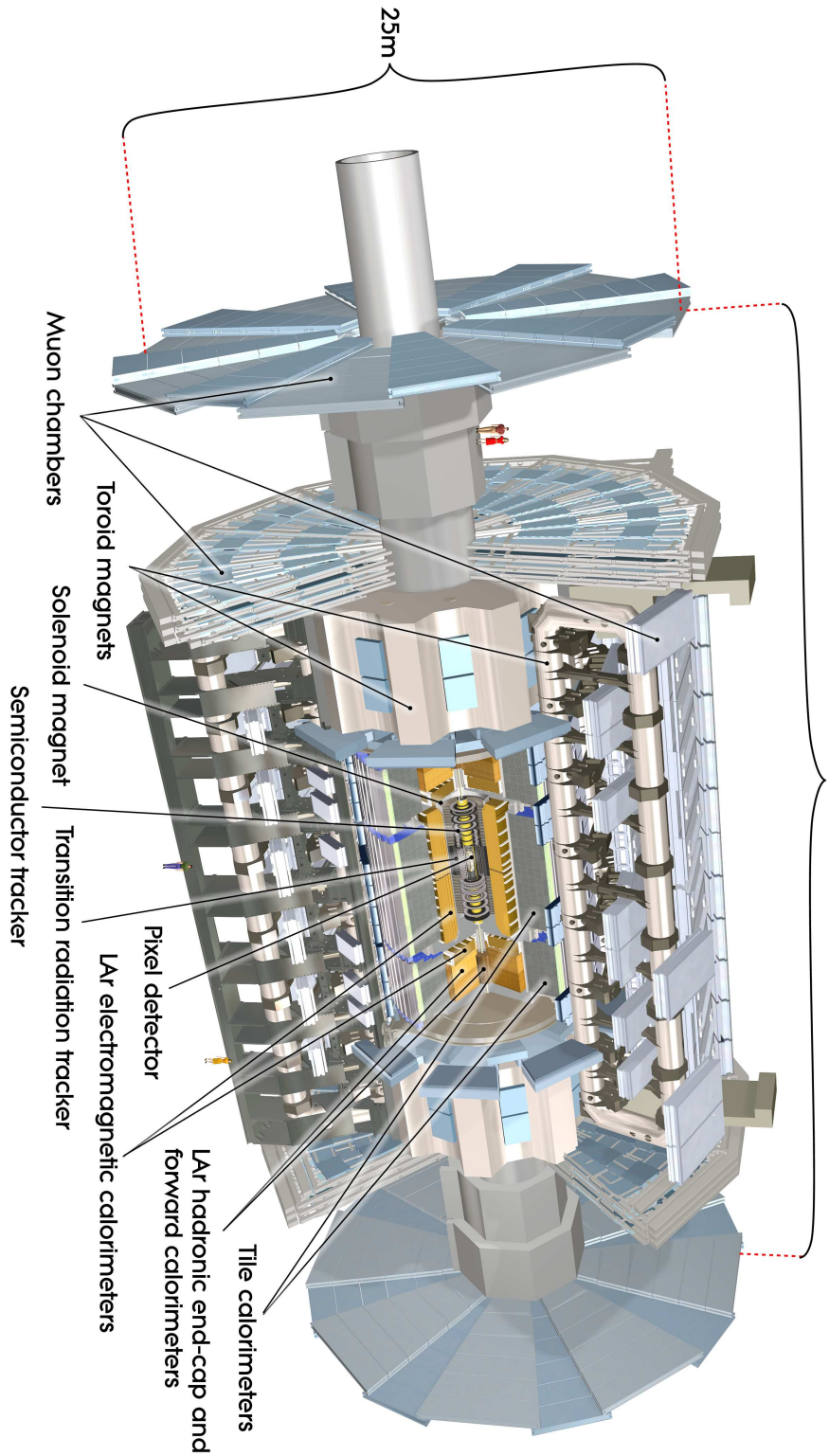

Figure 2.7: Schematic view of the ATLAS detector [111].

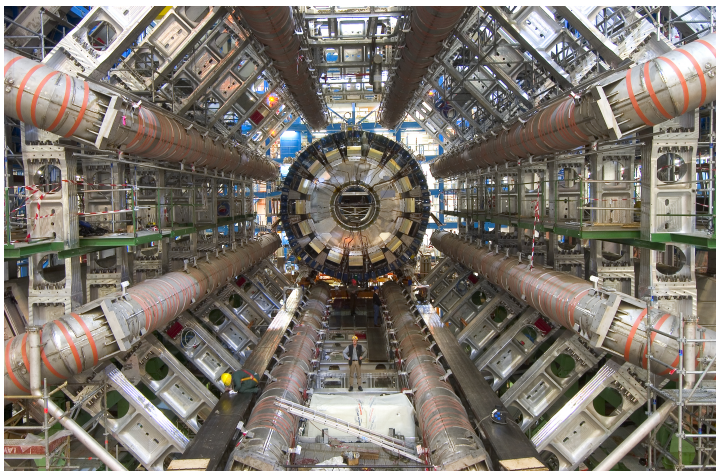

Figure 2.8: Photo of the barrel toroid magnet of the ATLAS detector with its eight superconducting coils [112].

in the endcaps (extending up to $|\eta| = 2.7$). The air-core toroid magnetic field allows for precise muon momentum measurement independent of the inner detector.

Inner detector

The inner detector provides high precision track measurement of charged particles in the 2 T solenoid field. It consists of three subdetectors (see Figure 2.9): The silicon pixel detector is surrounded by the silicon strip detector layers of the semiconductor central tracker (SCT) and the transition radiation tracker (TRT). Between Run-1 and Run-2 an additional inner pixel layer, the Insertable B-Layer (IBL) was installed between a new beam pipe with smaller radius and the already existing pixel tracker. It was added in order to provide measurements closer to the interaction point which improves track vertex reconstruction and identification of b-jets [113, 114]. In addition to continuous tracking the TRT provides the electron identification in up to 36 layers of straw drift tubes by means of the characteristic emission of transition radiation. It covers a pseudorapidity range of $|\eta| < 2.0$, while the SCT provides precise track reconstruction up to $|\eta| = 2.5$. The inner detector measures the momenta of charged particles in the 2 T solenoid magnetic field with a resolution of $\sigma_{p_\mathrm{T}}/p_\mathrm{T} = 0.05\,\% \, p_\mathrm{T} \oplus 1\,\%$.

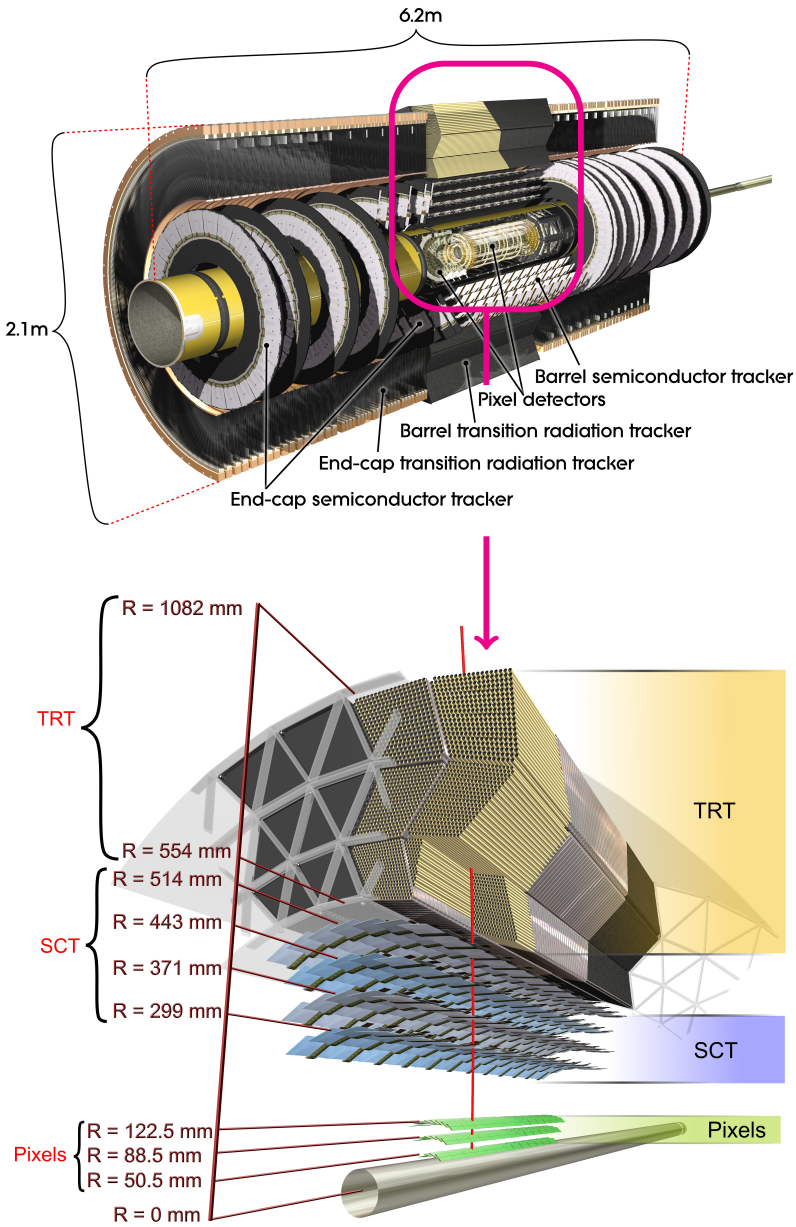

Figure 2.9: Cut-away views of the ATLAS inner tracker [115]. The bottom part shows an enlarged view of a section of the barrel part

Electromagnetic and hadronic calorimeters

The energies of particles are determined by the calorimeter system. The particles are stopped in the calorimeter loosing their energies in interactions with the detector material and producing particle showers. The energy of the initial particle is determined from the energies of the shower particles. The calorimeter system consists of two subsystems: the energies of electromagnetically interacting particles, especially electrons and photons, are measured in the electromagnetic calorimeter, while hadrons interacting via the strong force are stopped mostly in the surrounding hadronic calorimeter.
The ATLAS calorimeter system covers the solid angle up to $|\eta| = 4.9$. It consists of the following components (see Figure 2.10): the electromagnetic calorimeter surrounds the inner detector covering $|\eta| < 3.2$, it is followed by the hadronic calorimeters. Including the forward calorimeter they cover the solid angle up to $|\eta| = 4.9$. The electromagnetic calorimeter, which is divided into a barrel part within $|\eta| < 1.475$ and two endcaps covering $1.375 < |\eta| < 3.2$, uses liquid argon as active medium and lead as absorber materials. The hadronic calorimeter employs steel as absorber and scintillating tiles as active medium in the barrel region ($|\eta| < 1.7$), while the two hadronic endcap calorimeters in the region $1.5 < |\eta| < 3.2$ use copper and liquid argon, respectively. The two forward calorimeters in the range $3.1 < |\eta| < 4.9$ use copper and liquid argon, and tungsten and liquid argon for electromagnetic and hadronic shower measurements, respectively. In total, the calorimeters contain more than 188000 readout channels and provide an energy resolution of $\sigma_E/E = 10\,\%/\sqrt{E} \oplus 0.7\,\%$ in the electromagnetic and of $\sigma_E/E = 50\,\%/\sqrt{E} \oplus 3\,\%$ and $\sigma_E/E = 100\,\%/\sqrt{E} \oplus 10\,\%$ in the barrel and endcap hadronic calorimeters.

Muon spectrometer

The muon spectrometer, depicted in Figure 2.11, is the outermost subdetector defining the large dimension of the ATLAS detector. Muons are the only charged particles that pass the calorimeter system. The ATLAS muon system is designed to detect muons with high efficiency in the pseudorapidity range $|\eta| < 2.7$ and measure their momenta with high precision in the magnetic field of the three toroid magnets. It consists of a barrel part with $|\eta| < 1.05$ and two endcap regions in the range $1.05 < |\eta| < 2.7$. High precision muon tracking is performed in three layers of Monitored Drift Tube (MDT) chambers. For $|\eta| > 2$, the inner layer consists of Cathode Strip Chambers

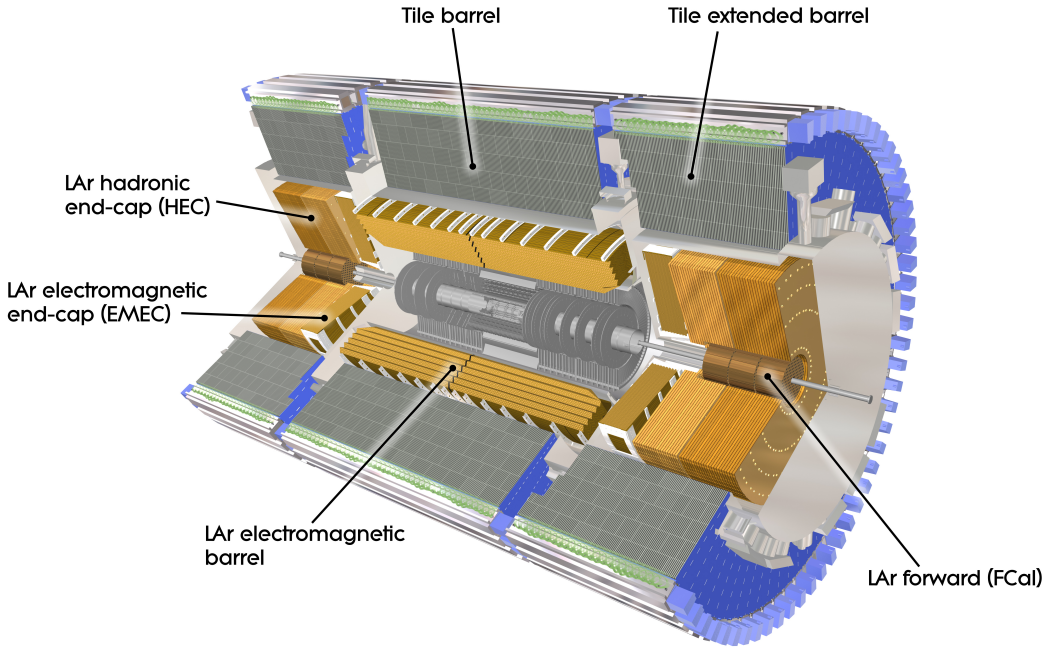

Figure 2.10: Schematic view of the electromagnetic and hadronic calorimeters of the ATLAS detector [116].

(CSC) instead of MDTs.

During the shut down after LHC Run-1, the muon spectrometer was equipped with additional MDT chambers in the transition region between barrel and endcaps in the range $1.0 < |\eta| < 1.4$. Additional small-diameter Muon Drift Tube (sMDT) chambers [117] with a doublet of RPC chambers (see below) were installed in access shafts in the barrel bottom middle layer. Dedicated fast chambers, Resistive Plate Chambers (RPC) in the barrel and Thin Gap Chambers (TGC) in the endcaps, provide level-1 muon trigger signals up to $|\eta| = 2.4$ and position measurement along the drift tubes. The muon spectrometer is designed to achieve a relative muon momentum resolution of better than 3 % over a wide range of transverse momenta and almost 10 % at $p_{\mathrm{T}} \approx 1$ TeV.

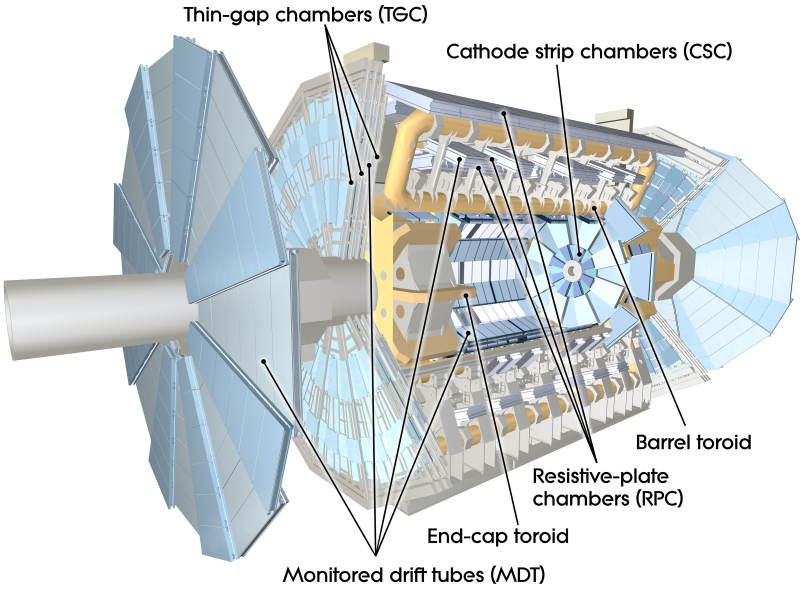

Figure 2.11: Cut-away view of the muon spectrometer of the ATLAS detector [118].

Trigger and data acquisition system

In ATLAS, a multi-level trigger system is employed [119, 120]. The schematics of the Run-2 trigger system is shown in Figure 2.12. It consists of a hardware-based level-1 trigger and a software-based high-level trigger (HLT). The Run-1 trigger system was similar, except that the high-level trigger was split into two stages. The event rate is reduced from 40 MHz, the proton bunch collision frequency, to 100 kHz by the level-1 trigger, and further to about 1.5 kHz by the HLT resulting in a data rate of 1.5 GB per second written to long-term storage.

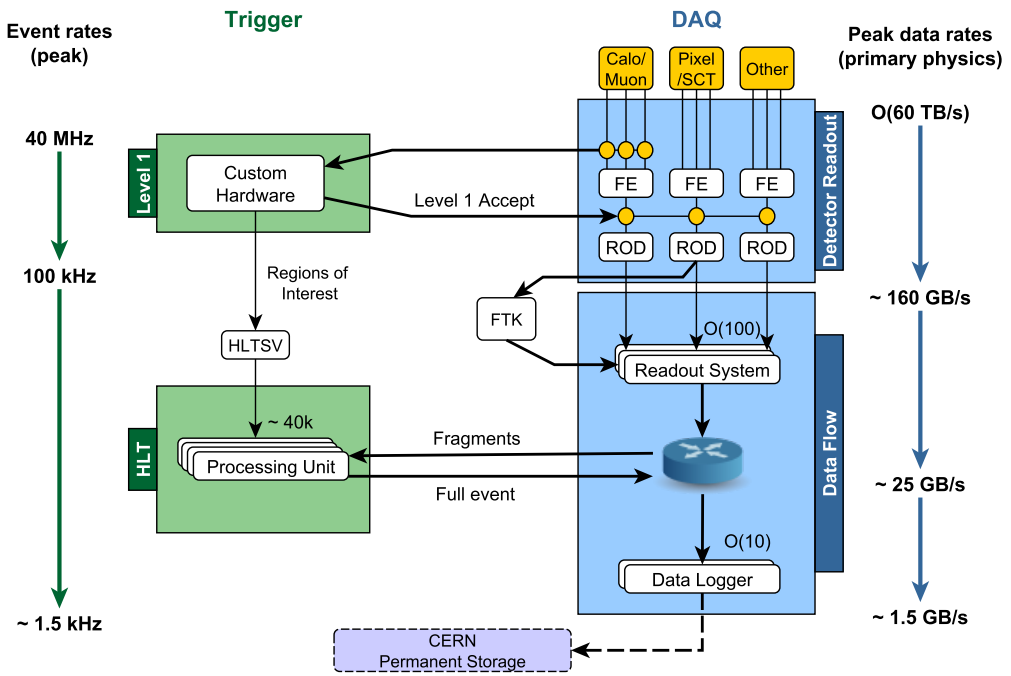

Figure 2.12: Schematics of the trigger and data acquisition system of the ATLAS detector for Run-2 [121].

2.3.3 Pile-up

In addition to the hard-scattering process, that is triggering the event, on average 24 collisions per bunch crossing occur at the present maximum LHC luminosity, an effect called *pile-up*. The amount of pile-up events depends on the run conditions and increases with the instantaneous luminosity. In Figure 2.13, the mean numbers of interactions per bunch crossing in the years 2011, 2012, 2015 and 2016 are shown. On average 9, 21 and 23 interactions per crossing have taken place in the runs with $\sqrt{s} = 7$, 8 and 13 TeV, respectively. The maximum number of pile-up interactions can be twice as large.

These additional collisions can be viewed as a background of soft energy depositions, which affect the ATLAS object reconstruction. The following pile-up effects affecting the detector performance can be distinguished: In-time pile-up, which arises from additional

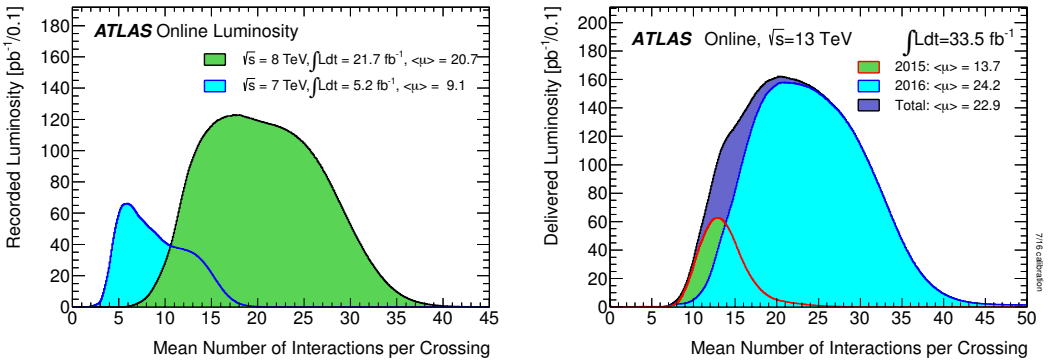

Figure 2.13: Distributions of the mean numbers μ of inelastic interactions per proton-proton bunch crossing for data taking in 2011 and 2012 (left), and for the runs in 2015 and 2016 (right).

proton-proton interactions in the same bunch crossing as the hard scattering process, and out-of-time pile-up, which is due to residual signals in the ATLAS calorimeter bunch-crossings before and after the triggering event. Especially the liquid argon calorimeters are affected by out-of-time pile-up. Large effort has been spent to make the reconstruction performance as independent as possible of the pile-up level.

2.3.4 Luminosity measurement

The number of expected events of a process is directly proportional to the integrated luminosity delivered by the LHC (see Equation 2.1). Precise knowledge of the luminosity is needed for the determination of cross sections. Dedicated detectors are employed to independently determine the luminosity [98] which is given by

$$L_{inst} = \frac{R_{inel}}{\sigma_{inel}}, \tag{2.12}$$

with the rate of inelastic collisions R_{inel} and the cross section σ_{inel} for inelastic proton-proton scattering. The inelastic collision rate depends on the number of proton bunches n_b colliding at frequency f and on the mean number μ of inelastic interactions per bunch crossing:

$$R_{inel} = n_b f \mu. \tag{2.13}$$

Inserting Equation 2.13 into Equation 2.12 gives

$$L_{inst} = \frac{R_{inel}}{\sigma_{inel}} = n_b f \frac{\mu}{\sigma_{inel}}, \tag{2.14}$$

where the only unknown quantity to be measured is the ratio $\frac{\mu}{\sigma_{inel}}$. While μ is directly measured by different subdetectors (see Figure 2.13), the connection with σ_{inel} is determined with the luminosity calibration in van der Meer scans [122] (see below). Three types of algorithms are used for the measurement of μ:

1. *Event counting* algorithms use the number of events satisfying a given selection requirement.

2. *Hit counting* algorithms use the number of hits, active electronic channels or energy deposits above a certain threshold, in a given sub- or luminosity detector per bunch crossing.

3. *Particle counting* algorithms use the number of particles (reconstructed tracks) in a given sub- or luminosity detector per bunch crossing.

For ATLAS physics analysis, mostly event counting methods are used. There are two dedicated luminosity detectors, the BCM (Beam Conditions Monitor) located in the inner detector, and the LUCID (LUminosity measurement using a Cherenkov Integrating Detector) at high pseudorapidities in the beam pipe in front of the forward calorimeters [94].
The absolute luminosity is calibrated with beam separation scans, so-called van der Meer scans [122], where the two beams are moved with respected to each other in horizontal (x) and in vertical (y) direction to measure the horizontal and vertical beam profiles Σ_x and Σ_y. With this input the luminosity can then be computed by using Equation 2.2.

The luminosity of the analysed Run-1 data in 2011 and 2012 is measured with a precision of 1.8 % [123] and 2.8 %, respectively, while the luminosity uncertainty for the Run-2 data set is 3.2 % [98].

2.3.5 Data taking periods

An overview of the luminosities delivered by the LHC and recorded by ATLAS in the years 2011, 2012, 2015 and 2016 is shown in Figure 2.14 and Table 2.3. The data taking

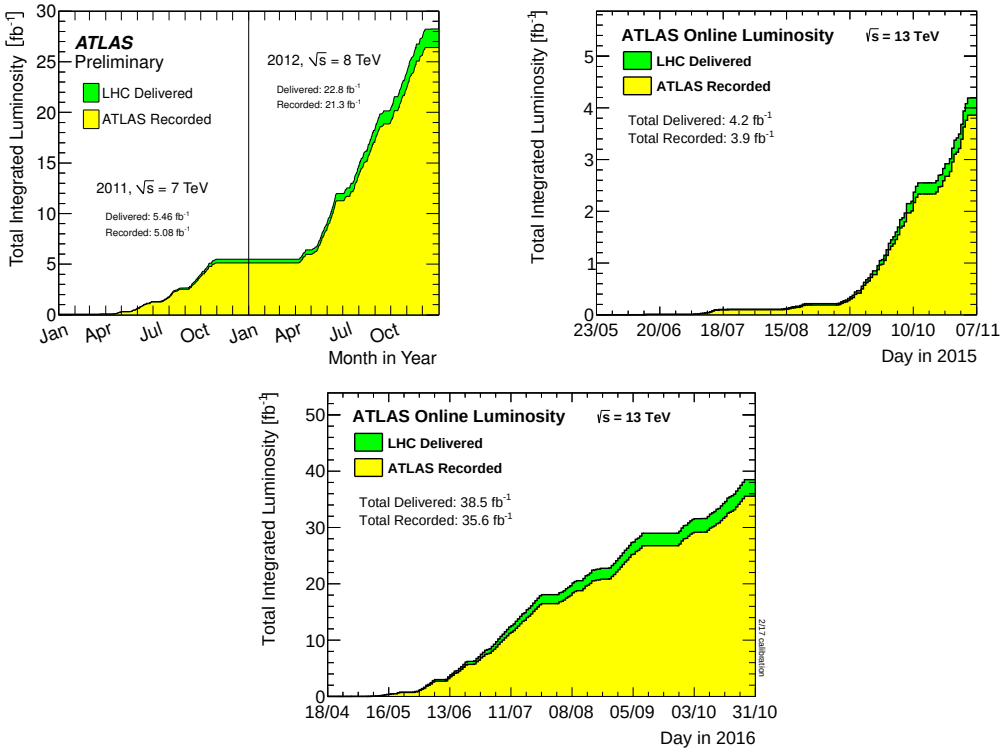

Figure 2.14: The total integrated luminosity delivered by the LHC (green) and recorded by ATLAS (yellow) as a function of time in proton-proton collisions at 7 and 8 TeV centre-of-mass energies in 2011 and 2012 [124](top left) and at 13 TeV in 2015 (top right) and 2016 (bottom) [99].

efficiency of ATLAS was high, around 93.5 % for Run-1 and 92.4 % for Run-2 [99, 124]. The Run-1 data set (without the data from 2010) and the Run-2 data set until December 2016 has been analysed in this thesis. The data sets relevant for this thesis are summarised in Table 2.3.

Table 2.3: Overview of the ATLAS data sets used in this thesis.

Data set	$\sqrt{s}$	L	Data taking period
Run-1	7 TeV and 8 TeV	$4.5\,\text{fb}^{-1}$ and $20.3\,\text{fb}^{-1}$	2011, 2012
Run-2	13 TeV	$36.1\,\text{fb}^{-1}$	2015, 2016

2.3.6 Simulation framework

The measurements have to be compared with the prediction using detailed simulation of the theoretical matrix element calculation and of the detector response and performance. The ATLAS experiment uses a multi-step software framework [125] for the simulation of physics processes in proton-proton collisions at the LHC and of the detector response. It consists of:

1. Event generation:
   Monte Carlo event generators are used to model the hard-scattering process. The hadronisation of final state quarks and gluons as well as initial and final state radiation are simulated with dedicated parton shower programs that are interfaced to the event generators. The simulation of the parton showers and of the fragmentation are tuned to measurements.

2. Simulation of the ATLAS detector:
   The final state particles of the generated events are tracked through the materials and subdetectors of ATLAS using the `GEANT4` program [126].

3. Digitisation of the detector response and object reconstruction:
   The energy depositions in the detector elements are converted into electronic signals and digitised and afterwards reconstructed in the same way as the real data.

4. Pile-up:
   Finally, the effects of multiple proton-proton collisions in the same or adjacent bunch crossings (pile-up) are taken into account by overlapping simulated minimum-bias events generated with PYTHIA 8 [127] using the PDF set MSTW2008LO [128] and with the parton shower simulation tuned to data using the A2 parameter set [129]. The mean number of interactions per bunch crossing is matched to the data by weighting the simulated pile-up events.

The detailed simulation programs used for this thesis are discussed in Section 4.2.

Chapter 3

Particle reconstruction with the ATLAS detector

The methods and performance of particle reconstruction with the ATLAS detector are described in this chapter. The reconstruction, identification and energy-momentum calibration of electrons, muons, hadron jets and b-quark jets relevant for this analysis are explained followed by a discussion of the lepton isolation requirements. The specific analysis-related selection requirements for the reconstructed objects are summarised in Chapter 4.

3.1 Lepton isolation

The amount of lepton isolation is important for electron and muon identification in multi-particle final states, especially with jets. Leptons produced in prompt decays of heavy particles such as the Z-boson, are produced isolated, i.e. without other particles in their vicinity. On the other hand, non-prompt leptons produced in decays of hadrons in jets are usually surrounded by detector activity from other hadrons or hadron decay products. The following two isolation variables are used to suppress the background processes with non-prompt leptons:

Track-based isolation: Sum of the transverse momenta p_{T}^{i} of all charged particle tracks within a cone of size $\Delta\mathrm{R}$ around the lepton candidate direction divided by the transverse momentum p_{T}^{lepton}:

$$I_{track} = \left(\sum_{\Delta\mathrm{R}(i,lepton)<\Delta\mathrm{R}} p_{\mathrm{T}}^{i,track} \right) / p_{\mathrm{T}}^{lepton}. \tag{3.1}$$

The p_{T} of the lepton candidate is excluded from the sum.

Calorimeter-based isolation: Sum of the transverse energies of the calorimeter clusters around the lepton candidate direction divided by the transverse energy E_{T}^{lepton} of the lepton which is subtracted from the sum:

$$I_{calo} = \left(\sum_{\Delta \mathrm{R}(i,lepton)<\Delta \mathrm{R}} E_{\mathrm{T}}^{i,cluster} \right) / E_{\mathrm{T}}^{lepton}. \tag{3.2}$$

Pile-up corrections are applied.

In the $H \to ZZ^* \to 4\ell$ selection described in Chapter 4, electrons and muons are required to be isolated. Similar to the lepton identification efficiency scale factors, that are described in the following, scale factors for isolation efficiency differences between data and simulation are applied.

3.2 Electron reconstruction

The electron track is bent in the solenoid magnetic field, is measured in the inner detector. After traversing the inner detector, electrons deposit their whole energy in the electromagnetic calorimeter by producing electromagnetic showers. Electron candidates are reconstructed by combining inner detector tracks with energy clusters in the electromagnetic calorimeter [130, 131]. The radiative energy losses in the inner detector due to Bremsstrahlung processes are taken into account in a re-fit using the Gaussian Sum Filter algorithm [132].

The ATLAS electron identification distinguishes between prompt electrons and background electrons from misidentified hadron jets, photon conversions, Dalitz decays of pions and semi-leptonic heavy-flavor hadron decays. Three electron identification criteria, *working points*, with increasing background rejection are used: *loose*, *medium* and *tight*. The requirements are based on inner detector and calorimeter measurements including track quality, electromagnetic shower shapes and quality of track-cluster matching. While the electron identification for the 2011 data set at $\sqrt{s} = 7$ TeV is cut-based, an improved identification algorithm based on a likelihood discriminant [130] is used for the remaining data sets.

The identification efficiencies at the three working points are determined by means

of a tag-and-probe method. Pairs of electron candidates from $Z \to e^+e^-$ decays are selected by requiring that their invariant mass is consistent with the Z-boson mass, i.e. that $75 < m_{ee} < 105$ GeV. The tag electron has to fulfil the *tight* identification criteria in addition to the trigger requirements and $p_{\mathrm{T}} > 25$ GeV within $|\eta| < 2.47$. The so-called probe electron is the second reconstructed electron candidate. Here, no identification criteria are imposed. The identification efficiency ϵ at a specific working point is given by the ratio of the number of probe electron candidates identified at that working point $N_{probe}^{identified}$, and of the total number of probe electron candidates N_{probe}:

$$\epsilon = \frac{N_{probe}^{identified}}{N_{probe}}. \tag{3.3}$$

The efficiencies are determined as a function of the transverse energy E_{T} and pseudorapidity η of the probe electron. The number of probe electrons in $Z \to e^+e^-$ and background events is determined from a fit to the dielectron invariant mass distribution.

The electron identification efficiency measurements for Run-2 used for this thesis are based on $Z \to e^+e^-$ events in 2015 data corresponding to an integrated luminosity of $85\,\mathrm{pb}^{-1}$ [131]. For the Run-1 analysis, a data set of $20.3\,\mathrm{fb}^{-1}$ recorded at $\sqrt{s} = 8$ TeV is used, combining $Z \to e^+e^-$ events and $J/\Psi \to e^+e^-$ decays [130]. The efficiency measurements for Run-1 and Run-2 agree very well. The electron identification efficiencies for the *loose*, *medium* and *tight* identification criteria in Run-2 are shown in Figure 3.1 as a function of E_{T} and η. The efficiency is increasing with E_{T} due to lower background rates at high transverse energy. The η-dependence of the efficiency follows the material distribution in the inner detector and the calorimeters. In particular, the efficiency drops in the transition region between the barrel and endcap electromagnetic calorimeters around $|\eta| = 1.5$. The average measured efficiencies for the *loose*, *medium* and *tight* selection are about 95 %, 90 % and 85 %, respectively. The measured electron identification efficiencies differ in general from the simulated values due to detector mismodelling. Each simulated electron candidate is therefore weighted by the scale factor SF^e defined as the ratio of the measured and the simulated electron efficiency in $Z \to e^+e^-$ decays:

$$\mathrm{SF}^e = \frac{\epsilon^{data}(\eta, E_{\mathrm{T}})}{\epsilon^{MC}(\eta, E_{\mathrm{T}})}. \tag{3.4}$$

The uncertainties on the scale factors are taken into account in the analysis as experimental uncertainties.

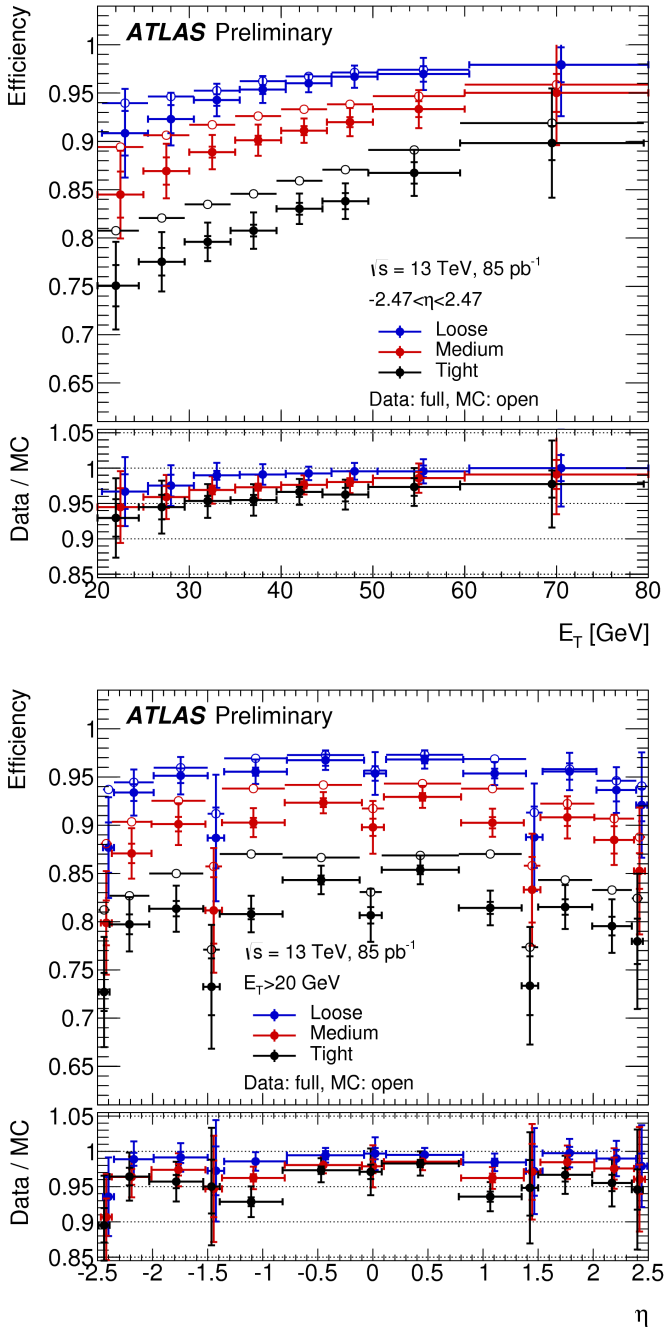

Figure 3.1: Electron identification efficiency for *loose*, *medium* and *tight* identification requirements as a function of the transverse energy E_{T} (top) and pseudorapidity η (bottom). The measurements performed with $Z \to e^{+}e^{-}$ data are compared to the Monte Carlo simulation [131].

The electron energy is calibrated using the Z-boson mass reconstructed in $Z \to e^+e^-$ decays as a constraint [133]. The calibration uncertainty is about 0.05 % over a wide phase space region, rising up to a maximum of 0.2% in detector regions with large amount of passive material and to 1% for electrons with $p_{\mathrm{T}} < 10$ GeV. The transverse energy resolution of electrons is determined with 10 % accuracy.

3.3 Muon reconstruction

Muons are the only particles from the interaction point which reach the muon spectrometer. All other particles (except neutrinos) are absorbed in the calorimeter system. The muon reconstruction methods are the same for all analysed data sets, but with improved reconstruction software for Run-2. The muon reconstruction relies on tracks measured in the inner detector and the muon spectrometer. In the central detector region ($|\eta| < 0.1$), where there is a gap in the muon spectrometer coverage, minimum ionising depositions in the calorimeters are used for muon identification. Four types of muon candidates are defined based on the subdetector information used [134, 135]:

Combined muons: Majority of reconstructed muons. The muon tracks measured in the inner detector and in the muon spectrometer are combined using a global track refit.

Segment-tagged muons: The inner detector track is combined with a track segment in one or more layers of the muon spectrometer.

Stand-alone muons: This algorithm is used to extend the muon acceptance in the region where no inner detector measurement is available, i.e. for $2.5 < |\eta| < 2.7$. Only the stand-alone measurement of tracks in the muon spectrometer and no inner detector information is used. Impact parameter information is obtained by extrapolating the muon spectrometer track to the beam line. The measured muon momenta are corrected for expected energy losses in the calorimeters.

Calorimeter-tagged muons: The inner detector track is combined with an energy deposition in the calorimeter, that is compatible with a minimum ionising particle. This reconstruction algorithm provides the lowest purity, but it extends the muon acceptance into the central

detector region with $|\eta| < 0.1$ where the muon spectrometer is only partially instrumented.

If a muon is reconstructed by two or more algorithms, only one of the respective muon tracks is chosen. Overlaps are resolved giving priority to combined, then segment-tagged and, at last, calorimeter-tagged muons. In the case of overlaps between stand-alone muons, the ones with better track fit quality and with larger numbers of subdetector hits are preferred.

The ATLAS muon identification separates prompt muons from fake muons originating mainly from pion or kaon decays. Discriminating variables are the quality of the track fit and, if applicable, the compatibility of inner detector and muon spectrometer momentum measurements. In addition, a minimum number of hits on the track in the inner detector and the muon spectrometer is required.
Similar to the electron identification, different identification working points with increasing purity are used: *loose*, *medium* and *tight* muon candidates. Muons with higher quality always form subsets of collections with looser requirements. In the $H \to ZZ^* \to 4\ell$ analysis, the *loose* working point is used aiming at a maximum efficiency. *Loose* muons comprise all muons reconstructed by the four reconstruction algorithms. Good muon quality is ensured by requirements on the quality of the muon spectrometer and inner detector track matching for combined muons, as well as on the minimal number of subdetector hits for all muon types. The *Medium* muon collection consists of combined and stand-alone muons passing the *loose* requirements, segment-tagged and calorimeter-tagged muons are omitted in this class. The *tight* collection maximises the muon purity. Only combined muons are used.

The muon identification efficiency at a given working point, is determined using two different methods for muons within the inner detector acceptance ($|\eta| < 2.5$) and outside ($2.5 < |\eta| < 2.7$). In the former case, a tag-and-probe method, similarly as in the case of electrons, is applied. For low-p_{T} muons with $4\ \mathrm{GeV} < p_{\mathrm{T}} < 12\ \mathrm{GeV}$, $J/\Psi \to \mu^+\mu^-$ events are used, while for high-p_{T} muons with $p_{\mathrm{T}} > 12\ \mathrm{GeV}$ $Z \to \mu^+\mu^-$ decays are analysed. Dimuon candidates are required to have invariant masses close to the mass of the resonance. The tag muon is required to pass *medium* identification, isolation and trigger requirements, while the probe muon is either an inner detector track, muon spectrometer track or a calorimeter-tagged muon. For *medium* and *tight* identification efficiencies, the probes are calorimeter-tagged muons. The efficiency is calculated in two steps. First the efficiency $\epsilon(\mathit{medium}\,/\,\mathit{tight}|\mathrm{CT})$ of measuring an

inner-detector track using calorimeter-tagged probe muons is calculated, which then is corrected by multiplying with inner-detector track reconstruction efficiency $\epsilon(\text{ID}|\text{MS})$ determined using muon-spectrometer probes:

$$\epsilon(medium\,/\,tight) = \epsilon(medium\,/\,tight|\text{CT}) \cdot \epsilon(\text{ID}|\text{MS}). \tag{3.5}$$

For the *loose* identification efficiency determination, reconstructed muons are separated into calorimeter-tagged muons within $|\eta| < 0.1$ and all other muons. Muon spectrometer tracks are used as probes for $|\eta| < 0.1$, while the efficiency in the rest of the η-range is calculated as for the *medium* and *tight* collections. The muon efficiencies are given by the ratio of the number $N_{probe}^{identified}$ of probe muons that are reconstructed as *loose*, *medium* or *tight*, to the number N_{probe} of all probes:

$$\epsilon = \frac{N_{probe}^{identified}}{N_{probe}}. \tag{3.6}$$

The numbers $N_{probe}^{identified}$ and N_{probe} are estimated using a maximum-likelihood fit with $J/\Psi \to \mu\mu$ data. For $Z \to \mu\mu$ events, background contributions are subtracted from the measured values $N_{probe}^{identified}$ and N_{probe}.
Efficiency differences between data and simulation are corrected for physics analyses by weighting simulated muons by a scale factor

$$\text{SF}^{\mu} = \frac{\epsilon^{data}(\eta, \phi)}{\epsilon^{MC}(\eta, \phi)}. \tag{3.7}$$

The uncertainty on the scale factor contributes to the systematic uncertainty.

For muons in the high-η region ($|\eta| > 2.5$), the identification efficiency is not calculated using the tag-and-probe method. The number of observed muons in the high-η region in $Z \to \mu^+\mu^-$ events is normalised to the one in a nearby central detector region ($2.2 < |\eta| < 2.5$). All central muons are corrected as discussed in the previous paragraph. This ratio is calculated for simulation and data, and the double-ratio is applied as scale factor in physics analyses [134].

Data sets with an integrated luminosity of $20.3\,\text{fb}^{-1}$ collected in 2012 and with $3.2\,\text{fb}^{-1}$ in 2015 are used for the measurement of muon identification efficiencies for analyses of Run-1 and Run-2 data, respectively. The Run-2 muon identification efficiencies for *loose* and *medium* muon identification criteria in the central detector region ($|\eta| < 2.5$)

are shown in Figure 3.2. The Run-1 results are very similar. The efficiency of the *medium* working point decreases rapidly in the region $|\eta| < 0.1$. It is recovered by using *loose* identification which also takes segment-tagged and calorimeter-tagged muons into account. The loose efficiency is above 99 % almost independent of the muon p_{T} and η. The muon efficiency in the forward region ($|\eta| > 2.5$) is above 95% over most of the transverse momenta range. As in the case of the electron identification efficiency, the ratio of data to simulation is applied as correction factor to the simulated events.

The muon momentum scale is calibrated using the invariant mass of the muon pairs in J/Ψ and Z-boson decays [135]. The calibration accuracy is 0.05% in the central detector region, degrading to about 2.9% for muons with $p_{\mathrm{T}} > 20$ GeV in the outer detector region ($|\eta| > 2.2$). The muon momentum resolution is measured with an accuracy of 2.3%.

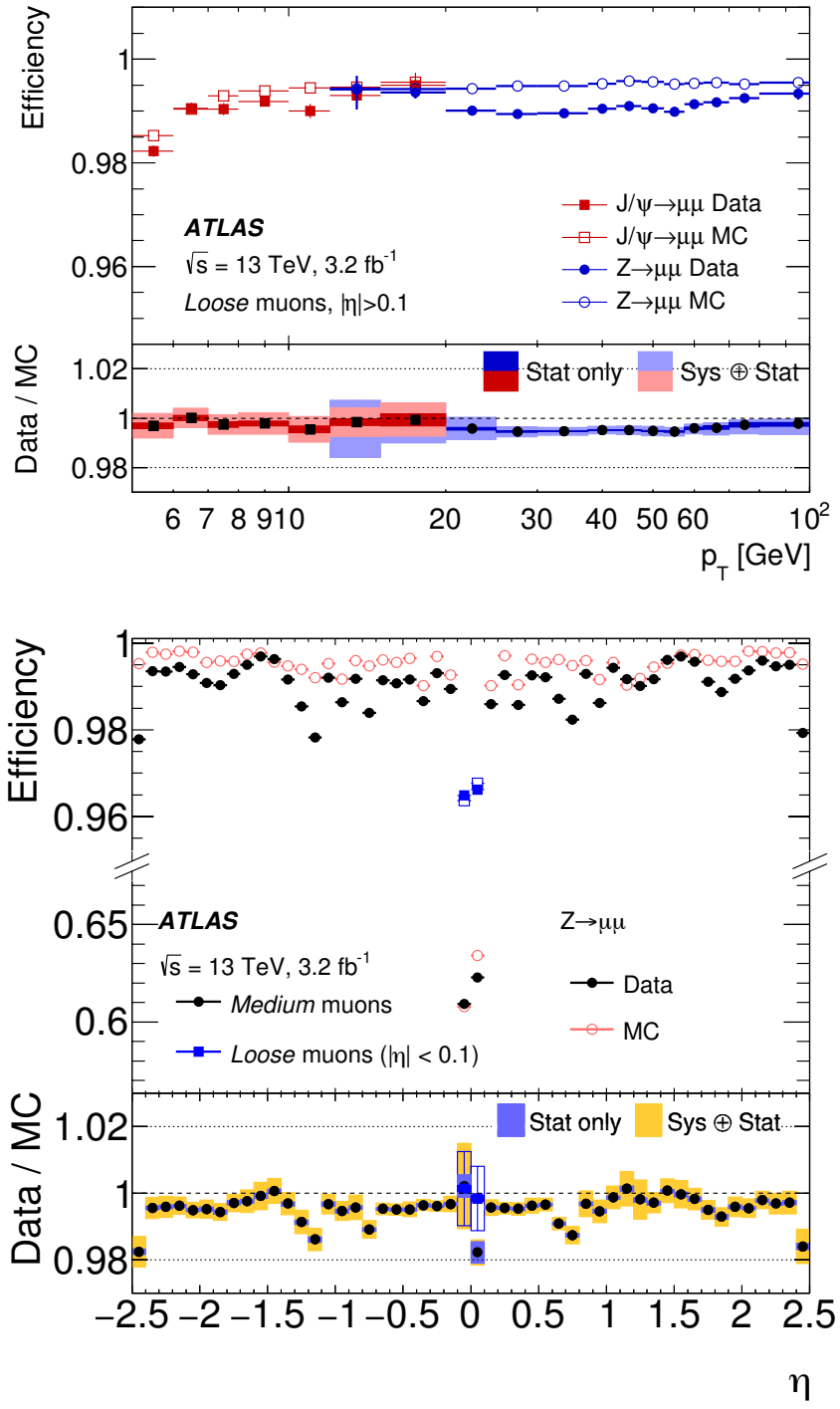

Figure 3.2: *Loose* and *medium* muon identification efficiencies as a function of p_{T} (top) and η (bottom) measured with 3.2 fb^{-1} of data collected at $\sqrt{s} = 13$ TeV in 2015 [135]. The lower panels show the ratio of the observed and simulated data.

3.4 Jet reconstruction

Jets from the hadronisation of strongly interacting particles (quarks and gluons) are frequently produced in proton-proton collisions. The hadrons induce showers in the calorimeters and are reconstructed as narrow cones of energy deposits in the calorimeters or of charged particle tracks in the inner detector. Pile-up has a large effect on jet reconstruction and jet energy calibration, increasing on the one hand the jet multiplicity (so-called pile-up jets), and changing on the other hand the measured jet shape and energy.

The ATLAS jet reconstruction is described in detail in [136]. Jets are reconstructed from topological clusters [137] of energy depositions in the calorimeter cells. The clusters are formed by an iterative seed-and-collect algorithm. A calorimeter cell with high signal-to-noise ratio acts as a seed to form a topological cluster. The neighbouring cells as well as the neighbours of neighbours are added to the topological cluster, if their signal-to-noise ratio passes a certain threshold.

Jets are reconstructed from the topological clusters using the anti-k_t jet algorithm [138] as implemented in the FastJet program [139]. The jet reconstruction with the anti-k_t algorithm is stable with respect to infrared and collinear radiative corrections. In the first step, the distances d_{ij} between each pair of topological clusters i and j and the distance d_{iB} between the topological cluster i and the beam direction B are calculated,

$$d_{ij} = \min\left(k_{ti}^{2p}, k_{tj}^{2p}\right)\frac{\Delta R_{ij}^2}{R^2}, \tag{3.8}$$

$$d_{iB} = k_{ti}^{2p}, \tag{3.9}$$

with $p = -1$ for the anti-k_t algorithm and where k_{ti} is the transverse momentum of the i-th topological cluster, ΔR is the distance between clusters in the (y,ϕ)-space and R a fixed radius parameter determining the cone-size of the jet. $R = 0.4$ is used in this thesis. If $d_{ij} < d_{iB}$, the clusters i and j are combined. Otherwise cluster i is defined as a jet and removed from the list of clusters for the subsequent jet reconstruction. Distances d_{ij} and d_{iB} are then recalculated and the process is repeated until no topological clusters are left.

The four-momenta of the resulting jets are calibrated in several steps (see Figure 3.3) based on simulation and control data [136]. The most important calibration steps are

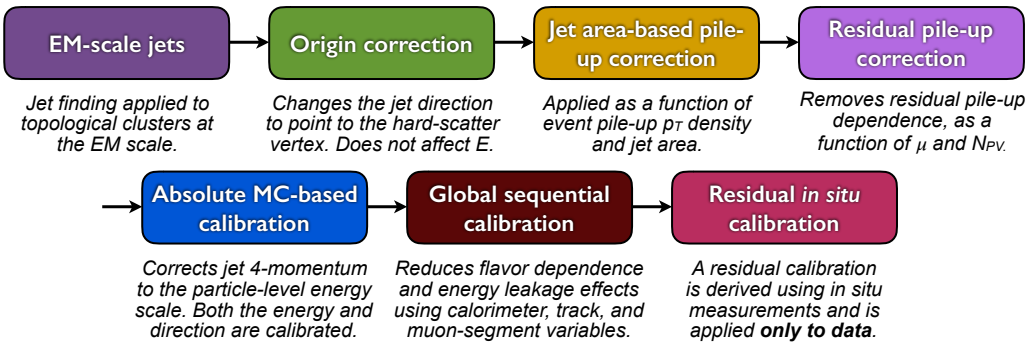

Figure 3.3: Schematic overview of the jet energy scale calibration [136].

the subtraction of pile-up induced energy from the same or nearby proton bunches (*jet area-based pile-up correction* and *residual pile-up correction*), and the determination of the absolute jet energy scale by matching in the simulation the reconstructed jet four-momentum to the energy of the jet at particle level (*absolute MC-based calibration*). Particle-level jets are reconstructed with the anti-k_t algorithm from stable final state particles produced with Monte Carlo generators. For the pile-up energy subtraction, first, the jet-p_{T} density distribution for specific LHC run conditions is obtained from dijet Monte Carlo simulation. The jet-p_{T} density is the ratio of the jet transverse momentum to the area occupied by the jet in (η-ϕ)-space. The pile-up contribution to a specific jet is the median of this distribution times the area occupied by the jet. The p_{T}-density distribution is calculated for central jets. Residual pile-up dependence remains for forward-jets. This contribution is subtracted by a final pile-up correction. Residual dependence of the jet energy scale on the longitudinal and transverse jet shape is removed in the *global sequential calibration* by the use of calorimeter, muon spectrometer and inner detector track information. The first five steps of the calibration are based on Monte Carlo simulation. The last correction step (*residual in situ calibration*) is performed using well-measured photons, Z-bosons and calibrated jets in data as reference. The jet energy scale in the central detector region is calibrated with an accuracy of better than 1 % for jets with 100 GeV $< p_{\mathrm{T}} <$ 500 GeV and of better than 4.5 % for lower-p_{T} jets. An additional uncertainty of 2 % is added for forward jets ($|\eta| > 0.8$).

The transverse energy from pile-up interactions is subtracted from the energy of signal jets. However, local fluctuations in pile-up activity can lead to additional pile-up jets. The rejection of those is crucial for the data analysis. Within the coverage of

the inner detector ($|\eta| < 2.4$) a highly efficient method based on track information is employed. The jet-vertex-tagger (JVT) discriminant combines two discriminating variables measuring how many of the tracks associated to the jet originate from the primary vertex [140, 141]. For signal jets large JVT values are expected, while pile-up jets tend to have significantly lower values.

3.5 *b*-jet identification

The identification of b-jets (b-tagging) is important for the selection of processes involving b-quarks, such as $b\bar{b}H$ or $t\bar{t}H$ production. The top-quark decays into a W-boson and a b-quark. The discrimination of jets originating from b-quark decays from those from light quarks, gluons and c-jets is based on the low lifetime of b hadrons and the reconstruction of their decay vertices. As a consequence, the b-jet identification is only possible within the coverage of the inner detector ($|\eta| < 2.5$). Three complementary algorithms search for secondary vertices or test the primary vertex association. The outputs of these algorithms are combined into a multivariate discriminant called MV2c20 [142, 143]. For data analysis, a specific b-tagging efficiency is chosen corresponding to a cut on the discriminant. Operating points with b-tagging efficiency of 60 %, 70 %, 77 % and 80 % have been studied. The simulated events are weighted with a scale factor correcting for b-tagging efficiency differences between data and simulation. The scale factor is obtained from data of leptonic $t\bar{t} \to e\mu$ decays and Z+jet events with $Z \to \mu\mu$ decays [142, 144].

Chapter 4

$H \to ZZ^* \to 4\ell$ event selection

The measurement of the Higgs boson tensor interaction is performed for $H \to ZZ^* \to 4\ell$ Higgs boson decays. In this chapter, the selection of Higgs boson candidates in the four-lepton final state is described, the so-called inclusive selection, which serves as input to the tensor structure measurement (see Chapter 5). In the inclusive selection all Higgs boson candidates in the four-lepton final state are selected regardless with which production mechanism they have been produced, while in the tensor structure measurement based on the Run-2 data set the Higgs boson candidates are categorised according to their production mode. The data from two LHC run periods are analysed separately: the full data set of LHC Run-1 collected in the years 2011 and 2012 at centre-of-mass energies of 7 and 8 TeV, respectively, and a partial data set from LHC Run-2 taken in 2015 and 2016 at $\sqrt{s} = 13$ TeV. The selection of $H \to ZZ^* \to 4\ell$ candidate events is very similar for both data sets. A summary of the analysed data sets is given in Table 2.3 in Chapter 2. A detailed description of the selection requirements can be found in [14] and [145] for Run-1, and in [146] for Run-2.

After the introduction of the $H \to ZZ^* \to 4\ell$ decay channel and the relevant background processes in Section 4.1, a description of the simulation of the signal and background processes is given in Section 4.2. The inclusive $H \to ZZ^* \to 4\ell$ event selection and the estimation of the background contributions are discussed in Section 4.3. Finally the results of the inclusive selection are reported. Differences between the selection criteria of Run-1 and Run-2 analyses are explained.

4.1 Overview

The tensor structure of the Higgs boson couplings to gauge bosons is studied in the $H \to ZZ^* \to 4\ell$ decays ($\ell \equiv e, \mu$). The Feynman diagram of the decay is shown in Figure 4.1.

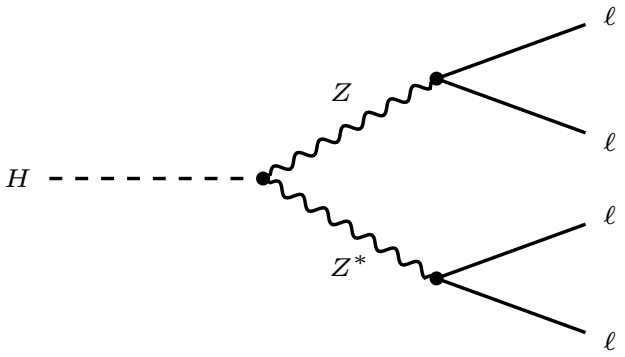

Figure 4.1: Tree-level Feynman diagram of the $H \to ZZ^* \to 4\ell$ decay process, where $\ell \equiv e, \mu$.

About 3% of the decays of the SM Higgs boson with a mass of 125 GeV are into a pair of Z-bosons. Since the Higgs boson mass is below the resonant ZZ production threshold of $2 \cdot m_Z \approx 180$ GeV, one of the Z-bosons (Z_1) is produced on-shell, while the other one (Z_2) is off-shell. Only decays of the Z-bosons into charged leptons are considered. $Z \to e^+e^-$ and $Z \to \mu^+\mu^-$ decays provide a very clear signature. $Z \to \tau\tau$ decays with leptonically decaying τ leptons are also taken into account in the signal process contributing about 6 % of the leptonic decay channels to the total branching ratio. The reconstruction of hadronically decaying τ leptons suffers from a much higher misidentification rate and worse energy resolution compared to electrons and muons. Because of the four leptons in the final state the branching ratio is $BR_{H\to 4\ell} = (1.250 \pm 0.027) \cdot 10^{-2}$ % [27] and high electron and muon identification and reconstruction efficiencies as well as high energy and momentum resolution are crucial. The signal is characterised by four prompt leptons originating from the same primary vertex and very low energy deposition around each lepton, i.e. high lepton isolation.

The main background process to the $H \to ZZ^* \to 4\ell$ decays is non-resonant ZZ^* production with decays into four prompt leptons. The dominant production mechanism is quark-antiquark annihilation, followed by gluon fusion (see Figure 4.2). Above the

Z-boson resonance, i.e. the kinematic region of the on-shell Higgs boson production, the production predominantly occurs through $q\bar{q} \to ZZ^*$ production (see Figure 4.2 top right). At the Z-boson resonance, the main diagram for quark initiated processes is the $q\bar{q} \to Z/\gamma^* \to 2\ell$ production with associated radiative decays to an additional lepton pair (see Figure 4.2 top left).
This process has very similar final state as the signal and can only be distinguished by the four-lepton invariant mass and slightly different kinematic properties of the decay products.

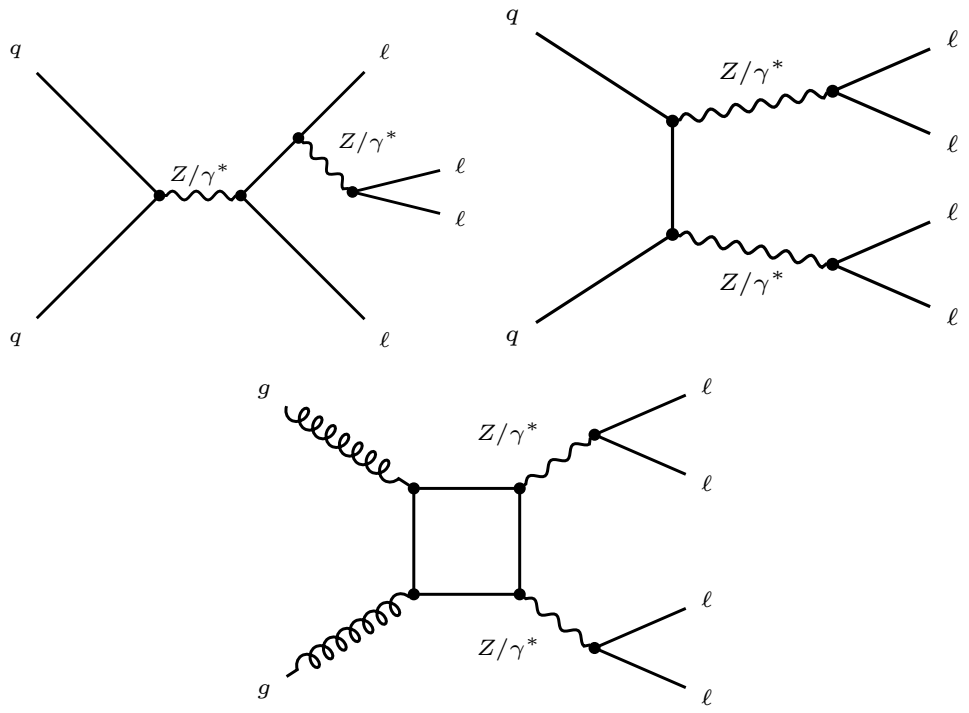

Figure 4.2: Tree-level Feynman diagrams for non-resonant $ZZ^* \to 4\ell$ production via quark-antiquark annihilation (top) and gluon fusion (bottom).

The reducible background contributions are Z+jets, $t\bar{t}$ and WZ+jets production (see Figure 4.3) with less than four prompt leptons, but one or more leptons originating from hadron decays (leptons within jets) or due to jets misidentified as electrons or muons. Such leptons are usually non-isolated, i.e. surrounded by relatively large inner detector and calorimeter activity, and their trajectories are displaced from the primary hard-scattering vertex. Additional minor background processes are the triboson ($VVV \equiv WWZ, WZZ, ZZZ$) and $t\bar{t}Z$ production (see Figure 4.4).

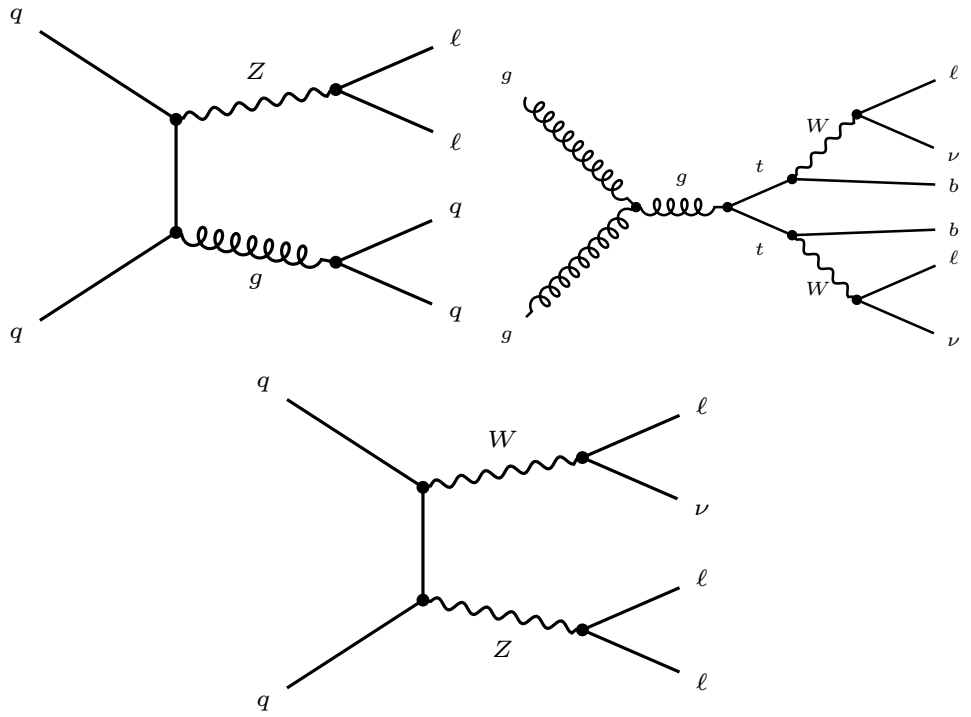

Figure 4.3: Tree-level Feynman diagrams for the main reducible background processes with less than four prompt charged leptons contributing to the $H \to ZZ^* \to 4\ell$ channel: Z+jets (top left), $t\bar{t}$ (top right) and WZ (bottom).

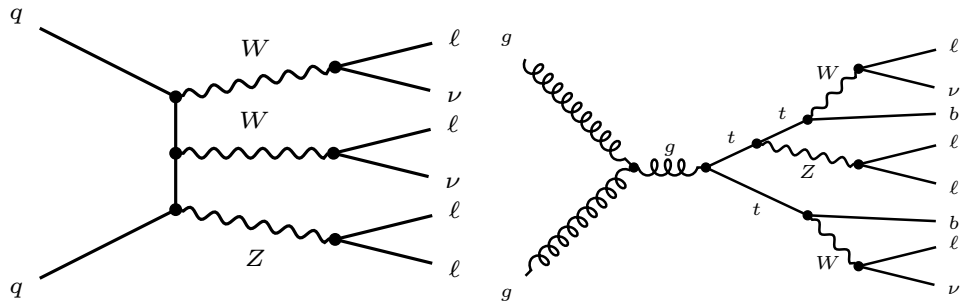

Figure 4.4: Tree-level Feynman diagrams for the minor reducible background processes with four prompt charged leptons contributing to the $H \to ZZ^* \to 4\ell$ channel: WWZ (left) as an example for VVV processes and $t\bar{t}Z$ (right).

While background contributions from ZZ^*, VVV and $t\bar{t}Z$ processes are estimated from simulation, the reducible backgrounds with less than four prompt leptons are estimated using dedicated signal-depleted control data.

4.2 Simulated signal and background processes

A multitude of Higgs boson signal and SM background processes have been simulated for the Run-1 and Run-2 analyses using state-of-the-art programs and tools available at the time (see Appendix C). The generated events have been passed through the ATLAS detector simulation as described in Section 2.3.6.

The simulated signal and background processes together with the programs used for the simulation of the event generation, the parton shower and hadronisation (if different from the matrix element event generator) and the parton distribution functions (PDFs) are summarised in Tables 4.1 and 4.2 for Run-1 and Run-2, respectively.
The *additional simulation programs* in the overview tables are used in addition to the hard-scattering and parton shower generators to improve the modelling accuracy. The total and differential cross section predictions for the background processes have been further improved as explained in detail in Appendix C.

The SM $H \to ZZ^* \to 4\ell$ signal has been simulated taking into account the main production modes ggF, VBF, VH ($V = Z$, W), $t\bar{t}H$ and $b\bar{b}H$ (only for Run-2). For Run-1, the contribution of $b\bar{b}H$ production is estimated assuming the same m_H dependence of the production rate as for $t\bar{t}H$ and the same signal efficiency as for ggF production.

The $H \to ZZ^* \to 4\ell$ signal with BSM contributions parametrised within an effective field theory (see Section 1.4.2) is referred to BSM Higgs boson signal in the following. The BSM $H \to ZZ^* \to 4\ell$ signal for Run-1 has been simulated for the ggF production, while ggF, VBF and VH production processes with BSM contributions have been generated for Run-2. The BSM VBF and VH production processes for Run-2 are simulated at leading-order (LO) and at next-to-leading-order (NLO) in QCD. The NLO samples are only used for the estimation of systematic uncertainties. The full BSM signal models is built based on the listed Run-1 and Run-2 samples. The signal modelling will be described in Sections 5.1.1 and 5.2.2 for the shape-based and rate-based analyses, respectively.

The $q\bar{q} \to ZZ^*$ and $gg \to ZZ^*$, as well as the $t\bar{t}$, Z+jets and WZ background processes with less than four prompt leptons have been simulated. The latter are used for modelling the background shape in case of the rate-based analysis, while the yield is in most cases estimated with data-driven methods (see Section 4.3.2). For Run-2, the rare $t\bar{t}Z$ and triboson processes have been simulated in addition. These processes cause a negligible contribution to the smaller Run-1 data set and can thus be neglected.

The Higgs boson production cross sections and branching ratios have been scaled to the highest-accuracy prediction available in Run-1 [147, 148] and Run-2 [29, 147, 148], respectively. The values are listed in Tables 1.2 and 1.3. The precision of the calculations can be found in Appendix D.

Table 4.1: Monte Carlo event generators used for the modelling of the physics processes in the $H \to ZZ^* \to 4\ell$ tensor structure analysis in Run-1. Additional programs have been used for the simulation of lepton decays TAUOLA, QED radiative corrections (PHOTOS) are also listed.

Process	Hard-scattering	Parton Shower	Tune	PDF set	Additional programs	Radiative corrections
SM signal						
ggF	POWHEG-BOX	PYTHIA 8	AU2 CT10	CT10	PHOTOS	NLO QCD (p_{T}^{4l} at
					HRES2.1	NNLO & NNLL QCD)
VBF	POWHEG-BOX	PYTHIA 8	AU2 CT10	CT10	PHOTOS	NLO QCD
WH	PYTHIA 8		AU2 CTEQ6L1	CTEQ6L1lo	PHOTOS	LO
$ZH + gg \to ZH$	PYTHIA 8		AU2 CTEQ6L1	CTEQ6L1lo	PHOTOS	LO
$t\bar{t}H$	PYTHIA 8		AU2 CTEQ6L1	CTEQ6L1lo	PHOTOS	LO
BSM signal						
ggF	JHU	PYTHIA 8	AU2 CT10	CT10	PHOTOS	LO
Background						
$q\bar{q} \to ZZ^*$	POWHEG-BOX	PYTHIA 8	AU2 CT10	CT10	PHOTOS	NLO QCD
$gg \to ZZ^*$	GG2ZZ	HERWIG++	AUET2 CT10	CT10	PHOTOS, TAUOLA	LO
Z+jets	ALPGEN	PYTHIA 6	Perugia2011C	CTEQ6L1lo	PHOTOS, MLM	LO
$t\bar{t}$	POWHEG-BOX	PYTHIA 6	Perugia2011C	CTEQ6L1lo	PHOTOS, TAUOLA	NLO QCD
WZ	SHERPA		CT10	CT10		LO

Table 4.2: Monte Carlo event generators used for the modelling of the physics processes in the $H \to ZZ^* \to 4\ell$ tensor structure analysis in Run-2. Additional programs have been used for the simulation of lepton decays TAUOLA, for the simulation of decays of hadrons containing bottom or charm quarks (EvtGen v1.2.0). QED radiative corrections (Photos) are also listed. (MadGraph5_aMC@NLO ≡ MG5aMC@NLO).

Process	Hard-scattering	Parton Shower	Tune	PDF set	Additional programs	Radiative Corrections
SM signal						
ggF	Powheg-Box v2	Pythia 8	AZNLO CTEQ6L1	PDF4LHCnlo	MiNLO, HNNLO, EvtGen v1.2.0	NNLO QCD
VBF	Powheg-Box v2	Pythia 8	AZNLO CTEQ6L1	PDF4LHCnlo	EvtGen v1.2.0	NLO QCD
WH	Powheg-Box v2	Pythia 8	AZNLO CTEQ6L1	PDF4LHCnlo	MiNLO, EvtGen v1.2.0	NLO QCD
ZH	Powheg-Box v2	Pythia 8	AZNLO CTEQ6L1	PDF4LHCnlo	MiNLO, EvtGen v1.2.0	NLO QCD
$gg \to ZH$	Powheg-Box v2	Pythia 8	AZNLO CTEQ6L1	PDF4LHC	EvtGen v1.2.0	LO
$t\bar{t}H$	MG5aMC@NLO v2.2.3	Herwig++	CTEQ6L1-UE-EE-5	CT10nlo	EvtGen v1.2.0	NLO QCD
$b\bar{b}H$	MG5aMC@NLO v2.3.3	Pythia 8	A14 NNPDF2.3lo	NNPDF2.3	EvtGen v1.2.0	NLO QCD
BSM signal						
ggF	MG5aMC@NLO	Pythia 8	A14 NNPDF2.3lo	NNPDF3.0nlo	EvtGen v1.2.0, FxFx	NLO QCD
VBF + $V(\to qq)H$	MG5aMC@NLO	Pythia 8	A14 NNPDF2.3lo	NNPDF2.3lo	EvtGen v1.2.0	LO
$V(\to \ell\nu/\ell\ell)H$	MG5aMC@NLO	Pythia 8	A14 NNPDF2.3lo	NNPDF2.3lo	EvtGen v1.2.0	LO
VBF	MG5aMC@NLO	Pythia 8	A14 NNPDF2.3lo	NNPDF3.0nlo	EvtGen v1.2.0	NLO QCD
WH	MG5aMC@NLO	Pythia 8	A14 NNPDF2.3lo	NNPDF3.0nlo	EvtGen v1.2.0	NLO QCD
ZH	MG5aMC@NLO	Pythia 8	A14 NNPDF2.3lo	NNPDF3.0nlo	EvtGen v1.2.0	NLO QCD
Background						
$q\bar{q} \to ZZ^*$	Sherpa 2.2.2	Sherpa	NNPDF3.0nnlo	NNPDF3.0nnlo	ME+PS@NLO	NLO QCD (0,1 jets) LO ($\geq$ 2 jets) NLO EW corr. $f(m_{ZZ})$
$gg \to ZZ^*$	gg2VV	Pythia 8	A14 NNPDF2.3lo	CT10	Powheg, EvtGen v1.2.0	LO, scaled to NLO with $f_{\text{NLO/LO}} = 1.7 \pm 1.0$
Z+jets	Sherpa 2.2.2	Sherpa	NNPDF3.0nnlo	NNPDF3.0nnlo	Comix, OpenLoops ME+PS@NLO	NLO QCD (up to 2 partons) LO (4 partons)
$t\bar{t}$	Powheg-Box v2	Pythia 6	Perugia2012 CTEQ6L1	CT10	EvtGen v1.2.0, Photos, tauola	NLO QCD
WZ	Powheg-Box v2	Pythia 8	AZNLO CTEQ6L1	CT10nlo	EvtGen v1.2.0	NLO QCD
VVV	Sherpa 2.1.1		CT10	CT10		LO
$t\bar{t}Z(\to \ell\ell)$	MadGraph	Pythia 8	A14 NNPDF2.3lo	NNPDF2.3lo	EvtGen v1.2.0	LO

4.3 Inclusive analysis

4.3.1 Selection of the Higgs boson candidates

The event selection exploits the signal properties to discriminate it against the background. The selection requirements are described in the following and summarised in Table 4.4. Corrections to the four-lepton invariant mass of the selected Higgs boson candidate are listed in Table 4.5. The selection criteria differ only slightly between Run-1 and Run-2.

Trigger and data quality

First of all, a trigger with at least one electron or muon is required. Targeting multi-lepton final states, a combination of single-lepton, dilepton and trilepton (only Run-2) triggers is used with increasing p_{T} and E_{T} thresholds with increasing instantaneous luminosities during the data taking periods. All triggers used are summarised in Appendix E.
In order to ensure a reliable event reconstruction, only data with all ATLAS subdetectors operational have been analysed. Events are required to have at least one reconstructed primary vertex with at least three (two) associated inner detector tracks with transverse momenta $p_{\mathrm{T}} > 400$ GeV in Run-1 (Run-2).

Object selection

The reconstruction, identification and calibration of particle objects is described in Chapter 3.
The additional requirements imposed on each reconstructed particle in Run-1 and Run-2 are summarised in Table 4.3. It is possible that the same collection of hits is assigned to more than one particle type by the different reconstruction algorithms. For instance, a true electron may be reconstructed as a jet and as an electron candidate. Such ambiguities are resolved by the so-called overlap removal, where precedence is given to one interpretation.

For the $H \to ZZ^* \to 4\ell$ selection, electrons are required to satisfy *loose* identification criteria (see Section 3.2), which provide the highest electron reconstruction efficiency.

Table 4.3: Requirements on the reconstructed particles in the final state. The jet-vertex-tagger discriminant (JVT) is used to suppress pile-up jets.

Lepton selection	
Electrons:	*Loose* identification, $E_{\mathrm{T}} > 7$ GeV, $\lvert\eta\rvert < 2.47$
	Identification based on cuts (for $\sqrt{s} = 7$ TeV Run-1 data set)
	or likelihood discriminant
	Longitudinal impact parameter $\lvert z_0\rvert$:
	$\lvert z_0\rvert < 10\,\mathrm{mm}$ ($\lvert z_0 \sin(\theta)\rvert < 0.5\,\mathrm{mm}$) for Run-1 (Run-2)
Muons:	*Loose* identification, $p_{\mathrm{T}} > 6$ GeV (5 GeV) for Run-1 (Run-2)
	Combined muons: $\lvert\eta\rvert < 2.5$
	Segment-tagged muons: $\lvert\eta\rvert < 2.5\,(0.1)$ for Run-1 (Run-2)
	Stand-alone muons: $2.5 < \lvert\eta\rvert < 2.7$
	Calorimeter-tagged muons: 15 GeV $< p_{\mathrm{T}} < 100$ GeV, $\lvert\eta\rvert < 0.1$
	Longitudinal ($\lvert z_0\rvert$) and transverse ($\lvert d_0\rvert$) impact parameter:
	$\lvert d_0\rvert < 1\,\mathrm{mm}$, $\lvert z_0\rvert < 10\,\mathrm{mm}$ ($\lvert z_0 \cdot \sin(\theta)\rvert < 0.5\,\mathrm{mm}$) for Run-1 (Run-2);
	not applied for stand-alone muons
Jet selection (for Run-2)	
Jets:	Anti-k_t jet algorithm with distance parameter $R = 0.4$
	$p_{\mathrm{T}} > 30$ GeV, $\lvert\eta\rvert < 4.5$
	Pile-up suppression:
	JVT > 0.64 for jets with $p_{\mathrm{T}} < 60$ GeV and $\lvert\eta\rvert < 2.4$
b-jets:	MV2c20 b-jet identification algorithm using working point
	with 70 % efficiency, $\lvert\eta\rvert < 2.4$

Overlap removal:	Resolves ambiguities between lepton-lepton or lepton-jet pairs
	reconstructed close to each other

This is important for efficiently reconstructing four-lepton final states. Electrons are required to be within the coverage of the inner detector, $|\eta| < 2.47$, and to have a transverse energy larger than 7 GeV. Signal electrons are expected to originate from the hard-scattering vertex. Therefore, a minimum longitudinal distance $|z_0|$ from the production vertex is required: $|z_0| < 10\,\text{mm}$ in Run-1 and $|z_0 \cdot \sin(\theta)| < 0.5\,\text{mm}$ in Run-2. The Run-2 threshold is reduced due to the additional pixel detector layer installed after Run-1.

Muons identified with *loose* criteria are used yielding a muon identification efficiency above 99% in most of the acceptance region (see Section 3.3). The muons are required to have a minimum transverse momentum of $p_{\text{T}} > 6$ GeV in Run-1 and $p_{\text{T}} > 5$ GeV in Run-2. The momentum threshold was lowered in Run-2 to increase the signal acceptance. Because of their lower purity, calorimeter-tagged muons are required to have higher momenta of $p_{\text{T}} > 15$ GeV. Combined and segment-tagged muons are only reconstructed within the coverage of the inner detector, $|\eta| < 2.5$. In the central detector region, where no coverage of the muon spectrometer is provided, the muon reconstruction efficiency of combined muons drops. Therefore calorimeter-tagged muons, and segment-tagged muons in Run-2, are used in addition within $|\eta| < 0.1$ to close the efficiency gap.
The cosmic muon background is reduced by the requirement of a maximum transverse impact parameter: $|d_0| < 1\,\text{mm}$. Muon tracks from heavy quark jets are displaced from the primary production vertex. In order to reduce those backgrounds the longitudinal impact parameter $|z_0|$ is required to be less than 10 mm for Run-1, while $|z_0 \cdot \sin(\theta)| < 0.5\,\text{mm}$ is required for Run-2. As for the electrons, the lower Run-2 threshold is made possible by the additional pixel layer installed for Run-2.

For the Run-2 $H \to ZZ^* \to 4\ell$ tensor coupling structure analysis, jets and b-tagged jets are selected. The reconstruction of jets and b-tagged jets is described in Sections 3.4 and 3.5, respectively. Jets with transverse momenta $p_{\text{T}} > 30$ GeV and within $|\eta| < 4.5$, calibrated at the electromagnetic scale, are used. Pile-up jets are suppressed by imposing a cut on the value of the jet-vertex-tagger discriminant (see Section 3.4), JVT > 0.64 for jets with transverse momenta $p_{\text{T}} < 60$ GeV and $|\eta| < 2.4$. The chosen cut value leads to 92% selection efficiency for jets from the hard-scattering process. Similar to the lepton efficiency scale factor, the simulated data is corrected by a scale factor accounting for difference between the JVT selection efficiencies in simulation and data.
The identification of b-jets is available within the coverage of the inner detector, $|\eta| < 2.5$.

In the $H \to ZZ^* \to 4\ell$ analysis, the cut on the MV2c20 b-tagging discriminant is chosen such that the b-jet selection efficiency is 70% and light quarks and c-quark rejection rates are larger than 87 % and 99 %, respectively.

Lepton quadruplet selection

All combinations of four leptons in an event (called quadruplets) satisfying the object selection criteria are formed to reconstruct a candidate Higgs boson decaying into four leptons according to the following procedure:

1. The Z-boson decay candidates are formed by requiring at least two pairs of same-flavour and opposite-charge leptons in the final state. The transverse momenta of the three highest-p_{T} leptons are required to be above 20 GeV, 15 GeV and 10 GeV, respectively. The momentum threshold for the fourth lepton depends on flavour: 7 GeV for electrons and 6 GeV (5 GeV) for muons in Run-1 (Run-2). In the Run-1 analysis it is required that at least one reconstructed lepton matches a triggered one.

2. The lepton pairs are then combined to a quadruplet. The lepton pair with invariant mass closest to the Z-boson mass (m_Z) is considered as the on-shell Z-boson candidate (Z_1), while the second lepton pair is the off-shell Z-boson candidate (Z_2).

The quadruplets are classified into the four channel: $4e$, 4μ, $2e2\mu$ and $2\mu2e$, where the first two leptons always belongs to the Z_1 and the second two leptons to the Z_2. If more than one Higgs boson candidate is selected in an event, the best of the candidates is chosen by a procedure described below.
In the decay channels with muons, at most one muon is allowed to be stand-alone or calorimeter-tagged ensuring low misidentification rate. In the Run-1 analysis, at most one quadruplet of each type is accepted with invariant masses m_{12} and m_{34} of the lepton pairs closest and second-closest to the Z-boson mass, respectively. For the Run-2 analysis, the same requirements are used, unless the quadruplet is accompanied by one or more leptons with $p_{\mathrm{T}} > 12$ GeV and satisfying the same lepton selection requirements as the quadruplet leptons. In this case, the following criteria are used for all possible quadruplets.
The lepton pairs in all selected quadruplets in an event are required to have invariant masses consistent with on- and off-shell Z-boson decays: 50 GeV $< m_{Z_1} <$ 106 GeV

and $m_{\text{min}} < m_{Z_2} < 115$ GeV, respectively, with $m_{\text{min}} = 12$ GeV for four-lepton invariant masses $m_{4\ell}$ below 140 GeV, rising linearly to a maximum value of 50 GeV for $m_{4\ell} \geq 190$ GeV. The leptons must have large angular separation $\Delta R(\ell, \ell') > 0.1\,(0.2)$ for same-(different-) flavour lepton pairs. Leptons from J/Ψ decays are removed by requiring that the invariant masses of alternative same-flavour and opposite-sign leptons pairs (only 4μ and $4e$ combinations) are above the resonance mass, $m_{\ell\ell} > 5$ GeV.

Further lepton selection criteria are applied to reduce the contribution of background processes with non-prompt leptons, mostly from $t\bar{t}$ and Z+jets production:

- Lepton isolation: While signal leptons are isolated from other particles, background leptons are often produced in jets and therefore are surrounded by large activity in the detector. Calorimeter and track isolation criteria are imposed on both muons and electrons. The relative track and calorimeter isolation parameters, I_{track} and I_{calo}, are defined in Section 3.1. The relative track isolation parameter I_{track} of quadruplet leptons is required to be less than 15 % summing over all tracks within a cone of size $\Delta R = 0.2$ around the lepton. For muons in the Run-1 analysis, a slightly larger cone size of $\Delta R = 0.3$ is used. The sum of the calorimeter energy deposits within a cone of size of $\Delta R = 0.2$ around the lepton I_{calo} is required to be less than 30 % (20 %) for muons (electrons). For the $\sqrt{s} = 7$ TeV data set, the calorimeter isolation requirement is 30% for electrons too, while a tighter calorimeter isolation requirement of 15 % is imposed on the stand-alone muons.

- Impact parameter significance: while signal leptons have their origin at the primary vertex due to the short Higgs boson lifetime, background leptons from b-quark decays originate from secondary vertices leading to an impact parameter offset with respect to the primary vertex. Therefore, the transverse impact parameter significance, defined as the ratio of the transverse impact parameter (d_0) and its measurement error (σ_{d_0}), is required to be below 6.5 (3.5) for electrons (muons) in Run-1. The installation of an additional pixel detector layer in Run-2 allows for tighter transverse impact parameter significance criteria: $\frac{|d_0|}{\sigma_{d_0}} < 5.0\,(3.0)$ for electrons (muons).

The lowering of the muon transverse momentum threshold from 6 GeV to 5 GeV in the Run-2 analysis increases the signal acceptance, but it also leads to increased background rates. Therefore an additional requirement was added in Run-2: the inner detector tracks of all leptons of a selected quadruplet are fitted to a common

vertex. The quality of the fit is expected to be high for the Higgs signal, since all four leptons originate from the same vertex, while it is expected to be worse for background processes with heavy-flavour jets in which the leptons from hadron decays are produced displaced from the primary vertex. The ratio χ^2 over the number of degrees of freedom N_{dof} of the fit is used as a measure of the goodness of the fit, requiring $\frac{\chi^2}{N_{dof}} < 6$ for the 4μ channel and $\frac{\chi^2}{N_{dof}} < 9$ for all channels containing electrons. These criteria maintain very high signal selection efficiency, while the background rates are reduced by 20%, to 30%.

Higgs boson candidate selection

The selection of a single Higgs boson candidate among all quadruplets per event passing the selection criteria has been improved for Run-2 compared to Run-1. In Run-1, and in Run-2 in the case of events with not more than four leptons, the final Higgs boson candidate chosen is the quadruplet with the highest expected selection efficiency. The ordering from highest to lowest selection efficiency is 4μ, $2\mu 2e$, $2e2\mu$ and $4e$ due to the higher muon identification efficiency at high-p_{T} compared to low-p_{T} muons and electrons. In the case of signal events with more than four leptons, which originate from VH and $t\bar{t}H$ production, an optimised selection procedure is applied in Run-2. With the default selection, it is possible that the leptons are wrongly paired so that leptons from the t-quark or vector boson decays are associated to the quadruplet replacing one of the leptons from the Higgs boson decay. In the Run-2 analysis, the selection of the best quadruplet is performed based on the matrix element value for the $H \to ZZ^* \to 4\ell$ decay computed at LO with the MadGraph5_aMC@NLO generator [149]. The matrix element is a measure of how well a quadruplet matches the expected kinematic from a $H \to ZZ^* \to 4\ell$ decay. The quadruplet with the highest matrix element value is selected as the final Higgs boson candidate.

Corrections to the four-lepton invariant mass

The Higgs boson mass resolution is improved by means of the following corrections to the four-lepton invariant mass. The single-lepton energy resolution is improved by taking into account the energy losses due to the lepton final state radiation (FSR). The radiated photon energy is restored using nearby reconstructed calorimeter clusters. About 4 % of all signal events are affected by this correction. The overall improvement

of this correction is less than one percent.
In addition, the Z-boson mass constraint is applied to the leptons from the on-shell Z-boson candidate Z_1. With the knowledge of the Z-boson line shape and the lepton momentum resolution, a kinematic fit is performed that corrects the lepton transverse momenta and thus improving the four-lepton invariant mass resolution by about 15 % [57].
Finally, the energy resolution of low-energy electrons ($E_{\mathrm{T}} < 30$ GeV) has been further improved in Run-1 by combining the track momentum and cluster energy measurements [60].

In total, about 25% of all produced Higgs bosons decaying to four-leptons are selected. The results of the event selections applied in Run-1 and Run-2 are shown in Section 4.3.3.

Table 4.4: Selection criteria for $H \to ZZ^* \to 4\ell$ decays. The track-based (calorimeter-based) isolation is denoted with I_{track} (I_{calo}) and defined as the sum of transverse momenta (energies) of all charged particle tracks within a cone around a lepton relative to the transverse momenta (energy) of the lepton itself.

	Event selection
Good run list:	All detector components must be fully operational
Vertex:	At least one reconstructed vertex with three (two) associated tracks in Run-1 (Run-2)
Trigger:	Single-lepton, dilepton or trilepton (only Run-2) trigger
	Lepton quadruplet selection
Quadruplet formation:	Two same-flavour and opposite-sign lepton pairs satisfying object selection, and with p_{T} thresholds for three leading leptons 20, 15 and 10 GeV Building quadruplets with all possible combinations of lepton pairs On-shell Z-boson called Z_1, closes to the Z mass Off-shell Z-boson Z_2 is the remaining lepton pair Classification to sub-channels: 4μ, $4e$, $2e2\mu$ and $2\mu2e$; analysed in parallel Run-1 and Run-2 with no additional leptons: select in each sub-channel the quadruplet with m_{12} closest to m_Z
Kinematic requirements:	Only Run-1: At least one lepton in the quadruplet matched to the trigger On-shell Z-boson candidate: 50 GeV $< m_{Z_1} <$ 106 GeV Off-shell Z-boson candidate: $m_{\min} < m_{Z_2} <$ 115 GeV ($m_{\min} = 12$ GeV for $m_{4\ell} <$ 140 GeV, rising linearly to $m_{\max} = 50$ GeV at $m_{4\ell} \geq 190$ GeV) $\Delta R(\ell, \ell') > 0.10\,(0.20)$ for all same (different) flavour lepton combinations in the quadruplet J/Ψ veto: Remove quadruplet if alternative SF OS dilepton gives $m_{\ell\ell} < 5$ GeV
Isolation requirements:	Electron track isolation ($\Delta R = 0.2$): $I^e_{track} < 15\,\%$ Muon track isolation ($\Delta R = 0.2\,(0.3)$ for Run-1 (Run-2)): $I^\mu_{track} < 15\,\%$ Electron calorimeter isolation ($\Delta R = 0.2$) : $I^e_{calo} < 20\,\%$ (For $\sqrt{s} = 7$ TeV Run-1 data set $I^e_{calo} < 30\,\%$) Muon calorimeter isolation ($\Delta R = 0.2$) : $I^\mu_{calo} < 30\,\%$ (For Run-1 stand-alone muons: $I^\mu_{calo} < 15\,\%$)
Impact parameter significance:	Electrons: $\lvert d_0\rvert/\sigma_{d_0} < 6.5\,(5.0)$ for Run-1 (Run-2) Muons: $\lvert d_0\rvert/\sigma_{d_0} < 3.5\,(3.0)$ for Run-1 (Run-2)
Common vertex:	Only Run-2: Fit of the four lepton common vertex, with $\frac{\chi^2}{N_{dof}} < 6$ for 4μ and $\frac{\chi^2}{N_{dof}} < 9$ for $4e$, $2e2\mu$ and $2\mu2e$
Final quadruplet selection:	Select the quadruplet from the sub-channel with the highest expected signal efficiency (order of priority: 2μ, $2e2\mu$, $2\mu2e$, $4e$) Only Run-2: Updated lepton pairing for events with additional leptons ($p_{\mathrm{T}} > 12$ GeV) based on the highest matrix-element value

Table 4.5: Corrections to the four-lepton invariant mass in $H \to ZZ^* \to 4\ell$ decays.

Corrections to the four-lepton invariant mass	
On final quadruplet:	FSR correction
	Z-boson mass constraint
	Only Run-1: Combination of electron E_{T} and p_{T} measurements for electrons with $E_{\mathrm{T}} < 30$ GeV

4.3.2 Background estimation

The contribution of other SM processes that also produce four leptons and populate the signal region has to be estimated in order to evaluate the Higgs signal significance. Two types of background processes do contribute:

1. Processes with four prompt, isolated leptons: ZZ^*, $t\bar{t}V$, triboson production.

2. Processes with less than four isolated leptons and a misidentified lepton contained within a jet: $t\bar{t}$, Z+jets, WZ production.

The lowest-order Feynman diagrams for these background processes can be found at the beginning of this chapter. The contribution of the first type is estimated from Monte Carlo simulation, while the second type is estimated using data-driven techniques. The Monte Carlo estimation of the first type is reliable because the final states consist of isolated leptons. This is in general not the case for the second type of background. In addition, lepton misidentification is rare and a large number of simulated events would be necessary to produce enough events with misidentified leptons.

The methods for the background estimation used in the $H \to ZZ^* \to 4\ell$ analysis are described below. The final results are shown in Section 4.3.3. The systematic uncertainties related to the background estimation are discussed in Sections 5.1.3 and 5.2.4 for the Run-1 and Run-2 tensor structure analyses, respectively.

Background determination from simulation

The SM $ZZ^* \to 4\ell$ production, where both Z-bosons decay into a pair of muons or electrons, has the same signature as the $H \to ZZ^* \to 4\ell$ signal and therefore is the dominant background. Its contribution to the signal region is estimated with Monte Carlo simulation. Additional minor backgrounds, like $t\bar{t}Z$ and triboson (ZZZ, WZZ, WWZ) production with leptonic decays are also estimated by simulation. Contributions from $t\bar{t}W$ production are found to be negligible. The simulated event samples are described in detail in Section 4.2. Validation of the Monte Carlo event modelling is performed using signal-depleted regions which are in this case the side bands of the four-lepton mass window.

Data-driven background estimation

Processes with less than four prompt and isolated leptons are estimated from data. The modelling of these backgrounds depends on the flavour of the lepton pair associated with the off-shell Z-boson, Z+ee or Z+$\mu\mu$ because

- the fourth lepton, which is either a lepton within a jet or misidentified, has usually low transverse momentum and therefore, likely originates from the off-shell Z-boson (Z_2) candidate, and
- sources of non-prompt leptons are different for electrons and muons.

The strategy for data-driven background estimation is to construct so-called control regions, which are enriched with a specific background contribution and depleted in signal events. The control regions are constructed by following the signal selection as closely as possible for the on-shell Z-boson candidate (Z_1), but inverting the selection criteria for background reduction, the isolation and impact parameter requirements, and/or the lepton identification criteria for the Z_2 candidate. With the higher available data set in the control regions, several variables can be used to estimate the different background contributions. The background contributions expected in the signal region are obtained by extrapolating from the control region (CR) to the signal region (SR) by using so-called transfer factors which are given by the efficiency ϵ of the inverted selection requirements:

$$N_{bkg}^{\mathrm{SR},data} = f \cdot N_{bkg}^{\mathrm{CR},data} \qquad \text{with} \qquad f = \frac{N_{bkg}^{\mathrm{SR},MC}}{N_{bkg}^{\mathrm{CR},MC}} = \frac{\epsilon}{1-\epsilon}. \tag{4.1}$$

The Z+jets, $t\bar{t}$ and WZ background components can be differentiated according to the flavour of the jet containing the misidentified lepton:

1. Heavy-flavour jets in Z+jets and $t\bar{t}$ production where the leptons are from weak decays of heavy-flavour hadrons.
2. Light-flavour jets from gluons and light quarks in Z+jets and WZ production where muons from π or K decays in-flight or light jets are misidentified as electrons.

The contribution from the WZ process is estimated from Monte Carlo simulation except for the Z+ee background estimation in Run-2, where it is retrieved together

with Z+jets and $t\bar{t}$ contributions from control data. The results are cross-checked with Monte Carlo simulation and using different control regions.

Z+ee background estimation

For the $Z + ee$ final states the reducible background components from Z+jets, $t\bar{t}$ and WZ are divided into: light jets misidentified as electrons (f), electrons from photon conversions (γ) and electrons from semi-leptonic decays of heavy-flavour quark jets (q). The dominant processes are the f and q components which contribute with the same amount. In Run-1, the WZ contribution is estimated with Monte Carlo simulation, while it is included in the data-driven estimate in Run-2.

The total background yields of the different contributions are estimated from data with a template fit in a dedicated control region, called 3ℓ+X *CR*, enriched with reducible background sources by the following means: the leading three leptons in the quadruplet are required to pass the standard $H \to ZZ^* \to 4\ell$ selection, while the selection and identification of X, which is the low-E_{T} electron in Z_2, is relaxed. Only basic track quality criteria are required from X instead of the full identification requirements (see Section 3.2), and the isolation requirement is not applied. The q contribution from heavy-flavour Z+jets and $t\bar{t}$ processes can be reduced by applying the d_0 requirement since leptons from heavy quark decays are produced with an offset to the hard-scattering vertex. Therefore, in Run-2, the d_0 requirement is additionally applied for X resulting into a control region enriched in γ and f components. The q component is retrieved from Monte Carlo simulation in Run-2. In Run-1, the d_0 requirement is not applied, thus the control region is enriched with all three components γ, f and q. The ZZ^* contribution is suppressed by requiring a same-sign lepton pair as Z_2 candidate instead of an opposite-charged one. Any residual contamination from the ZZ^* background process is evaluated with Monte Carlo simulation and subtracted from the yields in the control regions. The common vertex criteria is applied in Run-2. The requirements defining the control regions are summarised in Table 4.6.

The efficiencies for extrapolation from the control to the signal region are retrieved from Monte Carlo simulation and corrected with data in an additional control region, Z+X *CR*, which provides a larger sample set of reducible background events with respect to the 3ℓ+X *CR*. This control region is defined by requiring a lepton pair as Z-boson decay candidate, and an electron candidate X defined as in the 3ℓ+X *CR*.

Table 4.6: Definition of the control regions for the estimation of the reducible Z+ee background. The symbols ✓ and ✗ refer to applied and omitted requirements from the signal selection, respectively. A standard Z-boson candidate consists of a same-flavour opposite-sign lepton pair (SF OS), while SF SS stands for the requirement of a same-flavour same-sign pair.

Control region (CR)	Common vertex	Z_2	X requirements			Enhanced
	req. (only Run-2)	Dilepton	Identification	d_0 req.	Isolation req.	with
3ℓ+X *CR* (Run-1)	–	SF SS	Relaxed	✗	✗	γ, f and q
3ℓ+X *CR* (Run-2)	✓	SF SS	Relaxed	✓	✗	γ and f

Possible efficiency differences in the 3ℓ+X *CR* and Z+X *CR* are covered by correction factors retrieved from data. The common vertex requirement is not applied in Run-2 since it is not defined for three leptons. The efficiencies are retrieved in two-dimensional bins of electron p_{T} and η (N_j) in Run-1 (Run-2) to account for efficiency differences with the electron or event kinematic.
A two-dimensional discriminant is used in Run-1 to entangle γ, f and q contributions in the $3\ell + X$ *CR*, while an one-dimensional discriminant is sufficient for Run-2, where only γ and f components need to be differentiated. For both runs the n_{InnerPix} variable is used which is the hit count in the subdetector closest to the beam pipe, i.e. the inner-most pixel layer for Run-1 and the IBL in Run-2. The n_{InnerPix} variable is redefined in Run-2 to recover the photon efficiency in case of dead modules: the hits in the next-to-innermost pixel layer are counted instead. The γ and f+q components can be well separated with the n_{InnerPix} variable, since photons as neutral particles do not have hits in the tracker, $n_{\mathrm{InnerPix}} = 0$, while electron candidates from f+q processes have at least one hit, $n_{\mathrm{InnerPix}} > 0$. In Run-1, n_{InnerPix} is combined with r_{TRT}, which is the ratio of high-threshold to low-threshold TRT hits. By using the r_{TRT} variable, the different background contributions can be further entangled: γ and q contributions have higher values since they convert or decay before the TRT into electrons, which produce transition radiation, while this is not the case for light jets faking electrons, i.e. the f component. Templates for γ, f and q contributions are retrieved from simulation with applied data correction in the Z+X *CR*.

The result of the Z+ee background estimation is listed in Table 4.7 for Run-1 and Run-2 data sets. Yields for the different background components in the 3ℓ+X *CR* and

in the signal region are shown together with the transfer factors. The contamination from ZZ^*, and the q component (only Run-2), which is 5 % and 9 % for Run-1 and Run-2 respectively, need to be subtracted from the control region yields to obtain the signal region yields.

Table 4.7: The result of the Z+ee reducible background estimation in the $H \to ZZ^* \to 4\ell$ analysis using the Run-1 and Run-2 data sets. The uncertainties are the combined statistical and systematic uncertainties.

Type $4e$+$2\mu 2e$	3ℓ+X CR yield	Transfer factor	Signal region yield
	Run-1, 4.5 fb^{-1} at $\sqrt{s} = 7$ TeV		
f	391 ± 29	0.010 ± 0.001	3.9 ± 0.9
γ	19 ± 9	0.10 ± 0.02	2.0 ± 1.0
q	5.1 ± 1.0	0.10 ± 0.03	0.51 ± 0.15
	Run-1, 20.3 fb^{-1} at $\sqrt{s} = 8$ TeV		
f	894 ± 44	0.0034 ± 0.0004	3.1 ± 1.0
γ	48 ± 15	0.024 ± 0.004	1.1 ± 0.6
q	18.3 ± 3.6	0.10 ± 0.02	1.8 ± 0.5
	Run-2, 36.1 fb^{-1} at $\sqrt{s} = 13$ TeV		
f	3075 ± 56	0.0020 ± 0.0004	5.7 ± 1.2
γ	208 ± 17	0.0072 ± 0.0014	1.34 ± 0.44
q	Simulation based estimation		6.3 ± 1.9

Z+$\mu\mu$ background estimation

For the Z+$\mu\mu$ background estimation the Z+jets component is divided into the heavy-flavour, Z+HF, and light-flavour, Z+LF, contributions since the dominant background component is comprised of leptons from heavy-flavour hadrons in Z+HF or $t\bar{t}$ processes. Minor contributions are leptons from light-flavour jets, Z+LF, and the WZ diboson process. The WZ contribution with Z+$\mu\mu$ final states is estimated from simulation. The total yield of Z+jets and $t\bar{t}$ components are estimated in data with control regions, while transfer factors to the signal region or between control regions are retrieved from simulation. See Section 4.2 for details on the simulated samples.

A global fit method using an unbinned maximum likelihood fit with multiple control regions, each enriched in different background components, is employed. The method is applied in both Run-1 and Run-2, but was slightly modified for Run-2, because of difficulty in simulating the Z+LF component: a generator level filter is applied to the Run-2 Z+jets sample resulting into a sample almost entirely populated in the Z+HF component and little Z+LF contribution.

The control regions are summarised in Table 4.8. They are all built by either applying the common vertex requirement or not (only Run-2), and following the standard selection of the Z_1 candidate closely, but relaxing or inverting the selection of the Z_2 candidate.
Four control regions, that are orthogonal to each other and the signal region are defined:

- The *Inverted d_0 CR* enhances the Z+HF plus $t\bar{t}$ components, that are characterised by a large d_0 significance by inverting the d_0 significance requirement for at least one lepton contained in Z_2. The isolation requirements are not applied for the Z_2 leptons.

- The $t\bar{t}$ background component can be isolated with the *$e\mu$+$\mu\mu$ CR* by requiring a different flavour lepton pair as Z_1 candidate and removing therefore the on-shell Z-boson contributions. In Run-1, an additional requirement on the invariant mass of the Z_1 candidate is imposed to further remove contributions from on-shell Z-bosons. The Z_1 candidate is required to pass all standard selection criteria. The Z_2 dilepton can be of opposite or same charge with the d_0 and isolation requirements not applied.

- The Z+LF component can be retrieved with the *Inverted isolation CR*, in which the heavy-flavour component is removed by applying the d_0 requirement for the Z_2 leptons, but allowing that at least one lepton fails the isolation criteria.

- All background components are contained in the *Same-sign CR*, in which the d_0 and isolation requirements for Z_2 are not applied, and the Z_2 dilepton is built with same-signed leptons.

A fifth control region, the *Relaxed CR*, is not orthogonal to the other control regions and to the signal region, but it contains a large number of events for all background components by not applying the d_0 and isolation requirements for the leptons contained in Z_2. This control region is used to validate the normalisation of the different

Table 4.8: Definition of the control regions for the estimation of the reducible Z+$\mu\mu$ background. The symbols ✓ and ✗ refer to applied and omitted requirements from the signal selection, respectively. A standard Z-boson candidate consists of a same-flavour opposite-sign lepton pair (SF OS), OF OS and SF SS stand for the requirement of a opposite-flavour opposite-charge lepton pair, or a same-flavour same-sign pair, respectively.

	Control region (CR)	Common vertex req. (only Run-2)	Z_1 dilepton	Z_2 requirements			Enhanced with
				Dilepton	d_0 req.	Isolation req.	
Orthogonal CRs	*Inverted d_0 CR*	✗	–	–	Inverted	✗	Z+HF, $t\bar{t}$
	$e\mu$+$\mu\mu$ CR	✗	OF OS	SF OS + SF SS	✗	✗	$t\bar{t}$
	Inverted isolation CR	✓	–	–	✓	Inverted	Z+LF
	Same-sign CR	✗	–	SF SS	✗	✗	Z+HF, Z+LF, $t\bar{t}$
	Relaxed CR	✗	–	–	✗	✗	Z+HF, Z+LF, $t\bar{t}$

background contributions after their yields are estimated by the global fit.

The $m_{4\ell}$ distribution gives good separation for the Z+HF contribution resonant at the Z-boson mass, and the non-resonant $t\bar{t}$ process. It is used as discriminating variable in the control regions included in the fit. All components with an on-shell Z-boson are modelled with a Breit-Wigner convoluted with a Crystal-Ball function, while the non-resonant $t\bar{t}$ process is modelled with a second order Chebyshev polynomial. In the $e\mu + \mu\mu$ *CR*, where the resonant Z-boson contribution is removed, the Z+HF background is modelled with a first order polynomial. Contaminations from ZZ^*, WZ or Higgs boson processes, if present, are modelled with the function used for the Z+HF component, while their yield is retrieved from simulation.
In Run-1, all four orthogonal control regions are fitted together in a simultaneous fit. The Z+LF component is enhanced in the *Inverted isolation CR* and *Same-sign CR* by requiring a minimum value of the so-called p_{T}-balance $\left(p_{\mathrm{T}}^{\mathrm{ID}} - p_{\mathrm{T}}^{\mathrm{MS}}\right)/p_{\mathrm{T}}^{\mathrm{ID}} > 0.2$ for at least one lepton contained in Z_2. The p_{T}-balance is a measure for the balance between p_{T} measurements in the inner detector (ID) and in the muon spectrometer (MS). The Z+LF leptons tend to larger discrepancies in the measurements since the light mesons decay after the inner detector, while the heavy hadrons in Z+HF decay immediately in the inner detector.
In Run-2 only the *Inverted d_0 CR* and *$e\mu$+$\mu\mu$ CR* are included in the global fit to estimate Z+HF and $t\bar{t}$ contributions. After those contributions are fixed, the Z+LF is retrieved with a fit to the *Inverted isolation CR*. The Z+LF yield is extrapolated to the signal region by using Z+HF transfer factors. The efficiencies for the transfer

factor calculation are retrieved from simulation corrected with data in another control region called $Z+\mu$ *CR*. In this control region an on-shell Z-boson candidate is required together with a muon. Control samples enriched in Z+HF and Z+LF are constructed by a requirement on the p_{T}-balance.

In Table 4.9, the results of the $Z+\mu\mu$ background estimation for Run-1 and Run-2 are summarised. The yields of the different background components in the reference control region *Relaxed CR* and in the signal region are given as well as the transfer factors.

Table 4.9: The result of the $Z+\mu\mu$ reducible background estimation in the $H \to ZZ^* \to 4\ell$ analysis using the Run-1 and Run-2 data sets. The uncertainties are the combined statistical and systematic uncertainties.

Type	*Relaxed CR*	Transfer factor	Signal region
4μ+$2e2\mu$	yield	$[10^{-2}]$	yield
Run-1, 24.8 fb^{-1} at $\sqrt{s} = 7$ TeV and $\sqrt{s} = 8$ TeV			
$t\bar{t}$	210 ± 12	0.55 ± 0.09	1.13 ± 0.13
Z+HF	159 ± 20	3.10 ± 0.19	4.92 ± 0.47
Z+LF	49 ± 10	3.0 ± 1.8	1.48 ± 0.77
WZ	Simulation based estimation		1.13 ± 0.14
Run-2, 36.1 fb^{-1} at $\sqrt{s} = 13$ TeV			
$t\bar{t}$	918 ± 23	0.25 ± 0.03	2.29 ± 0.27
Z+HF	908 ± 52	0.75 ± 0.09	6.82 ± 0.91
Z+LF	50 ± 21	0.75 ± 0.75	0.38 ± 0.41
WZ	Simulation based estimation		0.91 ± 0.50

4.3.3 Results of the $H \to ZZ^* \to 4\ell$ selection

After the inclusive selection of Higgs boson candidates (see Section 4.3.1), only the events within a mass window around the measured Higgs boson mass are used for the study of the tensor structure of Higgs boson couplings. The central value of the mass window is given by the best measurement at the time of the analysis: $m_H = 125.5$ GeV for Run-1 and $m_H = 125.09$ GeV for Run-2. The number of observed signal and background events are compared to the expectations, for each 4ℓ final state separately

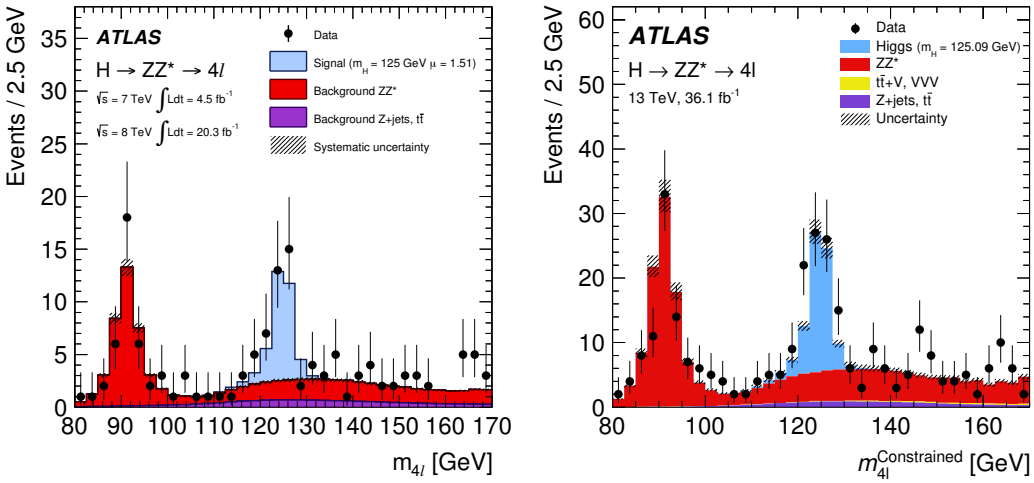

Figure 4.5: The expected and observed distribution of the four-lepton invariant mass $m_{4\ell}$ from Run-1 (left) and Run-2 (right) data after the $H \to ZZ^* \to 4\ell$ selection [146, 150].

and for the combination. The mass window is 115 GeV $< m_H <$ 130 GeV for Run-1 data and 118 GeV $< m_H <$ 129 GeV in Run-2, tighter because of the larger available data set. The observed and expected four-lepton invariant mass distributions from Run-1 and Run-2 are shown in Figure 4.5. The Higgs boson signal can be clearly seen. The peak at the Z-boson mass, $m_Z = 91$ GeV, is from $q\bar{q} \to Z\gamma^* \to \ell$ production with associated radiative decays to an additional lepton pair (see Figure 4.2 top left).
The invariant mass m_{12} of the dilepton pair associated with the on-shell Z-boson is consistent with the Z-boson mass and the off-shell Z-boson mass distribution m_{34} shows values around 30 GeV as expected (see Figure 4.6).

The results of the inclusive analysis at $\sqrt{s} = 7$, 8 and 13 TeV with integrated luminosities of 4.5 fb^{-1}, 20.3 fb^{-1} and 36.1 fb^{-1}, respectively, are shown in Table 4.10. The expected signal-to-background ratio is 1 to 1.5 for the Run-1 data sets and 2 for Run-2, primarily because of the tighter mass window. In all three data sets there is a slight excess of observed Higgs boson candidates compared to the SM expectation. The signal strength parameter μ is the measured Higgs boson production rate relative to the SM prediction, $\mu_{\text{SM}} = 1$. The Run-1 and Run-2 signal strength parameters have been measured in specially optimised analyses: $\mu = 1.44^{+0.40}_{-0.33}$ [145] in Run-1 and $\mu = 1.28^{+0.21}_{-0.19}$ [146] in Run-2. The observed signal strength parameters are enhanced compared to the SM prediction due to the observed excess of events. The measurements

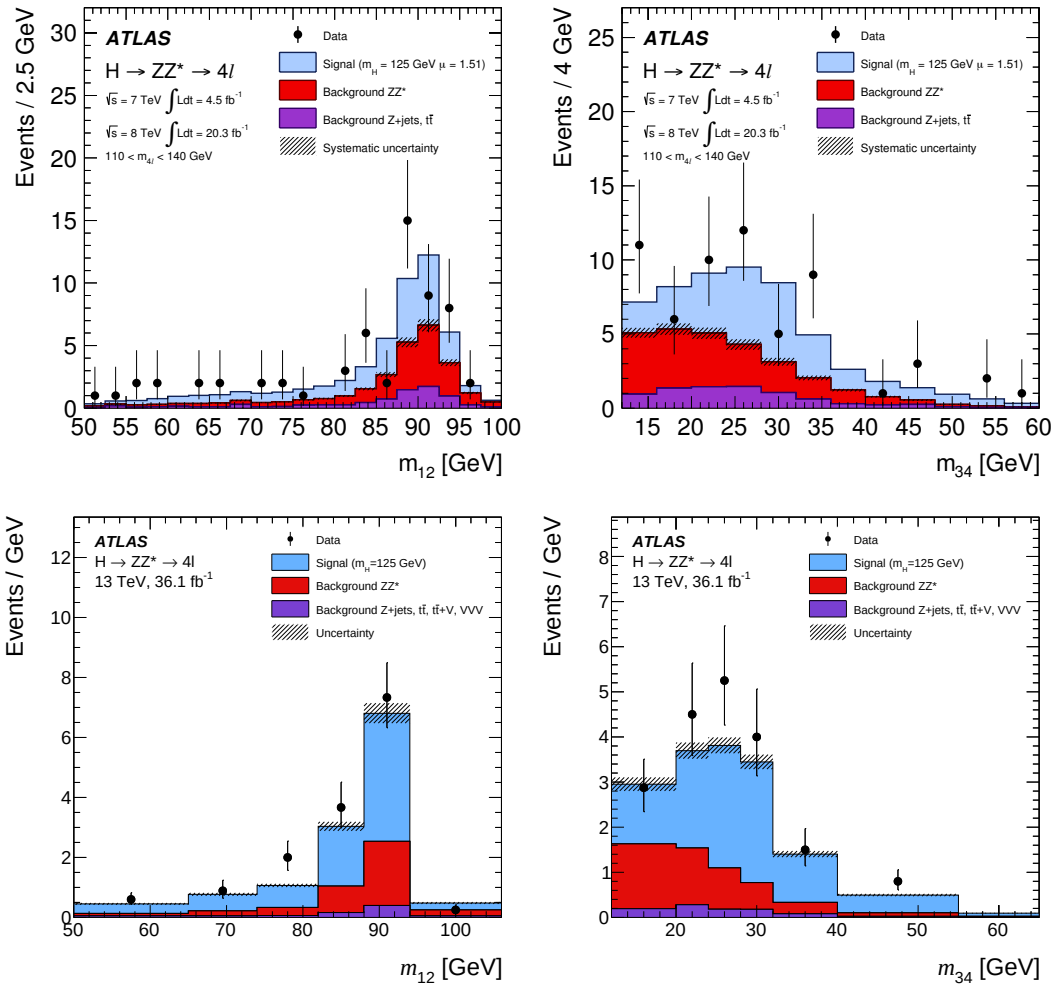

Figure 4.6: The expected and observed distributions of the mass m_{12} and m_{34} of the reconstructed on-shell and off-shell Z-boson candidates, respectively, in Run-1 (top) and Run-2 (bottom) after the $H \to ZZ^* \to 4\ell$ selection [150, 151].

are compatible with the SM prediction within the measurement uncertainties.

Different spin and parity hypotheses have been tested against the SM assumption by the ATLAS and CMS experiments in Run-1 (see Section 1.5): the SM hypothesis of a scalar particle with CP-even eigenstate is always favoured, but it is still possible that small admixtures of BSM contributions are present in the Higgs boson tensor coupling structure. Therefore, based on the assumption that the discovered boson is a scalar, the tensor structure of Higgs boson to gauge boson couplings has been tested on the presence of BSM CP-even and CP-odd contributions within the scope of this thesis. The results of the inclusive analysis serve as input to these measurements described in the next Chapter.

Table 4.10: The observed and expected numbers of SM $H \to ZZ^* \to 4\ell$ and ZZ^* background events for the Run-1 [14] and Run-2 [146] data sets. The best known Higgs boson mass values m_H at the time of the analysis has been used. Mass windows around m_H have been applied. Other backgrounds considered are $t\bar{t}$ and Z+jets and, for $\sqrt{s} = 13$ TeV data, rare triboson and $t\bar{t}Z$ production which are negligible at lower centre-of-mass energies. Statistical and systematic uncertainties are added in quadrature.

	SM Higgs boson Signal	ZZ^*	Other backgrounds	Total expected	Observed
Run-1, $\sqrt{s} = 7$ TeV, $m_H = 125.5$ GeV, 115 GeV $< m_H <$ 130 GeV					
4μ	1.02 ± 0.10	0.65 ± 0.03	0.14 ± 0.06	1.81 ± 0.12	3
$2e2\mu$	0.64 ± 0.06	0.45 ± 0.02	0.13 ± 0.05	1.22 ± 0.08	2
$2\mu 2e$	0.47 ± 0.05	0.29 ± 0.02	0.53 ± 0.12	1.29 ± 0.13	1
$4e$	0.45 ± 0.04	0.26 ± 0.02	0.59 ± 0.12	1.30 ± 0.13	2
Total	2.58 ± 0.25	1.65 ± 0.09	1.39 ± 0.26	5.62 ± 0.37	8
Run-1, $\sqrt{s} = 8$ TeV, $m_H = 125.5$ GeV, 115 GeV $< m_H <$ 130 GeV					
4μ	5.81 ± 0.58	3.36 ± 0.17	0.97 ± 0.18	10.14 ± 0.63	13
$2e2\mu$	3.72 ± 0.37	2.33 ± 0.11	0.84 ± 0.14	6.89 ± 0.41	9
$2\mu 2e$	3.00 ± 0.30	1.59 ± 0.10	0.52 ± 0.12	5.11 ± 0.34	8
$4e$	2.91 ± 0.29	1.44 ± 0.09	0.52 ± 0.11	4.87 ± 0.32	7
Total	15.4 ± 1.5	8.72 ± 0.47	2.85 ± 0.39	27.0 ± 1.6	37
Run-2, $\sqrt{s} = 13$ TeV, $m_H = 125.09$ GeV, 118 GeV $< m_H <$ 129 GeV					
4μ	19.7 ± 1.6	7.5 ± 0.6	1.00 ± 0.21	28.1 ± 1.7	32
$2e2\mu$	13.5 ± 1.0	5.4 ± 0.4	0.78 ± 0.17	19.7 ± 1.1	30
$2\mu 2e$	10.4 ± 1.0	3.57 ± 0.35	1.09 ± 0.19	15.1 ± 1.0	18
$4e$	9.9 ± 1.0	3.35 ± 0.32	1.01 ± 0.17	14.3 ± 1.0	15
Total	54 ± 4	19.7 ± 1.5	3.9 ± 0.5	77 ± 4	95

Chapter 5

Measurement of the tensor structure of the Higgs boson couplings to gauge bosons

The study presented in this thesis probes for the presence of BSM contributions to the Higgs boson tensor couplings to weak vector bosons in the HZZ (and HWW) interaction vertex and to gluons in the Hgg interaction vertex. Both CP-even and CP-odd contributions are considered. The analysis is predominantly performed in four-lepton final states from $H \to ZZ^* \to 4\ell$ decays. The BSM coupling contributions are modelled in the Higgs characterisation framework, an effective field theory (EFT) approach (see Section 1.4.2). Due to the limited amount of data, only a reduced set of coupling parameters is probed. The inclusive event selection for Run-1 and Run-2 data described in the previous chapter forms the basis for the tensor structure analysis.

The tensor structure of the Higgs boson couplings in $H \to ZZ^* \to 4\ell$ decays is accessible via two types of observables affected by BSM coupling parameters:

- The distributions of the kinematic variables describing the four-lepton final state (referred to as the shape information), and
- the total production and decay rate for a given Higgs boson production process (referred to as rate information).

In general, BSM coupling parameters in the EFT approximation affect more strongly the rate rather than the kinematic properties of a given Higgs boson production process. The rate information is, however, not sensitive to CP violation in Higgs boson

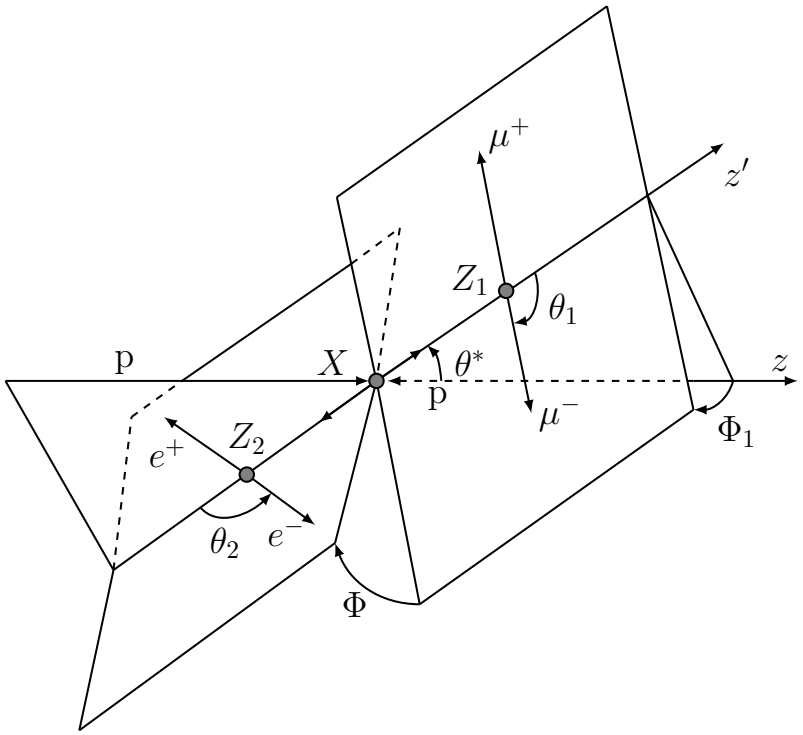

Figure 5.1: Definition of the decay angles describing the four-lepton final states of $H \to ZZ^* \to 4\ell$ decays in the Higgs boson rest frame which are sensitive to spin and parity of the Higgs boson (denoted with X) [14].

interactions, while the shape information can be used to probe for CP violating effects. The Higgs boson candidate four-lepton decays from the inclusive event selection are analysed using two complementary approaches.

In the first approach, used for the Run-1 data, a shape analysis of distributions of kinematic variables is performed without making use of the overall rate information, since the Run-1 data set is not large enough to discriminate between different Higgs boson production modes in $H \to ZZ^* \to 4\ell$ decays. The CP-sensitive kinematic variables are defined in the Higgs boson decay system illustrated in Figure 5.1. The $H \to ZZ^* \to 4\ell$ measurement is combined with a similar measurement of $H \to WW^* \to e\nu\mu\nu$ decays assuming that the BSM coupling parameters of the two decay channels are related as the ones in the SM.

The Run-2 data set is significantly larger such that discrimination of different Higgs

boson production modes becomes possible. The second analysis approach employed for Run-2 data mainly relies on the rate information.
While the rate-based analysis probes BSM couplings in the XVV vertex in VBF and VH production and decay to VV as well as a CP-odd BSM coupling in the Xgg vertex in ggF production, only the XVV interaction vertex is studied in the shape-based analysis. An overview of the coupling parameters probed in the two analyses is given in Table 5.1.

The signal strength parameter μ is defined as the ratio of the observed Higgs boson production and decay rate to the SM expectation:

$$\mu = \frac{\sigma \cdot BR}{(\sigma \cdot BR)_{\mathrm{SM}}}. \tag{5.1}$$

The signal strength is related to the coupling parameters in the Higgs characterisation framework. For SM interactions with gauge bosons, the signal strength is given by

$$\mu_{\mathrm{ggF}} = (c_\alpha \kappa_{\mathrm{Hgg}})^2 \cdot (c_\alpha \kappa_{\mathrm{SM}})^2 \quad \text{and} \quad \mu_{\mathrm{VBF}/VH} = (c_\alpha \kappa_{\mathrm{SM}})^4 \tag{5.2}$$

for the ggF and for the VBF and VH production mechanisms, respectively. The Higgs boson coupling to weak gauge bosons $V = W, Z$ in the SM is given by $c_\alpha \kappa_{\mathrm{SM}}$. In the case of additional BSM couplings, μ can be expressed as a polynomial of all coupling parameters contributing to the process both in the Higgs boson production and the decay vertex (see Appendix B). It should be noted, that in the shape-based analysis discussed in Section 5.1 the signal strength is used as an additional free normalisation parameter in the likelihood fit, not as a function of coupling parameters. In the rate-based measurement described in Section 5.2, the signal strength is parametrised in terms of SM and BSM coupling parameters as in Equation 5.2 for the SM case.

Table 5.1: Summary of the BSM coupling parameters probed by the shape and the rate-based analyses in the $H \to ZZ^* \to 4\ell$ decay channel using ATLAS Run-1 and Run-2 data. The coupling parameters are defined in the Higgs characterisation framework. It is assumed that beyond the Standard Model (BSM) W- and Z-boson couplings are related as in the SM: $\kappa_{\mathrm{HVV}} = \kappa_{\mathrm{HZZ}} = \kappa_{\mathrm{HWW}}$ and $\kappa_{\mathrm{AVV}} = \kappa_{\mathrm{AZZ}} = \kappa_{\mathrm{AWW}}$. The SM coupling of the Higgs boson to weak gauge bosons ($V = W, Z$) and gluons is given by $c_\alpha \kappa_{\mathrm{SM}}$ and $c_\alpha \kappa_{\mathrm{Hgg}}$, respectively.

Analysis	Vertex with BSM couplings	Coupling parameters SM	BSM CP-even	BSM CP-odd	Data set	Reference
Shape-based	XVV	κ_{SM}, κ_{Hgg} (not probed in shape analysis)	κ_{HVV}	κ_{AVV}	Run-1	[14]
Rate-based	XVV	κ_{SM}, κ_{Hgg}	κ_{HVV}	κ_{AVV}	Run-2	[146]
	Xgg	κ_{SM}, κ_{Hgg}		κ_{Agg}		

5.1 Shape-based measurement

The search for BSM contributions to the Higgs boson coupling to gauge bosons is performed in the framework of the Higgs characterisation model introduced in Section 1.4.2. In the analysis of the Run-1 data, the Higgs kinematic properties of the $H \to ZZ^* \to 4\ell$ decay (see Figure 5.2) are used for this purpose [14]. Additional information from the production and decay rate is not employed in order to achieve best sensitivity to CP violating contributions to the decay. The relevant coupling parameters are summarised in Table 5.1. The shapes of the distributions of kinematic variables are used to discriminate between SM and non-SM coupling contributions. The signal shapes are normalised to data by means of the signal strength parameter μ that is independent from the Higgs characterisation coupling parameters. The analysis of the four-lepton channel is later combined with the similar analysis of the $H \to WW^* \to e\nu\mu\nu$ decay channel.

The analysis uses a slightly different nomenclature than the Higgs characterisation framework (see Equation 1.36). A factor $\frac{v}{4\Lambda}$ is absorbed into the BSM couplings,

$$\widetilde{\kappa}_{\mathrm{HVV}} = \frac{1}{4}\frac{v}{\Lambda}\kappa_{\mathrm{HVV}}, \qquad \widetilde{\kappa}_{\mathrm{AVV}} = \frac{1}{4}\frac{v}{\Lambda}\kappa_{\mathrm{AVV}}, \tag{5.3}$$

where Λ is the cut-off energy of the effective theory assumed to be 1000 GeV and

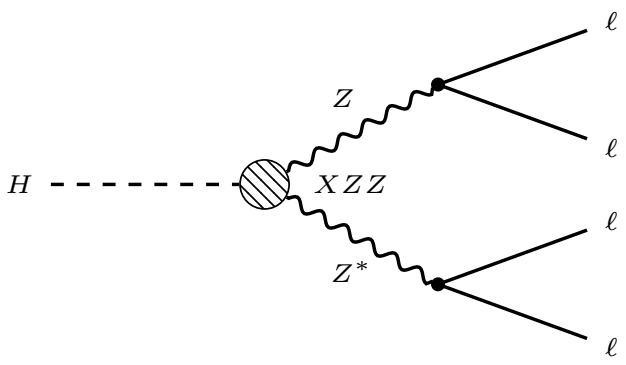

Figure 5.2: Tree-level Feynman diagram of the $H \to ZZ^* \to 4\ell$ decay with effective Higgs to Z-boson coupling.

$v = 246$ GeV the vacuum expectation value of the Higgs field. The results are given in terms of the ratios of coupling strengths from non-SM and SM tensor terms:

$$c_\alpha \widetilde{\kappa}_{\mathrm{HVV}} / c_\alpha \kappa_{\mathrm{SM}} = \widetilde{\kappa}_{\mathrm{HVV}} / \kappa_{\mathrm{SM}} \quad \text{and} \quad s_\alpha \widetilde{\kappa}_{\mathrm{AVV}} / c_\alpha \kappa_{\mathrm{SM}} = (\widetilde{\kappa}_{\mathrm{AVV}} / \kappa_{\mathrm{SM}}) \cdot \tan\alpha. \quad (5.4)$$

where α is the mixing angle of CP-even and CP-odd terms in the Higgs characterisation framework (see Equation 1.36 in Section 1.4.2). Throughout this thesis the short notations defined in Equation 1.41 are used: $c_\alpha \equiv \cos\alpha$ and $s_\alpha \equiv \sin\alpha$. The CP-even and CP-odd non-SM couplings to Z and W-bosons are assumed to be related in the same way as in the SM, i.e. $\widetilde{\kappa}_{\mathrm{HZZ}} = \widetilde{\kappa}_{\mathrm{HWW}}$ and $\widetilde{\kappa}_{\mathrm{AZZ}} = \widetilde{\kappa}_{\mathrm{AWW}}$. Using the ratios is possible for the shape information in the matrix element squared can be factorised with BSM contributions depending on ratios of the BSM couplings relative to the SM couplings, while this is not true for the rate information. The advantage of the ratios is that most systematic uncertainties cancel.

5.1.1 Signal modelling and CP-sensitive observables

The simulated Run-1 Higgs boson signal samples are generated for a mass value of $m_H = 125.5$ GeV. In the data analysis, however, the best Higgs mass value known at the time of $m_H = 125.4$ GeV [60] was used selecting Higgs boson candidates within a four-lepton mass window of 115 GeV $< m_{4\ell} <$ 130 GeV.

The final discriminants used in the shape-based measurement are functions of three-dimensional variables, two CP-sensitive observables and an additional variable for

suppression of the ZZ^* background. The dependence of the three-dimensional distributions on the non-SM couplings is modelled by Monte Carlo simulation using the following procedure. A large signal Monte Carlo sample generated with the JHU program [51, 52] with tensor coupling strengths $g_1 = 1$, $g_2 = 1 + i$ and $g_4 = 1 + i$ is used as reference (see also Section 4.2 and Appendix H.1). The tensor couplings g_i are defined in the anomalous coupling scheme described in Section 1.4.2. The ratios g_2/g_1 and g_4/g_1 are equivalent to $\widetilde{\kappa}_{\mathrm{HVV}}/\kappa_{\mathrm{SM}}$ and $(\widetilde{\kappa}_{\mathrm{AVV}}/\kappa_{\mathrm{SM}}) \cdot \tan\alpha$ in the Higgs characterisation framework. The events in this sample are reweighted using the matrix element method described in Section 6.1 to provide samples for a grid of representative points in the $(\widetilde{\kappa}_{\mathrm{HVV}}/\kappa_{\mathrm{SM}}, (\widetilde{\kappa}_{\mathrm{AVV}}/\kappa_{\mathrm{SM}}) \cdot \tan\alpha)$ parameter space. The matrix element (ME) reweighting method weights events with the ratios $\frac{\mathrm{ME}_{\mathrm{target}}}{\mathrm{ME}_{\mathrm{reference}}}$ of the target matrix element calculated for modified coupling parameters relative to the matrix element used for the reference sample. The matrix elements are calculated at LO with the `JHUGenME` program [52]. The distributions of CP-sensitive observables predicted by the reweighting method are validated with independent smaller Monte Carlo samples with the same target coupling ratio values. The reference sample assumes Higgs boson production via gluon fusion. It is assumed that other production mechanisms do not change the shape of the distributions of the kinematic observables of the Higgs boson decay products. Between the distributions for the discrete non-SM coupling points obtained by reweighting, a linear interpolation is performed as described in [152].

The CP-sensitive observables of the Higgs to four-lepton decay system are the five angles in the Higgs boson rest frame shown in Figure 5.1 as well as the invariant masses m_{12} and m_{34} of the two dilepton pairs from Z-boson decays. The angle θ_1 (θ_2) is measured between the negatively charged lepton from Z_1 (Z_2) and the Z_1 (Z_2) momentum vector, while Φ is the angle between the decay planes of the two Z-bosons around their momentum direction, Φ_1 the angle between the Z_1 decay plane and the plane defined by the Z_1 momentum vector and the beam axis, and θ^* the Z_1 production angle. The distributions of the angles and the invariant masses for SM and BSM couplings normalised to the expected SM signal yield in Run-1 are shown in Figure 5.3, 5.4 and 5.5. The distribution of the angle Φ is sensitive to CP-odd admixtures and, therefore, CP violation. The angles θ_1, θ_2 and Φ are related to the Higgs boson decay and sensitive to the Higgs parity quantum number, while θ^* and Φ_1 are related to the Higgs boson production and sensitive to the Higgs boson spin. The m_{12} and m_{34} distributions are sensitive to the Higgs parity quantum number with m_{34} being especially sensitive to CP-even BSM contributions.

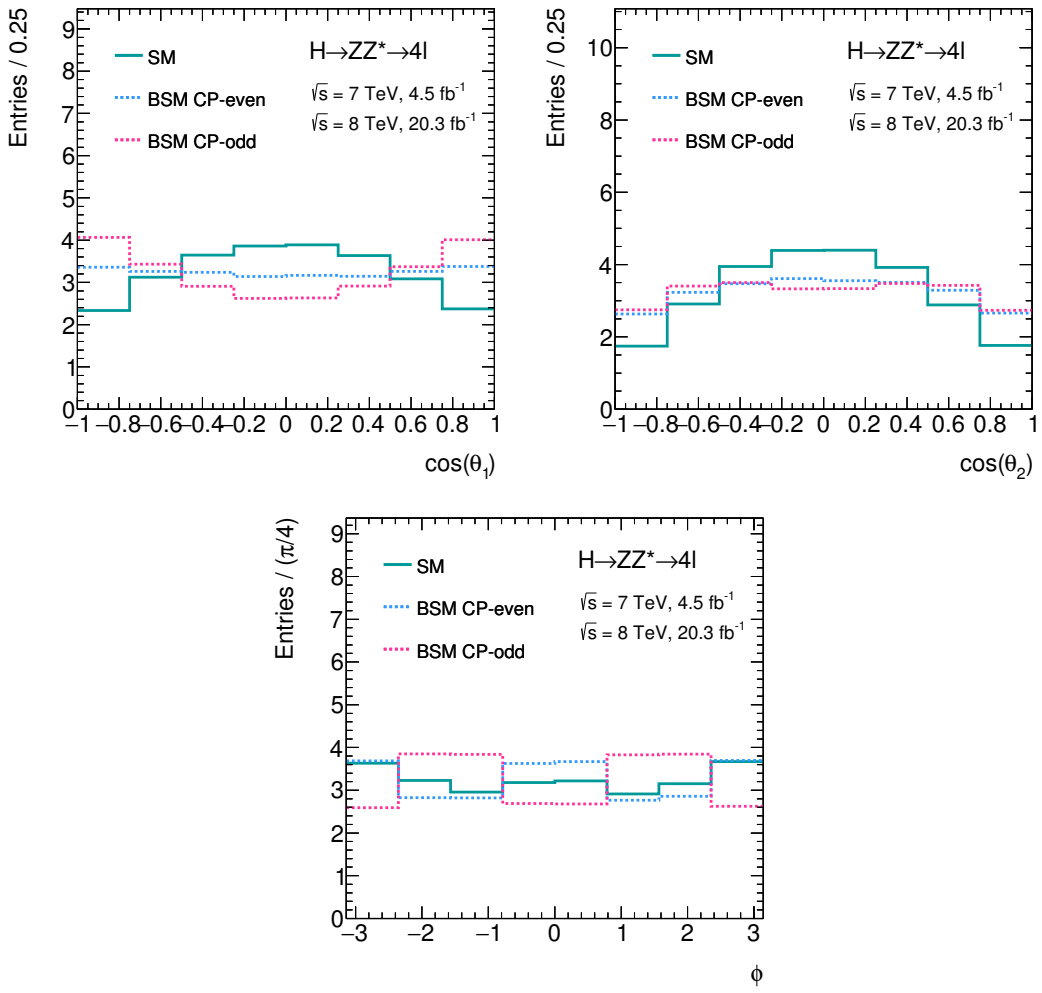

Figure 5.3: The expected distributions of the CP-sensitive angles θ_1, θ_2 and Φ in $H \to ZZ^* \to 4\ell$ decays in Run-1. The pure BSM scenarios with CP-even (dotted blue) and CP-odd (dotted magenta) couplings are shown in comparison with the SM signal expectation (solid green). The uncertainty associated with the Monte Carlo statistics is less than 1 % and therefore not visible.

Instead of the kinematic observables described above, so-called optimal observables are used, which are constructed from the matrix elements $\mathrm{ME_{SM}}$ and $\mathrm{ME_{BSM}}$ for SM and BSM Higgs boson decays [153–156] depending on the non-SM coupling parameters. The ME values are calculated for the measured lepton four-momenta of the leptons from the decaying Higgs boson candidate. They are a measure of how well a specific coupling

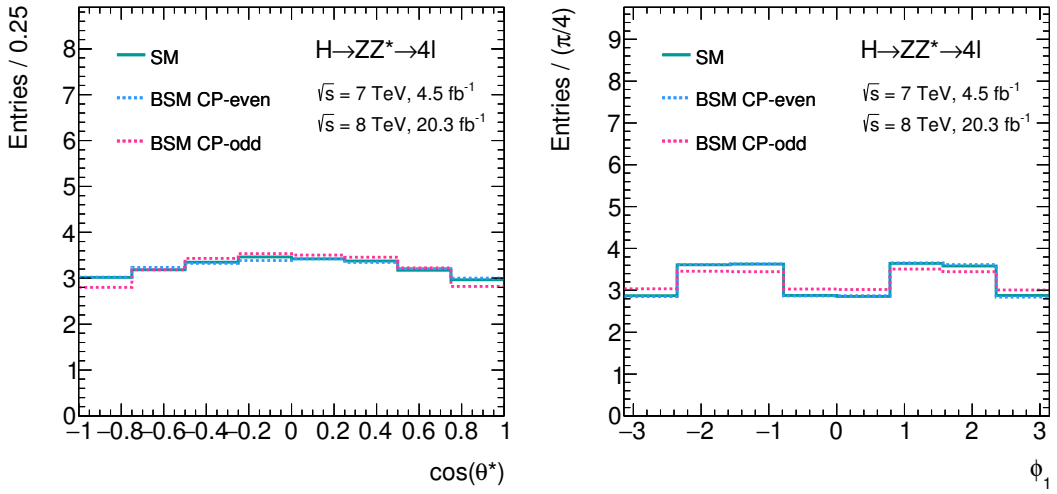

Figure 5.4: The expected distributions spin-sensitive angles θ^* and Φ_1 in $H \to ZZ^* \to 4\ell$ decays in Run-1. The pure BSM scenarios with CP-even (dotted blue) and CP-odd (dotted magenta) couplings are shown in comparison with the SM signal expectation (solid green). The uncertainty associated with the Monte Carlo statistics is less than 1 % and therefore not visible.

configuration includes the kinematics of an event. Two kinds of optimal observables are built from the matrix elements: a first-order optimal observable (O_1), which is sensitive to the sign of the non-SM coupling parameter, and a second-order optimal observable (O_2) sensitive to the absolute value of the coupling parameter. The sensitivity to the sign of a BSM coupling comes from the interference term $2\,\mathrm{Re}\,[\mathrm{ME}^*_{\mathrm{SM}} \cdot \mathrm{ME}_{\mathrm{BSM}}]$ of the SM and BSM matrix elements contributing to the four-lepton final state while the magnitudes of the SM and BSM couplings derive from the amplitudes squared, $|\mathrm{ME}_{\mathrm{SM}}|^2$ and $|\mathrm{ME}|^2_{\mathrm{BSM}}$, respectively.

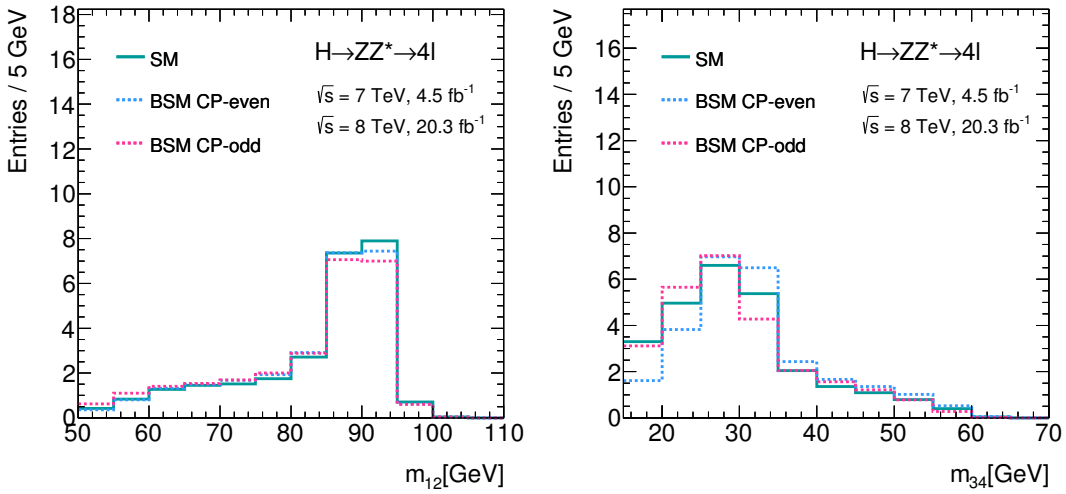

Figure 5.5: The expected distributions of the CP-sensitive invariant masses m_{12} and m_{34} in $H \to ZZ^* \to 4\ell$ decays in Run-1. The pure BSM scenarios with CP-even (dotted blue) and CP-odd (dotted magenta) couplings are shown in comparison with the SM signal expectation (solid green). The uncertainty associated with the Monte Carlo statistics is less than 1 % and therefore not visible.

For the two coupling ratios $\widetilde{\kappa}_{\mathrm{HVV}}/\kappa_{\mathrm{SM}}$ and $(\widetilde{\kappa}_{\mathrm{AVV}}/\kappa_{\mathrm{SM}}) \cdot \tan\alpha$ studied, the optimal observables of first and second order are given by

$$\mathrm{O}_1(\widetilde{\kappa}_{\mathrm{HVV}}) = \frac{2\,\mathrm{Re}\left[\mathrm{ME}^*_{\mathrm{BSM}}\left(\widetilde{\kappa}_{\mathrm{HVV}}/\kappa_{\mathrm{SM}}\right) \cdot \mathrm{ME}_{\mathrm{SM}}\right]}{|\mathrm{ME}_{\mathrm{SM}}|^2}, \tag{5.5}$$

$$\mathrm{O}_2(\widetilde{\kappa}_{\mathrm{HVV}}) = \frac{|\mathrm{ME}_{\mathrm{BSM}}\left(\widetilde{\kappa}_{\mathrm{HVV}}/\kappa_{\mathrm{SM}}\right)|^2}{|\mathrm{ME}_{\mathrm{SM}}|^2}, \tag{5.6}$$

$$\mathrm{O}_1(\widetilde{\kappa}_{\mathrm{AVV}}, \alpha) = \frac{2\,\mathrm{Re}\left[\mathrm{ME}^*_{\mathrm{BSM}}\left((\widetilde{\kappa}_{\mathrm{AVV}}/\kappa_{\mathrm{SM}}) \cdot \tan\alpha\right) \cdot \mathrm{ME}_{\mathrm{SM}}\right]}{|\mathrm{ME}_{\mathrm{SM}}|^2}, \tag{5.7}$$

$$\mathrm{O}_2(\widetilde{\kappa}_{\mathrm{AVV}}, \alpha) = \frac{|\mathrm{ME}_{\mathrm{BSM}}\left((\widetilde{\kappa}_{\mathrm{AVV}}/\kappa_{\mathrm{SM}}) \cdot \tan\alpha\right)|^2}{|\mathrm{ME}_{\mathrm{SM}}|^2}. \tag{5.8}$$

In order to get the easiest possible input for later signal modelling steps, the optimal observables are further transformed to make them normally distributed in the SM case using the *change-of-variable* technique for probability density functions described in Appendix F conserving the total probability. A two-step transformation with an intermediate uniformly distributed variable $\tilde{y}$ is applied. The transformation function for the first step, $\mathrm{O} \mapsto \tilde{y}$, is the cumulative probability distribution (CDF) of O for the

SM case. While the second step, $\tilde{y} \mapsto \mathrm{TO}$, is performed by the inverse error function (erf^{-1}). The combined transformation $\mathrm{O} \mapsto \mathrm{TO}$ is given by

$$\mathrm{TO} \equiv T(\mathrm{O}) = \sqrt{2} \cdot \mathrm{erf}^{-1}\left[2 \cdot \mathrm{CDF}_{\mathrm{SM}}\left(\mathrm{O}\right)\right] \quad \text{with } \mathrm{CDF}_{\mathrm{SM}}\left(\mathrm{O}\right) = \int_{-\infty}^{\mathrm{O}} p_{\mathrm{SM}}(\mathrm{O}')\,\mathrm{dO}', \tag{5.9}$$

where $p_{\mathrm{SM}}(\mathrm{O})$ is the Standard Model probability density function of the optimal observable O. The same transformation is used for all observables. The functions TO_1 and TO_2 of $\widetilde{\kappa}_{\mathrm{HVV}}/\kappa_{\mathrm{SM}}$ are linearly correlated. In order to achieve maximum sensitivity, the correlation is minimised by using the combinations $\mathrm{TO}_1 \pm \mathrm{TO}_2$ as final observables.

The expected distributions of the transformed optimal observables normalised to the expected SM yield in Run-1 are shown in Figure 5.6 for the SM and for BSM couplings with positive and negative sign. The distribution of the observable $\mathrm{TO}_1(\widetilde{\kappa}_{\mathrm{HVV}}) + \mathrm{TO}_2(\widetilde{\kappa}_{\mathrm{HVV}})$ shows a pronounced sign-dependent shape differing from the SM expectation, while the discrimination power of the observable $\mathrm{TO}_1(\widetilde{\kappa}_{\mathrm{HVV}}) - \mathrm{TO}_2(\widetilde{\kappa}_{\mathrm{HVV}})$ is mainly in the bin around -0.5. The discriminant $\mathrm{TO}_1\left(\widetilde{\kappa}_{\mathrm{AVV}}, \alpha\right)$ is sensitive to the sign of the CP-odd BSM coupling, while $\mathrm{TO}_2\left(\widetilde{\kappa}_{\mathrm{AVV}}, \alpha\right)$ is independent of the sign and therefore identical for $(\widetilde{\kappa}_{\mathrm{AVV}}/\kappa_{\mathrm{SM}}) \cdot \tan\alpha = \pm 5$.

In order to improve the discrimination of the Higgs boson signal from the dominant ZZ^* background, a multivariate discriminant $\mathrm{BDT(ZZ)}' = f(\eta_{4l}, p_{\mathrm{T}}^{4l}, m_{4\ell}, \cos\theta^*, \Phi_1)$ based on a *Boosted Decision Tree* algorithm [157] is used which combines kinematic variables which are not CP-sensitive, the pseudorapidity (η_{4l}), transverse momentum (p_{T}^{4l}) and the invariant mass ($m_{4\ell}$) of the four-lepton system, as well as the angular variables $\cos\theta^*$ and Φ_1 introduced above. The Boosted Decision Tree is trained separately for the four different four-lepton final states.

The $\mathrm{BDT(ZZ)}'$ discriminant is transformed in a similar way as the optimal observables to follow a uniform distribution in the case of the SM:

$$\mathrm{BDT(ZZ)} \equiv T(\mathrm{BDT(ZZ)}') = \mathrm{CDF}_{\mathrm{SM}}\left(\mathrm{BDT(ZZ)}'\right), \tag{5.10}$$

with

$$\mathrm{CDF}_{\mathrm{SM}}\left(\mathrm{BDT(ZZ)}'\right) = \int_{-\infty}^{\mathrm{BDT(ZZ)}'} p_{\mathrm{SM}}(\mathrm{BDT(ZZ)}'')\,\mathrm{dBDT(ZZ)}'', \tag{5.11}$$

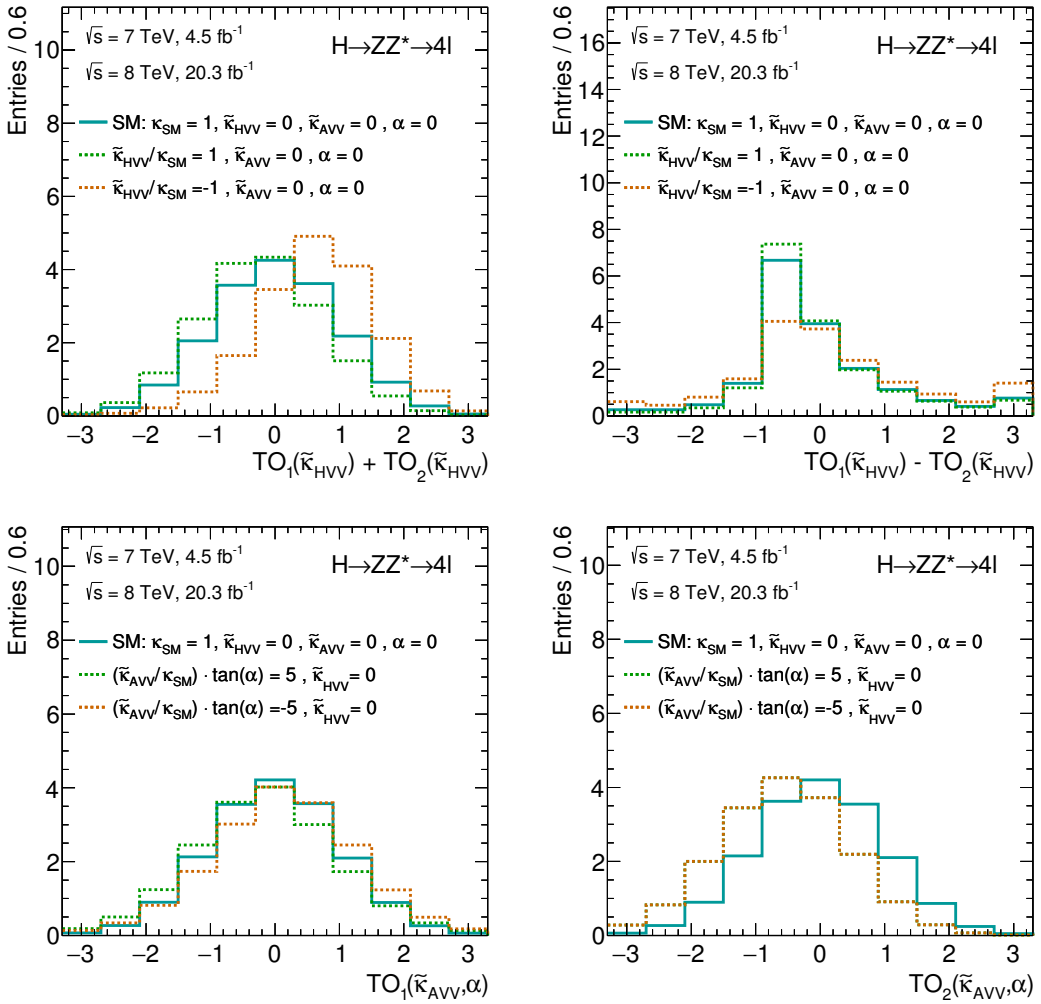

Figure 5.6: The expected distributions of the CP-sensitive observables $\mathrm{TO}_1(\widetilde{\kappa}_{\mathrm{HVV}}) + \mathrm{TO}_2(\widetilde{\kappa}_{\mathrm{HVV}})$, $\mathrm{TO}_1(\widetilde{\kappa}_{\mathrm{HVV}}) - \mathrm{TO}_2(\widetilde{\kappa}_{\mathrm{HVV}})$, $\mathrm{TO}_1(\widetilde{\kappa}_{\mathrm{AVV}}, \alpha)$ and $\mathrm{TO}_2(\widetilde{\kappa}_{\mathrm{AVV}}, \alpha)$ in $H \to ZZ^* \to 4\ell$ decays in Run-1. The BSM contributions with positive (dotted green) and negative (dotted orange) BSM couplings are shown in comparison with the SM signal expectation (solid green). The uncertainty associated with the Monte Carlo statistics is less than 1 % and therefore not visible.

where $p_{\mathrm{SM}}(\mathrm{BDT(ZZ)}')$ is the SM probability distribution function for $\mathrm{BDT(ZZ)}'$.

Final three-dimensional discriminants for CP-even and CP-odd BSM couplings, respectively, are formed with two optimal observables and the multivariate discriminant

BDT(ZZ)′:

$$D_{\tilde{\kappa}_{\mathrm{HVV}}/\kappa_{\mathrm{SM}}}\left((\mathrm{TO}_1-\mathrm{TO}_2),(\mathrm{TO}_1+\mathrm{TO}_2),\mathrm{BDT(ZZ)}\right) \tag{5.12}$$

and

$$D_{(\tilde{\kappa}_{\mathrm{AVV}}/\kappa_{\mathrm{SM}})\cdot\tan\alpha}\left(\mathrm{TO}_1,\mathrm{TO}_2,\mathrm{BDT(ZZ)}\right) \tag{5.13}$$

separately for each of the four final states ($4e$, 4μ, $2e2\mu$, $2\mu2e$). The *Kernel Density Estimation* method [158] with a Gaussian kernel is employed to interpolate between nearby bins of the three-dimensional discriminant distributions in order to be less sensitive to statistical fluctuations.

5.1.2 Background estimation

The shapes of the three-dimensional discriminant distributions for the background processes are determined using the background estimation methods described in Section 4.3.2. The dominant background from ZZ^* continuum production is modelled by Monte Carlo simulation, while the reducible backgrounds with non-prompt or non-isolated leptons, mostly $t\bar{t}$ and Z+jets production, are estimated using data-driven techniques. The expected distributions of the BDT(ZZ) discriminant for SM and BSM couplings with positive and negative sign in the $H \to ZZ^* \to 4\ell$ events and for the ZZ^* and the Z+jets background processes are shown in Figure 5.7. By construction, the BDT(ZZ) distribution for the Higgs signal is flat and similar in the SM and BSM case. The ZZ^* and Z+jets backgrounds prefer small values of BDT(ZZ) and can therefore be distinguished from the Higgs boson signal.

5.1.3 Systematic uncertainties

In general, a measurement is affected by two sources of uncertainties: the statistical uncertainty of the data, and the systematic uncertainty related to the limitations in experimental equipment or methods. Systematic uncertainties in the tensor structure measurement arise from uncertainties in the detector response to the final state particles and from uncertainties in the theoretical predictions.
The systematic uncertainties can change the normalisation and the shape of the signal and background contributions to the three-dimensional discriminants $D_{\tilde{\kappa}_{\mathrm{HVV}}/\kappa_{\mathrm{SM}}}$ and $D_{(\tilde{\kappa}_{\mathrm{AVV}}/\kappa_{\mathrm{SM}})\cdot\tan\alpha}$. The shape and normalisation uncertainties are included as nuisance parameters in the maximum likelihood function (see Section 5.1.4). Only

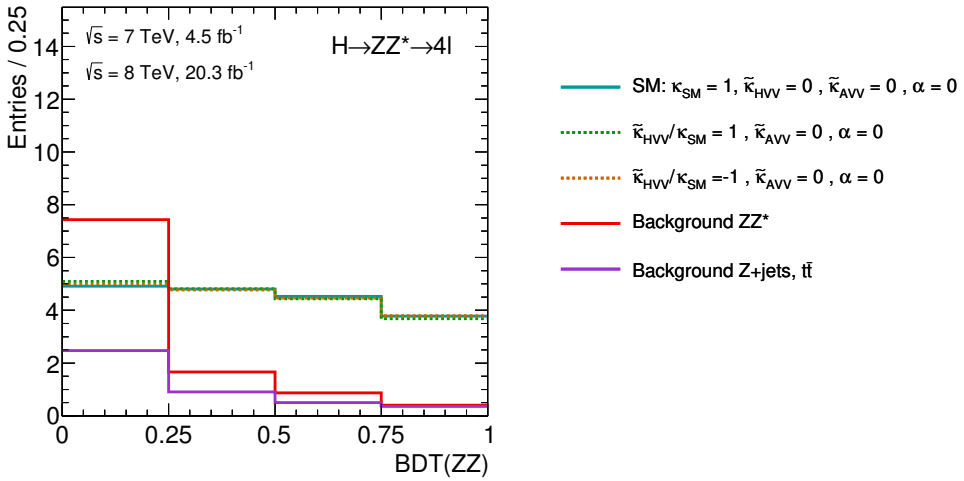

Figure 5.7: The expected distributions for the Higgs signal, ZZ^* background (solid red) and Z+jets background (solid purple) of the BDT(ZZ) discriminant in $H \to ZZ^* \to 4\ell$ decays in Run-1. The BSM contributions with positive (dotted green) and negative (dotted orange) BSM couplings are shown in comparison with the SM signal expectation (solid green). The uncertainty associated with the Monte Carlo statistics is less than 1 % and therefore not visible.

nuisance parameters with relative impact higher than 0.5 % on the limits of non-SM coupling contributions are included. The lists of experimental and theoretical systematic uncertainties, given in the following, are general and also valid for the rate-based measurement. The tensor structure measurements in Run-1 and Run-2 still are statistically limited.

Experimental uncertainties

The experimental systematic uncertainties include

- the error on the integrated luminosity determination,
- uncertainties related to the reconstruction of leptons and jets in the final state, including uncertainties in the lepton momenta and jet energies
- uncertainties in the modelling of the pile-up events, and
- uncertainties in the data-driven background estimation.

The first three uncertainties are propagated to all signal and background predictions from simulation, while the last uncertainty is intrinsic to data-driven background estimation. For the shape-based analysis, the uncertainty related to jets is not relevant since jets are not required in the signal selection, while for the rate-based analysis described in Section 5.2, the uncertainty related to jet reconstruction and energy measurement is important.
The luminosity of the analysed Run-1 data set is measured as described in Section 2.3.4 with a precision of 1.8 % and 2.8 % for 2011 and 2012 data, respectively.
The electron energy and muon momentum scale uncertainties depend on the detector region and reach maximum values of 1 % and 0.2 %, respectively. The uncertainties in trigger efficiency and lepton reconstruction and identification affect the inclusive signal yield by up to 1.6 %
The reducible background contributions, $t\bar{t}$ and Z+jets production, are estimated from data separately for the Z+$\mu\mu$ and Z+ee final states as described in Section 4.3.2. For Z+$\mu\mu$ final states, the systematic uncertainty is related to the estimation of the extrapolation factors from the control regions to the signal region. The transfer factor uncertainty due to limited Monte Carlo statistics amounts to 6 %, 60 % and 16 % for the Z+HF, Z+LF and $t\bar{t}$ contributions, respectively. An additional error of 1.6 % is added to account uncertainties in the estimation of the transfer factor from Z+μ control data. For Z+ee final states, the transfer factors are also the dominant source of uncertainty. It amounts to 30 %, 20 % and 25 % for f, γ and q contributions, respectively.
Finally, an uncertainty is assigned to the smoothing of the discriminant distributions with the *Kernel Density Estimation* method. The nominal bandwidth 0.16 (0.5) for smoothing of signal and ZZ^* background (reducible background) shapes is varied within 20 %, i.e. 0.13 and 0.20 (0.4 and 0.6).

Theoretical uncertainties

The predictions of the total cross section and of the final state topology of both signal and background processes, are affected by theoretical uncertainties. The theoretical systematic uncertainties include the following sources:

- The QCD scale uncertainty is evaluated by varying the renormalisation and factorisation scales each by factors 0.5 and 2.0.
- The uncertainty from the PDF sets is determination by variation of parameters

of the parton distribution functions. The strong coupling constant α_S is varied within its present error margins.

- The uncertainty due to the parton shower simulation is evaluated by variation of parameters of the parton shower algorithm concerning initial and final state radiation and multi-parton interactions. In addition, the default algorithm, PYTHIA, is compared to an alternative simulation by the HERWIG++ program.

The QCD scale uncertainty is $+7\,\%$ and $-8\,\%$ for the ggF process, $\pm 1\,\%$ and $\pm 2\,\%$ for VBF and associated VH production, respectively, and $+4\,\%$ and $-9\,\%$ for the $t\bar{t}H$ production process.
The Higgs boson signal uncertainty related to the PDF set and the strong coupling constant is estimated following the PDF4LHC prescription [159] by comparing the results for the CTEQ [160], MSTW [128] and NNPDF2.1 [106] PDF sets. For each PDF set, a different α_S value has been used by the authors, 0.118, 0.1207 and 0.119 for CTEQ, MSTW and NNPDF2.1, respectively. The α_S value is varied within one standard deviation, ± 0.0012. The associated uncertainties in the cross sections amount to $\pm 8\,\%$ for gluon-induced and to $\pm 4\,\%$ for quark-induced processes and are fully correlated between signal and background processes with the same initial state.
The PDF+α_S and QCD scale uncertainties of the ZZ^* background process are a parametrised function of the four-lepton invariant mass $m_{4\ell}$. The quark-(gluon-)induced ZZ^* background processes have a QCD scale uncertainty of $\pm 5\,\%$ ($\pm 25\,\%$), and a PDF+α_S uncertainty of $\pm 4\,\%$ ($\pm 8\,\%$).

5.1.4 Fitting method and results

A binned maximum likelihood fit of the expected distributions of the three-dimensional discriminating variables, i.e. $D_{\widetilde{\kappa}_{\mathrm{HVV}}/\kappa_{\mathrm{SM}}}((\mathrm{TO}_1 - \mathrm{TO}_2), (\mathrm{TO}_1 + \mathrm{TO}_2), \mathrm{BDT(ZZ)})$ and $D_{(\widetilde{\kappa}_{\mathrm{AVV}}/\kappa_{\mathrm{SM}})\cdot\tan\alpha}(\mathrm{TO}_1, \mathrm{TO}_2, \mathrm{BDT(ZZ)})$ (see Equations 5.12 and 5.13), to the data is performed with the BSM coupling parameters as free parameters. Each of the two BSM coupling parameters is probed independently while the other one is set to zero.

Systematic uncertainties are taken into account via nuisance parameters θ_m, that are constrained by auxiliary measurements as described in the previous section. The likelihood function is the product of the Poisson probabilities for signal and background over all bins of the discriminating variable distributions for all final states and all data sets with different centre-of-mass energies, multiplied by the product of the constraint terms A_m of nuisance parameters:

$$\mathcal{L}(\kappa_{\mathrm{BSM}}, \theta) = \prod_{k}^{N_{\sqrt{s}}} \prod_{j}^{N_{\mathrm{FS}}} \prod_{i}^{N_{\mathrm{bins}}} P(n_{ijk} | \mu \cdot s_{ijk}(\kappa_{\mathrm{BSM}}, \theta) + b_{ijk}(\theta)) \times \prod_{m}^{N_{\mathrm{nuisance}}} A_m(\theta_m) \quad (5.14)$$

where κ_{BSM} is either $\widetilde{\kappa}_{\mathrm{HVV}}/\kappa_{\mathrm{SM}}$ or $(\widetilde{\kappa}_{\mathrm{AVV}}/\kappa_{\mathrm{SM}}) \cdot \tan\alpha$, $\theta = (\theta_m)$ is the vector of nuisance parameters, n_{ijk} the number of observed events for each centre-of-mass energy $\sqrt{s} = 7$ and 8 TeV, final state (FS=$4e$, 4μ, $2e2\mu$ and $2\mu2e$) and bin of the discriminant distributions with N_{bins} bins. The distributions of signal and background events are denoted by s_{ijk} and b_{ijk}, respectively. The signal contribution is normalised by means of the signal strength parameter μ which is used as a free parameter independent of the BSM coupling parameters and separately for the two Run-1 data sets. $A_m(\theta)$ are Gaussian distributions with the mean and width given by the auxiliary measurements described in the previous section. The background normalisation are free parameters in the fit and contained in the nuisance parameter set θ.

Confidence intervals at 68 % and 95 % confidence level (CL) on the BSM coupling parameters are determined using the profiled likelihood-ratio test statistic [161]:

$$t = -2 \ln \lambda(\kappa_{\mathrm{BSM}}) \quad \text{with} \quad \lambda(\kappa_{\mathrm{BSM}}) = \frac{\mathcal{L}(\kappa_{\mathrm{BSM}}, \hat{\hat{\theta}})}{\mathcal{L}(\widehat{\kappa}_{\mathrm{BSM}}, \widehat{\theta})} \quad (5.15)$$

where $\widehat{\kappa}_{\mathrm{BSM}}$ and $\widehat{\theta}$ are the best-fit values maximising the likelihood and $\hat{\hat{\theta}}$ denotes the value of θ that maximises the likelihood function for a fixed value of κ_{BSM}. The

numerator $\mathcal{L}(\kappa, \hat{\hat{\theta}})$ is the conditional ML estimator, where the likelihood is maximised for specific values of κ. The denominator $\mathcal{L}(\widehat{\kappa}_{\mathrm{BSM}}, \widehat{\theta})$ is the maximised (unconditional) likelihood function. The probability p of observing a value of the test statistic that is equal or larger than a certain threshold t_p is given by

$$p = \int_{t_p}^{\infty} f(t|\kappa_{\mathrm{BSM}})\,\mathrm{d}t\,, \tag{5.16}$$

where $f(t|\kappa_{\mathrm{BSM}})$ is the probability density function of t for a given κ_{BSM}. The level of discrepancy can be defined with $p = (1 - \mathrm{CL})$, i.e. when testing for 95 % CL (68 % CL) $p = 0.05$ ($p = 0.32$). Assuming $f(t|\kappa_{\mathrm{BSM}})$ is known, confidence level intervals can be constructed for the parameter of interest, i.e. κ_{BSM}. In this thesis, asymptotic behaviour [161] of $f(t|\kappa_{\mathrm{BSM}})$ is assumed. Based on an approximation by Wilks and Wald [162, 163], it has been shown that $f(t|\kappa_{\mathrm{BSM}})$ follows a Chi-squared distribution with the number of degrees of freedom equal to the number of parameters of interest [161]. In the shape-based measurement one parameter of interest, either $\widetilde{\kappa}_{\mathrm{HVV}}/\kappa_{\mathrm{SM}}$ or $(\widetilde{\kappa}_{\mathrm{AVV}}/\kappa_{\mathrm{SM}}) \cdot \tan\alpha$, is probed. In case of one parameter of interest and assuming asymptotic approximation, the values of t defining 68 % and 95 % confidence intervals are given by $t_{0.32} = 0.99$ and $t_{0.05} = 3.84$, respectively (see Appendix A).

The constraints on the BSM coupling parameters are evaluated under the SM hypothesis in two scenarios. Asimov Monte Carlo data sets [161] for the SM expectation with different settings of μ and θ are used:

1. The signal normalisation is fixed to the SM expectation $\mu = 1$ and all nuisance parameters assume their nominal values.

2. The signal normalisation μ and the nuisance parameters are determined from data and fixed to the best-fit values $\widehat{\mu}$ and $\widehat{\theta}$, respectively. The second scenario allows for deviations from the SM in the signal normalisation.

The expected and observed distributions of the transformed optimal observables and of the BDT(ZZ) discriminant are shown in Figures 5.8 and 5.9. In addition to the expected SM distributions, the BSM expectations are shown for selected values of the BSM couplings with positive and negative sign. As discussed in Section 5.1.1, the distributions of the $\mathrm{TO}_1(\widetilde{\kappa}_{\mathrm{HVV}}) + \mathrm{TO}_2(\widetilde{\kappa}_{\mathrm{HVV}})$ and $\mathrm{TO}_1\,(\widetilde{\kappa}_{\mathrm{AVV}}, \alpha)$ observables are sign-sensitive, while the discrimination power of the $\mathrm{TO}_1(\widetilde{\kappa}_{\mathrm{HVV}}) - \mathrm{TO}_2(\widetilde{\kappa}_{\mathrm{HVV}})$ observable is mainly in the bin around -0.5. The $\mathrm{TO}_2\,(\widetilde{\kappa}_{\mathrm{AVV}}, \alpha)$ observable is only sensitive

to the absolute value of the BSM coupling ratio and not to its sign. The expected distributions correspond to the SM normalisation $\mu = 1$. Except for an offset in the normalisation, the data are in agreement with the SM predictions. The BDT(ZZ) distribution for the SM and the BSM couplings are similar by design. The background processes tend towards smaller values of BDT(ZZ) allowing for discrimination against the Higgs boson signal.

The expected and observed values of the profiled likelihood ratio test statistic are shown in Figure 5.10 as a function of the BSM couplings. The regions where the test statistic curves fall below the lower and upper dotted lines correspond to the 68 % and 95 % confidence intervals, respectively, of the BSM coupling parameters. An excess of $H \to ZZ^* \to 4\ell$ events over the prediction has been observed, as discussed in Section 4.3.3 (Table 4.10). The BDT(ZZ) distribution in Figure 5.9 assigns the excess to both signal and background processes. The best-fit signal strengths $\widehat{\mu}_{7\,\mathrm{TeV}} = 1.9$ and $\widehat{\mu}_{8\,\mathrm{TeV}} = 1.6$ corresponding to best-fit values of the BSM coupling parameters are higher than the SM value $\mu = 1$ but consistent with the signal strength $\mu = 1.44^{+0.40}_{-0.33}$ from a dedicated measurement of the signal strength and Higgs boson mass in $H \to ZZ^* \to 4\ell$ decays [145].

The expected and observed best-fit values of the BSM couplings and 68 % CL and 95 % CL confidence intervals are summarised in Table 5.2. The observed BSM coupling values are consistent with the SM predictions of zero. The observed limits are stronger than the expected ones for best-fit signal strengths $\widehat{\mu}$. The difference is even larger assuming $\mu = 1$. This is due to the excess of observed events compared to the SM prediction. The asymmetric shape of the test statistic for the CP-even coupling is due to the interference term between the CP-even SM and BSM contributions which has a maximum at $\widetilde{\kappa}_{\mathrm{HVV}}/\kappa_{\mathrm{SM}} = -1$. The sensitivity is maximal for this value of the CP-even BSM coupling and the difference in the overall rate plays a minor role.

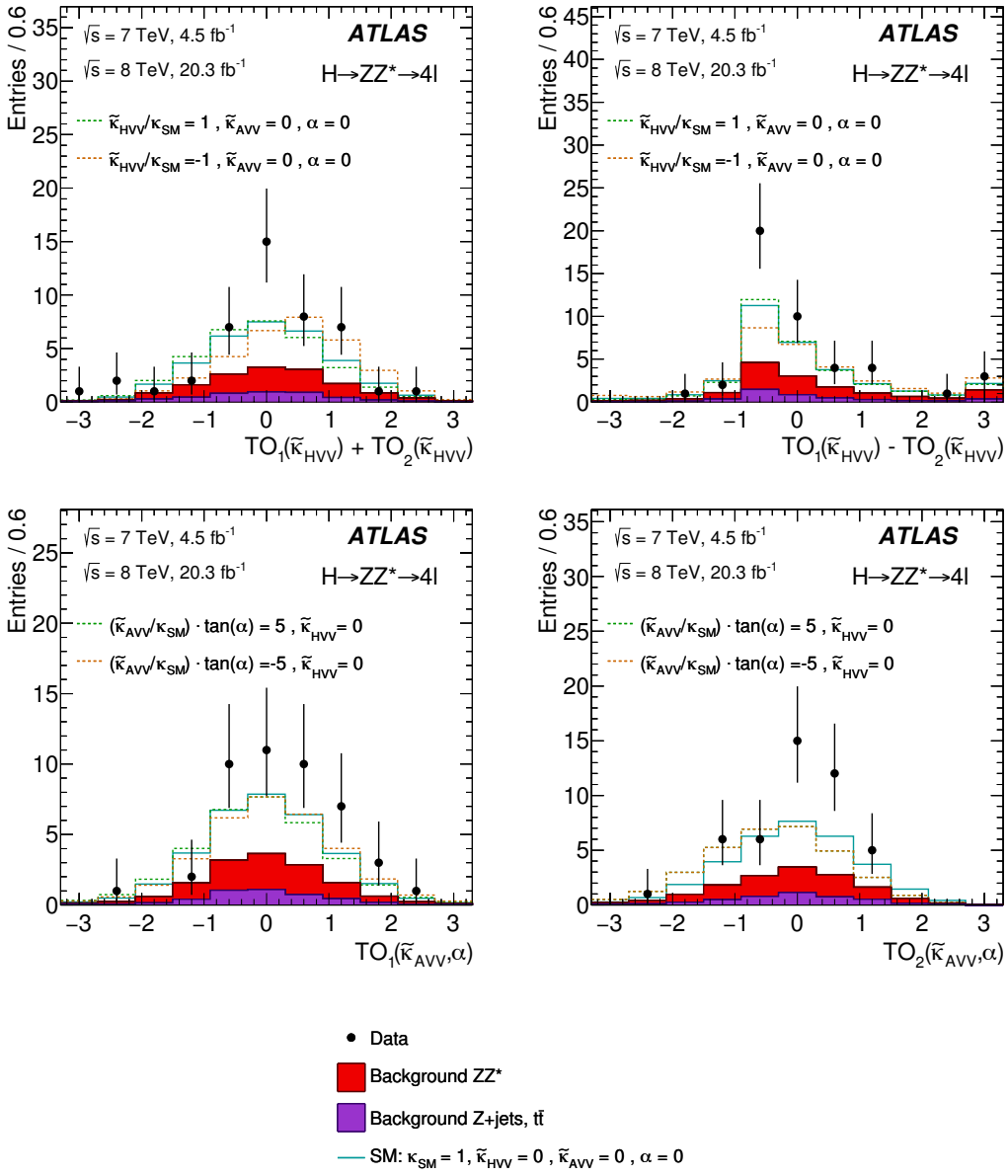

Figure 5.8: Observed and expected distributions of the CP-sensitive observables $\mathrm{TO}_1(\widetilde{\kappa}_{\mathrm{HVV}}) + \mathrm{TO}_2(\widetilde{\kappa}_{\mathrm{HVV}})$, $\mathrm{TO}_1(\widetilde{\kappa}_{\mathrm{HVV}}) - \mathrm{TO}_2(\widetilde{\kappa}_{\mathrm{HVV}})$, $\mathrm{TO}_1(\widetilde{\kappa}_{\mathrm{AVV}}, \alpha)$ and $\mathrm{TO}_2(\widetilde{\kappa}_{\mathrm{AVV}}, \alpha)$ for the Higgs signal and background in Run-1. The BSM contributions with positive (dotted green) and negative (dotted orange) BSM couplings are shown in addition to the SM signal expectation (solid green) [14].

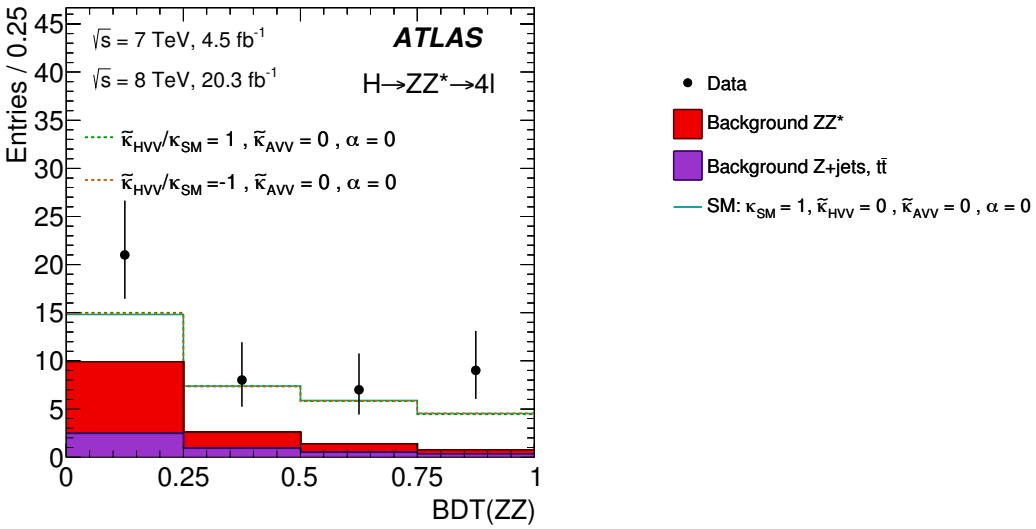

Figure 5.9: The observed and the expected distributions of the BDT(ZZ) discriminant for the Higgs signal and backgrounds in Run-1. The BSM expectations for positive (dotted green) and negative (dotted orange) couplings are shown in addition to the SM expectation (solid green) [14].

Table 5.2: Observed and expected best-fit values as well as 68 % and 95 % confidence intervals for BSM CP-even and CP-odd coupling parameters from the $H \to ZZ^* \to 4\ell$ shape analysis of Run-1 data. The SM expectation corresponds to the observed signal strength $\widehat{\mu}$ and best-fit values for all nuisance parameters [14].

Coupling ratio	68 % CL confidence interval		95 % CL confidence interval		Best-fit value
$H \to ZZ^* \to 4\ell$	Expected	Observed	Expected	Observed	Observed
$\widetilde{\kappa}_{\mathrm{HVV}}/\kappa_{\mathrm{SM}}$	$[-0.44, 1.01]$	$[-0.54, 0.49]$	$[-0.75, 6.95]$	$[-0.75, 2.45]$	-0.2
$(\widetilde{\kappa}_{\mathrm{AVV}}/\kappa_{\mathrm{SM}}) \cdot \tan\alpha$	$[-1.46, 1.46]$	$[-1.66, 0.01]$	$[-2.95, 2.95]$	$[-2.85, 0.95]$	-0.8

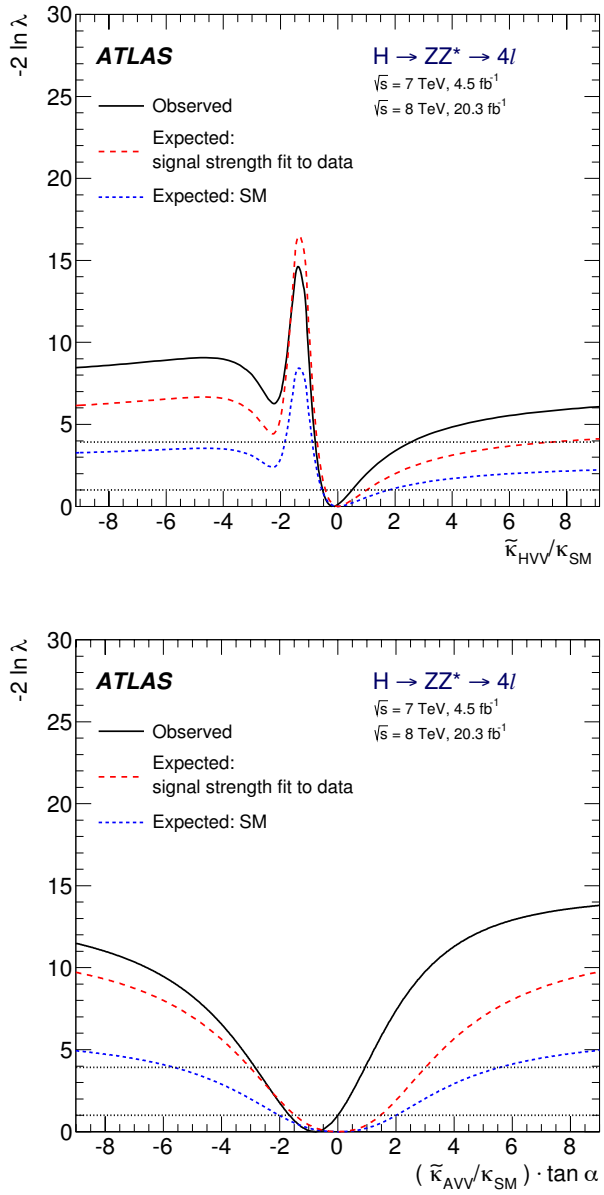

Figure 5.10: The observed (black) and expected profiled likelihood ratio test statistic for CP-even (top) and CP-odd (bottom) BSM couplings in the $H \to ZZ^* \to 4\ell$ shape-analysis of Run-1 data. The SM expectations for the SM signal strength $\mu = 1$ (blue), and for the observed (best-fit) signal strength $\widehat{\mu}$ (red) are also shown. The intersections of the lower and upper dotted horizontal lines define the 68 % and 95 % confidence intervals, respectively, of the BSM coupling parameters [14].

Systematic errors of the $H \to ZZ^* \to 4\ell$ measurement

The impact of each systematic uncertainty is evaluated independently from all other uncertainties. The nominal limits of the BSM coupling parameters is compared to the ones obtained when varying a systematic uncertainty within one standard deviation margins. The systematic uncertainties with the largest impact are related to the background normalisation. The dominant systematic uncertainty is from the data-driven background estimation, the effect is $\pm 1\,\%$ on the upper and lower limits of the non-SM coupling contributions. The second most important systematic uncertainty is the theoretical error in the ZZ^* background cross section with an impact of less than $\pm 1\,\%$.

Combination with the $H \to WW^* \to e\nu\mu\nu$ measurement

The shape-analysis of $H \to ZZ^* \to 4\ell$ decays has been combined with the shape-analysis of $H \to WW^* \to e\nu\mu\nu$ decays with 8 TeV data [164] under the assumption that the BSM Higgs boson couplings to W and Z-bosons have the same strength. A common test statistic is constructed by combining the likelihood functions for both channels. The signal normalisation μ for both channels and, in the case of the $H \to ZZ^* \to 4\ell$ analysis, for both Run-1 centre-of-mass energies are treated as separate free parameters. Correlations of the experimental and theoretical systematic uncertainties between the two decay channels and between the two data taking periods are taken into account.

The $H \to WW^* \to e\nu\mu\nu$ analysis has been performed with $20.3\,\text{fb}^{-1}$ of Run-1 data recorded at $\sqrt{s} = 8$ TeV. A veto is applied against events with jets reconstructed in the final state to prevent contributions from VBF production and study only the BSM coupling contributions to the decay. A slight excess of events has been observed. The observed Higgs boson signal is fitted to 270 ± 70 events assuming the SM hypothesis, which is in good agreement with 238 events expected from Monte Carlo simulation of ggF production. Two BDT discriminants are used one (BDT_0) discriminating between signal and background and the other one (BDT_{CP}) sensitive to BSM coupling contributions. For the BDT_0 variable, the invariant mass of the two final state leptons $m_{\ell\ell}$, the dilepton transverse momentum $p_{\text{T}}^{\ell\ell}$, the angle between the two leptons $\Delta\Phi_{\ell\ell}$ and the transverse mass of the dilepton and missing momentum system m_{T} serve as input. The BDT_{CP} output is trained separately for BSM CP-even

and CP-odd couplings using also different sets of input variables: $m_{\ell\ell}$, $p_{\mathrm{T}}^{\ell\ell}$, $\Delta\Phi_{\ell\ell}$ and the missing transverse momentum $p_{\mathrm{T}}^{\mathrm{miss}}$ for the CP-even coupling and $m_{\ell\ell}$, $\Delta\Phi_{\ell\ell}$, $E_{\ell\ell\nu\nu} = p_{\mathrm{T}}^{\ell_1} - 0.5p_{\mathrm{T}}^{\ell_2} + 0.5p_{\mathrm{T}}^{\mathrm{miss}}$ and the absolute value of the lepton transverse momenta difference $\Delta p_{\mathrm{T}} = |\vec{p_{\mathrm{T}}}^{\ell_1} - \vec{p_{\mathrm{T}}}^{\ell_2}|$ with the leading/subleading lepton transverse momenta $p_{\mathrm{T}}^{\ell_{1/2}}$ for the CP-odd coupling.

The observed and expected dependence of the test statistic on the BSM coupling parameters for the $H \to WW^* \to e\nu\mu\nu$ analysis are shown in Figure 5.11. The corresponding expected and observed best-fit values and 68 % and 95 % confidence regions of the BSM coupling parameters are given in Table 5.3. The observed values are compatible with the SM expectations. The observed limits are again tighter than the expected ones. The $H \to WW^* \to e\nu\mu\nu$ measurement is less sensitive than the one in the $H \to ZZ^* \to 4\ell$ channel, since the four-momenta of the neutrinos in the final state cannot be fully reconstructed. In addition, the $H \to WW^* \to e\nu\mu\nu$ decay channel has a very large SM background contribution.

Table 5.3: Observed and expected best-fit values as well as 68 % and 95 % confidence intervals for the BSM CP-even and CP-odd coupling parameters from the $H \to WW^* \to e\nu\mu\nu$ shape-analysis using 20.3 fb^{-1} of Run-1 data recorded at $\sqrt{s} = 8$ TeV. The SM expectation corresponds the observed signal strength $\widehat{\mu}$ and the best-fit values for all nuisance parameters [14].

Coupling ratio	68 % CL confidence interval		95 % CL confidence interval		Best-fit value
$H \to WW^* \to e\nu\mu\nu$	Expected	Observed	Expected	Observed	Observed
$\widetilde{\kappa}_{\mathrm{HWW}}/\kappa_{\mathrm{SM}}$	$]-\infty, -1.4]$ $\cup$ $[-0.5, +\infty[$	$[-1.5, -1.2]$ $\cup$ $[-0.65, -0.5]$	$]-\infty, -1.2]$ $\cup$ $[-0.7, +\infty[$	$[-2.22, -1]$ $\cup$ $[-0.85, 0.4]$	-1.3
$(\widetilde{\kappa}_{\mathrm{AWW}}/\kappa_{\mathrm{SM}}) \cdot \tan\alpha$	$[-2, 2]$	$[-1.6, 1.3]$	n.a.	$[-6, 5]$	-0.2

The sensitivity can be increased by combining both measurements. The SM expected test statistics from the individual $H \to WW^* \to e\nu\mu\nu$ and $H \to ZZ^* \to 4\ell$ analyses and their combination are shown in Figure 5.12 for the observed signal strengths $\widehat{\mu}$, which are different in both channels. The observed test statistic is shown in Figure 5.13 (top) for the individual analyses and their combination. A comparison of observed and expected test statistics for the combined measurement can be seen in Figure 5.13 (bottom). A summary of the combined measurement results is given in Table 5.4. The results are in agreement with the SM prediction within 1.5 and 1 standard deviation for the BSM CP-even and CP-odd coupling parameters, respectively. The

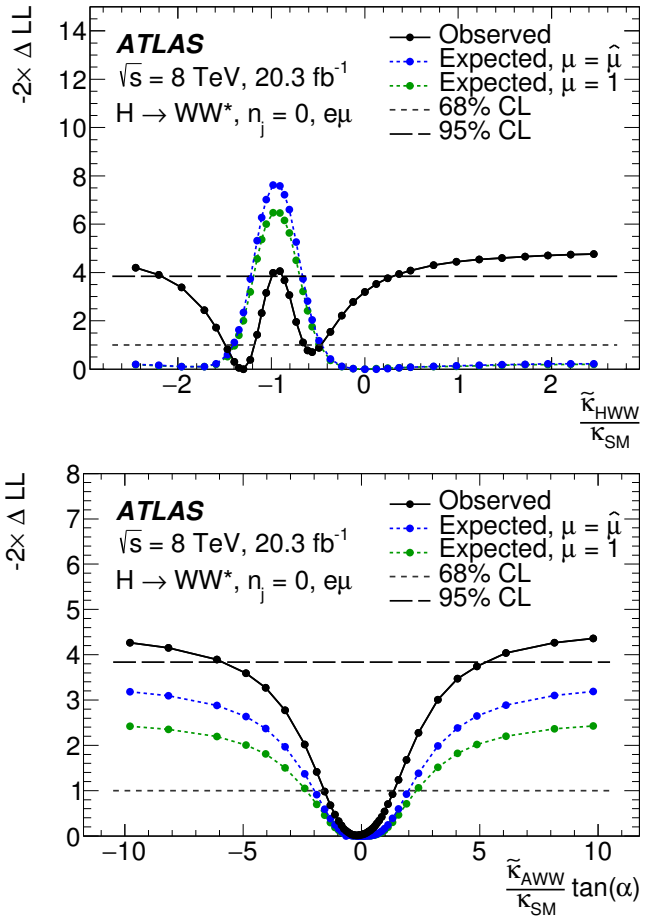

Figure 5.11: Observed (black) and expected profiled likelihood ratio test statistic for CP-even (top) and CP-odd (bottom) BSM couplings in the $H \to WW^* \to e\nu\mu\nu$ shape-analysis using 20.3 fb^{-1} of Run-1 data recorded at $\sqrt{s} = 8$ TeV. The SM expectations for the SM signal strength $\mu = 1$ (green) and for the observed (best-fit) signal strength $\hat{\mu}$ (blue) are also shown. The intersections of the dotted and dashed horizontal lines define the 68 % CL and 95 % CL intervals, respectively, of the BSM coupling parameters [164].

CP-even coupling parameter $\tilde{\kappa}_{\mathrm{HVV}}/\kappa_{\mathrm{SM}}$ is excluded at 95 % CL in the range below -0.73 and above 0.63, while the CP-odd coupling parameter $(\tilde{\kappa}_{\mathrm{AVV}}/\kappa_{\mathrm{SM}}) \cdot \tan\alpha$ is excluded at 95 % CL in the range below -2.18 and above 0.83. The 95 % confidence intervals obtained with the $H \to ZZ^* \to 4\ell$ analysis are reduced by 60 % and 20 % in the combination with the $H \to WW^* \to e\nu\mu\nu$ measurement for $\tilde{\kappa}_{\mathrm{HVV}}/\kappa_{\mathrm{SM}}$ and $(\tilde{\kappa}_{\mathrm{AVV}}/\kappa_{\mathrm{SM}}) \cdot \tan\alpha$, respectively.

Table 5.4: Observed and expected best-fit values, 68 % and 95 % confidence regions for the CP-even and CP-odd coupling parameters from the $H \to WW^* \to e\nu\mu\nu$ and $H \to ZZ^* \to 4\ell$ combined analysis using 20.3 fb^{-1} of data recorded at $\sqrt{s} = 8$ TeV and, in case of the four-lepton channel, additional 4.5 fb^{-1} of data recorded at $\sqrt{s} = 7$ TeV. The SM expectation assumes the observed signal strengths $\widehat{\mu}$ and the best-fit values for all other nuisance parameters [14].

Coupling ratio	68 % CL confidence interval		95 % CL confidence interval		Best-fit value
Combined	Expected	Observed	Expected	Observed	Observed
$\widetilde{\kappa}_{\mathrm{HVV}}/\kappa_{\mathrm{SM}}$	$[-0.4, 0.8]$	$[-0.6, -0.2]$	$[-0.55, 4.80]$	$[-0.73, 0.63]$	-0.48
$(\widetilde{\kappa}_{\mathrm{AVV}}/\kappa_{\mathrm{SM}}) \cdot \tan\alpha$	$[-1.2, 1.2]$	$[-1.4, 0.1]$	$[-2.33, 2.30]$	$[-2.18, 0.83]$	-0.68

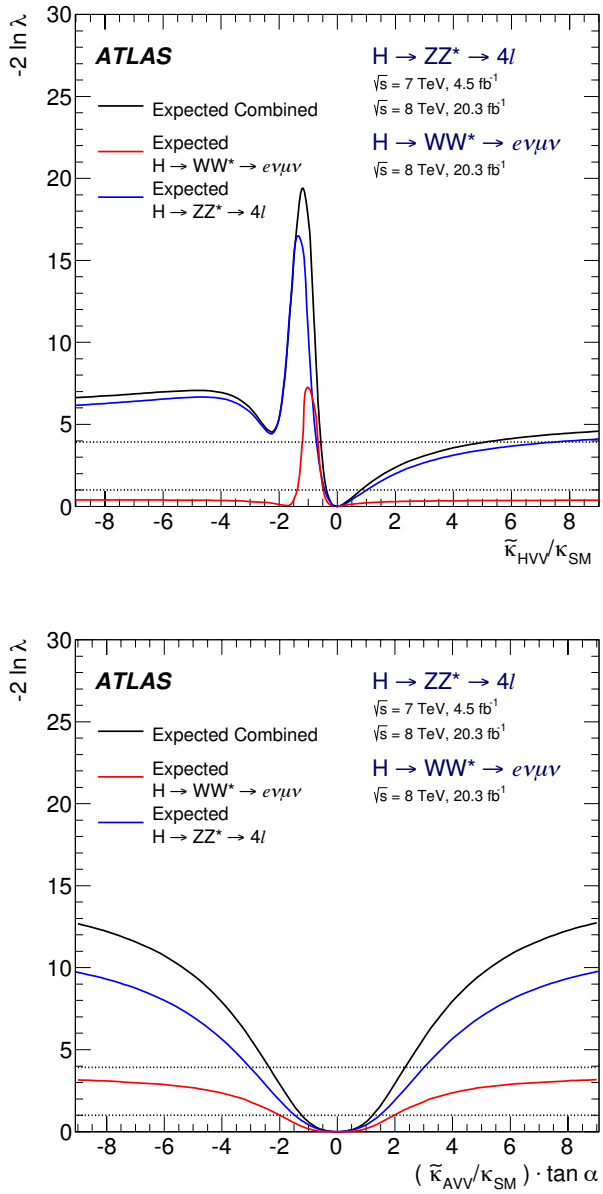

Figure 5.12: Expected dependence of the test statistic on the CP-even (top) and CP-odd (bottom) BSM couplings for the individual analyses of $H \to ZZ^* \to 4\ell$ and $H \to WW^* \to e\nu\mu\nu$ decays and their combination for Run-1 data assuming best-fit values for the signal strength $\widehat{\mu}$ and the nuisance parameters. The intersections of the dotted and dashed horizontal lines define the 68 % CL and 95 % CL intervals, respectively, of the BSM coupling parameters [14].

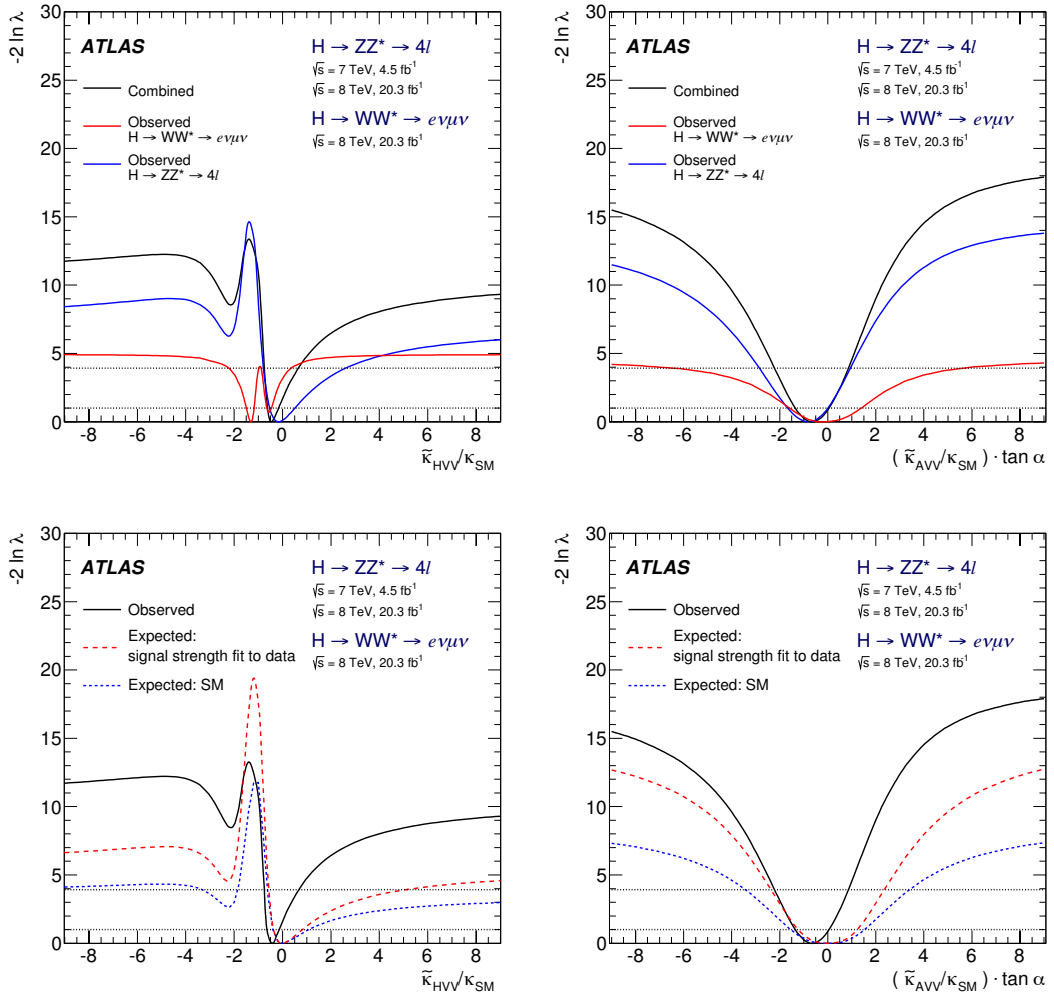

Figure 5.13: Observed distributions of the test statistic on the CP-even (top) and CP-odd (bottom) BSM couplings for the individual analyses of the $H \to WW^* \to e\nu\mu\nu$ and $H \to ZZ^* \to 4\ell$ decays and their combination for Run-1 data. A comparison of the observed and expected combined functions is shown at the bottom left and right. The SM expectation is shown assuming the nominal signal strength $\mu = 1$ and nuisance parameters (blue) and the best-fit values for the signal strength $\hat{\mu}$ (red) and the nuisance parameters. The intersections of the dotted and dashed horizontal lines define the 68 % CL and 95 % CL intervals, respectively, of the BSM coupling parameters [14].

5.2 Rate-based measurement

Due to the increased size of the Run-2 data set and the higher signal production cross section at the increased centre-of-mass energy, it has become possible to distinguish vector boson fusion (VBF) and even associated Higgs boson production with vector bosons (VH) from the dominant gluon fusion process in $H \to ZZ^* \to 4\ell$ decays. Measurement of VBF and VH production rates adds additional sensitivity for BSM Higgs boson couplings to W and Z-bosons, since they are present both in the production and the decay (see Figure 5.14). The cross section of these production processes can be significantly enhanced by additional BSM couplings to weak gauge bosons changing also the relative contributions of the different production mechanism compared to the SM. In addition, CP-odd BSM contributions to the coupling of the Higgs boson to gluons, $s_\alpha \kappa_{\mathrm{Agg}}$, modify the gluon fusion production cross section (see Figure 5.15). The expected dependence of the ggF, $V(\to \ell\nu/\ell\ell)H$ and combined VBF and$V(\to qq)H$ Higgs boson production cross sections on the BSM coupling parameters is shown in Figures 5.16 and 5.17. The VBF and $V(\to qq)H$ production mechanism are simulated together to take possible interference effects due to the same final state into account (see Section 4.2). In the analysis, the vector boson fusion and associated productions are treated in a single signal model, VBF $+VH$. The interference between CP-even SM and BSM couplings leads to a minimum Higgs boson production cross-section at non-zero $c_\alpha \kappa_{\mathrm{HVV}}$ values (see Figure 5.16). For VH production the interference is strongest for positive $c_\alpha \kappa_{\mathrm{HVV}}$, while the cross section minimum is located at negative BSM couplings for ggF and VBF productions. The latter effect cannot be seen in Figure 5.16 due to the combined VBF $+V(\to qq)H$ signals. Separate distributions for VBF, WH and ZH productions can be found in Appendix G.

An analysis strategy has been developed, that differentiates between the Higgs boson production mechanisms and introduces additional observables related to the production vertex which are sensitive to the BSM couplings. The decay kinematic variables are not further considered, since they provide less sensitivity. This analysis [146], performed on Run-2 data, is referred to as the rate-based analysis since the rate information is dominant in sensitivity. Nevertheless, it is important to stress that shape information is used in this analysis. One should notice, that the measurements of production rates is not sensitive to CP violation although they strongly increase the sensitivity to CP-even and CP-odd BSM couplings. CP violating effects can only be detected in distributions of final state kinematic variables.

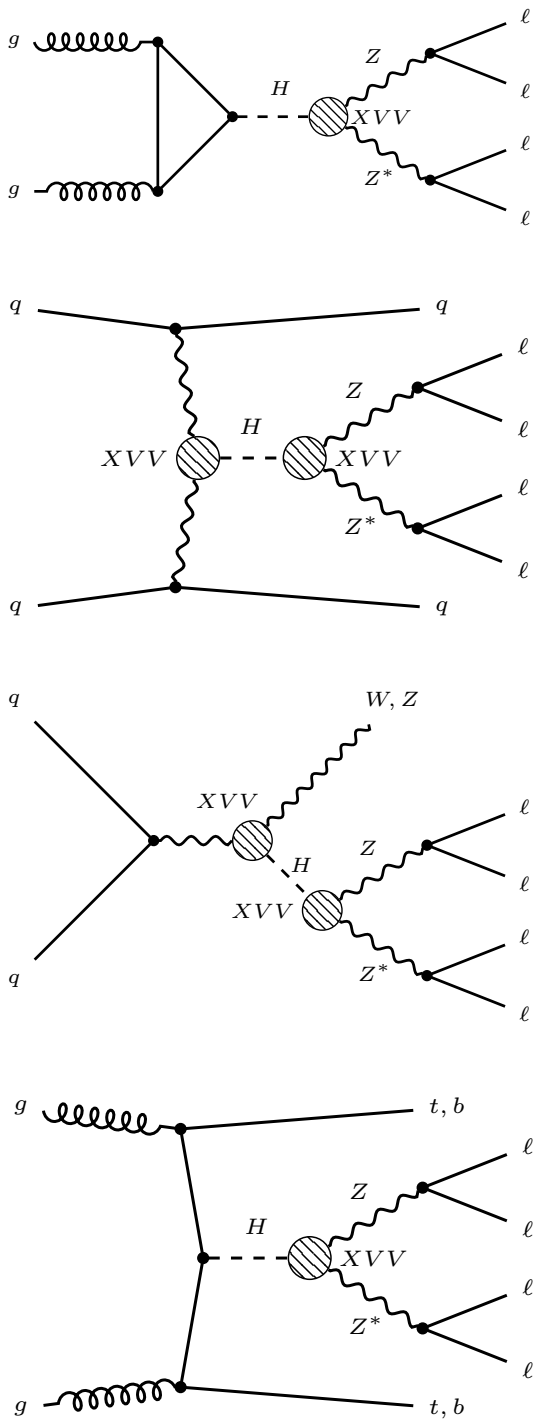

Figure 5.14: From top to bottom: Feynman diagrams of Higgs boson production via ggF, VBF, VH and $t\bar{t}H/b\bar{b}H$ with effective XVV interaction vertices with potential BSM contributions. At the XVV production vertices both W and Z-bosons contribute.

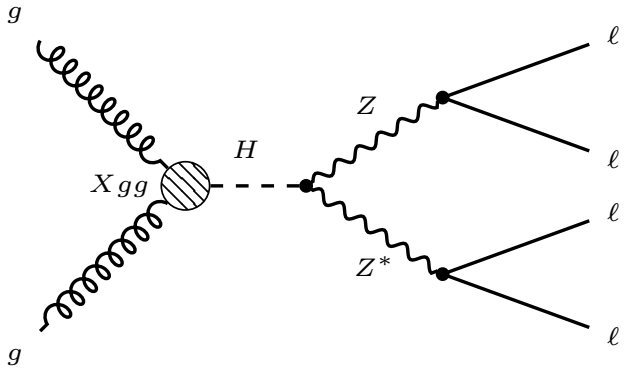

Figure 5.15: Feynman diagram of Higgs boson production via ggF with effective Xgg interaction vertex with potential BSM contributions.

The Higgs boson couplings to heavy vector bosons (XVV effective interaction vertex, $V = W, Z$) and to gluons (Xgg effective interaction vertex) are probed separately for BSM coupling contributions as summarised in Table 5.5:

1. In the XVV interaction vertices between the Higgs boson and heavy vector bosons CP-even and CP-odd BSM couplings, $c_\alpha\kappa_{\mathrm{HVV}}$ and $s_\alpha\kappa_{\mathrm{AVV}}$ of the Higgs characterisation framework, are probed. They contribute both to the decay vertex and to the VBF and VH production vertices. Therefore, VBF and VH production cross sections of $H \to ZZ^* \to 4\ell$ decays are proportional to $(c_\alpha\kappa_{\mathrm{HVV}})^4$ and $(s_\alpha\kappa_{\mathrm{AVV}})^4$ providing the highest sensitivity to BSM coupling contributions at the XVV vertex.

2. In the effective interaction vertex (Xgg) between the Higgs boson and gluons the CP-odd BSM coupling $s_\alpha\kappa_{\mathrm{Agg}}$ in the Higgs characterisation framework is probed. This coupling affects only the gluon fusion production resulting in an enhanced event yield proportional to $(s_\alpha\kappa_{\mathrm{Agg}})^2$.

It is assumed that the BSM CP-even and CP-odd couplings to Z and W-bosons are related in the same way as in the SM, i.e. $c_\alpha\kappa_{\mathrm{HZZ}} = c_\alpha\kappa_{\mathrm{HWW}}$ and $s_\alpha\kappa_{\mathrm{AZZ}} = s_\alpha\kappa_{\mathrm{AWW}}$. Couplings to W-bosons contribute to the XVV ($V = W, Z$) production vertex.

The results are derived as couplings $s_\alpha\kappa_{\mathrm{Agg}}$, $c_\alpha\kappa_{\mathrm{HVV}}$ and $s_\alpha\kappa_{\mathrm{AVV}}$ in the Higgs characterisation framework, not as coupling ratios as in the shape-based analysis described in the previous section (see Equation 5.4). The shape information in the matrix element squared can be factorised with BSM contributions depending on ratios of the BSM

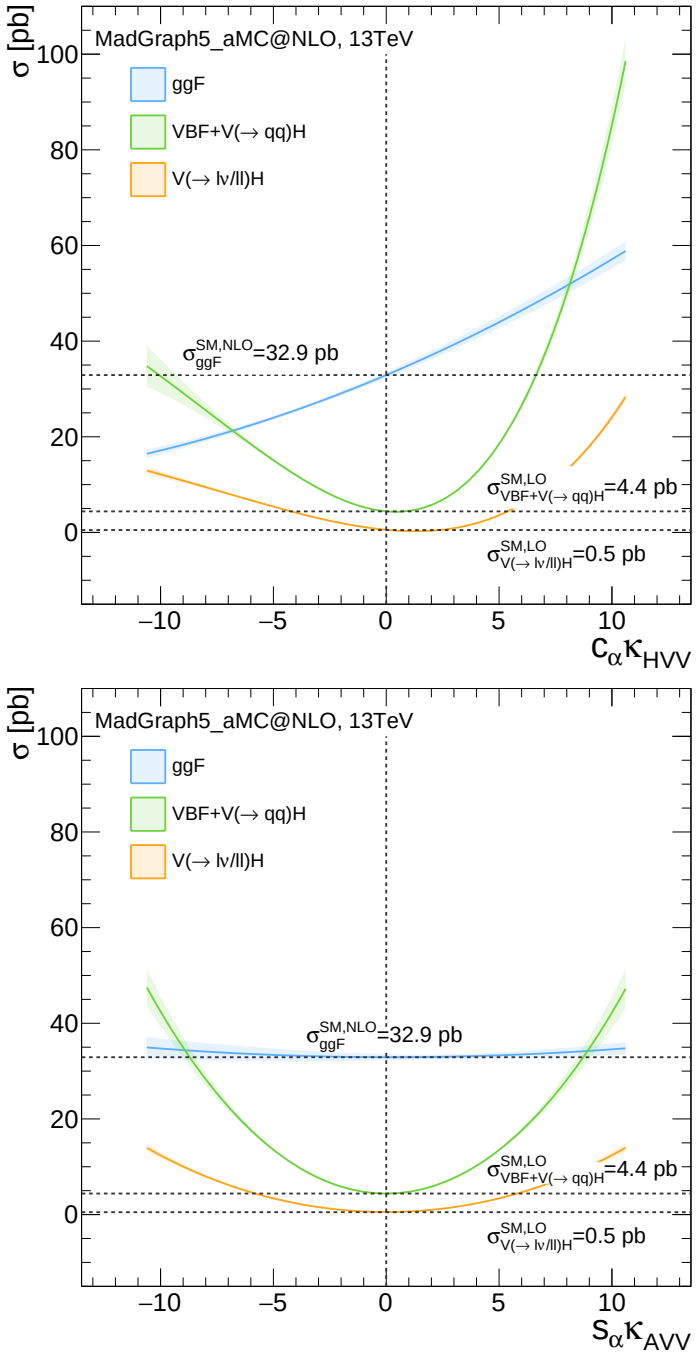

Figure 5.16: The ggF (blue), VBF $+V(\to qq)H$ (green) and $V(\to \ell\nu/\ell\ell)H$ Higgs boson production cross sections at $\sqrt{s} = 13$ TeV calculated at next-to-leading-order (ggF) and leading-order (VBF $+V(\to qq)H$ and $V(\to \ell\nu/\ell\ell)H$) with MadGraph5_aMC@NLO as a function of the CP-even and CP-odd non-SM coupling parameters $c_\alpha\kappa_{\mathrm{HVV}}$ (top) and $s_\alpha\kappa_{\mathrm{AVV}}$ (bottom), respectively.

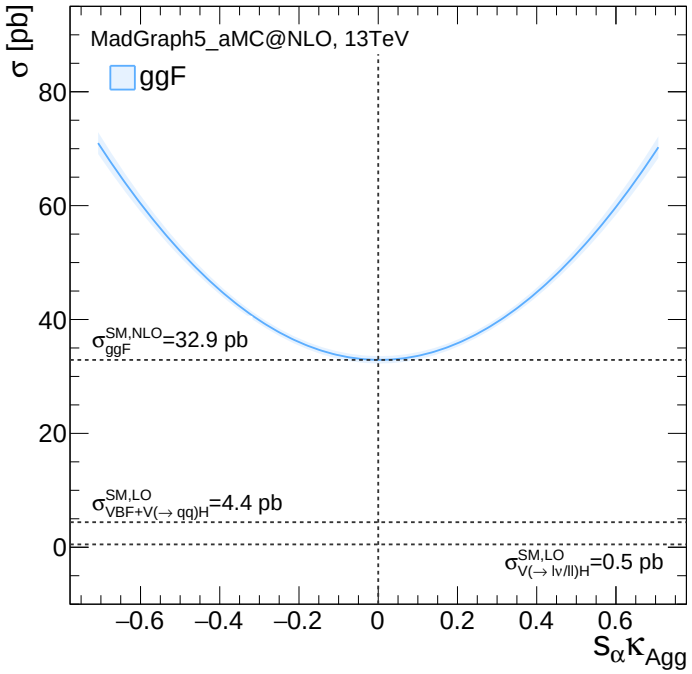

Figure 5.17: The ggF (blue) Higgs boson production cross section calculated at leading-order with MadGraph5_aMC@NLO as a function of the CP-odd non-SM coupling parameter $s_\alpha\kappa_{\mathrm{Agg}}$.

couplings g_{BSM} relative to the SM couplings g_{SM}:

$$|\mathrm{ME}|^2 = g_{\mathrm{SM}}^2 \cdot \underbrace{\left(|\mathrm{ME}_{\mathrm{SM}}|^2 + \frac{g_{\mathrm{BSM}}}{g_{\mathrm{SM}}} \cdot 2\,\mathrm{Re}\left[\mathrm{ME}_{\mathrm{SM}}^* \cdot \mathrm{ME}_{\mathrm{BSM}}\right] + \left(\frac{g_{\mathrm{BSM}}}{g_{\mathrm{SM}}}\right)^2 \cdot |\mathrm{ME}_{\mathrm{BSM}}|^2 \right)}_{\text{contains full shape information}} \tag{5.17}$$

This is not possible for the rate.

Table 5.5: Dependence of the $H \to ZZ^* \to 4\ell$ event rates in the different production modes on the BSM coupling contributions to the effective Xgg and in XVV interaction vertices. The BSM couplings are parametrised according to the Higgs characterisation framework with CP-odd BSM coupling contribution $s_\alpha \kappa_{\mathrm{Agg}}$ to the effective Xgg vertex and with CP-even and CP-odd BSM coupling contributions in the XVV vertex $c_\alpha \kappa_{\mathrm{HVV}}$ and $s_\alpha \kappa_{\mathrm{AVV}}$.

Interaction vertex	Rate dependence in BSM couplings				
with BSM couplings	ggF	VBF	VH	$t\bar{t}H$	$b\bar{b}H$
Xgg	$\propto (s_\alpha \kappa_{\mathrm{Agg}})^2$	const.	const.	const.	const.
XVV	$\propto (c_\alpha \kappa_{\mathrm{HVV}})^2$	$\propto (c_\alpha \kappa_{\mathrm{HVV}})^4$	$\propto (c_\alpha \kappa_{\mathrm{HVV}})^4$	$\propto (c_\alpha \kappa_{\mathrm{HVV}})^2$	$\propto (c_\alpha \kappa_{\mathrm{HVV}})^2$
	$\propto (s_\alpha \kappa_{\mathrm{AVV}})^2$	$\propto (s_\alpha \kappa_{\mathrm{AVV}})^4$	$\propto (s_\alpha \kappa_{\mathrm{AVV}})^4$	$\propto (s_\alpha \kappa_{\mathrm{AVV}})^2$	$\propto (s_\alpha \kappa_{\mathrm{AVV}})^2$

5.2.1 Categorisation of Higgs boson candidate events

In order to probe the BSM couplings via Higgs boson production rates in Run-2, the Higgs boson events within the four-lepton mass window of 118 GeV $< m_{4\ell} <$ 129 GeV are classified in categories enriched in different production modes. In addition, categories with sufficient numbers of events are further subdivided into categories depending on the transverse momentum of the four-lepton system or of the highest-p_{T} jet in the final state. These observables provide additional sensitivity to BSM couplings as discussed later. In total, ten categories are defined. Nine of them are identical to the categorisation scheme used for the measurement of the SM Higgs boson production cross sections using the simplified template cross sections framework [27], while one additional category is added to enhance the sensitivity to the BSM couplings. The categorisation scheme is summarised in Figure 5.22 and described in the following.

The four dominant Higgs production mechanisms ggF, VBF, VH with hadronic ($V \to qq$) and leptonic ($V \to \ell\nu/\ell\ell$) vector boson decays and $t\bar{t}H$ are disentangled by the categorisation based on their specific final state topology. Even though the $b\bar{b}H$ production cross section is comparable to the $t\bar{t}H$ cross section, no dedicated category is defined as it cannot be easily distinguished from the other modes.

First, events with topology similar to the one of the $t\bar{t}H$ production are selected. All remaining events are then probed with respect to VH production with leptonic vector boson decays. The remaining production modes, ggF, VBF and $V(\to qq)H$, can be distinguished by jet multiplicity. While the tree-level ggF process has no jets

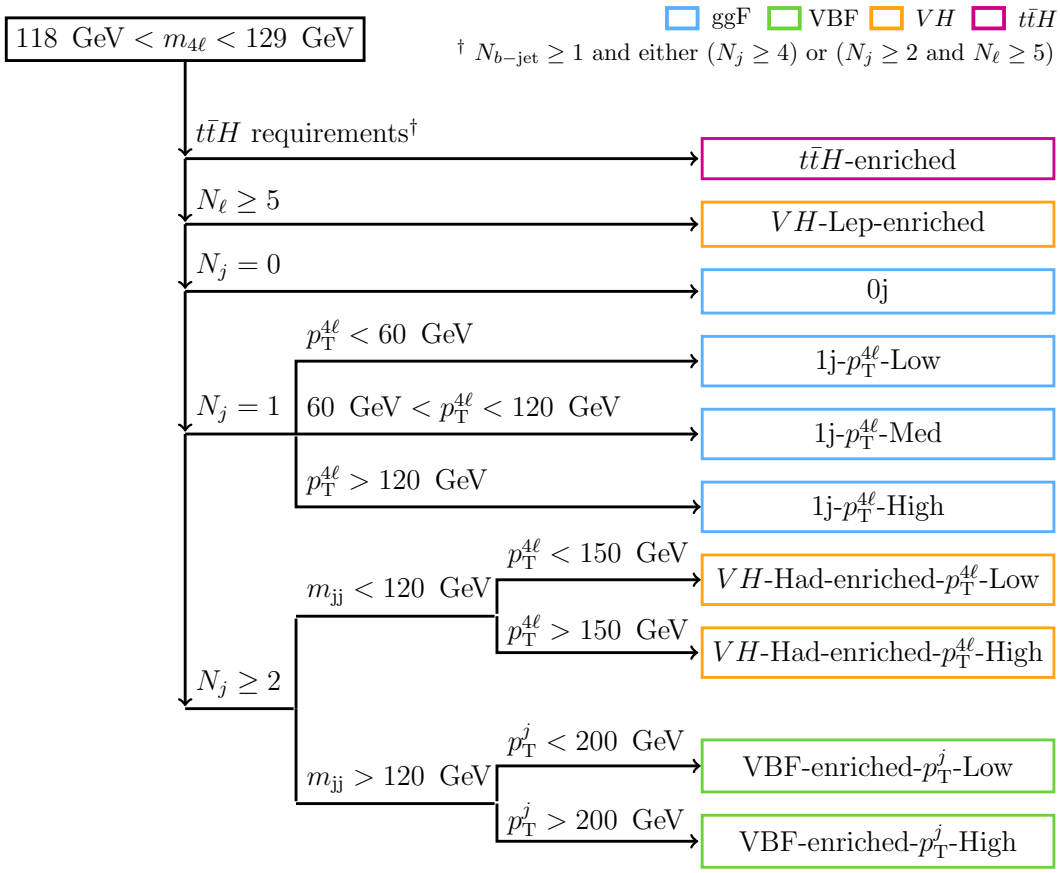

Figure 5.18: Schematic overview of the categorisation of Higgs boson candidate events. The production modes targeted by a given category are indicated by a coloured boxes.

in the final state, the Higgs boson is accompanied by two additional jets in the VBF and $V(\to qq)H$ processes. The VBF production can be distinguished from the VH process by means of the invariant mass m_{jj} of the two leading p_{T}-jets. While the m_{jj} distribution for $V(\to qq)H$ production peaks around the vector boson mass m_W or m_Z, the dijet system from VBF production tends to have higher invariant mass.

Some of the categories are further split to improve the discrimination between the production modes or to add additional discriminants sensitive to BSM couplings in the XVV interaction vertex. No additional discriminants are introduced for the study of the Xgg vertex. BSM couplings in the XVV vertex lead to harder p_{T} spectra of the Higgs boson and jets.

The event categorisation is implemented in the following sequence:

1. **Category enriched with $t\bar{t}H$ production ($t\bar{t}H$-enriched):**
   At first, the $t\bar{t}H$ production mechanism is specifically targeted by this category. Since top-quarks decay almost always into a b-quark and a W-boson, the final signature depends on the decay of the two W-bosons. The fully-leptonic decay of both W-bosons is rare, therefore only hadronic ($b\bar{b}q\bar{q}q'\bar{q'}$) and semi-leptonic ($b\bar{b}\ell\nu q\bar{q}$) final state products are selected in addition to the four final state leptons from the Higgs boson decay. At least one b-tagged jet $N_{b\text{-jet}} \geq 1$ together with either more than four reconstructed jets $N_j \geq 4$ (targeting the full hadronic decay) or at least two jets $N_j \geq 2$ and at least one additional lepton $N_\ell \geq 5$ (targeting the semi-leptonic final state) are required.

2. **Category enriched with $V(\to \ell\nu/\ell\ell)H$ production (VH-Lep-enriched):**
   Out of the remaining events, those targeting VH Higgs boson production with leptonic vector boson decay are selected. Together with the four leptons from the Higgs boson candidate, at least one additional lepton ($N_\ell \geq 5.$) is required in order to select processes with $Z \to \ell\ell$ or $W \to \ell\nu$ decays. This category provides sensitivity to the BSM couplings in the XVV interaction vertex.

3. **Category with zero jets ($0j$):**
   Subsequently, only events with no jets (j) in the final state are selected, targeting the ggF production: $N_j = 0$. This category contains the largest number of events and provides the highest sensitivity to BSM couplings in the Xgg vertex.

4. **Category with one jet, further split according to p_{T}^{4l} ($1j$-$p_{\mathrm{T}}^{4\ell}$-Low, $1j$-$p_{\mathrm{T}}^{4\ell}$-Med and $1j$-$p_{\mathrm{T}}^{4\ell}$-High):**
   In the next category, events with exactly one jet ($N_j = 1$) in the final state are selected. This category consists of contributions from ggF, VBF and $V(\to qq)H$ production modes. Events are further split according to the Higgs boson transverse momentum p_{T}^{4l} into categories with $p_{\mathrm{T}}^{4l} < 60$ GeV ($1j$-$p_{\mathrm{T}}^{4\ell}$-Low), 60 GeV $< p_{\mathrm{T}}^{4l} < 120$ GeV ($1j$-$p_{\mathrm{T}}^{4\ell}$-Med) and $p_{\mathrm{T}}^{4l} > 120$ GeV ($1j$-$p_{\mathrm{T}}^{4\ell}$-High) allowing for further discrimination between the production mechanisms and to isolate BSM effects. In Figure 5.19 the normalised Higgs boson transverse momentum distributions for SM and BSM Higgs boson signals produced with ggF and VBF $+VH$ production mechanism is shown. While no difference is visible between ggF SM and BSM distributions, the VBF distributions are harder and can be differentiated both from ggF and from each other.

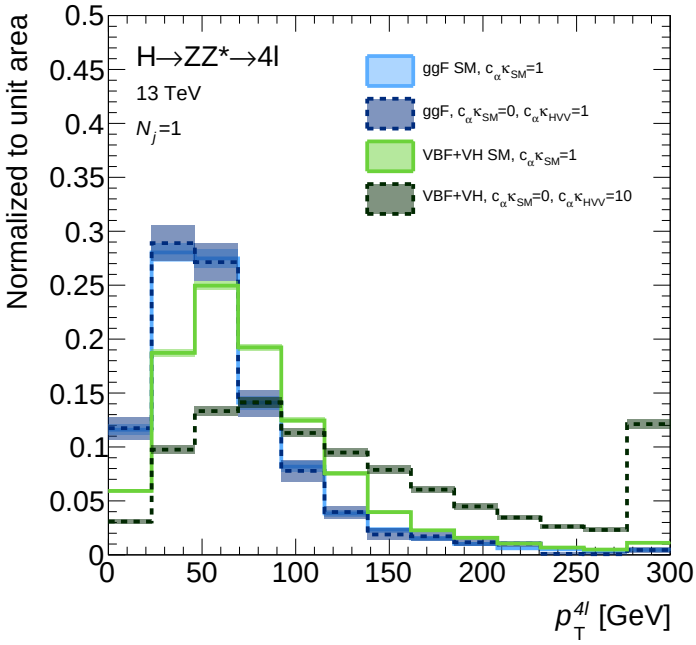

Figure 5.19: The normalised Higgs boson transverse momentum distributions for the SM and BSM Higgs boson signals in the four-lepton decay channel with one additional jet $N_j = 1$.

5. **Category enriched with $V(\rightarrow qq)H$ production, further split according to p_{T}^{4l} (VH-Had-enriched-$p_{\mathrm{T}}^{4\ell}$-Low and VH-Had-enriched-$p_{\mathrm{T}}^{4\ell}$-High):**
In the category containing events with at least two jets in the final state and with an invariant mass of the two leading jets below 120 GeV ($N_j \geq 2$ and $m_{\mathrm{jj}} < 120$ GeV) the VH production mode with hadronic vector boson decays is enhanced. The VH production is highly sensitive to BSM couplings in the XVV vertex. The category is further split into categories according to p_{T}^{4l} in order to further increase BSM sensitivity: $p_{\mathrm{T}}^{4l} < 150$ GeV (VH-Had-enriched-$p_{\mathrm{T}}^{4\ell}$-Low) and $p_{\mathrm{T}}^{4l} > 150$ GeV (VH-Had-enriched-$p_{\mathrm{T}}^{4\ell}$-High). The p_{T}^{4l} distribution for events with $N_j \geq 2$ and $m_{\mathrm{jj}} < 120$ GeV is shown in Figure 5.20 for the SM and BSM hypotheses.

6. **Category enriched with VBF production, further split according to p_{T}^{j1} (VBF-enriched-p_{T}^{j}-Low and VBF-enriched-p_{T}^{j}-High):**
Finally, the VBF production is enhanced for events with at least two jets and an invariant mass of the two leading jets above 120 GeV: $N_j \geq 2$ and $m_{\mathrm{jj}} > 120$ GeV.

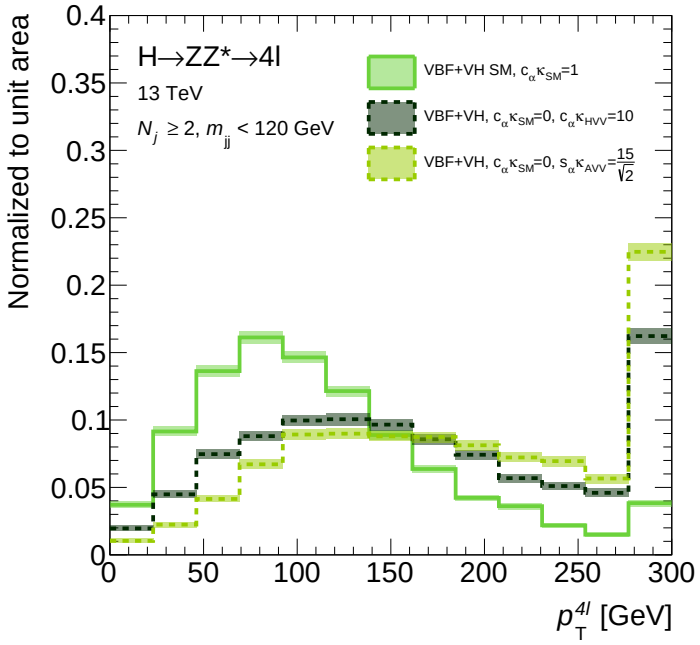

Figure 5.20: The normalised Higgs boson transverse momentum distributions for the SM and BSM Higgs boson signal in the four-lepton decay channel with at least two jets with invariant mass below 120 GeV.

As in the case of VH production, the VBF production is very sensitive to BSM couplings in the XVV vertex. In order to gain additional sensitivity, events are further split according to the p_{T} of the leading jet p_{T}^{j1}: $p_{\mathrm{T}}^{j1} < 200$ GeV (VBF-enriched-p_{T}^{j}-Low) and $p_{\mathrm{T}}^{j1} > 200$ GeV (VBF-enriched-p_{T}^{j}-High). The p_{T}^{j1} distribution for the SM and two BSM hypotheses is shown in Figure 5.21.

In total ten categories are built, from which three are specifically sensitive to BSM contributions ($1j$-$p_{\mathrm{T}}^{4\ell}$-High, VH-Had-enriched-$p_{\mathrm{T}}^{4\ell}$-High, VBF-enriched-p_{T}^{j}-High).

The relative fractions of each production mechanism in a given reconstructed category is shown in Figure 5.22 assuming the SM Higgs boson production. The $t\bar{t}H$-enriched and VH-Lep-enriched categories are very pure in $t\bar{t}H$ and VH production mechanism with 78 % and 83 % purity, respectively. For the presented tensor structure analysis, the $t\bar{t}H$ production plays a minor role. The ggF production process is present in all categories due to the high cross section. It has a very high purity in the $0j$ category with 97 %. The $1j$ categories have contributions from ggF, VBF and VH production mechanism,

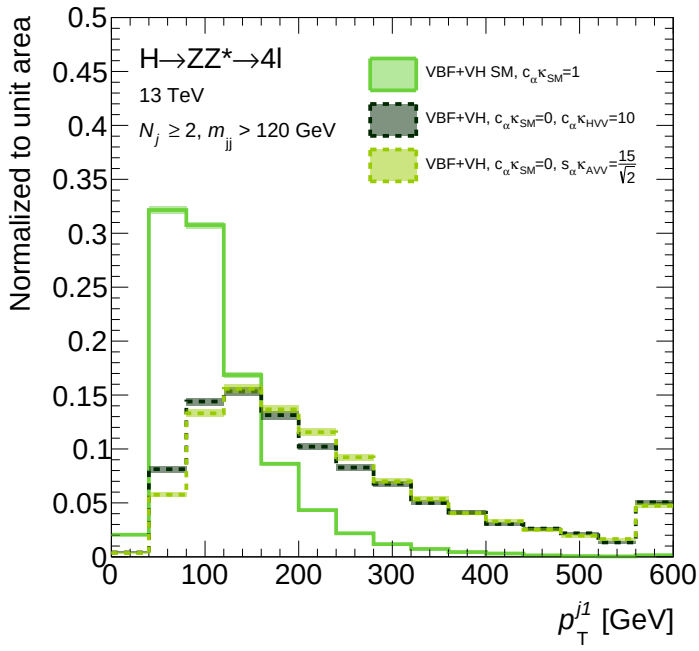

Figure 5.21: The normalised leading jet transverse momentum distributions for the SM and BSM Higgs boson signal in the four-lepton decay channel with at least two additional jets with invariant mass above 120 GeV.

where the ggF process has a dominant averaged fraction of 83 %, and VBF and VH have 12 % and 4 %, respectively. The ggF production fraction falls with increasing jet multiplicity from 91 % to 75 %, while the VBF and VH fractions rise from 6 % and 3 % in the $1j$-$p_{\mathrm{T}}^{4\ell}$-Low category to 18 % and 6 % in the $1j$-$p_{\mathrm{T}}^{4\ell}$-High category, respectively. The VH process is targeted in the VH-Lep-enriched and VH-Had-enriched categories. While the purity is high in the former one, a purity of only 14 % and 25 % is achieved for the VH-Had-enriched-$p_{\mathrm{T}}^{4\ell}$-Low and VH-Had-enriched-$p_{\mathrm{T}}^{4\ell}$-High categories, respectively. A large fraction from the ggF mechanism of 78 % and 66 % in VH-Had-enriched-$p_{\mathrm{T}}^{4\ell}$-Low and VH-Had-enriched-$p_{\mathrm{T}}^{4\ell}$-High categories, and a minor contribution from the VBF process are present. The VBF process has a purity of 32 % in the VBF-enriched categories. A high contamination from ggF with fraction of 62 % and 57 % in VH-Had-enriched-$p_{\mathrm{T}}^{4\ell}$-Low and VH-Had-enriched-$p_{\mathrm{T}}^{4\ell}$-High, and a minor one from VH are present. The $t\bar{t}H$ process has a fraction of 3 % in the VH-Had-enriched-$p_{\mathrm{T}}^{4\ell}$-High category.

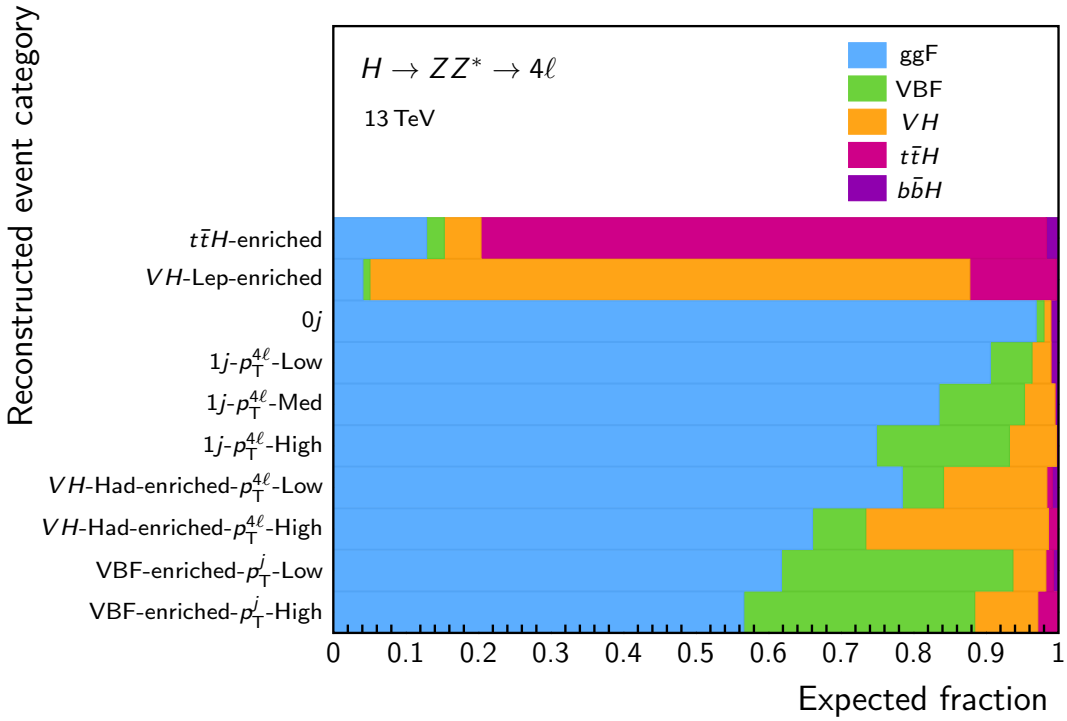

Figure 5.22: The expected fractions of $H \to ZZ^* \to 4\ell$ events with $m_H = 125$ GeV originating from ggF (blue), VBF (green), VH (orange), $t\bar{t}H$ (magenta) and $b\bar{b}H$ (purple) production mechanisms in each reconstructed event category for Run-2 data collected at $\sqrt{s} = 13$ TeV.

5.2.2 Signal modelling

The signal model predicts the Higgs event yield for the different production modes and event categories as a function of the coupling parameters κ. Separate signal models are used for the study of the Xgg and the XVV interaction vertex. Each production mode is modelled separately. In the Xgg study, the BSM CP-odd coupling parameter $s_\alpha \kappa_{\mathrm{Agg}}$ is probed assuming that there are no BSM contributions to the XVV vertex. In the XVV study, the CP-even and CP-odd BSM couplings $c_\alpha \kappa_{\mathrm{HVV}}$ and $s_\alpha \kappa_{\mathrm{AVV}}$ are probed both independently and, with decreased sensitivity, simultaneously in a multi-dimensional fit.

The signal predictions as continuous function of the coupling parameters are built in three steps:

1. Signal morphing [165]: the signal prediction for a given point in the BSM coupling

parameter space is obtained by interpolation between predictions for discrete points in the parameter space.

2. Best-prediction scaling: the signal yields obtained by the morphing method are scaled such that the yields at the SM point correspond to the best SM prediction including the highest-order corrections.

3. Scaling of the total decay width: the changes in the total width of the Higgs boson due to the presence of BSM couplings are taken into account.

The discriminating variables used are expected to be insensitive to the sign of the CP-odd BSM coupling. Sign changes due to statistical fluctuations in the simulated event samples are prevented by the averaging of the predictions for positive and negative CP-odd couplings in all modelling steps. The effect of each step on the three BSM couplings $s_\alpha\kappa_{\mathrm{Agg}}$, $c_\alpha\kappa_{\mathrm{HVV}}$ and $s_\alpha\kappa_{\mathrm{AVV}}$ is shown in Figure 5.23. The signal prediction as a function of $s_\alpha\kappa_{\mathrm{Agg}}$ ($c_\alpha\kappa_{\mathrm{HVV}}$ and $s_\alpha\kappa_{\mathrm{AVV}}$) is shown in the $0j$ (VBF-enriched-p_{T}^j-Low) category which is most sensitive to this coupling. The signal models in Figure 5.23 are projections of the multi-dimensional models. As example, the combined VBF and VH XVV signal model is shown in Figure 5.24 in the plane of the couplings $c_\alpha\kappa_{\mathrm{HVV}}$ and $s_\alpha\kappa_{\mathrm{AVV}}$ in the VBF-enriched-p_{T}^j-High category. The signal models for all categories and BSM couplings in the rate-based Xgg and XVV tensor structure analyses are shown in Appendix I.
The modelling steps are explained in detail in the following.

Signal morphing

The principal signal modelling procedure is based on the morphing method described in Section 6.2. Monte Carlo samples simulated for discrete points in the coupling parameter space are used as an input for the morphing procedure which produces a continuous signal description in the multi-dimensional BSM coupling space.

The signal samples with different values of the BSM coupling parameters $s_\alpha\kappa_{\mathrm{Agg}}$, $c_\alpha\kappa_{\mathrm{HVV}}$ and $s_\alpha\kappa_{\mathrm{AVV}}$ are generated with MadGraph5_aMC@NLO as described in Section 4.2, separately for ggF, $V(\to \ell\nu/\ell\ell)H$ and combined VBF and $V(\to qq)H$ production. The latter two processes are simulated together in the same sample taking possible interferences due to the common final state $pp \to qqH$ into account. The ggF process is simulated at NLO, while the LO simulation is used for the other processes.

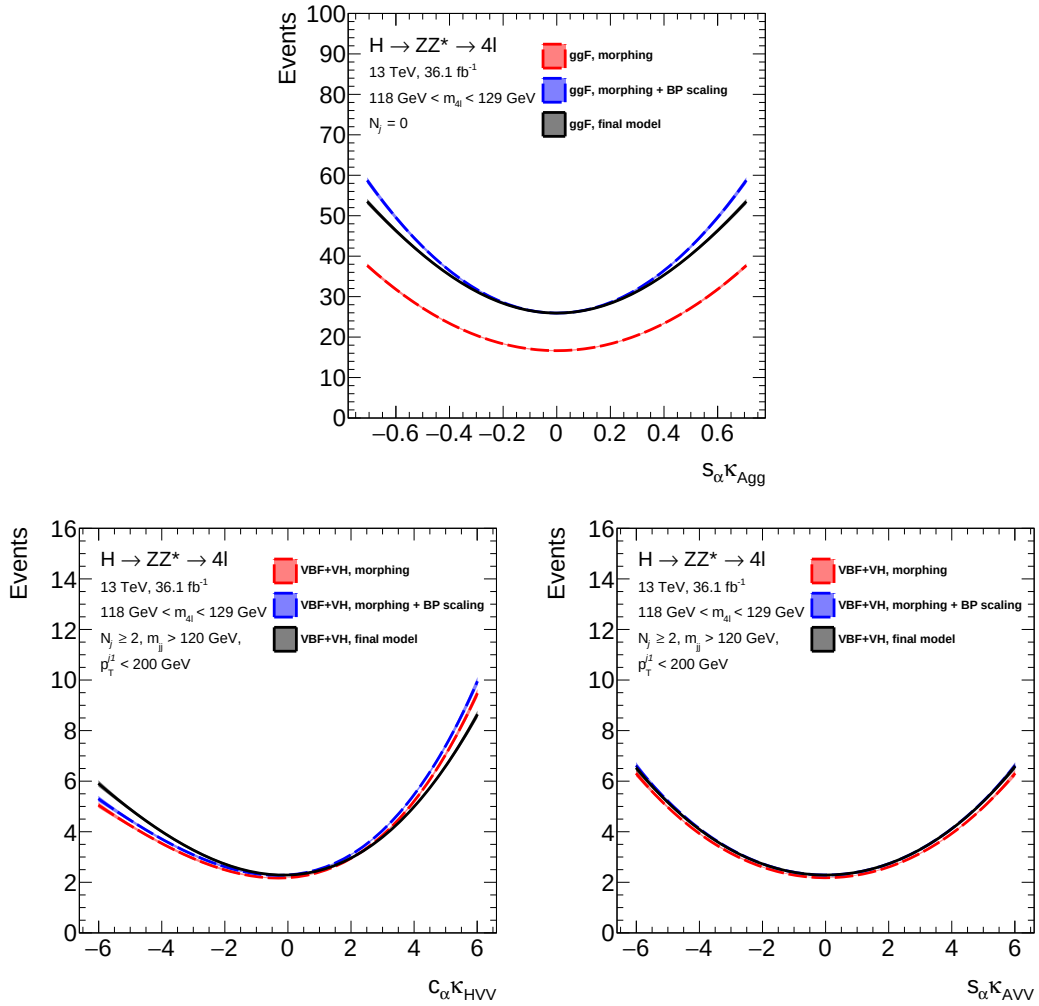

Figure 5.23: The predicted $H \to ZZ^* \to 4\ell$ event yields for $m_H = 125$ GeV in ggF production as a function of the BSM coupling $s_\alpha \kappa_{\mathrm{Agg}}$ (top), and in VBF and VH production as a function of $c_\alpha \kappa_{\mathrm{HVV}}$ (bottom left) and $s_\alpha \kappa_{\mathrm{AVV}}$ (bottom right) corresponds to the luminosity of the analysed Run-2 data set. The predictions are shown after each of the three modelling steps, signal morphing (dashed red), best-prediction (BP) scaling (dashed blue), and scaling of the total Higgs boson width (solid black). The error band of the signal morphing method is shown.

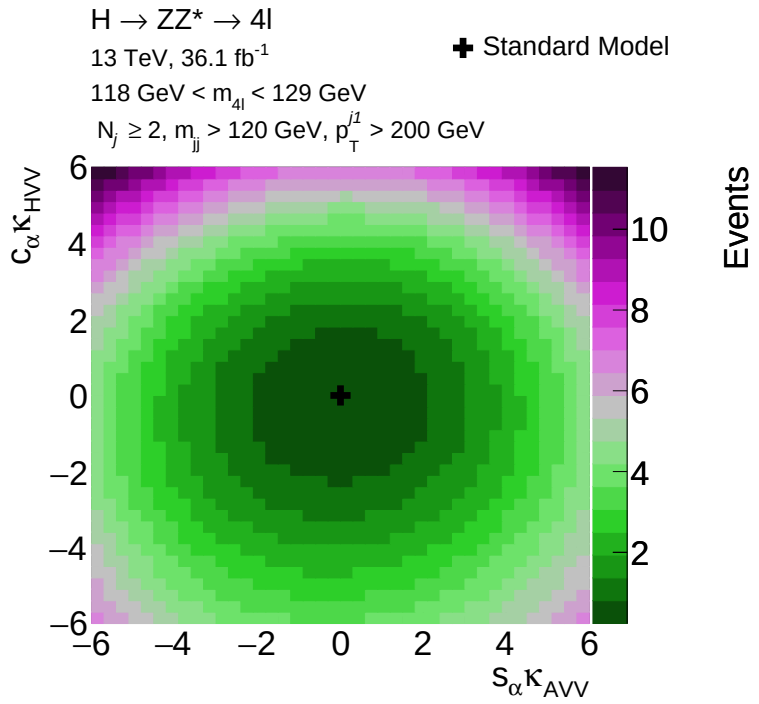

Figure 5.24: The predicted $H \to ZZ^* \to 4\ell$ event yield for $m_H = 125$ GeV in VBF and VH production as a function of the BSM couplings $c_\alpha\kappa_{\mathrm{HVV}}$ and $s_\alpha\kappa_{\mathrm{AVV}}$ coupling parameters corresponding to the luminosity of the analysed Run-2 data set.

No BSM Monte Carlo samples have been generated for $t\bar{t}H$ and $b\bar{b}H$ processes. These processes are only affected by the BSM couplings in the decay vertex (XVV) and it is assumed that the $t\bar{t}H$ and $b\bar{b}H$ production rates scale due to BSM XVV couplings by the same amount as the ggF process. These production modes are unaffected by the BSM couplings in the Xgg vertex. Since the analysis assumption is that the BSM couplings to W and Z-bosons are related like in the SM, all signal samples are generated with $\kappa_{\mathrm{HVV}} = \kappa_{\mathrm{HZZ}} = \kappa_{\mathrm{HWW}}$ and $\kappa_{\mathrm{AVV}} = \kappa_{\mathrm{AZZ}} = \kappa_{\mathrm{AWW}}$.

A continuous signal model is obtained from a linear combination of input signal samples simulated for discrete coupling parameter values. Each input sample is weighted according to the input and target coupling configuration (see Section 6.2). The number of input samples depends on the number of BSM parameters at the production and decay vertex and therefore depends on the Higgs production mode. The discrete input points in the parameter space have to be chosen with particular care to minimise

the statistical error on the signal prediction over the entire explored parameter space. The list of generated Monte Carlo samples used as morphing inputs can be found in Appendix H.2. The signal models produced with the morphing method are:

- ***Xgg* signal model:**
  BSM coupling modifications of the Xgg interaction vertex only affect ggF production. The signal yield is described as a function of $s_\alpha\kappa_{\text{Agg}}$, i.e.

  – $S_{\text{ggF}}(s_\alpha\kappa_{\text{Agg}})$,

  while the SM-like production and decay couplings are fixed to the SM expectations $c_\alpha\kappa_{\text{Hgg}} = 1$ and $c_\alpha\kappa_{\text{SM}} = 1$, respectively.

- **1D CP-odd *XVV* signal model:**
  For the study of the XVV interaction vertex with CP-odd BSM couplings, the Higgs boson yields are given as a function of $s_\alpha\kappa_{\text{AVV}}$, with $c_\alpha\kappa_{\text{Hgg}}$ and $c_\alpha\kappa_{\text{SM}}$ for the SM-like part of the tensor coupling. The signal yields for the different production modes affected are treated separately, i.e.

  – $S_{\text{ggF}}(c_\alpha\kappa_{\text{SM}}, s_\alpha\kappa_{\text{AVV}})$,

  – $S_{\text{VBF}+V(\to qq)H}(c_\alpha\kappa_{\text{SM}}, s_\alpha\kappa_{\text{AVV}})$ and

  – $S_{V(\to \ell\nu/\ell\ell)H}(c_\alpha\kappa_{\text{SM}}, s_\alpha\kappa_{\text{AVV}})$,

  where the SM-like production coupling is always fixed to the SM prediction $c_\alpha\kappa_{\text{Hgg}} = 1$. No BSM samples have been produced for $t\bar{t}H$ and $b\bar{b}H$ productions since it is assumed that the dependence on the CP-odd coupling $s_\alpha\kappa_{\text{AVV}}$ in the decay vertex is the same as for the ggF process. The signal models are, therefore, built from the ggF models, i.e.

  $$S_{t\bar{t}H/b\bar{b}H}(c_\alpha\kappa_{\text{SM}}, s_\alpha\kappa_{\text{AVV}}) = \frac{S_{\text{ggF}}(c_\alpha\kappa_{\text{SM}}, s_\alpha\kappa_{\text{AVV}})}{S_{\text{ggF,SM}}} \cdot S_{t\bar{t}H/b\bar{b}H,\text{SM}}, \tag{5.18}$$

  where $S_{t\bar{t}H/b\bar{b}H,\text{SM}}$ is derived from the SM $t\bar{t}H/b\bar{b}H$ simulation normalised to best accuracy inclusive cross section.

- **2D *XVV* signal model:**
  For the study of the XVV interaction vertex with CP-odd and CP-even BSM coupling contributions, the signal yields for the different production modes are described as a function of $c_\alpha\kappa_{\text{HVV}}$ and $s_\alpha\kappa_{\text{AVV}}$:

- $S_{\mathrm{ggF}}(c_\alpha\kappa_{\mathrm{SM}}, c_\alpha\kappa_{\mathrm{HVV}}, s_\alpha\kappa_{\mathrm{AVV}})$,
- $S_{\mathrm{VBF}+V(\to qq)H}(c_\alpha\kappa_{\mathrm{SM}}, c_\alpha\kappa_{\mathrm{HVV}}, s_\alpha\kappa_{\mathrm{AVV}})$ and
- $S_{V(\to \ell\nu/\ell\ell)H}(c_\alpha\kappa_{\mathrm{SM}}, c_\alpha\kappa_{\mathrm{HVV}}, s_\alpha\kappa_{\mathrm{AVV}})$,

where the SM-like production coupling is again fixed to the SM prediction $c_\alpha\kappa_{\mathrm{Hgg}} = 1$. The $t\bar{t}H$ and $b\bar{b}H$ predictions are obtained in the same way as in case of the 1D CP-odd XVV model.

The 2D XVV signal model is used to simultaneously describe the dependence on the CP-even and CP-odd BSM couplings and applies also for special cases in which one of the two couplings is set to zero. This model could in principal also be used for the measurement of the CP-odd BSM coupling with the CP-even coupling set to zero. It is, however, difficult to symmetrise the input samples in a two-dimensional model in order to avoid sign changes of the CP-odd BSM coupling due to statistical uncertainties in the simulation. Therefore, the dedicated 1D CP-odd XVV model is used for the CP-odd BSM coupling only. For both the Xgg and the 1D CP-odd XVV signal model, input samples have been symmetrised (averaged) in the sign of CP-odd BSM coupling $s_\alpha\kappa_{\mathrm{Agg}}$ or $s_\alpha\kappa_{\mathrm{AVV}}$ are used.

The $S_{\mathrm{VBF}+V(\to qq)H}$ and $S_{V(\to \ell\nu/\ell\ell)H}$ signal models are combined to a single $S_{\mathrm{VBF}+VH}$ model, in order to allow for the best-prediction scaling performed in the next step. The combination is possible, because the same set of input coupling configurations has been used for the generation of both models.

Best-prediction scaling

While the BSM signal samples are simulated using MadGraph5_aMC@NLO (MG5), the SM signal can be modelled using higher order generators and higher order inclusive cross section calculations as described in Section 4.2. In order to take this best SM prediction (BP) into account, the SM signal yields predicted by the MadGraph5_aMC@NLO generator in each event category are scaled to the predictions from the higher order generator (Powheg-Box) which in turn is normalised to the highest-order inclusive cross section calculation of each process. The same best-prediction scale factors f_{BP} are then applied on the BSM signal samples. Two sets of scale factors are calculated, one for ggF production and one for combined VBF and

Table 5.6: Best-prediction scale factors applied to the morphed signal model.

	Best-prediction scale factors f_{BP}	
Category	ggF	VBF + VH
$t\bar{t}H$-enriched	0.9	1.9
VH-Lep-enriched	1.2	1.3
$0j$	1.6	1.4
$1j$-$p_{\mathrm{T}}^{4\ell}$-Low	1.4	1.3
$1j$-$p_{\mathrm{T}}^{4\ell}$-Med	1.5	1.4
$1j$-$p_{\mathrm{T}}^{4\ell}$-High	1.2	1.5
VH-Had-enriched-$p_{\mathrm{T}}^{4\ell}$-Low	1.4	1.3
VH-Had-enriched-$p_{\mathrm{T}}^{4\ell}$-High	0.9	1.4
VBF-enriched-p_{T}^{j}-Low	1.2	1.0
VBF-enriched-p_{T}^{j}-High	1.0	1.0

VH production modes.

$$f_{BP,i}^{\mathrm{ggF}} = \frac{S_{\mathrm{ggF},i}^{\mathrm{SM}}(BP)}{S_{\mathrm{ggF},i}^{\mathrm{SM}}(MG5)}, \tag{5.19}$$

and

$$f_{BP,i}^{\mathrm{VBF}+VH} = \frac{S_{\mathrm{VBF},i}^{\mathrm{SM}}(BP) + S_{WH,i}^{\mathrm{SM}}(BP) + S_{ZH,i}^{\mathrm{SM}}(BP)}{S_{\mathrm{VBF}+VH,i}^{\mathrm{SM}}(MG5)}, \tag{5.20}$$

where i indicates the event category.

It is assumed that the impact of higher order corrections is independent of the presence of BSM coupling parameters. The BP scale factors therefore apply equally at every point in the BSM coupling space. They are listed in Table 5.6. The scale factors are in the range of 0.9 to 1.9 depending on the event category. While the scaling is between two different NLO predictions for ggF, it is from LO to NLO prediction for VBF $+VH$ production. In addition, the box diagram for gluon induced ZH production is not taken into account in the LO BSM signal samples. The highest scale factor for ggF production occurs for the $0j$ category, as Powheg-Box tends to predict a smaller jet multiplicity in the final state compared to MadGraph5_aMC@NLO.

Corrections to the total decay width of the Higgs boson

The total decay width of the Higgs boson is the sum of the partial decay widths,

$$\Gamma = \sum_i \Gamma_i. \tag{5.21}$$

The probability that the Higgs boson decays into a specific channel i, the branching ratio BR_i, is the ratio of partial and total decay width:

$$BR_i = \frac{\Gamma_i}{\Gamma}. \tag{5.22}$$

With the contributions of BSM couplings at the decay vertex, both the partial and the total width change. While the dependence of the partial decay width on BSM couplings is implemented in the MadGraph5_aMC@NLO generator for Higgs decays into heavy vector bosons and gluons, the total Higgs boson decay width is always kept at the value Γ_{SM}. An additional correction function depending on the BSM couplings is used to correct the total decay width and, consequently, the branching ratios.

The event yield is proportional to the BR and, thus, to the inverse of the Higgs boson width. The correction function $f_\Gamma(g_{\text{BSM}})$ applied to the event yield for a given configuration of BSM coupling parameters can therefore be written as

$$\begin{aligned} f_\Gamma(g_{\text{BSM}}) &= \frac{\Gamma_{\text{SM}}}{\Gamma_{\text{BSM}}} \\ &= \frac{\Gamma_{\text{SM}}}{\sum_i \Gamma_{i,\text{BSM}}} \\ &= \frac{\Gamma_{\text{SM}}}{\sum_i \Gamma_{i,\text{SM}} \cdot f_i(g_{\text{BSM}})} \\ &= \frac{1}{\sum_i BR_{i,\text{SM}} \cdot f_i(g_{\text{BSM}})}, \end{aligned} \tag{5.23}$$

where the index i indicates the decay channels of the Higgs boson. The functions $f_i(g_{\text{BSM}})$ are polynomial functions of BSM coupling parameters at the decay vertices i. In the case of SM couplings ($g_{\text{SM}} = 1, g_{\text{BSM}} = 0$), all f_i are equal to one.

In the present analysis, correction functions have to be assigned for $H \to WW$, $H \to ZZ$ and $H \to gg$ decays. Strictly speaking, the BSM XWW couplings also affect the loop-induced $H \to Z\gamma$ or $H \to \gamma\gamma$ decays. However, since the SM branching ratios for this latter decays are very small, the impact on the total width is negligible. The

correction function f_Γ derived in Equation 5.23 is then given by

$$\begin{aligned} & f_\Gamma(g_{\mathrm{BSM}}) = \\ & = \frac{1}{BR^{\mathrm{SM}}_{\mathrm{Other}} + BR^{\mathrm{SM}}_{WW} \cdot f_{WW}(g_{\mathrm{BSM}}) + BR^{\mathrm{SM}}_{ZZ} \cdot f_{ZZ}(g_{\mathrm{BSM}}) + BR^{\mathrm{SM}}_{gg} \cdot f_{gg}(g_{\mathrm{BSM}})} \\ & = \frac{1}{0.67 + 0.21 \cdot f_{WW}(g_{\mathrm{BSM}}) + 0.03 \cdot f_{ZZ}(g_{\mathrm{BSM}}) + 0.09 \cdot f_{gg}(g_{\mathrm{BSM}})}, \end{aligned} \tag{5.24}$$

with the SM Higgs boson branching ratios BR^{SM}_{WW}, BR^{SM}_{ZZ}, BR^{SM}_{gg} to WW, ZZ and gg and with $BR^{\mathrm{SM}}_{\mathrm{Other}}$ the sum of SM branching ratios of all other decay modes. The correction function for $H \to gg$ decays is

$$f_{gg}(c_\alpha\kappa_{\mathrm{Hgg}}, s_\alpha\kappa_{\mathrm{Agg}}) = (c_\alpha\kappa_{\mathrm{Hgg}})^2 + c_1^{gg} \cdot (s_\alpha\kappa_{\mathrm{Agg}})^2 + c_2^{gg} \cdot c_\alpha\kappa_{\mathrm{Hgg}} s_\alpha\kappa_{\mathrm{Agg}} \tag{5.25}$$

with constant factors $c_{1,2}^{gg}$. The polynomial form derives from the matrix elements describing the process. The same procedure is used in the morphing matrix (see Section 6.2). Similarly,

$$\begin{aligned} f_{WW}(c_\alpha\kappa_{\mathrm{SM}}, c_\alpha\kappa_{\mathrm{HVV}}, s_\alpha\kappa_{\mathrm{AVV}}) =& (c_\alpha\kappa_{\mathrm{SM}})^2 + c_1^{WW} \cdot (c_\alpha\kappa_{\mathrm{HVV}})^2 + c_2^{WW} \cdot (s_\alpha\kappa_{\mathrm{AVV}})^2 \\ & + c_3^{WW} \cdot c_\alpha\kappa_{\mathrm{SM}} c_\alpha\kappa_{\mathrm{HVV}} + c_4^{WW} \cdot c_\alpha\kappa_{\mathrm{SM}} s_\alpha\kappa_{\mathrm{AVV}} + c_5^{WW} \cdot c_\alpha\kappa_{\mathrm{HVV}} s_\alpha\kappa_{\mathrm{AVV}} \end{aligned} \tag{5.26}$$

and

$$\begin{aligned} f_{ZZ}(c_\alpha\kappa_{\mathrm{SM}}, c_\alpha\kappa_{\mathrm{HVV}}, s_\alpha\kappa_{\mathrm{AVV}}) =& (c_\alpha\kappa_{\mathrm{SM}})^2 + c_1^{ZZ} \cdot (c_\alpha\kappa_{\mathrm{HVV}})^2 + c_2^{ZZ} \cdot (s_\alpha\kappa_{\mathrm{AVV}})^2 \\ & + c_3^{ZZ} \cdot c_\alpha\kappa_{\mathrm{SM}} c_\alpha\kappa_{\mathrm{HVV}} + c_4^{ZZ} \cdot c_\alpha\kappa_{\mathrm{SM}} s_\alpha\kappa_{\mathrm{AVV}} + c_5^{ZZ} \cdot c_\alpha\kappa_{\mathrm{HVV}} s_\alpha\kappa_{\mathrm{AVV}} \end{aligned} \tag{5.27}$$

with constant factors $c_{1,..,5}^{WW}$ and $c_{1,..,5}^{ZZ}$.

The constant factors c_i^{gg}, c_i^{WW} and c_i^{ZZ} are calculated with the matrix element morphing method (see Section 6.2). For a discrete set of coupling parameter configurations, the cross section times branching ratio values are calculated for ggF production with BSM couplings entering either in production, for f_{gg} calculation, or in the decay, for $f_{WW/ZZ}$ calculation. The Higgs boson decays into ZZ and WW for the calculation of f_{ZZ} and f_{WW}, respectively. The input configurations, three for f_{gg} and six for $f_{WW/ZZ}$, and their respective cross section times branching ratio values are summarised in Table 5.7. The morphing procedure provides the analytic functions of the coupling parameters in Equations 5.25, 5.26 and 5.27, which interpolate the cross section times branching ratio values between the input values. The coefficients c_i^{gg}, c_i^{WW} and c_i^{ZZ} are given

Table 5.7: The input parameter configurations and respective cross section times branching ratio values for the calculation of the correction functions f_{gg}, f_{ZZ} and f_{WW}. The cross section times branching ratio values have been symmetrised with respect to the sign of $s_\alpha\kappa_{\mathrm{Agg}}$ and $s_\alpha\kappa_{\mathrm{AVV}}$ to avoid non-physical asymmetric values†.

Configuration	$\cos(\alpha)$	κ_{SM}	κ_{Hgg}	κ_{Agg}	κ_{AVV}	κ_{HVV}	$\sigma_{\mathrm{ggF}} \cdot BR$ [fb]	
Description							$H \to 4\ell$	$H \to \ell\nu\ell\nu$
							$(\ell \equiv e, \mu)$	$(\ell \equiv e, \mu, \tau)$
Parameter configurations and $\sigma \cdot BR$ for f_{gg} calculation								
SM	1	1	1	0	0	0	4.1	–
Mixture	$\frac{1}{\sqrt{2}}$	1	1	0.5	0	0	1.6†	–
Mixture	$\frac{1}{\sqrt{2}}$	1	1	−0.5	0	0	1.6†	–
Parameter configurations and $\sigma \cdot BR$ for f_{ZZ} and f_{WW} calculation								
SM	1	1	1	0	0	0	4.1	745
BSM CP-even	1	0	1	0	0	1	$5.3 \cdot 10^{-3}$	2
Mixture	1	1	1	0	0	−6	2.8	418
BSM CP-odd	$\frac{1}{\sqrt{2}}$	0	1	0	1	0	$0.5 \cdot 10^{-3}$	0.2
Mixture	$\frac{1}{\sqrt{2}}$	1	1	0	6	6	1.5	317
Mixture	$\frac{1}{\sqrt{2}}$	1	1	0	−6	−6	0.7	120

Table 5.8: Coefficients of the correction functions f_{VV} with $VV = gg$, ZZ, WW.

Function	Polynomial coefficients				
Name	c_1^{VV}	c_2^{VV}	c_3^{VV}	c_4^{VV}	c_5^{VV}
f_{gg}	2.3	0	–	–	–
f_{ZZ}	$1.2 \cdot 10^{-3}$	$0.5 \cdot 10^{-3}$	0.06	$-0.4 \cdot 10^{-3}$	$0.02 \cdot 10^{-3}$
f_{WW}	$3.0 \cdot 10^{-3}$	$1.3 \cdot 10^{-3}$	0.09	$-3.2 \cdot 10^{-3}$	$0.5 \cdot 10^{-3}$

relatively to the coefficients of the SM term. Therefore, the coefficients to the SM terms in the above equations, i.e. $(c_\alpha\kappa_{\mathrm{Hgg}})^2$ for f_{gg} and $(c_\alpha\kappa_{\mathrm{SM}})^2$ for $f_{WW/ZZ}$, are one. The obtained coefficient values are listed in Table 5.8.

It is important to mention that even if the modified couplings have the SM-like tensor structure but the coupling strengths $c_\alpha\kappa_{\mathrm{SM}}$ or $c_\alpha\kappa_{\mathrm{Hgg}}$ are free parameters, the branching ratio needs to be corrected by a factor $(c_\alpha\kappa_{\mathrm{SM}})^2$ or $(c_\alpha\kappa_{\mathrm{Hgg}})^2$, respectively.

In Figure 5.25 the correction factor f_Γ to the inverse of the total Higgs boson width is shown as a function of $s_\alpha\kappa_{\mathrm{Agg}}$, $c_\alpha\kappa_{\mathrm{HVV}}$ and $s_\alpha\kappa_{\mathrm{AVV}}$. The event yield is overestimated before the correction over the entire range of CP-odd BSM couplings $s_\alpha\kappa_{\mathrm{Agg}}$ and $s_\alpha\kappa_{\mathrm{AVV}}$, reaching up to 9 % deviation for $s_\alpha\kappa_{\mathrm{Agg}} = \pm 0.7$ and 1 % for $s_\alpha\kappa_{\mathrm{AVV}} = \pm 6$. Symmetric input was used to compute the f_{gg} correction function with the morphing method. While $f_\Gamma(s_\alpha\kappa_{\mathrm{Agg}})$ thus is symmetric a small sign asymmetry still exists in correction function $f_\Gamma(s_\alpha\kappa_{\mathrm{AVV}})$, which is an artefact due to using two-dimensional signal morphing in $c_\alpha\kappa_{\mathrm{HVV}}$ and $s_\alpha\kappa_{\mathrm{AVV}}$ for the calculation of the constants c_i^{WW} and c_i^{ZZ}. As the effect is very small, no further symmetrisation has been performed. The event yield as a function of $c_\alpha\kappa_{\mathrm{HVV}}$ is underestimated for negative coupling values and overestimated for positive ones. This is caused by the interference between CP-even SM and BSM interactions with coupling parameters $c_\alpha\kappa_{\mathrm{SM}}$ and $c_\alpha\kappa_{\mathrm{HVV}}$, respectively. The event yield is scaled up by +11 % for $c_\alpha\kappa_{\mathrm{HVV}} = -6$ and down by −13 % for $c_\alpha\kappa_{\mathrm{HVV}} = +6$.

5.2.3 Background estimation

The estimation of background contributions after the inclusive selection of the Higgs boson candidates is discussed in Section 4.3.2. Here, the estimation of relative fractions of these background contributions in each reconstructed category is explained.

The fraction of ZZ^*, $t\bar{t}Z$ and VVV background events in each reconstructed category is estimated from simulation. The simulation is also used to simulate the relative contributions of reducible Z+jets, $t\bar{t}$ and WZ background with muons in the subleading lepton pair ($Z \to \mu\mu$ final state). As a cross check, the background fractions in the $Z \to \mu\mu$ final state are also evaluated in the *relaxed* and *same sign* control regions showing a good agreement between data and simulation. Due to low number of WZ events after the full selection, the fractions of the WZ events per category in the $Z+\mu\mu$ final state (relative to the total number of WZ events) is assumed to be the same as the fractions obtained for the Z+jets process. These fractions are in agreement with the prediction of the WZ simulation.

The relative fractions of $Z + ee$ events from Z+jets and WZ production is estimated for each category using the same procedure as for the inclusive analysis, applying it to each reconstructed category in the $3\ell + X$ control region individually.

The expected number of background events after the inclusive selection and fraction

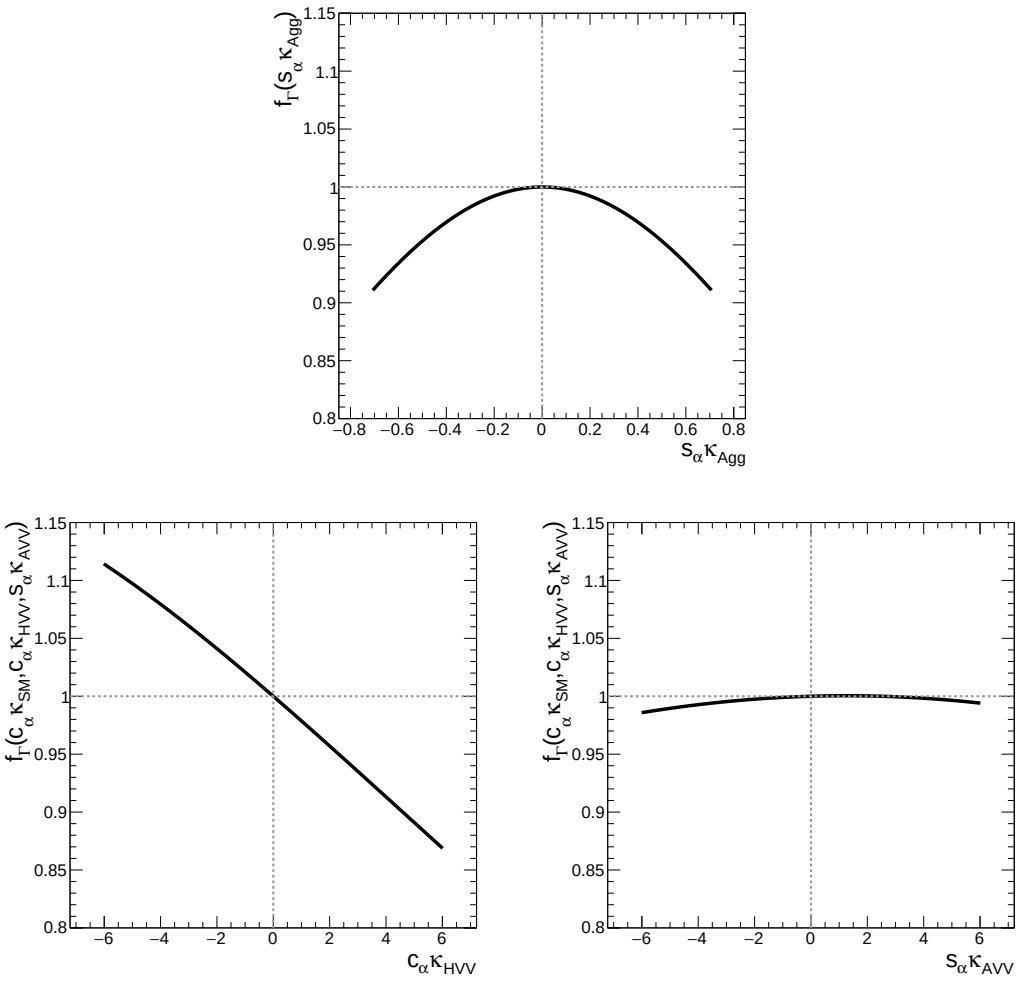

Figure 5.25: The correction factor f_Γ to the inverse of the width of the Higgs boson as a function of $s_\alpha\kappa_{\mathrm{Agg}}$ (top), $c_\alpha\kappa_{\mathrm{HVV}}$ (bottom left) and $s_\alpha\kappa_{\mathrm{AVV}}$ (bottom right).

Table 5.9: The expected total number of background events after the inclusive analysis selection and fractions per reconstructed category in the four-lepton final state for the Run-2 data set. $Z + ee$ and $Z + \mu\mu$ backgrounds include $t\bar{t}$ and Z+jets and WZ processes. Statistical and systematic uncertainties are added in quadrature.

		ZZ^*	$Z + ee$	$Z + \mu\mu$	$t\bar{t}Z, VVV$
Total number of events		19.7 ± 1.5	2.0 ± 0.3	1.6 ± 0.3	0.26 ± 0.07
Fraction per category	$t\bar{t}H$-enriched	0.1 %	1 %	1 %	12 %
	VH-Lep-enriched	0.2 %	< 0.1 %	0.2 %	3 %
	$0j$	70 %	63 %	60 %	5 %
	$1j$-$p_{\mathrm{T}}^{4\ell}$-Low	16 %	15 %	13 %	6 %
	$1j$-$p_{\mathrm{T}}^{4\ell}$-Med	4 %	8 %	12 %	10 %
	$1j$-$p_{\mathrm{T}}^{4\ell}$-High	1 %	2 %	0.3 %	1 %
	VH-Had-enriched-$p_{\mathrm{T}}^{4\ell}$-Low	3 %	3 %	4 %	15 %
	VH-Had-enriched-$p_{\mathrm{T}}^{4\ell}$-High	0.1 %	1 %	0.2 %	1 %
	VBF-enriched-p_{T}^{j}-Low	5 %	6 %	9 %	42 %
	VBF-enriched-p_{T}^{j}-High	0.5 %	1 %	1 %	6 %

(in percent) for each reconstructed category are shown in Table 5.9. The of ZZ^*, $Z + ee$ and $Z + \mu\mu$ background contribute mainly to the $0j$ category, followed by the $1j$-$p_{\mathrm{T}}^{4\ell}$-Low category. Relative contributions to categories with high p_{T}^{4l} and p_{T}^{j1} values, as well as to the VH-Lep-enriched and $t\bar{t}H$-enriched categories are small. Rare $t\bar{t}Z$ and VVV processes have a different decay topology, resulting in a highest fractional contribution to categories with at least two jets, steered by the contribution of the $t\bar{t}Z$ process. The total contribution of these rare background processes is however very small.

5.2.4 Systematic uncertainties

A pedagogical introduction to measurement uncertainties and in particular to systematic uncertainties can be found in Section 5.1.3 where the uncertainties of the shape-based analysis are described. The precision of the rate-based tensor structure measurement is dominated by the statistical error. Systematic uncertainties have very little impact on the final results. The general sources of systematic uncertainties in the four-lepton

final state described in Section 5.1.3 are also valid for the rate-based measurement. The rate-based measurement of the tensor structure of the Higgs boson couplings is based on the event yields per category. Therefore, any uncertainty on the total yield or on the relative fractions per category will affect the final measurement, as discussed in the following. First the experimental and then theoretical systematic uncertainties will be discussed, followed by a summary of the impact from the most dominant sources shown in Table 5.10.

Experimental uncertainties

The experimental uncertainties include the uncertainty on the measurement of the integrated luminosity, the uncertainty related to the reconstruction of leptons and jets, uncertainties from the modelling of pile-up events, and also the uncertainty related to the data-driven background estimation.

The luminosity of the analysed Run-2 data set is measured with a precision of 3.2 % (see Section 2.3.4).

The uncertainties related to leptons and jets are evaluated as described in detail in Section 3. The uncertainties in the predicted yield due to the lepton identification efficiency is up to 1 % for muons and up to 1.3 % for electrons. The lepton isolation efficiency uncertainty is about 2 %. The electron energy and muon momentum scale uncertainties are negligible for the presented measurement. The uncertainties on the jet energy scale and resolution are up to 7 % and up to 4 %, respectively. The flavour tagging uncertainty for identifying b-jets is at the level of a few percent over most of the range of the jet transverse momentum.

The modelling of the pile-up events is corrected using the measured inelastic cross sections [166]. The related uncertainty is evaluated by varying the average number of pile-up events according to the uncertainty of the ratio of predicted to the measured cross section values. The corresponding uncertainty amounts to 2 % on the predicted yields and is propagated to all simulated events.

Several sources contribute to the uncertainty of the data-driven background estimate. The systematic uncertainty of the inclusive $Z + \mu\mu$ background estimate and the $Z + ee$ background estimate in each reconstructed category is evaluated by comparing data with an on-shell Z-boson decay accompanied by an electron or muon to the

corresponding simulation. Additional small uncertainty is assigned to these estimates due to limited statistical precision of the control data. These two uncertainties are considered to be correlated across the reconstructed categories.

Theoretical uncertainties

Theoretical uncertainties include the uncertainty on the theoretical modelling of the signal and the background processes. They are grouped into QCD scale uncertainty, the PDF+α_S uncertainty and the parton shower uncertainty. A detailed description of each group and of the estimation of the related uncertainty can be found in Section 5.1.3.

The theory uncertainty of the signal prediction is the main systematic uncertainty of the measurement. The impact of PDF, QCD scale and parton shower uncertainties is evaluated separately for all Higgs boson production modes using simulated SM samples and applied to the SM and BSM signals.
For the evaluation of the Higgs signal uncertainty related to the parton distribution function (PDF), the strong coupling constant α_s with nominal vale 0.118 was varied by ± 0.0015.
The prediction of the ggF contribution in categories with different jet multiplicities is particularly sensitive to the QCD scale choice. The impact on the inclusive cross sections and migration of events between different jet bins is studied using the approach described in [167].
An additional 2 % uncertainty of the $H \to ZZ^*$ branching ratio calculation is applied to all SM and BSM predictions.
An uncertainty is assigned to the best-prediction scaling of the VBF $+VH$ signal model for the XVV interaction vertex: The VBF and VH models are generated at LO in QCD, while the best-prediction for the SM is at NLO. It is assumed that higher order scale factors (i.e. best-prediction scale factors) are the same for the SM and the BSM signal. The uncertainty on this assumption is obtained by comparing NLO simulations of VBF and VH processes to the standard LO samples. The deviation from the best-prediction scale factors shown in Table 5.6 is up to 15 % for non-zero BSM couplings. No such uncertainty is assigned at the SM point in the coupling parameter space, since the best-prediction scale factors are evaluated at that point.

The theory uncertainty of the dominant ZZ^* background consists of an uncertainty

related to the scaling of the predicted yield due to missing higher order electroweak and QCD effects, and the PDF and QCD scale uncertainties for the gluon fusion and quark induced productions. These uncertainties are also taken into account for the rare $t\bar{t}Z$ background. Due to the small contribution to this process to the total expected yield, this uncertainty has a negligible impact on the final results.

Impact of systematic uncertainties on measurement results

The impact of one or a group of sources of systematic uncertainties is evaluated by comparing the nominal prediction with the one in which a given quantity (such as electron energy scale) is shifted by one standard deviation uncertainty on the quantity. The uncertainties of the event yields in each reconstructed category are implemented as nuisance parameters in the framework for the statistical interpretation of data (see Section 5.2.5). The theoretical uncertainties calculated for the SM signal are assumed to be the same for all BSM points with exception of the best-prediction uncertainty, which is evaluated separately for each BSM morphing input sample. The experimental uncertainties are also calculated separately for the SM and each BSM sample. The best-prediction and experimental uncertainties for an arbitrary BSM point are obtained by interpolation during the morphing. In Table 5.10 the impact of systematic uncertainties on the total expected signal yield is summarised.

All experimental uncertainties have a similar impact on the expected total yield with the luminosity uncertainty having the largest impact. The theory uncertainty with the largest impact is due to the QCD scale uncertainty in the ggF signal prediction. The impact of the ZZ^* and signal PDF uncertainties is of the similar size of the impact of experimental uncertainties, while the impact of the parton shower uncertainties is very small. As discussed previously, the uncertainty on the best-prediction scaling of the VBF $+VH$ signal model has no impact on the SM expectation and a small impact for BSM scenarios in the parameter range under study.

Table 5.10: The relative change of the predicted total event yield for different sources of systematic uncertainties, obtained for the Run-2 data set.

	Experimental uncertainties [%]				Theory uncertainties [%]					
	Lumi	e, μ pile-up	Jets, flavour tagging	Reducible backgr.	ZZ^* backgr.	Signal theory PDF	QCD scale ggF	QCD scale Total	Parton shower	Best-prediction scaling VBF $+VH$
Relative impact on the total predicted yield										
SM	3 %	2 %	1 %	1 %	2 %	2 %	6 %	5 %	0.1 %	–
BSM ($c_\alpha\kappa_{\mathrm{HVV}} = 3.0$)										0.6 %
($s_\alpha\kappa_{\mathrm{AVV}} = 3.2$)										0.3 %

5.2.5 Results of model fits to the data

Fitting method

The constraints on the BSM coupling parameters are obtained in a similar manor as for the shape-based measurement (see Section 5.1.4) from binned maximum likelihood fits to the data using the profiled likelihood ratio method. The likelihood functions are the product of Poisson probabilities with mean $s_i(\kappa, \theta) + b_i(\theta)$ multiplied with the constraint terms for the nuisance parameters θ

$$\mathcal{L}(\kappa, \theta) = \prod_{i}^{N_{\mathrm{Categories}}} P(n_i | s_i(\kappa, \theta) + b_i(\theta)) \times \prod_{m}^{N_{\mathrm{Nuisance}}} A_m(\theta), \tag{5.28}$$

where $\kappa = (c_\alpha\kappa_{\mathrm{Hgg}}, s_\alpha\kappa_{\mathrm{Agg}}, c_\alpha\kappa_{\mathrm{SM}}, c_\alpha\kappa_{\mathrm{HVV}}, s_\alpha\kappa_{\mathrm{AVV}})$ is the vector of coupling parameters, $\theta = (\theta_m)$ is the vector of nuisance parameters corresponding to systematic uncertainties, n_i the observed number of events in category i of in total $N_{\mathrm{Categories}} = 10$ categories and s_i and b_i signal and background models for category i, respectively. All systematic uncertainties summarised in Section 5.2.4 are included in the statistical model with N_{Nuisance} nuisance parameters, where each nuisance parameter m is constrained with a Gaussian constraint term A_m that represents an external measurement.

A combined likelihood fit of the expected event yields in the different categories performed with the couplings as free parameters. While the event yields are not sensitive to the sign of the CP-odd BSM couplings $s_\alpha\kappa_{\mathrm{AVV}}$ and $s_\alpha\kappa_{\mathrm{Agg}}$, there is a sign sensitivity for the CP-even BSM coupling $c_\alpha\kappa_{\mathrm{HVV}}$, due to the interference with

the CP-even SM coupling contribution ($c_\alpha\kappa_{\mathrm{SM}}$). For VBF production the interference leads to a larger expected yield for positive values of $c_\alpha\kappa_{\mathrm{HVV}}$. The effect is opposite for the VH production.

Fits with different assumptions on the BSM coupling parameters have been performed. First, coupling parameters $s_\alpha\kappa_{\mathrm{Agg}}$, $c_\alpha\kappa_{\mathrm{HVV}}$ and $s_\alpha\kappa_{\mathrm{AVV}}$ are measured one at a time, always assuming that all other BSM coupling parameters are equal to zero, and with $c_\alpha\kappa_{\mathrm{Hgg}}$ and $c_\alpha\kappa_{\mathrm{SM}}$ parameters fixed to the SM expectation, i.e. equal to one. Second, the above measurements of XVV coupling parameters $c_\alpha\kappa_{\mathrm{HVV}}$ and $s_\alpha\kappa_{\mathrm{AVV}}$ are additionally performed by allowing the different strength of the SM-like interaction term, i.e by letting $c_\alpha\kappa_{\mathrm{SM}}$ be a free parameter of the fit. This measurement is performed in order to study to which extent the deviations from SM observed in data can be assigned to the SM-like interaction with modified strength and how compatible/big is the remaining BSM coupling contribution. Finally, the $c_\alpha\kappa_{\mathrm{HVV}}$ and $s_\alpha\kappa_{\mathrm{AVV}}$ parameters have been probed simultaneously under assumption of $c_\alpha\kappa_{\mathrm{SM}} = 1$ or with free $c_\alpha\kappa_{\mathrm{SM}}$. As a last correction to CP-odd symmetrising (see Section 5.2.2), the two-dimensional likelihoods in $c_\alpha\kappa_{\mathrm{HVV}}$ and $s_\alpha\kappa_{\mathrm{AVV}}$ are averaged with respect to the sign of the CP-odd parameter. This is necessary, because for the two-dimensional signal model in $s_\alpha\kappa_{\mathrm{AVV}}$ and $c_\alpha\kappa_{\mathrm{HVV}}$ space, it is difficult to symmetrise inputs. A complete symmetric $s_\alpha\kappa_{\mathrm{AVV}}$ basis would lead to an insufficient modelling of the $c_\alpha\kappa_{\mathrm{HVV}}$ parameter.
The BSM couplings are assumed to have no influence on the SM background processes.

The limits on the coupling parameters are again evaluated under the asymptotic approximation [161]. The 68 % and 95 % CL intervals are computed assuming that the test statistic is following a Chi-squared distribution with one or two degrees of freedom in case of one or two parameters of interest, respectively (see Appendix A). Provided the best-fit values for the BSM coupling parameters are not given by the SM expectation, i.e. $\kappa_{\mathrm{BSM}} \neq 0$, the discrepancy is quantified by converting the p-value at the SM point into an equivalent significance Z using a two-sided fluctuation of a normal distributed variable:

$$Z = \Phi^{-1}\left(1 - \frac{p}{2}\right), \tag{5.29}$$

where Φ^{-1} is the quantile (inverse of the cumulative distribution) of a normal distribution.

Observed event yields

The observed event yields (per event category and total) and the corresponding expectation from the SM prediction are shown in Table 5.11 for the Run-2 data set with an integrated luminosity of 36.1 fb^{-1} at $\sqrt{s} = 13$ TeV. A moderate excess of events above the SM prediction is observed. In the rate-based measurement the signal strength μ, which has been introduced in Section 5.1.4, is specifically modelled as function of coupling parameters, see Equation 5.2 in case of the SM. The observed moderate excess can be assigned to an enhanced signal strength of $\mu = 1.28^{+0.21}_{-0.19}$ when all other BSM parameters are set to zero and assuming that $\mu_{\text{ggF}} = \mu_{\text{VBF}/VH}$. The excess is mainly observed in the VBF-enriched categories, while all other categories have a moderate excess ($0j$, $1j$-$p_{\text{T}}^{4\ell}$-Med and $1j$-$p_{\text{T}}^{4\ell}$-High) or agree with the SM expectation ($1j$-$p_{\text{T}}^{4\ell}$-Low and VH-Had-enriched-$p_{\text{T}}^{4\ell}$-Low). Also in agreement with the SM expectation, no events have been observed in the $t\bar{t}H$-enriched, VH-Lep-enriched and VH-Had-enriched-$p_{\text{T}}^{4\ell}$-High categories.

Additional BSM Higgs boson couplings will affect the total event yield and the fractional yield per reconstructed category. A comparison of the observed event yields, and those

Table 5.11: Observed and SM expected numbers of signal and background events in the different categories of the four-lepton decay channel after the rate-based analysis selection for the Run-2 data set. Other backgrounds than ZZ^* are $t\bar{t}$, Z+jets, rare triboson and $t\bar{t}Z$ processes. Statistical and systematic uncertainties have been added in quadrature [146].

Reconstructed event category	Signal	ZZ^* background	Other backgrounds	Total expected	Observed
$t\bar{t}H$-enriched	0.39 ± 0.04	0.014 ± 0.006	0.07 ± 0.04	0.47 ± 0.05	0
VH-Lep-enriched	0.318 ± 0.019	0.049 ± 0.008	0.0137 ± 0.0019	0.380 ± 0.020	0
$0j$	26.8 ± 2.5	13.7 ± 1.0	2.23 ± 0.31	42.7 ± 2.7	49
$1j$-$p_{\text{T}}^{4\ell}$-Low	8.8 ± 1.1	3.1 ± 0.4	0.53 ± 0.07	12.5 ± 1.2	12
$1j$-$p_{\text{T}}^{4\ell}$-Med	5.4 ± 0.7	0.88 ± 0.12	0.38 ± 0.05	6.7 ± 0.7	9
$1j$-$p_{\text{T}}^{4\ell}$-High	1.47 ± 0.24	0.139 ± 0.022	0.045 ± 0.007	1.65 ± 0.24	3
VH-Had-enriched-$p_{\text{T}}^{4\ell}$-Low	2.9 ± 0.5	0.63 ± 0.16	0.169 ± 0.021	3.7 ± 0.5	3
VH-Had-enriched-$p_{\text{T}}^{4\ell}$-High	0.64 ± 0.09	0.029 ± 0.008	0.0182 ± 0.0022	0.69 ± 0.09	0
VBF-enriched-p_{T}^{j}-Low	6.3 ± 0.8	1.08 ± 0.32	0.40 ± 0.04	7.7 ± 0.9	16
VBF-enriched-p_{T}^{j}-High	0.57 ± 0.10	0.093 ± 0.032	0.054 ± 0.006	0.72 ± 0.10	3
Total	54 ± 4	19.7 ± 1.5	3.9 ± 0.5	77 ± 4	95

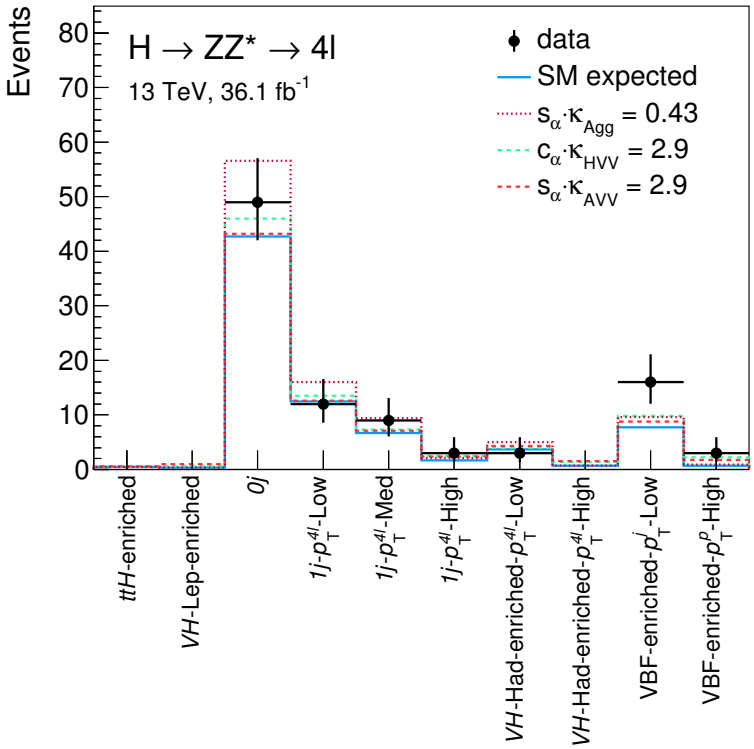

Figure 5.26: Observed (black points) and expected event yields in the different categories of the four-lepton decay channel after the rate-based analysis selection for the Run-2 data set. Predictions are shown for the case of the SM signal, $c_\alpha\kappa_{\mathrm{SM}} = 1$, $c_\alpha\kappa_{\mathrm{Hgg}} = 1$ and others zero, (solid blue), and for additional BSM couplings $s_\alpha\kappa_{\mathrm{Agg}}$ (dotted red), $c_\alpha\kappa_{\mathrm{HVV}}$ (dashed green) or $s_\alpha\kappa_{\mathrm{AVV}}$ (dashed red).

expected for several different values of BSM coupling parameters (SM, $s_\alpha\kappa_{\mathrm{Agg}} = 0.43$, $c_\alpha\kappa_{\mathrm{HVV}} = 2.9$ and $s_\alpha\kappa_{\mathrm{AVV}} = 2.9$) is shown in Figure 5.26. The coupling values have been chosen according to the best-fit values obtained from the fit to data discussed later on. Observed and expected SM event yields are in a reasonable agreement. The BSM scenarios show a better agreement with data in most of the categories. The signal models in all categories together with the observed data can be found in Appendix I.

In Figure 5.27, the observed and the expected distributions predicted by the SM are shown for the variables employed in the categorisation of Higgs boson candidates: the

jet multiplicity N_j after the inclusive analysis selection, the transverse momentum p_{T}^{4l} of the four-lepton system in the $1j$ categories, the invariant mass m_{jj} of the dijet system in the $2j$ categories, p_{T}^{4l} in the VH-Had-enriched and the transverse momentum p_{T}^{j1} of the leading jet in the VBF-enriched categories. Reasonable agreement between data and expectation can be seen for all distributions except the dijet invariant mass and the jet transverse momentum, which are affected by the observed excess of events in VBF-enriched categories.

Categorisation studies

The splitting of the VH-Had-enriched and VBF-enriched categories specifically target BSM couplings in the HVV vertex. The performance of p_{T}^{4l} and p_{T}^{j1} with different cut values has been tested resulting into the categorisation scheme discussed in Section 5.2.1. The results of the study are summarised in Table 5.12. While all categorisations with splitting in the $N_j \geq 2$ categories improve the limits up to 10%, no large difference between variables is observed. At the end, variables in agreement with the simplified template cross section framework are used: For VBF production p_{T}^{j1} is recommended, the VBF-enriched category is split into two sub-categories: $p_{\mathrm{T}}^{j1} < 200$ GeV and $p_{\mathrm{T}}^{j1} > 200$ GeV. For VH-hadronic production no variable is suggested in the simplified template cross section framework, but the transverse momentum of the vector boson p_{T}^{V} is recommended for VH-leptonic production. Therefore, p_{T}^{4l} is chosen, as it is closely related to p_{T}^{V}, but has a better experimental resolution and less associated uncertainty than the dijet transverse momentum. The VH-Had-enriched category is split into two sub-categories: $p_{\mathrm{T}}^{4l} < 150$ GeV and $p_{\mathrm{T}}^{4l} > 150$ GeV.

Systematic uncertainties

In Table 5.13 the impact of systematic uncertainties on the observed best-fit values of coupling parameters is summarised. For the impact of uncertainties on the best-fit value of a given coupling parameter, the maximum relative shift between the nominal ($\widehat{\kappa}$) and the new ($\widehat{\kappa}'$) best-fit value $\frac{\widehat{\kappa}'-\widehat{\kappa}}{\widehat{\kappa}}$ is shown.
The largest impact is caused by QCD scale uncertainty (mainly ggF) in the Higgs boson signal prediction. The impact of this systematic uncertainty is the largest for the $s_\alpha \kappa_{\mathrm{Agg}}$ coupling parameter due to the rapid increase of expected event yields with increasing parameter values. The second largest impact on the best-fit value originates

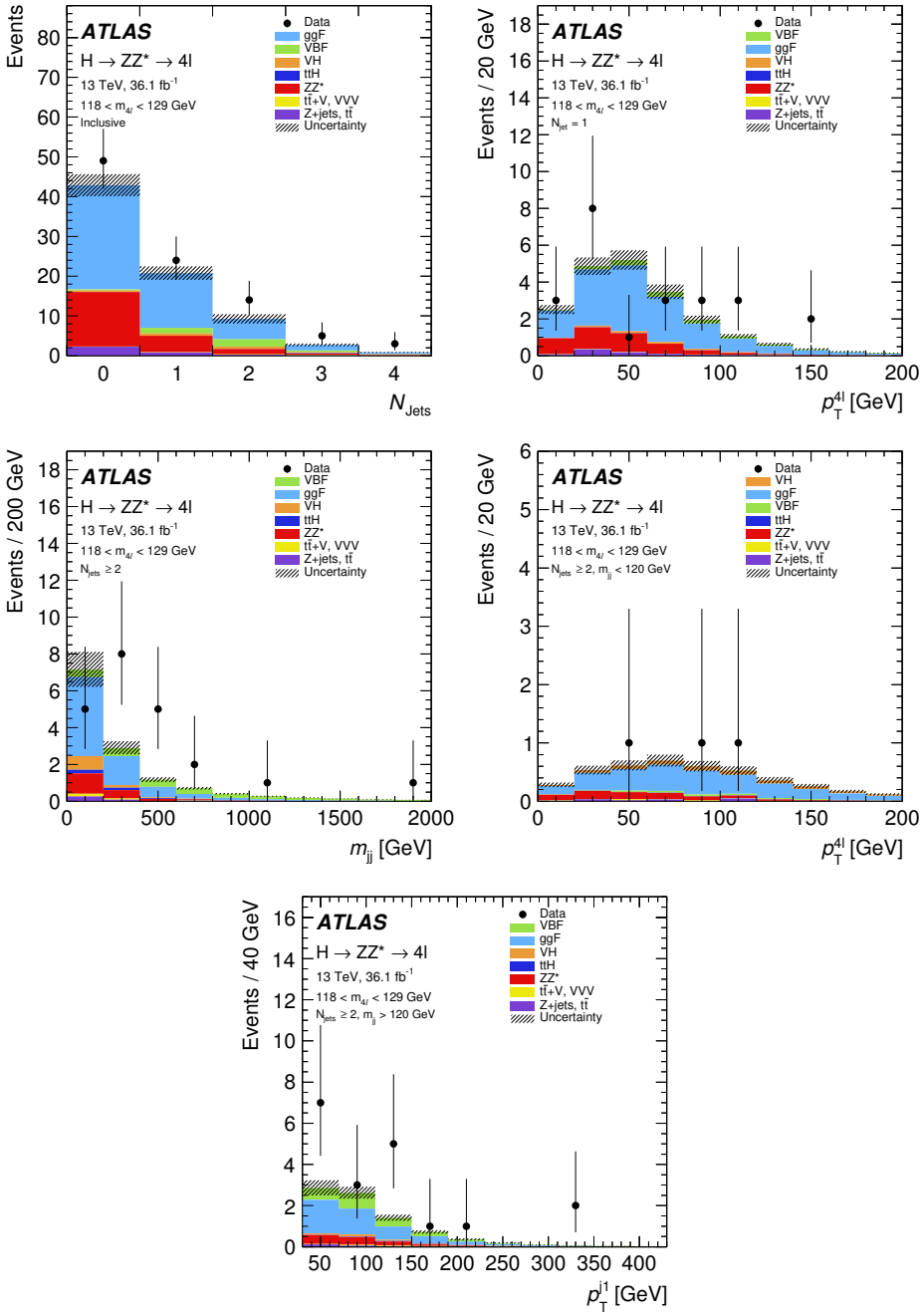

Figure 5.27: The observed and SM expected distributions of categorisation variables for the Run-2 data set assuming a Higgs boson mass of 125.09 GeV. From top left to bottom: the jet multiplicity N_j after the inclusive analysis selection, the transverse momentum p_{T}^{4l} of the four-lepton system in the $1j$ categories, the invariant mass m_{jj} of the dijet system in the $2j$ categories, p_{T}^{4l} in the VH-Had-enriched and the transverse momentum p_{T}^{j1} of the leading jet in the VBF-enriched categories [146].

Table 5.12: Confidence intervals at 95 % CL for BSM CP-even $c_\alpha\kappa_{\mathrm{HVV}}$ and CP-odd $s_\alpha\kappa_{\mathrm{AVV}}$ couplings in the interaction XVV vertex estimated with a SM Asimov data set for the Run-2 data. Different variables and values for a splitting of the VH-Had-enriched and VBF-enriched categories have been compared with no splitting. Only statistical uncertainties have been taken into account. Non-physical asymmetric regions for the CP-odd coupling have been symmetrised by taking the maximum value[†].

95 % CL confidence interval on BSM coupling in XVV vertex with different categorisations					
VBF-enriched	no splitting	p_{T}^{j1}, 200 GeV			
VH-Had-enriched		p_{T}^{j1} 150 GeV	p_{T}^{4l} 120 GeV	p_{T}^{4l} 150 GeV	p_{T}^{4l} 200 GeV
BSM CP-even $c_\alpha\kappa_{\mathrm{HVV}}$	[−3.5, 2.9]	[−3.2, 2.7]	[−3.2, 2.8]	[−3.1, 2.7]	[−3.1, 2.7]
CP-odd $s_\alpha\kappa_{\mathrm{AVV}}$	[−3.9, 3.9][†]	[−3.5, 3.5]	[−3.5, 3.5]	[−3.5, 3.5]	[−3.5, 3.5]

from the experimental systematic uncertainties in particular the luminosity uncertainty and the combined jets and flavour tagging uncertainties.
Because the event yield is the measured quantity, the main systematic uncertainties follow, as expected, the rating based on the change of the event yield shown in Table 5.10.

Table 5.13: The relative change of the observed best-fit value of the BSM coupling parameters for different sources of systematic uncertainties, obtained for the Run-2 data set.

	Experimental uncertainties [%]				Theory uncertainties [%]					
	Lumi	e, μ pile-up	Jets, flavour tagging	Reducible backgr.	ZZ^* backgr.	PDF	Signal theory QCD scale ggF	Signal theory QCD scale Total	Parton shower	Best-prediction scaling VBF $+VH$
Relative impact on the observed best-fit value										
$s_\alpha\widehat{\kappa}_{\mathrm{Agg}}$	10 %	−10 %	−12 %	−2 %	5 %	7 %	−14 %	−14 %	0 %	–
$c_\alpha\widehat{\kappa}_{\mathrm{HVV}}$	5 %	−4 %	−6 %	−1 %	−3 %	1 %	−19 %	−15 %	−2 %	3 %
$s_\alpha\widehat{\kappa}_{\mathrm{AVV}}$	6 %	−4 %	−9 %	1 %	−4 %	1 %	−29 %	−24 %	−3 %	4 %

Sensitivity per category

The analysis sensitivity per reconstructed category is evaluated by performing the statistical interpretation in only one category at the time. The results for the most sensitive categories are summarised in Table 5.14. Only categories in which the sensitivity allows for exclusion at 95 % CL limits within the explored parameter range are shown.
For the $s_\alpha\kappa_{\mathrm{Agg}}$ parameter, the expected most sensitive category is the $0j$ category which is very pure in gluon fusion production. In data, the VBF-enriched categories also provide constraints due to the observed excess of events, both the $0j$ and VBF-enriched categories contribute to the observed non-zero best-fit value of $s_\alpha\widehat{\kappa}_{\mathrm{Agg}}$ of the combined fit, which will be discussed in the next section.
Categories enriched with VH or VBF production modes provide the highest sensitivity to $c_\alpha\kappa_{\mathrm{HVV}}$ and $s_\alpha\kappa_{\mathrm{AVV}}$ coupling parameters because the event yield in these categories increases proportionally with κ^4_{BSM}. The observed excess of events in VBF-enriched categories results in non-zero best-fit values $c_\alpha\widehat{\kappa}_{\mathrm{HVV}}$ and $s_\alpha\widehat{\kappa}_{\mathrm{AVV}}$ of the combined fit which will be discussed below. In the VH-enriched categories a slightly higher yield is expected from the SM prediction than observed. Therefore, the non-zero $c_\alpha\kappa_{\mathrm{HVV}}$ best-fit values for the VH-enriched categories reported in Table 5.14 may be surprising at first. This becomes more intuitive when recalling that the minimum of the VH signal yield is not expected at the SM point, but rather shifted to positive $c_\alpha\kappa_{\mathrm{HVV}}$ values due to the interference between the SM and BSM CP-even coupling interactions (see Appendix G). Thus, smaller number of observed events compared to SM prediction in these categories results in a positive best-fit $c_\alpha\kappa_{\mathrm{HVV}}$ parameter value.

Constraints on the coupling parameters

The results of one-dimensional likelihood scans probing one of the coupling parameters at the time ($s_\alpha\kappa_{\mathrm{Agg}}$, $c_\alpha\kappa_{\mathrm{HVV}}$ or $s_\alpha\kappa_{\mathrm{AVV}}$) are summarised in Table 5.15. The expected and observed confidence interval at 95 % CL, the best-fit values and the number of standard deviations from the SM prediction are shown. The SM prediction includes Higgs boson signal and background processes. For the $c_\alpha\kappa_{\mathrm{HVV}}$ and $s_\alpha\kappa_{\mathrm{AVV}}$ parameters, both results with the SM-like coupling $c_\alpha\kappa_{\mathrm{SM}}$ parameter set to one or left floating are reported.

Table 5.14: Observed and expected 95 % confidence intervals for the BSM coupling parameters $\kappa_{\text{BSM}} = (s_\alpha\kappa_{\text{Agg}},\ c_\alpha\kappa_{\text{HVV}},\ s_\alpha\kappa_{\text{AVV}})$ in the Xgg and XVV interaction vertices from the rate-based analysis of the Run-2 data together with the corresponding best-fit values and the deviations from the SM prediction evaluated separately for each and for combination of all categories. Only the most sensitive categories are listed, in which the 95 % confidence interval lies within the scan boundaries (SB), SB= ± 0.7 for $s_\alpha\kappa_{\text{Agg}}$ parameter, and SB= ± 6 for $c_\alpha\kappa_{\text{HVV}}$ and $s_\alpha\kappa_{\text{AVV}}$. The SM couplings $c_\alpha\kappa_{\text{Hgg}}$ and $c_\alpha\kappa_{\text{SM}}$ are fixed to the SM expectation. Non-physical asymmetric intervals for the CP-odd coupling have been symmetrised by taking the maximum of the positive and negative limits (marked by †).

BSM coupling κ_{BSM}	95 % CL confidence interval		Observed	Deviation
and fit configuration	Expected	Observed	Best-fit $\widehat{\kappa}_{\text{BSM}}$	from SM
$\kappa_{\text{BSM}} = s_\alpha\kappa_{\text{Agg}}$, $c_\alpha\kappa_{\text{SM}} = 1$ and $c_\alpha\kappa_{\text{Hgg}} = 1$				
$0j$	$[-0.54, 0.54]$	$[-0.67, 0.67]$	± 0.33	$0.8\,\sigma$
VBF-enriched-p_{T}^j-Low		$]\text{SB}, -0.36] \cup [0.36, \text{SB}[$	± 1.12	$2.4\,\sigma$
VBF-enriched-p_{T}^j-High		$]\text{SB}, -0.08] \cup [0.08, \text{SB}[$	± 2.13	$2.0\,\sigma$
Combined	$[-0.47, 0.47]$	$[-0.68, 0.68]$	± 0.43	$1.8\,\sigma$
$\kappa_{\text{BSM}} = c_\alpha\kappa_{\text{HVV}}$, $c_\alpha\kappa_{\text{SM}} = 1$ and $c_\alpha\kappa_{\text{Hgg}} = 1$				
VH-Lep-enriched	$[-4.9, 5.8]$	$[-3.6, 5.0]$	1.1	$0.5\,\sigma$
VH-Had-enriched-$p_{\text{T}}^{4\ell}$-High	$[-5.6, 5.3]$	$[-4.1, 4.3]$	0.5	$0.2\,\sigma$
VBF-enriched-p_{T}^j-Low	$]\text{SB}, 6.0]$	$]\text{SB}, -4.4] \cup [2.0, \text{SB}[$	6.3	$2.4\,\sigma$
VBF-enriched-p_{T}^j-High	$[-5.8, 4.2]$	$]\text{SB}, -0.4] \cup [0.1, \text{SB}[$	3.5	$2.0\,\sigma$
Combined	$[-2.9, 3.2]$	$[0.8, 4.5]$	2.9	$2.3\,\sigma$
$\kappa_{\text{BSM}} = s_\alpha\kappa_{\text{AVV}}$, $c_\alpha\kappa_{\text{SM}} = 1$ and $c_\alpha\kappa_{\text{Hgg}} = 1$				
VH-Lep-enriched		$[-5.3, 5.3^\dagger]$	0.0	–
VH-Had-enriched-$p_{\text{T}}^{4\ell}$-High	$[-5.8, 5.8^\dagger]$	$[-4.5, 4.5]$	0.0	–
VBF-enriched-p_{T}^j-Low		$]\text{SB}, -3.2] \cup [3.2^\dagger, \text{SB}[$	± 8.0	$2.4\,\sigma$
VBF-enriched-p_{T}^j-High	$[-5.2, 5.2^\dagger]$	$]\text{SB}, -0.1] \cup [0.1, \text{SB}[$	± 4.3	$2.0\,\sigma$
Combined	$[-3.5, 3.5]$	$[-5.2, 5.2]$	± 2.9	$1.4\,\sigma$

Table 5.15: Observed and expected confidence intervals at 95 % CL for the BSM coupling parameters $s_\alpha\kappa_{\text{Agg}}$, $c_\alpha\kappa_{\text{HVV}}$ and $s_\alpha\kappa_{\text{AVV}}$ in Xgg and XVV interactions together with the corresponding best-fit values and deviations from the SM prediction obtained for the Run-2 data set [146].

BSM coupling	Fit	95 % CL confidence interval		Observed best-fit		Deviation
κ_{BSM}	configuration	Expected	Observed	$\widehat{\kappa}_{\text{BSM}}$	$c_\alpha\widehat{\kappa}_{\text{SM}}$	from SM
$s_\alpha\kappa_{\text{Agg}}$	($c_\alpha\kappa_{\text{Hgg}} = 1$, $c_\alpha\kappa_{\text{SM}} = 1$)	[−0.47, 0.47]	[−0.68, 0.68]	±0.43	–	$1.8\,\sigma$
$c_\alpha\kappa_{\text{HVV}}$	($c_\alpha\kappa_{\text{Hgg}} = 1$, $c_\alpha\kappa_{\text{SM}} = 1$)	[−2.9, 3.2]	[0.8, 4.5]	2.9	–	$2.3\,\sigma$
$c_\alpha\kappa_{\text{HVV}}$	($c_\alpha\kappa_{\text{Hgg}} = 1$, $c_\alpha\kappa_{\text{SM}}$ free)	[−3.1, 4.0]	[−0.6, 4.2]	2.2	1.2	$1.7\,\sigma$
$s_\alpha\kappa_{\text{AVV}}$	($c_\alpha\kappa_{\text{Hgg}} = 1$, $c_\alpha\kappa_{\text{SM}} = 1$)	[−3.5, 3.5]	[−5.2, 5.2]	±2.9	–	$1.4\,\sigma$
$s_\alpha\kappa_{\text{AVV}}$	($c_\alpha\kappa_{\text{Hgg}} = 1$, $c_\alpha\kappa_{\text{SM}}$ free)	[−4.0, 4.0]	[−4.4, 4.4]	±1.5	1.2	$0.5\,\sigma$

In data, a non-zero best-fit value of $s_\alpha\widehat{\kappa}_{\text{Agg}} = \pm 0.43$ corresponding to a non-significant deviation from the SM prediction of $1.8\,\sigma$ is preferred due to the observed excess of events in the $0j$ and VBF-enriched categories as discussed previously.
The observed excess of events in VBF-enriched categories results in non-zero best-fit values $c_\alpha\widehat{\kappa}_{\text{HVV}} = 2.9$ and $s_\alpha\widehat{\kappa}_{\text{AVV}} = \pm 2.9$. If the $c_\alpha\kappa_{\text{SM}}$ coupling parameter is left free in the fit, the expected confidence interval at 95 % CL increase by 10 %. The observed excess is partially absorbed in an enhancement of the $c_\alpha\kappa_{\text{SM}}$ value by 20 %. As a consequence, the best-fit values of $c_\alpha\kappa_{\text{HVV}}$ ($s_\alpha\kappa_{\text{AVV}}$) parameters decrease and the deviation from the SM prediction is reduced from $2.3\,\sigma$ ($1.4\,\sigma$) to $1.7\,\sigma$ ($0.5\,\sigma$).
The observed and expected distributions of the test statistic dependence on the given BSM coupling parameters are shown in Figures 5.28 and 5.29. No sign sensitivity is available for the BSM CP-odd $s_\alpha\kappa_{\text{Agg}}$ and $s_\alpha\kappa_{\text{AVV}}$ parameters, while the positive sign of the BSM CP-even parameter $c_\alpha\kappa_{\text{HVV}}$ is preferred by the fit. Due to the observed excess of events above the SM prediction, non-zero values of BSM coupling parameters are favoured. However, the corresponding deviations from the SM prediction are all deviations within $2\,\sigma$ at most, i.e. not significant enough to claim any evidence of new couplings.

The findings of the one-dimensional likelihood scans of the BSM coupling parameters in the XVV interaction vertex with free SM coupling parameter in the fit can be extended by a two-dimensional likelihood function where the $c_\alpha\kappa_{\text{HVV}}$ or $s_\alpha\kappa_{\text{AVV}}$ and $c_\alpha\kappa_{\text{SM}}$ coupling parameters are probed simultaneously. The observed and expected two-dimensional contours of the test statistic surrounding the confidence regions at

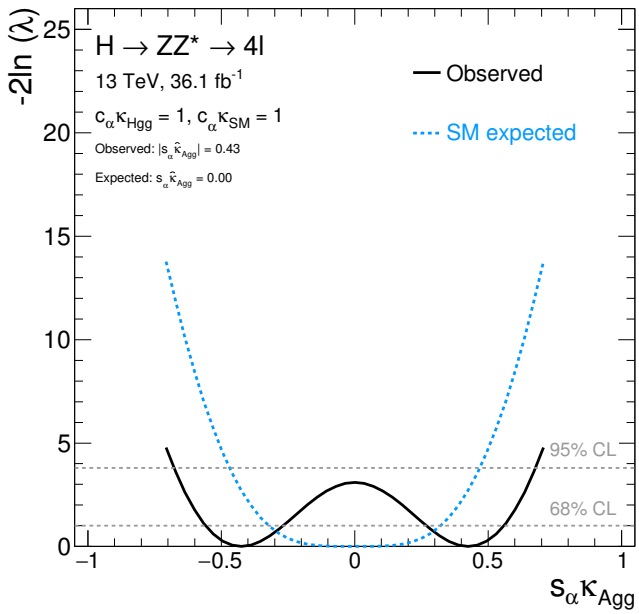

Figure 5.28: Observed (black) and SM expected (blue) dependence of the test statistic on the $s_\alpha \kappa_{\mathrm{Agg}}$ coupling parameter for the rate-based analysis of the Run-2 data set. The horizontal lines indicate the 68 % and 95 % confidence levels assuming a χ^2 distribution of the profiled likelihood ratio.

95 % CL in parameter space are shown in Figure 5.30 for the $c_\alpha \kappa_{\mathrm{HVV}}$ (left) and $s_\alpha \kappa_{\mathrm{AVV}}$ (right) coupling parameters. The coupling parameter values inside the elliptical form encasing the SM point are allowed at 95 % CL, while the values outside are excluded. The two-dimensional test statistic contour in case of $s_\alpha \kappa_{\mathrm{AVV}}$ and $c_\alpha \kappa_{\mathrm{SM}}$ coupling parameters is fully symmetric, while the BSM CP-even and SM CP-even coupling parameters can be distinguished for negative $c_\alpha \kappa_{\mathrm{HVV}}$ values where the interference is highest. Thus, the two-dimensional test statistic contour is asymmetric. The resulting best-fit values and deviations from the SM prediction are shown in Table 5.16. The findings of the one-dimensional scans are confirmed, the best-fit values are almost identical, only a small difference in best-fit $c_\alpha \widehat{\kappa}_{\mathrm{HVV}}$ coupling parameter is observed. The tension to the SM prediction is enhanced with respect to the one-dimensional scans, but still at the level of two standard deviations. Therefore, no significant difference is observed.

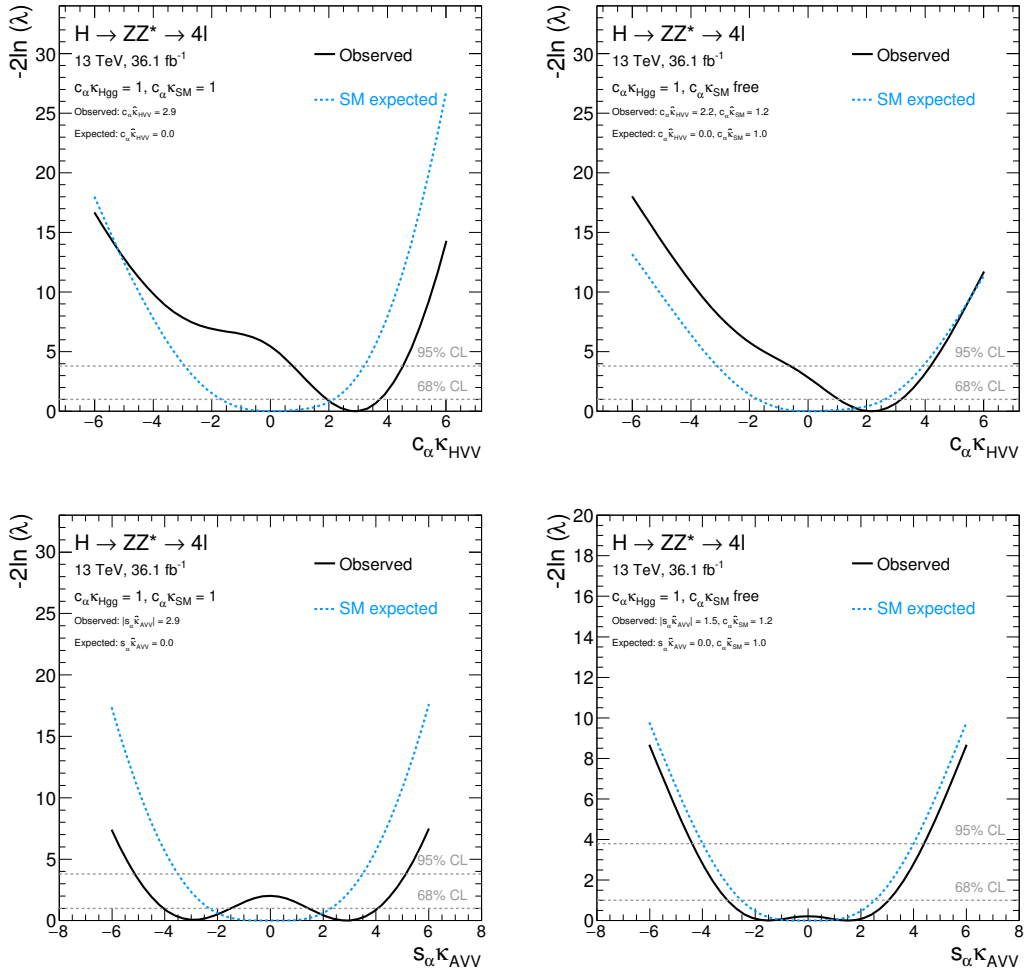

Figure 5.29: Observed (black) and SM expected (blue) dependence of the test statistic on $c_\alpha\kappa_{\mathrm{HVV}}$ (top) and $s_\alpha\kappa_{\mathrm{AVV}}$ (bottom) coupling parameters for the rate-based analysis of the Run-2 data set. The test statistic distribution is shown with SM coupling parameters fixed to the SM expectation (left) and free (right) in the fit. The horizontal lines indicate the 68 % and 95 % confidence levels assuming a χ^2 distribution of the profiled likelihood ratio.

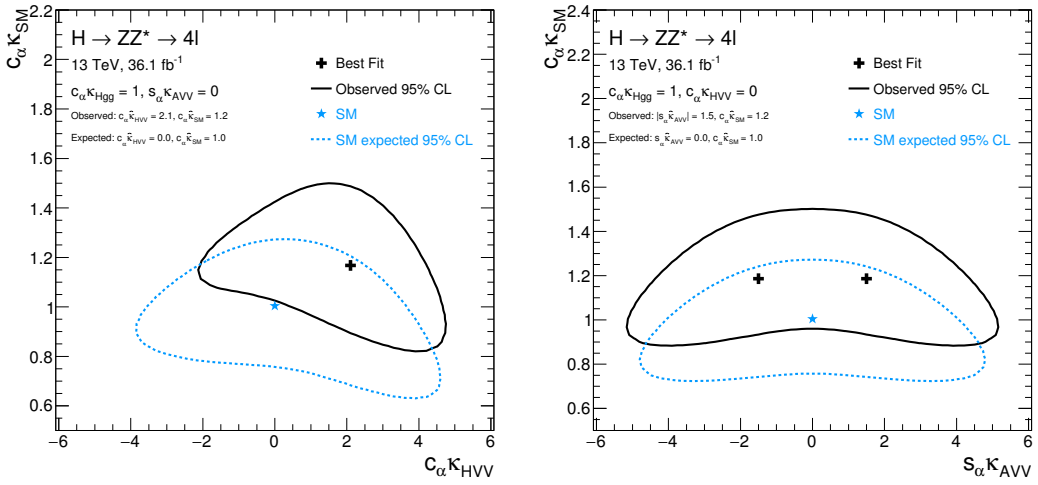

Figure 5.30: Observed (black) 95 % CL contour of the test statistic compared to the SM expectation (blue), obtained from a two-dimensional fit of CP-even (left) and CP-odd (right) BSM couplings $c_\alpha\kappa_{\mathrm{HVV}}$ and $s_\alpha\kappa_{\mathrm{AVV}}$ and the CP-even SM coupling $c_\alpha\kappa_{\mathrm{SM}}$ at the XVV vertex to Run-2 data. The coupling $c_\alpha\kappa_{\mathrm{Hgg}}$ is set to the SM value in both cases, while $s_\alpha\kappa_{\mathrm{AVV}}$ ($c_\alpha\kappa_{\mathrm{HVV}}$) are set to zero for the $c_\alpha\kappa_{\mathrm{HVV}}$ ($s_\alpha\kappa_{\mathrm{AVV}}$) scans.

Table 5.16: The best-fit values of the BSM coupling parameters $c_\alpha\kappa_{\mathrm{HVV}}$ and $s_\alpha\kappa_{\mathrm{AVV}}$ and deviation from the SM prediction obtained from the two-dimensional fits of the parameters ($c_\alpha\kappa_{\mathrm{HVV}}$,$c_\alpha\kappa_{\mathrm{SM}}$) and ($s_\alpha\kappa_{\mathrm{AVV}}$,$c_\alpha\kappa_{\mathrm{SM}}$) parameters to the Run-2 data set.

Fit configuration	Observed best-fit			Deviation from SM
	$c_\alpha\widehat{\kappa}_{\mathrm{HVV}}$	$s_\alpha\widehat{\kappa}_{\mathrm{AVV}}$	$c_\alpha\widehat{\kappa}_{\mathrm{SM}}$	
$c_\alpha\kappa_{\mathrm{Hgg}} = 1,\ s_\alpha\kappa_{\mathrm{AVV}} = 0$	2.1	–	1.2	$2.1\,\sigma$
$c_\alpha\kappa_{\mathrm{Hgg}} = 1,\ c_\alpha\kappa_{\mathrm{HVV}} = 0$	–	± 1.5	1.2	$1.5\,\sigma$

The CP-even and CP-odd BSM coupling parameters in the XVV interaction vertex are additionally probed simultaneously by a two-dimensional likelihood function. The observed and expected two-dimensional contours of the test statistic surrounding the 95 % CL confidence regions in parameters space are shown in Figure 5.31 for fit configurations with the fixed (left) and free-floating (right) SM coupling parameter $c_\alpha\kappa_{\mathrm{SM}}$. The best-fit value for the $c_\alpha\widehat{\kappa}_{\mathrm{HVV}}$ parameter is similar to the value obtained in one-dimensional scans, while the best-fit value for the $s_\alpha\kappa_{\mathrm{AVV}}$ parameter is reduced,

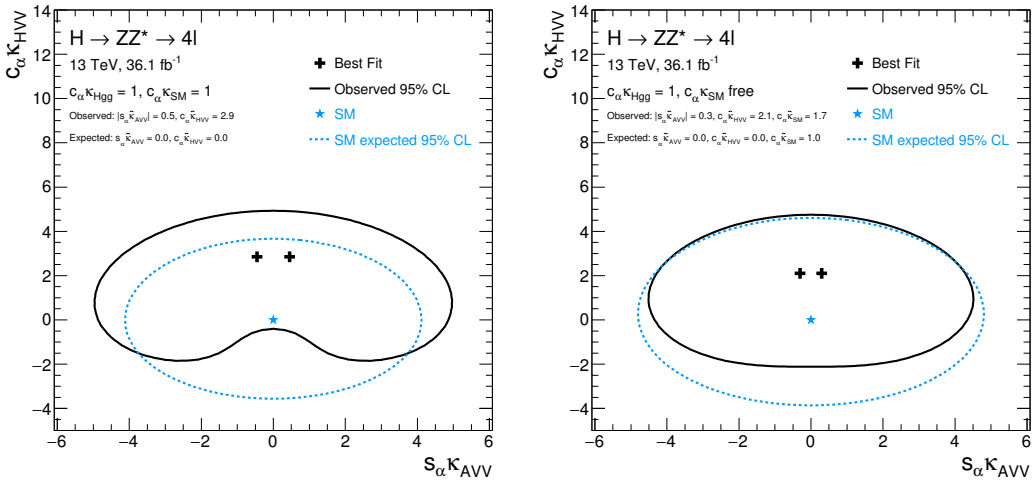

Figure 5.31: Observed (black) 95 % CL contour of the test statistic compared to the SM expectation (blue), obtained from a two-dimensional fit to Run-2 data of CP-even and CP-odd BSM couplings $c_\alpha\kappa_{\mathrm{HVV}}$ and $s_\alpha\kappa_{\mathrm{AVV}}$ at the XVV vertex with the CP-even SM coupling $c_\alpha\kappa_{\mathrm{SM}} = 1$ set to the SM value (left) and free (right). The coupling $c_\alpha\kappa_{\mathrm{Hgg}}$ is set to the SM value in both cases.

Table 5.17: The best-fit values of BSM coupling parameters $c_\alpha\kappa_{\mathrm{HVV}}$ and $s_\alpha\kappa_{\mathrm{AVV}}$ and their deviations from the SM predictions from the two-dimensional fit of $c_\alpha\kappa_{\mathrm{HVV}}$ and $s_\alpha\kappa_{\mathrm{AVV}}$ to the Run-2 data set [146].

Fit configuration	Observed best-fit			Deviation from SM
	$c_\alpha\widehat{\kappa}_{\mathrm{HVV}}$	$s_\alpha\widehat{\kappa}_{\mathrm{AVV}}$	$c_\alpha\widehat{\kappa}_{\mathrm{SM}}$	
$c_\alpha\kappa_{\mathrm{Hgg}} = 1$, $c_\alpha\kappa_{\mathrm{SM}} = 1$	2.9	± 0.5	–	$1.9\,\sigma$
$c_\alpha\kappa_{\mathrm{Hgg}} = 1$, $c_\alpha\kappa_{\mathrm{SM}}$ free	2.1	± 0.3	1.7	$1.2\,\sigma$

moving closer to the SM prediction. The resulting best-fit values and deviations from the SM prediction are quoted in Table 5.17.

The expected sensitivity is reduced with an additional free parameter in the fit, therefore a larger coupling parameter phase space can be excluded, when the SM coupling parameter is fixed compared to a free SM coupling parameter. This behaviour is opposite for the observed distribution of the test statistic. With free SM coupling parameter the observed excess is attributed to an enhanced value of the SM coupling

parameter of $c_\alpha \widehat{\kappa}_{\mathrm{SM}} = 1.7$. Subsequently, the deviation of the fit result from the SM prediction is reduced from $1.9\,\sigma$ to $1.2\,\sigma$. For the $s_\alpha \kappa_{\mathrm{AVV}}$ coupling parameter, a larger phase space can be excluded with free SM coupling parameter, since the excess is more SM-like and less $s_\alpha \kappa_{\mathrm{AVV}}$ BSM contribution is needed to explain the excess. For $c_\alpha \kappa_{\mathrm{HVV}}$, roughly the same area is excluded for fixed and free SM coupling parameter with exception of the area close to the SM point, where the interference with the SM CP-even coupling parameter is highest. At values of $c_\alpha \kappa_{\mathrm{HVV}}$ roughly at -1, the predicted event yield is at a minimum and can only be enhanced with a free SM coupling parameter or moving away from $s_\alpha \kappa_{\mathrm{AVV}} = 0$.

5.3 Comparison of the tensor structure measurements

The shape and the rate-based tensor structure measurements in Sections 5.1 and 5.2 are compared to each other and to other measurements of the ATLAS and CMS experiments.

5.3.1 Shape and rate-based analyses

As has been mentioned at the beginning of this chapter, there are two types of CP-sensitive observables available: the rate and shape information. While the shape-based analysis is purely based on the latter information the rate-based analysis uses a combination of both types of CP-sensitive observables. Both measurements constrain BSM coupling parameters in the XVV interaction vertex, therefore the confidence intervals at 95 % CL expected in the SM are compared. The comparison is not straightforward since the result of the shape-based analysis can be reported in terms of ratios of BSM and SM coupling parameters, while this is not possible for the rate-based analysis, as the total cross section depends on both BSM and SM coupling parameters. Thus, a comparison is only given for a specific configuration with the SM coupling parameters fixed to their SM values, i.e. $c_\alpha \kappa_{\mathrm{SM}} = 1$ and $c_\alpha \kappa_{\mathrm{Hgg}} = 1$ for the rate-based analysis. For the shape-based analysis, the sensitivity is retrieved by using a SM Asimov data set with $\mu = 1$. The comparison is still only approximate since the two analyses approaches are based on data sets with different integrated luminosities collected from collisions at different centre-of-mass energies.

The observed and expected confidence intervals at 95 % CL for the BSM coupling parameters are reported in Table 5.18 for both analyses in the $H \to ZZ^* \to 4\ell$ final states. The coupling parameters of the rate-based analysis are translated into the parameters of the shape-based analysis using Equation 5.3. In the present setup, only the shape-based analysis is sensitive to the sign of the CP-odd coupling κ_{AVV}, while both analyses are sensitive to the sign of the CP-even coupling parameter κ_{HVV} due to the interference of the SM and BSM CP-even couplings.

The shape-based analysis is over an order of magnitude less sensitive to the studied coupling parameters than the rate-based analysis since the rate information is much more sensitive to the presence of BSM coupling parameters. Since both measurements are dominated by statistical uncertainties, their sensitivity improves with the integrated

Table 5.18: Comparison of observed and expected 95 % confidence intervals for CP-even and CP-odd BSM couplings $c_\alpha\widetilde{\kappa}_{\mathrm{HVV}}$ and $s_\alpha\widetilde{\kappa}_{\mathrm{AVV}}$ at the XVV interaction vertex from the shape- and rate-based tensor structure measurements in the $H \to ZZ^* \to 4\ell$ channel with Run-1 and Run-2 data, respectively. In the rate-based analysis, the SM coupling parameters $c_\alpha\kappa_{\mathrm{Hgg}}$ and $c_\alpha\kappa_{\mathrm{SM}}$ are fixed to the SM expectation of 1.

Analysis type	BSM coupling	Fit configuration	95 % CL confidence interval Expected	Observed	Best-fit value Observed
Shape-based		$H \to ZZ^* \to 4\ell$ Run-1, 4.5 fb^{-1} and 20.3 at $\sqrt{s} = 7$ and 8 TeV			
	$\widetilde{\kappa}_{\mathrm{HVV}}/\kappa_{\mathrm{SM}}$		$[-\infty, -1.8] \cup [-0.85, \infty]$	$[-0.75, 2.45]$	-0.2
	$(\widetilde{\kappa}_{\mathrm{AVV}}/\kappa_{\mathrm{SM}}) \cdot \tan\alpha$		$[-5.7, 5.7]$	$[-2.85, 0.95]$	-0.8
Rate-based		$H \to ZZ^* \to 4\ell$ Run-2, 36.1 fb^{-1} at $\sqrt{s} = 13$ TeV			
	$c_\alpha\widetilde{\kappa}_{\mathrm{HVV}}$	$c_\alpha\kappa_{\mathrm{Hgg}} = 1$, $c_\alpha\kappa_{\mathrm{SM}} = 1$	$[-0.18, 0.20]$	$[0.05, 0.28]$	0.18
	$s_\alpha\widetilde{\kappa}_{\mathrm{AVV}}$	$c_\alpha\kappa_{\mathrm{Hgg}} = 1$, $c_\alpha\kappa_{\mathrm{SM}} = 1$	$[-0.22, 0.22]$	$[-0.32, 0.32]$	± 0.18

luminosity L by a factor $\sqrt{L}$ and the number of signal and background events in Run-2 data increases by a factor of two compared to Run-1. Even if the size of the analysed data set and the number of selected signal and background events would be the same for both analysis approaches, the shape-based sensitivity is still one order of magnitude worse than in the rate-based analysis. The disadvantage in using the rate information is, however, the loss of the direct sensitivity to CP violation since the CP-even contributions are always present in the total rate and a purely CP-odd sensitive discriminant cannot be defined anymore. The two approaches are therefore complementary: once a deviation from the SM has been found in the rate-based analysis, a shape-based analysis can be employed to identify more precisely the exact source of deviation and probe for the CP violation in the Higgs sector.

5.3.2 Other measurements

Other measurements studying the CP-structure of Higgs boson XVV interactions have been conducted assuming that it is a spin zero particle: the CMS collaborations published several studies with $H \to ZZ^* \to 4\ell$ and $H \to WW^* \to \ell\nu\ell\nu$ final states [16, 53–55], and the ATLAS collaboration studied the XVV structure in the VBF Higgs boson production reconstructing the Higgs boson in $H \to \tau\tau$ decays [168]. The Xgg interaction vertex has only been studied in the rate-based analysis presented within

this thesis. All Higgs boson tensor structure measurements are in agreement with the SM expectation.

The results of the tensor structure analysis in $H \to \tau\tau$ decays by ATLAS are formulated in an effective field theory framework using a similar strategy as the shape-based analysis to constrain CP violating admixtures to the XVV interaction vertex in VBF production. A CP-sensitive discriminating variable based on the kinematic properties of the dijet system in VBF production has been constructed using the matrix element method. No rate information has been employed. Deviations from the SM are parametrised with the parameter $\tilde{d} = -(\widetilde{\kappa}_{\mathrm{AVV}}/\kappa_{\mathrm{SM}}) \cdot \tan\alpha$, which is zero in the SM and non-zero in the case of CP violation [168]. So far only $20.3\,\mathrm{fb}^{-1}$ of data at $\sqrt{s} = 8$ TeV have been analysed which is not yet enough to obtain 95 % CL intervals. Therefore the analysis results are not used in the comparison. The 68 % CL interval, $\tilde{d} \in [-0.11, 0.05]$, is, however, a factor of ten better than the one of the shape-based and similar to the results from the rate-based measurement.

Eleven anomalous coupling parameters contributing to the XVV interaction vertex have been constrained by the CMS experiment based on $H \to ZZ^* \to 4\ell$ and $H \to WW^* \to \ell\nu\ell\nu$ events from the Run-1 data set [16]. The CMS results for parameters studied in this thesis ($c_\alpha\widetilde{\kappa}_{\mathrm{HVV}}$ and $s_\alpha\widetilde{\kappa}_{\mathrm{AVV}}$) have been superseded by new measurements based on the combined Run-1 and Run-2 data using only $H \to ZZ^* \to 4\ell$ decays [53].
The CMS strategy is similar to the one used in the shape-based analysis: a three dimensional matrix element based discriminant is constructed for each coupling parameter, where one discriminating variable suppresses the dominant ZZ^* background and the other two are sensitive to the magnitude of the BSM coupling parameter and its interference with the SM CP-even coupling, respectively. With the larger Run-2 data set a separate analysis of Higgs boson production via VBF and VH was possible. Therefore the Higgs boson events recorded in 2016 have been categorised into a VBF-enriched category, a $V(\to qq)H$-enriched category and an *untagged category* for the rest. The Run-1 data and the data collected in 2015 have been assigned to the untagged category. The CP-sensitive discriminants in the VBF and the $V(\to qq)H$-enriched categories have been constructed using the full kinematic information of the Higgs boson decay products and the two-tagging jets from the production process. The CP-sensitive discriminants in the untagged category use only the four-lepton kinematics. In the previous CMS publication [16], a two-dimensional analysis has been performed for the CP-even and CP-odd BSM coupling parameters, while the most-recent measurement

probed one coupling at a time. The ratio of observed rate and the corresponding SM expectation is parametrised with a set of signal strength parameters, that are left free in the fit: for the 2016 data μ_V is used for VBF and VH production and μ_F for all other production modes, while $\mu_{7\,\text{TeV}}$, $\mu_{8\,\text{TeV}}$ and $\mu_{13\,\text{TeV}}$ are the additional multiplicative signal strength parameters for data sets recorded in 2011, 2012 and 2015, respectively. The BSM coupling parameters are introduced within the framework of anomalous couplings [50], described in Section 1.4.2, where the most general amplitudes compatible with Lorentz and gauge invariance are written down. Under the assumption of real and constant anomalous couplings, the parameters can be translated into the Higgs characterisation framework formalism. The translation is given in Equations 1.43 and 1.44.

In Table 5.19 the expected and observed confidence interval at 95 % CL for BSM CP-even and CP-odd parameters in the XVV interaction vertex are shown as obtained by the CMS collaboration using the $H \to ZZ^* \to 4\ell$ decay channel in a combined Run-1 and Run-2 data set with 5.1 fb^{-1}, 19.7 fb^{-1} and 38.6 fb^{-1} recorded at $\sqrt{s} = 7$, 8 and 13 TeV, respectively [53]. The measurements presented within this thesis are reported in the same table. The nomenclature with coupling parameters of the shape-based analysis is used.

The comparison is only approximate due to the reasons mentioned in the previous section: the results of the rate-based analysis are not reported in terms of the ratios between the BSM and SM coupling parameters; data sets of different sizes at different centre-of-mass energies are analysed and different assumptions are made on the SM coupling parameters. The results with SM coupling parameter fixed to the SM expectation of 1 are shown for the rate-based analysis. The expected constraints are obtained with SM Asimov data sets with nominal values in case of the rate-based analysis, and, different to the setup of the previous comparison, with the signal strengths measured in data and assuming best-fit values for all other nuisance parameters for the shape-based analysis. No information about the SM Asimov data set is available for the CMS measurement.

The rate-based analysis yields the strongest constraints on BSM coupling parameters, while the sensitivity of the CMS measurement is similar to the sensitivity of the shape-based analysis. Due to the larger analysed data set and the use of the jet information from the VBF and VH production processes, the expected constraints of the CMS measurement are tighter by a factor 1.5 to 5 to the ones of the ATLAS shape-based analysis.

Table 5.19: Expected and observed best-fit values and confidence intervals at 95 % CL for CP-even $\widetilde{\kappa}_{\mathrm{HVV}}/\kappa_{\mathrm{SM}}$ and CP-odd $(\widetilde{\kappa}_{\mathrm{AVV}}/\kappa_{\mathrm{SM}}) \cdot \tan\alpha$ BSM coupling parameters from the CMS $H \to ZZ^* \to 4\ell$ analysis of Run-1 and Run-2 data sets of $5.1\,\mathrm{fb}^{-1}$, $19.7\,\mathrm{fb}^{-1}$ and $38.6\,\mathrm{fb}^{-1}$ at $\sqrt{s} = 7$, 8 and 13 TeV and from the ATLAS shape-based analysis of $H \to ZZ^* \to 4\ell$ and $H \to WW^* \to e\nu\mu\nu$ decays using $20.3\,\mathrm{fb}^{-1}$ of data at $\sqrt{s} = 8$ TeV and, in the case of the four-lepton channel, of additional $4.5\,\mathrm{fb}^{-1}$ of data at $\sqrt{s} = 7$ TeV. The ATLAS rate-based measurement of $c_\alpha\widetilde{\kappa}_{\mathrm{HVV}}$ (CP-even) and $s_\alpha\kappa_{\mathrm{AVV}}$ (CP-odd) BSM couplings is based on $36.1\,\mathrm{fb}^{-1}$ recorded at $\sqrt{s} = 13$ TeV. The SM expectation is obtained from an Asimov data set for best-fit values for the signal-strength $\widehat{\mu}$ and the nuisance parameters in the case of the shape-based analysis. For the rate-based analysis nominal values of the nuisance parameters have been assumed.

	Coupling	Fit configuration	95 % CL confidence interval Expected	Observed	Observed Best-fit value
Shape-based	ATLAS, $H \to ZZ^* \to 4\ell$ and $H \to WW^* \to e\nu\mu\nu$ combined				
	Run-1, $4.5\,\mathrm{fb}^{-1}$ and $20.3\,\mathrm{fb}^{-1}$ at $\sqrt{s} = 7$ and 8 TeV				
	$\widetilde{\kappa}_{\mathrm{HVV}}/\kappa_{\mathrm{SM}}$		$[-0.55, 4.80]$	$[-0.73, 0.63]$	-0.48
	$(\widetilde{\kappa}_{\mathrm{AVV}}/\kappa_{\mathrm{SM}}) \cdot \tan\alpha$		$[-2.33, 2.30]$	$[-2.18, 0.83]$	-0.68
Rate-based	ATLAS, $H \to ZZ^* \to 4\ell$				
	Run-2, $36.1\,\mathrm{fb}^{-1}$ at $\sqrt{s} = 13$ TeV				
	$c_\alpha\widetilde{\kappa}_{\mathrm{HVV}}$	$c_\alpha\kappa_{\mathrm{Hgg}} = 1$, $c_\alpha\kappa_{\mathrm{SM}} = 1$	$[-0.18, 0.20]$	$[0.05, 0.28]$	0.18
	$s_\alpha\widetilde{\kappa}_{\mathrm{AVV}}$	$c_\alpha\kappa_{\mathrm{Hgg}} = 1$, $c_\alpha\kappa_{\mathrm{SM}} = 1$	$[-0.22, 0.22]$	$[-0.32, 0.32]$	± 0.18
	CMS, $H \to ZZ^* \to 4\ell$				
	Run-1 and Run-2, $5.1\,\mathrm{fb}^{-1}$, $19.7\,\mathrm{fb}^{-1}$ and $38.6\,\mathrm{fb}^{-1}$ at $\sqrt{s} = 7$, 8 and 13 TeV				
	$\widetilde{\kappa}_{\mathrm{HVV}}/\kappa_{\mathrm{SM}}$		$[-0.42, 0.81]$	$[-0.34, 1.45]$	0.17
	$(\widetilde{\kappa}_{\mathrm{AVV}}/\kappa_{\mathrm{SM}}) \cdot \tan\alpha$		$[-1.48, 1.48]$	$[-2.00, 2.36]$	0.00

5.4 Outlook

In this thesis, it has been shown, that the combination of the CP-sensitive rate- and shape information increases the sensitivity by more than an order of magnitude compared to a purely shape-based method. Both approaches are complementary and it is important to pursue both: CP violation due to the presence of CP-odd Higgs couplings can only be probed with a shape-based analysis, while the rate-based approach provides a much stronger sensitivity for both CP-even and CP-odd BSM

coupling admixtures.

The SM and BSM Higgs boson couplings can have opposing effects on both event rates and shapes of distributions of kinematic variables. Thus, it is desirable for both approaches to combine the information sensitive to SM-like and to BSM (CP-even and CP-odd) couplings in a multi-dimensional fit with one or more couplings as free parameters. The morphing method has been specifically developed to model signal expectations in such a multi-dimensional parameter space.

There are two classes of differential distributions sensitive to the CP-structure of the Higgs to vector boson interaction vertex (see [29], Section 11):

1. Decay system:
    - Invariant masses and angular distributions of the Higgs boson decay, here into four leptons.
2. Production system:
    - The invariant mass m_{VH} in VH associated Higgs boson production [169],
    - the angular correlation and p_{T}^{j1} between the two tagging jets in VBF production [170–173], and
    - the Higgs boson transverse momentum p_{T}^{H}.

In the $H \to ZZ^* \to 4\ell$ channel, so far only shape information from the decay products has been used. The sensitivity can be increased by adding production system information. With increasing integrated luminosity, the differential distributions from the production system become usable. One of the interesting additional variables is the azimuthal angular distance $\Delta\phi_{\mathrm{jj}}^{\mathrm{sign}}$ between the two leading jets j_1 and j_2 from VBF production defined depending on the pseudorapidity of the jets:

$$\Delta\phi_{\mathrm{jj}}^{\mathrm{sign}} = \begin{cases} \phi^{j_1} - \phi^{j_2}, & \text{if } \eta^{j_1} > \eta^{j_2}, \\ \phi^{j_2} - \phi^{j_1}, & \text{if } \eta^{j_2} > \eta^{j_1}. \end{cases} \tag{5.30}$$

As can be seen in Figure 5.32, the $\Delta\phi_{\mathrm{jj}}^{\mathrm{sign}}$, unlike the rate information used so far, is sensitive to the sign of the CP-odd coupling parameter.

The CP-sensitive discriminants from the production and the decay system can be exploited individually or combined in a multivariate analysis by means of the matrix

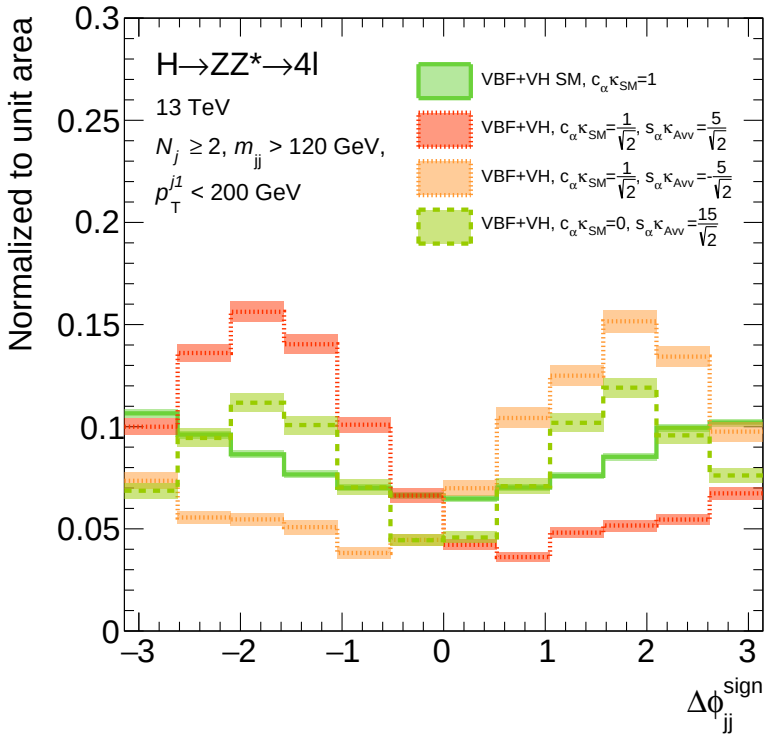

Figure 5.32: The normalised distribution of the azimuthal difference $\Delta\phi_{jj}^{sign}$ of the two tagging jets in VBF Higgs boson production for the SM (light green), BSM with CP-odd coupling parameter (black-green) and two mixtures of SM and BSM with positive (dashed green) and negative (dashed dark green) BSM CP-odd coupling parameter in the four-lepton decay channel with at least two additional jets with an invariant mass above 120 GeV and with leading jet below 200 GeV.

element method. The ATLAS search for CP-odd coupling admixtures in Higgs boson decays into τ lepton pairs [168] has shown that a matrix-element based multivariate discriminant provides higher sensitivity compared to only the $\Delta\phi_{jj}^{sign}$ discriminant. In the rate-based analyses of VBF, VH and ggF production in the $H \to ZZ^* \to 4\ell$ decay channel, only transverse momenta of the Higgs boson candidate and of the jets from the production have been used so far in addition to the rate information. The sensitivity can be improved by adding additional CP-sensitive discriminants such as $\Delta\phi_{jj}^{sign}$, which can also be applied for ggF +2 jets production [174], or a multivariate matrix-element observable using both decay and production system information for both production modes simultaneously.

Chapter 6

Methods for signal modelling

For the analysis in this thesis it is necessary to model the absolute and differential cross section in kinematic variables of the final state of both the SM and the BSM signal as a function of the interesting parameters. It is not feasible to continuously map the parameter space by Monte Carlo simulation due to finite computing time. Therefore, alternative methods are needed. Two different methods are used for the tensor structure analyses described in Chapter 4. The first method, the *matrix element reweighting* method, is well established. While this method is adequate for the shape-based analysis, the simultaneous modelling of the rate and shape information in kinematic variables as a function of BSM parameters required for the rate-based analysis made it necessary to develop a novel technique, the so-called *matrix element morphing* method. It has been developed within the work presented in this thesis and in cooperation with other groups. Both methods are discussed and compared in the following.

6.1 Matrix element reweighting

A Monte Carlo event sample for a certain parameter configuration, the *reference sample*, is reweighted to represent another *target* parameter configuration. The weights w are calculated and applied on an event-by-event basis as the ratio of the matrix elements for the event generation discussed in Section 2.3.6.

$$w\left(\overrightarrow{p^{\mu}}\right) = \frac{\mathrm{ME}_{\mathrm{target}}\left(\overrightarrow{p^{\mu}}\right)}{\mathrm{ME}_{\mathrm{reference}}\left(\overrightarrow{p^{\mu}}\right)}. \tag{6.1}$$

The kinematics of the event final state is represented by the vector $\overrightarrow{p^{\mu}}$ of the four-momenta of all final state particles. The method has to be validated. Large event weights indicate that the target phase space is not well represented by the reference sample. Large reference Monte Carlo statistics is required. The obtained signal model only describes one specific target parameter configuration. Target samples are produced for a whole grid of parameter configurations and interpolation methods are used between the grid points. The application of the method becomes difficult for multi-dimensional parameter spaces because too large reference sample Monte Carlo statistics would be needed to populate the reference parameter space with sufficient entries to prevent unreasonable large weights.

6.2 Matrix element morphing

Matrix element morphing [165] has been developed to create multi-dimensional parameter models and to simultaneously model rate and shape dependency on BSM coupling parameters. It is based on the assumption that a physical quantity T, which is a distribution or cross section, of a process is described by the squared process matrix element:

$$T(\vec{g}) \propto |\mathrm{ME}|^2 \quad \text{with} \quad \mathrm{ME} = \sum_{i}^{K} g_i \cdot \mathrm{ME}_i, \tag{6.2}$$

with the coupling strength vector $\vec{g} = \vec{g_i}, .., \vec{g_K}$. The squared matrix element is a sum of N individual components weighted with a polynomial of coupling parameters. The assumption of the morphing method is that T with arbitrary *target* coupling configuration can be described as a weighted sum of N inputs:

$$T_{\mathrm{target}}(\vec{g}) = \sum_{j=1}^{N} w_j(\vec{g}) \cdot T_{j,\mathrm{input}}. \tag{6.3}$$

Each input T_j is weighted with a function $w_j(\vec{g})$ that is a polynomial in coupling parameters and has the same structure as $|\mathrm{ME}|^2$. The morphing method is only applicable in use-cases where the matrix element can be decomposed into a sum of different components. It is for instance not suited to model a distribution as a function of a particle mass. The method is first described with a simple example, followed by a discussion of challenges and number of morphing inputs needed for the rate-based analysis. A general description of the morphing method in multi-dimensional parameter

space can be found in Appendix B.

6.2.1 Example

The method will be explained step-by-step with a simple example. There is one interaction vertex with contributions from two coupling parameters, see Figure 6.1, where one coupling parameter g_{SM} is SM-like and the other one g_{BSM} is a BSM coupling parameter.

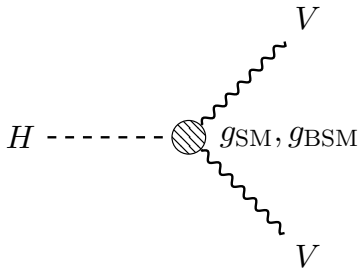

Figure 6.1: A three-particle interaction Feynman diagram with contributions from two coupling parameters, a SM (g_{SM}) and a BSM one (g_{BSM}).

The matrix element describing this interaction is the sum of both contributions:

$$\text{ME}_{\text{SM,BSM}}(g_{\text{SM}}, g_{\text{BSM}}) = g_{\text{SM}} \cdot \text{ME}_{\text{SM}} + g_{\text{BSM}} \cdot \text{ME}_{\text{BSM}} \tag{6.4}$$

Any physical quantity $T(g_{\text{SM}}, g_{\text{BSM}})$ is proportional to the squared matrix element:

$$\begin{aligned} &T(g_{\text{SM}}, g_{\text{BSM}}) \propto |\text{ME}_{\text{SM,BSM}}(g_{\text{SM}}, g_{\text{BSM}})|^2 \\ &= g_{\text{SM}}^2 \cdot |\text{ME}_{\text{SM}}|^2 + g_{\text{SM}} \cdot g_{\text{BSM}} \cdot 2\,\text{Re}\,[\text{ME}_{\text{SM}}^* \cdot \text{ME}_{\text{BSM}}] + g_{\text{BSM}}^2 \cdot |\text{ME}_{\text{BSM}}|^2, \end{aligned} \tag{6.5}$$

with the interference term $2\,\text{Re}\,[\text{ME}_{\text{SM}}^* \cdot \text{ME}_{\text{BSM}}]$. The squared matrix element has three individual components ($|\text{ME}_{\text{SM}}|^2$, $2\,\text{Re}\,[\text{ME}_{\text{SM}}^* \cdot \text{ME}_{\text{BSM}}]$ and $|\text{ME}_{\text{BSM}}|^2$), each is weighted by a polynomial of coupling parameters (g_{SM}^2, $g_{\text{SM}} \cdot g_{\text{BSM}}$ and g_{BSM}^2).

Let's assume the following three Monte Carlo samples have been generated:

1. T_1 with $(g_{\text{SM}}, g_{\text{BSM}}) = (1, 0)$
2. T_2 with $(g_{\text{SM}}, g_{\text{BSM}}) = (1, 1)$

3. T_3 with $(g_{\mathrm{SM}}, g_{\mathrm{BSM}}) = (0, 1)$

Each one is satisfying Equation 6.5:

$$T_1 \propto \mathbf{1} \cdot |\mathrm{ME}_{\mathrm{SM}}|^2 + \mathbf{0} \cdot 2\,\mathrm{Re}\,[\mathrm{ME}^*_{\mathrm{SM}} \cdot \mathrm{ME}_{\mathrm{BSM}}] + \mathbf{0} \cdot |\mathrm{ME}_{\mathrm{BSM}}|^2 \tag{6.6}$$

$$T_2 \propto \mathbf{1} \cdot |\mathrm{ME}_{\mathrm{SM}}|^2 + \mathbf{1} \cdot 2\,\mathrm{Re}\,[\mathrm{ME}^*_{\mathrm{SM}} \cdot \mathrm{ME}_{\mathrm{BSM}}] + \mathbf{1} \cdot |\mathrm{ME}_{\mathrm{BSM}}|^2 \tag{6.7}$$

$$T_3 \propto \mathbf{0} \cdot |\mathrm{ME}_{\mathrm{SM}}|^2 + \mathbf{0} \cdot 2\,\mathrm{Re}\,[\mathrm{ME}^*_{\mathrm{SM}} \cdot \mathrm{ME}_{\mathrm{BSM}}] + \mathbf{1} \cdot |\mathrm{ME}_{\mathrm{BSM}}|^2, \tag{6.8}$$

The above equations span a linear system of equations and can equally be formulated in matrix notation:

$$\underbrace{\begin{pmatrix} T_1 \\ T_2 \\ T_3 \end{pmatrix}}_{\vec{T}} \propto \underbrace{\begin{pmatrix} 1 & 0 & 0 \\ 1 & 1 & 1 \\ 0 & 0 & 1 \end{pmatrix}}_{\mathbb{M}} \cdot \underbrace{\begin{pmatrix} |\mathrm{ME}_{\mathrm{SM}}|^2 \\ 2\,\mathrm{Re}\,[\mathrm{ME}^*_{\mathrm{SM}} \cdot \mathrm{ME}_{\mathrm{BSM}}] \\ |\mathrm{ME}_{\mathrm{BSM}}|^2 \end{pmatrix}}_{\vec{M}} \tag{6.9}$$

with the *morphing matrix* $\mathbb{M}$, the vector of inputs $\vec{T}$ and the vector of the components of the squared matrix element $\vec{M}$.

If the morphing matrix is invertible, the matrix element components can be described as a function of the inputs, by multiplying the *inverted morphing matrix* $\mathbb{M}^{-1}$ to Equation 6.9:

$$\vec{M} \propto \mathbb{M}^{-1} \cdot \vec{T} \qquad \text{with} \qquad \mathbb{M}^{-1} = \begin{pmatrix} 1 & 0 & 0 \\ -1 & 1 & -1 \\ 0 & 0 & 1 \end{pmatrix} \tag{6.10}$$

T, with an arbitrary coupling parameter configuration, can be described as a weighted

sum of the three inputs by inserting Equation 6.10 into Equation 6.5:

$$
\begin{aligned}
T(g_{\mathrm{SM}}, g_{\mathrm{BSM}}) &= \sum_{j=1}^{3} w_j(\vec{g}) \cdot T_j \\
&= \begin{pmatrix} g_{\mathrm{SM}}^2 & g_{\mathrm{SM}} \cdot g_{\mathrm{BSM}} & g_{\mathrm{BSM}}^2 \end{pmatrix} \cdot \begin{pmatrix} 1 & 0 & 0 \\ -1 & 1 & -1 \\ 0 & 0 & 1 \end{pmatrix} \cdot \begin{pmatrix} T_1 \\ T_2 \\ T_3 \end{pmatrix} \\
&= (g_{\mathrm{SM}}^2 - g_{\mathrm{SM}} \cdot g_{\mathrm{BSM}}) \cdot T_1 + g_{\mathrm{SM}} \cdot g_{\mathrm{BSM}} \cdot T_2 + (g_{\mathrm{BSM}}^2 - g_{\mathrm{SM}} \cdot g_{\mathrm{BSM}}) \cdot T_3,
\end{aligned}
\tag{6.11}
$$

where the weight functions are polynomials in coupling parameters with constants given by the coefficients of the inverted morphing matrix:

$$w_1(g_{\mathrm{SM}}, g_{\mathrm{BSM}}) = \mathbf{1} \cdot g_{\mathrm{SM}}^2 - \mathbf{1} \cdot g_{\mathrm{SM}} \cdot g_{\mathrm{BSM}} + \mathbf{0} \cdot g_{\mathrm{BSM}}^2 \tag{6.12}$$

$$w_2(g_{\mathrm{SM}}, g_{\mathrm{BSM}}) = \mathbf{0} \cdot g_{\mathrm{SM}}^2 + \mathbf{1} \cdot g_{\mathrm{SM}} \cdot g_{\mathrm{BSM}} + \mathbf{0} \cdot g_{\mathrm{BSM}}^2 \tag{6.13}$$

$$w_3(g_{\mathrm{SM}}, g_{\mathrm{BSM}}) = \mathbf{0} \cdot g_{\mathrm{SM}}^2 - \mathbf{1} \cdot g_{\mathrm{SM}} \cdot g_{\mathrm{BSM}} + \mathbf{1} \cdot g_{\mathrm{BSM}}^2. \tag{6.14}$$

Equation 6.11 is the *morphing function* for variable T constructed with inputs $\vec{T}$. It should be noted that the only requirement for the choice of inputs is, that their corresponding morphing matrix is invertible. Other than that, they can be arbitrarily chosen.

6.2.2 Number of morphing inputs

The signal model for the rate-based tensor structure analysis in Section 5.2 is built with the morphing method. The usage of the method has been validated (see Appendix J). In the above simple example, only one interaction vertex and two coupling parameters were considered, while for the rate-based analysis two vertices are considered, a production and a decay one, with the contributions of at most three coupling parameters to each vertex. The generalisation of the morphing method with an arbitrary number of coupling parameters can be found in Appendix B.

The number N of morphing inputs depends on the number of coupling parameters in production and decay vertices:

- n_p **only** in the **production vertex**,
- n_d **only** in the **decay vertex**,
- and n_s **shared** by **both vertices**.

The general formula for $N(n_p, n_d, n_s)$ is [165]:

$$\begin{aligned} N(n_p, n_d, n_s) = & \binom{n_s+3}{4} \\ & + \binom{n_s+2}{3} \cdot \left[\binom{n_p}{1} + \binom{n_d}{1} \right] \\ & + \binom{n_s+1}{2} \cdot \left[\binom{n_p+1}{2} + \binom{n_p}{1} \cdot \binom{n_d}{1} + \binom{n_d+1}{2} \right] \\ & + \binom{n_p+1}{2} \cdot \binom{n_d+1}{2}. \end{aligned} \tag{6.15}$$

The number N of input samples for each BSM scenario are given in Table 6.1. The coupling parametrisation of the Higgs characterisation framework [30] is used.

The challenge of the method is to find an input set with sufficient statistical accuracy in the target phase space to prevent large weights and thus a large error. The statistical error for a specific input sample set can be computed as a function of the coupling parameters. It is increasing if the target coupling parameter configuration is not within the phase space grid spanned by the input samples, i.e. in case of extrapolation. Therefore, input samples with parameter configurations that include the interesting range have been generated. From the possible combinations of input sets, the ones with sufficiently small errors in the studied parameter range have been chosen (see Appendix J).

Table 6.1: The number of morphing input samples N for $pp \to H \to ZZ^*$ processes with additional BSM couplings described by the Higgs characterisation framework parameters in production and decay vertices. The ggF, VBF and VH productions are written as functions of BSM couplings. The SM coupling parameters $c_\alpha\kappa_{\text{SM}}$ or $c_\alpha\kappa_{\text{Hgg}}$ are omitted in the short notation. The number of couplings only in production (n_p) and only in decay vertices (n_d), as well as shared couplings in production and decay (n_s) are also listed.

Process	Production couplings	Decay couplings	n_p	n_d	n_s	N
ggF ($s_\alpha\kappa_{\text{Agg}}$)	$s_\alpha\kappa_{\text{Agg}}$, $c_\alpha\kappa_{\text{Hgg}}$	$c_\alpha\kappa_{\text{SM}}$	2	1	0	3
ggF ($s_\alpha\kappa_{\text{AVV}}$)	$c_\alpha\kappa_{\text{Hgg}}$	$c_\alpha\kappa_{\text{SM}}$, $s_\alpha\kappa_{\text{AVV}}$	1	2	0	3
ggF ($c_\alpha\kappa_{\text{HVV}}$,$s_\alpha\kappa_{\text{AVV}}$)	$c_\alpha\kappa_{\text{Hgg}}$	$c_\alpha\kappa_{\text{SM}}$, $c_\alpha\kappa_{\text{HVV}}$, $s_\alpha\kappa_{\text{AVV}}$	1	3	0	6
VBF/VH ($s_\alpha\kappa_{\text{AVV}}$)	$c_\alpha\kappa_{\text{SM}}$, $s_\alpha\kappa_{\text{AVV}}$	$c_\alpha\kappa_{\text{SM}}$, $s_\alpha\kappa_{\text{AVV}}$	0	0	2	5
VBF/VH ($c_\alpha\kappa_{\text{HVV}}$,$s_\alpha\kappa_{\text{AVV}}$)	$c_\alpha\kappa_{\text{SM}}$, $c_\alpha\kappa_{\text{HVV}}$, $s_\alpha\kappa_{\text{AVV}}$	$c_\alpha\kappa_{\text{SM}}$, $c_\alpha\kappa_{\text{HVV}}$, $s_\alpha\kappa_{\text{AVV}}$	0	0	3	15

6.3 Comparison of the methods

The reweighting method can only model the change of the distributions of kinematic variables, while the morphing method can model both CP-sensitive observables, rate and shape, simultaneously. With increasing number of coupling parameters, the matrix element reweighting method reaches its limit. The required statistics of the Monte Carlo reference sample needed to populate the whole multi-dimensional target parameter space becomes too large. The morphing method has been developed to overcome this limitation. For the morphing method it is essential to find an input sample with optimal statistical accuracy in the target space. When increasing the number of coupling parameters a combination of both methods could be beneficial: the number of inputs for the morphing method is increasing with the number of couplings, especially if couplings are shared between vertices. The morphing inputs could be generated by matrix element reweighting. While the signal model constructed with the morphing method is per se continuous in the coupling parameters, the matrix element reweighting is discrete and additional techniques have to be applied to generate a continuous model.

Summary

In 2012, the Standard Model (SM) of particle physics has been completed by the discovery of the Higgs boson in proton-proton collisions of the Large Hadron Collider (LHC). Since then, many measurements have been performed to probe the nature of the new boson by the ATLAS and CMS experiments. It was determined that the discovered boson is a scalar particle with a predominately CP-even quantum number. Small admixtures of CP-even and CP-odd components from beyond the Standard Model (BSM) physics, however, are not excluded. The latter case is especially interesting since it can lead to CP violation in the Higgs sector which may help understanding the matter-antimatter asymmetry in the universe.

In this thesis, the tensor structure of Higgs boson couplings to gauge bosons has been probed for the presence of additional, non-Standard Model couplings using two complementary approaches. The Higgs boson candidates are reconstructed in $H \to ZZ^* \to 4\ell$ ($\ell \equiv e\,\mu$) decays using data of the ATLAS detector at the LHC comprising the full LHC Run-1 data set at $\sqrt{s} = 7$ and 8 TeV from 2011 and 2012 with an integrated luminosity of $24.8\,\text{fb}^{-1}$ and the Run-2 data set of $36.1\,\text{fb}^{-1}$ from 2015 and 2016 collected at $\sqrt{s} = 13$ TeV.

Deviations of the Higgs boson couplings from the Standard Model predictions are parametrised within an effective field theory, the Higgs characterisation framework. Admixtures of CP-even (H) and CP-odd (A) BSM couplings $c_\alpha\kappa_{\text{HVV}}$ and $s_\alpha\kappa_{\text{AVV}}$ have been probed simultaneously in Higgs to weak gauge boson interactions, in particular HZZ^*. The mixing angle α describes the relative contributions of the two types of BSM couplings ($c_\alpha \equiv \cos\alpha$ and $s_\alpha \equiv \sin\alpha$). Additionally, CP violation in gluon fusion production induced by an additional CP-odd non-Standard Model coupling $s_\alpha\kappa_{\text{Agg}}$ has been studied.
In the first, shape-based analysis using the Run-1 data, the shape of CP-sensitive distributions of kinematic variables describing the decay final state are used. Multivariate discriminants based on the matrix element method are employed to distinguish

CP-even and CP-odd contributions. Constraints on the BSM coupling parameters $c_\alpha\kappa_{\mathrm{HVV}}$ and $s_\alpha\kappa_{\mathrm{AVV}}$ are derived separately. The results have been combined with a similar analysis of $H \to WW^* \to e\nu\mu\nu$ decays.
The second, rate-based approach uses the larger Run-2 data set. The dominant production rate information is combined with shape information from the final state to enhance the sensitivity to BSM contributions. Different production mechanisms are discriminated based on the final state topology. The VBF and VH production modes are especially sensitive to BSM contributions to the XVV interaction vertex ($X = H, A$ representing CP-even and CP-odd admixtures) which contributes to the initial and the final state in $H \to ZZ^* \to 4\ell$ decays such that the effects are proportional to κ^4_{BSM}. The other production modes, however, are only proportional to κ^2_{BSM}. In addition to the XVV interaction vertex, the effective Higgs to gluon interaction, Xgg, has been probed for the presence of CP-odd admixtures. The BSM coupling contribution to Xgg, $s_\alpha\kappa_{\mathrm{Agg}}$, has been probed independently, while $c_\alpha\kappa_{\mathrm{HVV}}$ and $s_\alpha\kappa_{\mathrm{AVV}}$ have been probed simultaneously for the XVV interaction vertex.

The results of the Higgs coupling tensor structure analyses are in agreement with the SM predictions. The rate-based approach for XVV couplings is more sensitive than the shape-based one leading to an order of magnitude tighter constraints on the BSM coupling parameters. Constraints on BSM XVV coupling parameters have also been obtained by other measurements of the ATLAS and CMS experiments using different parametrisations and data sets. The comparison of the 95 % confidence level (CL) intervals on the $c_\alpha\kappa_{\mathrm{HVV}}$ and $s_\alpha\kappa_{\mathrm{AVV}}$ coupling parameters shows that the ATLAS measurement of the VBF production with $H \to \tau\tau$ decays is least sensitive, while the sensitivities of the shape-based analysis and of the CMS combined Run-1 and Run-2 measurement using matrix element discriminants based on production and decay kinematic in four-lepton decays are similar. The strongest constraints on BSM contributions to the XVV interaction vertex have been obtained with the ATLAS rate-based method in this thesis: $-0.6 \leq c_\alpha\kappa_{\mathrm{HVV}} \leq 4.2$, $-4.4 \leq s_\alpha\kappa_{\mathrm{AVV}} \leq 4.4$ and $-0.68 \leq s_\alpha\kappa_{\mathrm{Agg}} \leq 0.68$ at 95 % CL. The presented analysis is the first one constraining CP-odd contributions to the ggF production.

Both, the rate- and shape-based methods must be considered in the future. CP violation in the Higgs sector can only be detected with the shape-based approach using final-state kinematic variables. The rate measurement is always affected by CP-even contributions. The distributions of the angle $\Delta\phi_{\mathrm{jj}}$ between the two tagging jets in VBF production and jet pairs from initial state gluon radiation in ggF production and the

angle ϕ between the two Z decay planes in the Higgs rest frame in $H \to ZZ^* \to 4\ell$ and $H \to WW^* \to \ell\nu\ell\nu$ decays are sensitive to CP-odd coupling admixtures and, therefore, CP violation. Discriminants sensitive to CP-odd contributions can be constructed with the matrix element method taking into account the interference of SM and CP-odd BSM contributions.

Appendix A

Statistical framework

In this appendix the concepts used for the statistical interpretation of the data in this thesis are explained.

In a physics analysis searching for new phenomena, the prediction of a theory is compared to data, i.e. the expectations from SM and BSM signal models and the corresponding background estimation are compared to the selected data. The outcome of the measurement is quantified in a statistical evaluation, that gives a measure of how well the theory describes the observed data, or, in case of more than one possible theories, which of them is in better agreement with the observation.
The theoretical prediction is represented by the signal model. The first part of this appendix will be dedicated to the building of a signal model, while the second part discusses tools for statistical interpretation.

The concepts of statistical evaluation at the LHC are described in [161]. A general overview about statistical interpretation in experimental physics can be found in [175].

Signal model

In Figure A.1, the discriminating variable Φ of a hypothetical physics analysis is shown. The aim is to test for deviations from the SM prediction.

The signal model is the combination of signal and background contributions, where the signal can either be SM- or BSM-like. It predicts $n_i^{\text{exp}}(\vec{\kappa}, \vec{\theta})$ events in bin i of the Φ distribution:

$$n_i^{\text{exp}}(\vec{\kappa}, \vec{\theta}) = s_i(\vec{\kappa}, \vec{\theta}) + b_i(\vec{\theta}). \tag{A.1}$$

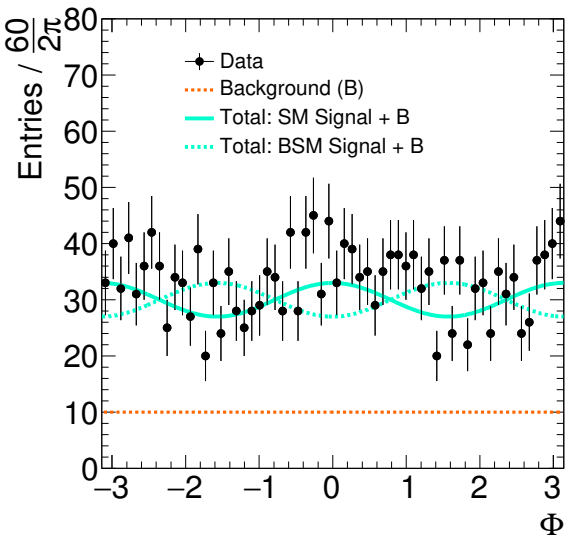

Figure A.1: Observed (black) and total expected events from background and SM signal (teal solid), or background and BSM signal (teal dashed) for a hypothetical analysis.

The predicted numbers s_i and b_i of signal and background events are given by the product of the respective cross section σ with the integrated luminosity L, and with efficiency factors covering selection efficiency and detector acceptance. The expected distribution depends on the set of coupling modification parameters $\vec{\kappa}$ describing the signal, which are zero in case of the SM, and on the set of additional parameters $\vec{\theta}$. The model parameters are divided into a subset of parameters that one wants to measure, the *parameters of interest*, e.g. $\vec{\kappa}$, and a subset of *nuisance parameters*, e.g. $\vec{\theta}$.

The probability to observe n_i events follows a Poisson distribution with mean $n_i^{\text{exp}}(\vec{\kappa}, \vec{\theta}) = s_i(\vec{\kappa}, \vec{\theta}) + b_i(\vec{\theta})$:

$$P\left(n_i | s_i(\vec{\kappa}, \vec{\theta}) + b_i(\vec{\theta})\right) = \exp\Big(-\left(s_i(\vec{\kappa}, \vec{\theta}) + b_i(\vec{\theta})\right)\Big) \cdot \frac{\left(s_i(\vec{\kappa}, \vec{\theta}) + b_i(\vec{\theta})\right)^{n_i}}{n_i!} \tag{A.2}$$

A Poisson distribution is asymmetric for small number of events and approaches a normal distribution for a large number.

The compatibility of the observed data to the model is retrieved with the *likelihood function*. It is assumed that the signal model truly describes the underlying physics process. The likelihood is then a measure that a manifestation of this model with n

observed events is realised in data. The likelihood function is the product over all bins of the discriminating variable distribution

$$\mathcal{L}(\vec{\kappa}, \vec{\theta}) = \prod_{i}^{N_{bins}} P(n_i | s_i(\vec{\kappa}, \vec{\theta}) + b_i(\vec{\theta})). \tag{A.3}$$

A Poisson probability density function is a function of n for a given fixed set of parameters. The likelihood on the other hand is a function of the parameters for a given number of events n. Moreover, the likelihood is not normalised.

The nuisance parameters include the description of deviations from the expectation due to systematic uncertainties ${\theta_m}^{(\text{syst.})}$ in the theoretical predictions and due to detector performance, which is derived from auxiliary measurements. These dedicated studies provide the $\pm 1\sigma$ variations from the nominal prediction of $\vec{\theta}$. This input is translated into constraint terms $A({\theta}^{(\text{syst.})})$ for the nuisance parameters $\vec{\theta}\,(\text{syst.}) = ({\theta_1}^{(\text{syst.})}, .., {\theta_m}^{(\text{syst.})})$, which are multiplied to the likelihood function:

$$\mathcal{L}(\vec{\kappa}, \vec{\theta}) = \prod_{i}^{N_{bins}} P(n_i | s_i(\vec{\kappa}, \vec{\theta}) + b_i(\vec{\theta})) \times \prod_{m}^{N_{nuisance}} A_m({\theta_m}^{(\text{syst.})}) \tag{A.4}$$

Gaussian, Gamma or Log-normal constraints are used depending on the type of systematic uncertainty [176]. In the tensor structure measurements described in Sections 5.1 and 5.2 only Gaussian constraints are employed. It should be noted, that the inclusion of systematic uncertainties is reducing the sensitivity of the measurement, i.e. a larger number of model parameters comes along with information loss.

A binned maximum likelihood fit of the expected signal model distributions to the data is performed by varying of the parameters of interest, $\vec{\kappa}$, in order to extract the values for which the model and the matches the best, i.e. the data has the highest likelihood. The value of parameters maximising the likelihood is called the maximum likelihood estimators.

Interpretation

At the LHC, the search for new phenomena indicating physics beyond the SM is done within the context of a frequentist statistical test [161]. For simplicity, it is assumed that either one or two parameters of interest are probed.

To test the reliability of the measurement, intervals at a certain *confidence level* (CL) are constructed around the maximum-likelihood estimator of the parameter of interest, $\widehat{\kappa}$. If the measurement would be repeated an infinite number of times, and each time a confidence interval is computed, then the fraction of intervals containing the true value of the parameter of interest matches the confidence level. The confidence level is set by the experimentalist, 68 % and 95 % CL intervals are reported in this thesis. The values of κ outside of the interval are said to be excluded at the confidence level.

The data analysis is simplified by using a test statistic, which quantifies the amount of agreement of the data and the model to one representative value. Depending on the physics case different choices of test statistic are available [161]. In this thesis a profiled likelihood ratio t is employed [161]:

$$t_\kappa = -2 \ln \lambda(\kappa) \quad \text{with} \quad \lambda(\kappa) = \frac{\mathcal{L}(\kappa, \hat{\hat{\vec{\theta}}})}{\mathcal{L}(\widehat{\kappa}, \widehat{\vec{\theta}})} \tag{A.5}$$

where $\hat{\hat{\vec{\theta}}}$ denotes the value of $\vec{\theta}$ that maximises the likelihood function for a fixed value of κ. The denominator $\mathcal{L}(\widehat{\kappa}, \widehat{\vec{\theta}})$ is the maximised (unconditional) likelihood function, where $\widehat{\kappa}$ and $\widehat{\vec{\theta}}$ are the maximum-likelihood (ML) estimators. The numerator $\mathcal{L}(\kappa, \hat{\hat{\vec{\theta}}})$ is the conditional ML estimator, where the likelihood is maximised for specific values of κ.

The likelihood ratio, i.e. $\lambda(\kappa)$, assumes values within $]0, 1]$, where values near 1 indicate good agreement with the data, and increasing discrepancy is given for values $\lambda(\kappa) \to 0$. This translates into a parameter interval of $t \in]\infty, 0]$ (see Figure A.2), where incompatibility with the data is given by increasing values of t, i.e. $t \to \infty$. The probability p of observing a value of the test statistic that is equal or larger than a certain threshold $t_{\kappa,p}$ is given by

$$p = \int_{t_{\kappa,p}}^{\infty} f(t_\kappa|\kappa) \, \mathrm{d}t_\kappa \,, \tag{A.6}$$

where $f(t_\kappa|\kappa)$ is the probability density function of t_κ under the assumption of κ. It is illustrated in Figure A.3 (left). The level of discrepancy can be quantified with $p = (1 - \mathrm{CL})$, i.e. $p = 0.05$ ($p = 0.32$) when testing for 95 % CL (68 % CL). Assuming $f(t_\kappa|\kappa)$ is known, confidence level intervals can be constructed for the parameter of

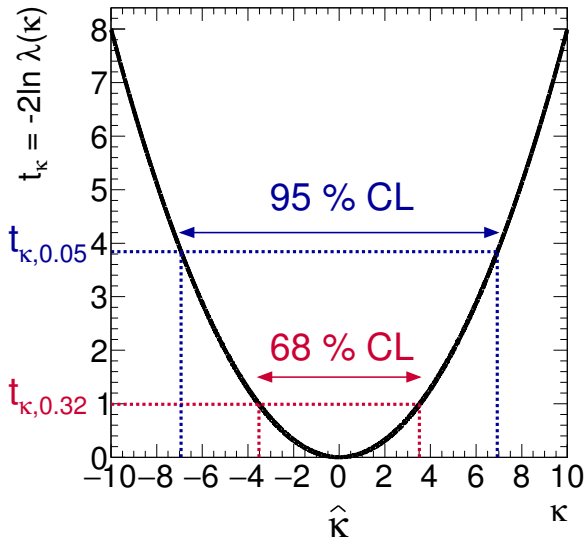

Figure A.2: The distribution of the profiled likelihood test statistic $t_\kappa = -2\ln\kappa(\lambda)$ in dependence of the parameter of interest κ.

interest. In Figure A.2, the 68 % CL and and 95 % CL intervals containing the ML estimator $\widehat{\kappa}$ are shown. The intervals are computed using the asymptotic approximation for $f(t_\kappa|\kappa)$ described below.

If the best-fit values are different from the SM expectation, it is of interest to quantify the discrepancy. This is done by converting the p-value at the SM point into an equivalent significance Z. It is defined such that the probability to find a Gaussian distributed variable within $\pm Z\,\sigma$ is $1-p$ [1]:

$$Z = \Phi^{-1}\left(1-\frac{p}{2}\right). \tag{A.7}$$

where Φ^{-1} is the quantile (inverse of the cumulative distribution) of a normal distribution, see Figure A.3 (right). Signal evidence is defined by $Z = 3$, discovery by $Z = 5$.

The probability density function of the test statistic has to be known for the statistical evaluation. Retrieving the probability density function from Monte Carlo simulation is computationally very expensive, therefore the asymptotic approximation which is

[1] for the Higgs discovery a one-sided definition was used [161], where a $5\,\sigma$ significance corresponds to $p = 2.87\cdot10^{-7}$, while in the two-sided definition used within this thesis this corresponds to $5.7\cdot10^{-7}$.

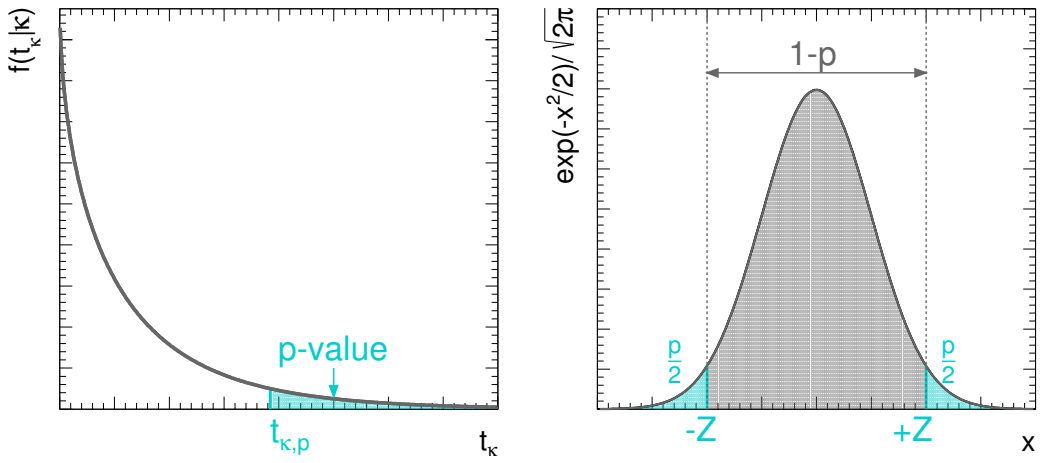

Figure A.3: Illustration of the p-value definition using the probability density distribution of the profiled likelihood ratio test statistic $t_{\vec{\kappa}} = 2 \ln \lambda(\vec{\kappa})$ in dependence on $t_{\vec{\kappa}}$ (left) and conversion of the p-value to the equivalent significance using a two-sided fluctuation of a normal distributed variable (right).

valid in the large sample limit is often used. Based on an approximation by Wilks and Wald [162, 163], it has been shown that $f(t_{\vec{\kappa}}|\vec{\kappa})$ follows a Chi-squared distribution with the number of degrees of freedom equal to the number of parameters of interest [161]. In this thesis, either one or two parameter of interest are measured. In the latter case, the likelihood function is two-dimensional, CL contours are retrieved instead of intervals. In Figure A.4 the Chi-squared distribution for one and two degrees of freedom is shown. The value $t_{\vec{\kappa},p}$ of the test statistic corresponding to a certain p-value, can be retrieved by integrating the Chi-squared distribution. In case of one parameter of interest, 68 % (95 %) of all values of t_κ are below 0.99 (3.84). Therefore, 68 % and 95 % CL intervals can be obtained in the asymptotic approximation by requiring a maximum value of the test statistic of $t_{\vec{\kappa},0.32} = 0.99$ and $t_{\vec{\kappa},0.05} = 3.84$, see Figure A.2. In case of two parameter of interest, 68 % and 95 % CL contours are determined at $t_{\vec{\kappa},0.32} = 2.28$ and $t_{\vec{\kappa},0.05} = 5.99$ as obtained by integrating the Chi-squared distribution with two degrees of freedom. The values of $t_{\vec{\kappa},p}$ in the asymptotic approximation for the calculation of 68 % and 95 % CL regions in case of one and two parameter of interest are summarised in Table A.1.

Before the start of an experiment, it is important to evaluate if it is actually sensitive

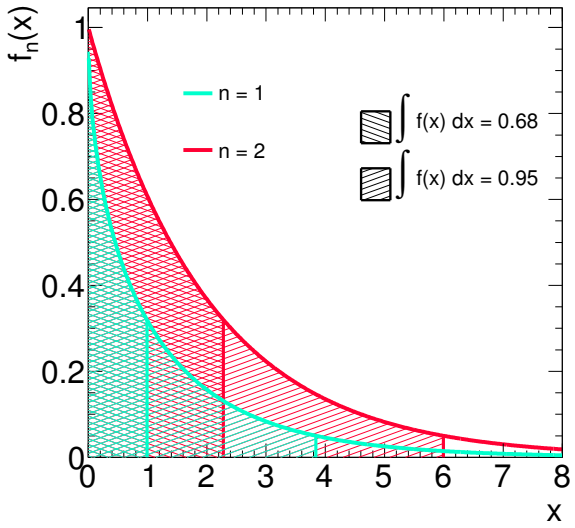

Figure A.4: The Chi-squared $f_n(x)$ distribution with n degrees of freedom.

Table A.1: Upper value $t_{\vec{\kappa},0.32}$ ($t_{\vec{\kappa},0.05}$) of the integral starting from zero of a Chi-squared distribution with n_{POI} degrees of freedom covering 68 % (95 %) of all values.

n_{POI}	68 % CL	95 % CL
	$t_{\vec{\kappa},0.32}$	$t_{\vec{\kappa},0.05}$
1	0.99	3.84
2	2.28	5.99

enough to achieve a given physics goal. For example, before the start of the LHC, it had to be proven that a Higgs boson discovery is possible, otherwise an investment in the experiment would have been difficult to defend.

To estimate the expected sensitivity of an experiment toy data is needed. Toy data can be generated by repeating Monte Carlo simulations many times, but this is computational-wise very expensive, therefore a single simulation is chosen instead as reference data. This single simulation is called *Asimov data set* [161]. The statistical evaluation of a measurement is performed with this data to estimate the expected sensitivity.

Asimov data sets are also often used in ATLAS and CMS analyses, which are usually blinded to keep the analysers unbiased. The analysis is not evaluated on data before it has been shown that everything is well understood.

Appendix B

Morphing method: General multi-dimensional description

In this appendix, the morphing method is formulated in case of two vertices with contributions from an arbitrary number of coupling parameters.

The matrix element of a process with N_v vertices with N_{v_i} individual matrix element components ME_j with coupling strength g_j per vertex i, is the product over all vertices:

$$\mathrm{ME}(\vec{g}) = \prod_{i=1}^{N_v} \left(\sum_{j=1}^{N_{v_i}} g_j \cdot \mathrm{ME}_j \right). \tag{B.1}$$

A matrix element contributing to one vertex can also appear in other vertices. The morphing function describing a distribution or variable $T \propto |\mathrm{ME}|^2$ can be constructed for this general case and can be found in [165].
In this section, the most common use-case with two vertices $N_v = 2$, e.g. one production and one decay vertex, with an arbitrary number of couplings per vertex is described by

$$\mathrm{ME}(\vec{g}) = \underbrace{\left(\sum_{i=1}^{N_p} g_i \cdot \mathrm{ME}_i \right)}_{\text{Production}} \cdot \underbrace{\left(\sum_{j=1}^{N_d} g_j \cdot \mathrm{ME}_j \right)}_{\text{Decay}}, \tag{B.2}$$

with N_p components in the production vertex, and with N_d ones in the decay. Matrix elements can be shared in production and decay. Any physical quantity describing this

process is proportional to it's squared matrix element:

$$T(\vec{g}) \propto |\mathrm{ME}|^2(\vec{g}) = \left[\left(\sum_{i=1}^{N_p} g_i \cdot \mathrm{ME}_i \right) \cdot \left(\sum_{j=1}^{N_d} g_j \cdot \mathrm{ME}_j \right) \right]^2 = \vec{G}^T(\vec{g}) \cdot \vec{M}, \tag{B.3}$$

where $\vec{g}^T = \begin{pmatrix} g_1 & g_2 & \dots & g_N \end{pmatrix}$ is the vector of coupling strength parameters with in total N individual coupling strengths. This formula is the core of the morphing method. It has N individual components, depending on the exact structure of the production and decay vertices, and can be simplified to a product of vectors $\vec{G}(\vec{g})$ and $\vec{M}$ that have length N. All individual matrix element components in $|\mathrm{ME}|^2$ are contained in $\vec{M}$ with prefactors from $\vec{G}(\vec{g})$, that are combinations of coupling strength parameters. A distribution or variable T of the described process can be written as the weighted sum of N input samples $\vec{T}$:

$$T(\vec{g}) = \vec{w}^T(\vec{g}) \cdot \vec{T} = \sum_{j=1}^{N} w_j(\vec{g}) \cdot T_j \tag{B.4}$$

The weight functions $\vec{w}(\vec{g})$ are polynomials in couplings $\vec{g}$ with the original structure of the squared matrix element. Evaluating $\vec{G}(\vec{g})$ for each input T_j with coupling configuration $\vec{g}_j$ a linear system of equations can be constructed:

$$\vec{T} \propto \mathbb{M} \cdot \vec{M} \quad \text{with} \quad \mathbb{M} = \begin{pmatrix} \vec{G}^T(\vec{g}_1) \\ \vdots \\ \vec{G}^T(\vec{g}_N) \end{pmatrix}. \tag{B.5}$$

The $N \times N$ matrix $\mathbb{M}$ is called *morphing matrix*. The inputs $\vec{T}$ can be freely chosen, but they have to be linear independent in $\vec{G}$-space, i.e. their morphing matrix has to be invertible. By multiplying the *inverted morphing matrix* $\mathbb{M}^{-1}$ to Equation B.5 the matrix elements $\vec{M}$ can be described as a function of inputs $\vec{T}$:

$$\vec{M} \propto \mathbb{M}^{-1} \cdot \vec{T} \tag{B.6}$$

A distribution or variable $T(\vec{g})$ can be described in terms of inputs $\vec{T}$ by inserting Equation B.6 into Equation B.3:

$$T(\vec{g}) = \vec{G}^T(\vec{g}) \cdot \mathbb{M}^{-1} \cdot \vec{T} = \vec{w}^T(\vec{g}) \cdot \vec{T} \quad \text{with} \quad \vec{w}(\vec{g}) = \left(\mathbb{M}^{-1}\right)^T \cdot \vec{G}(\vec{g}). \tag{B.7}$$

with weight functions $\vec{w}(\vec{g})$. Equation B.7 is called the *morphing function* for $T(\vec{g})$ constructed with inputs $\vec{T}$.

Appendix C

Simulated signal and background processes

In this Appendix details and references are given for the simulation of signal and background processes (see Section 4.2). The simulated processes in Run-1 and Run-2 are summarised in Tables 4.1 and 4.2, respectively.

Hard-scattering process

The next-to-leading-order (NLO) QCD generators Powheg-Box (v2) [177–182] and MadGraph5_aMC@NLO v2.2.3 and v2.3.3 [149, 183]) are used to model the hard-scattering process in proton-proton collisions for the SM Higgs boson signal, various background processes and the BSM Higgs boson signal processes.
Leading-order (LO) generators are used to simulate SM Higgs boson (Pythia 8 [127], BSM Higgs boson signals (JHU [51, 52]), and SM background processes (Alpgen [184], Sherpa 2.2.2 and Sherpa 2.1.1 [185], gg2VV [186], gg2ZZ [187] and MadGraph). For the Run-2 ggF VBF, VH and $b\bar{b}H$ Higgs boson signal samples the Higgs boson decay, $H \to ZZ^* \to 4\ell$, is modelled with Pythia 8.
The PDF sets used for the generation of the hard-scattering processes are CT10 [160] and CTEQ6L1 [188] for Run-1, and PDF4LHC [108], CT10 and NNPDF3.0 [107] for Run-2 (see Section 2.2.2).

Parton shower and hadronisation

For the modelling of the parton shower and hadronisation the following programs are interfaced to the hard-scattering generators: Pythia 6 [189] and Pythia 8 [127], Herwig++ [190] and Sherpa [191]. The parton shower programs are tuned to experimental data by using programs (so-called tunes) developed by either the authors of the programs or the ATLAS collaboration. In Run-1, the AU2 [129] tune is used for Pythia 8, the Perugia2011c [192] tune for Pythia 6 and AUET2 [193] for Herwig++. In Run-2, the AZNLO [194] tune is used for Powheg+Pythia 8, the A14 [195] tune for Pythia 8, the Perugia2012 tune for Pythia 6 and the UE-EE-5 [196] tune for Herwig++. The Sherpa parton shower tunes have been directly developed by the Sherpa authors. The parton shower tunes are listed together with the PDF sets used for the parton shower in the overview tables.

Improvements to the simulation

The *additional simulation programs* in the overview tables are used in addition to the hard-scattering and parton shower generators to improve the modelling accuracy.
The Higgs boson transverse momentum distribution in the simulation of the ggF Higgs boson production with the NLO QCD Powheg-Box generator has been improved in Run-1 by a p_{T}^{4l} dependent weighting of the events to each event to reproduce the NNLO and NNLL QCD predictions from the hres2.1 program [197, 198]. In Run-2, the MiNLO [199, 200] method for NLO description of the inclusive Higgs boson production is used and combined with the NNLO prediction from the HNNLO program [201, 202] by applying a reweighting procedure depending on the Higgs boson rapidity.
In addition, the effect of non-zero quark masses is taken into account for the ggF Higgs boson production in Run-1 [203] and Run-2 [198].
For the merging of jets from the hard-scattering process and from the parton shower, several different algorithms have been used: the MiNLO program [200] for the SM VH production in Run-2, the PowHeg method for the SM ggF Higgs boson production in Run-2, the FxFx program [149, 204] for the BSM ggF Higgs boson production in Run-2, the MLM scheme [205] for the Z+jets background in Run-1, and the ME+PS@NLO description for the $q\bar{q} \to ZZ^*$ and Z+jets background processes in Run-2.
In Run-2, the total and differential cross section predictions for the background processes have been further improved. The modelling of the ZZ^* production is improved

by adding NLO electroweak (EW) corrections as a function of the invariant ZZ^* mass m_{ZZ^*} [206, 207] to the $q\bar{q} \to ZZ^*$ simulation and by applying a correction factor $f_{\mathrm{NLO/LO}} = 1.7 \pm 1.0$ [208–213] to the LO $gg \to ZZ^*$ production to account for higher order effects. The LO QCD calculation of the $t\bar{t}Z$ cross section is scaled to the full NLO QCD + EW prediction of the two terms with dominant effects [214].
In order to compare the simulation with the data-driven estimation of the Z+jets background (see Section 4.3.2), the Run-1 and Run-2 simulations are normalised to the NNLO QCD predictions from FEWZ [215, 216] and to the NLO QCD predictions from MCFM [217, 218] (only Run-1).
The Z+jets process is simulated with Sherpa 2.2.2 interfaced to Comix [219] and OpenLoops [220] to achieve NLO precision for up to two partons, and LO precision for four partons.
The Photos program [221, 222] is used to take into account QED radiative corrections. Decays of hadrons containing bottom or charm quarks are modelled with the EvtGen v1.2.0 program [223]. The decays of the τ lepton are determined by tauola [224, 225].

Appendix D

Higgs boson production cross section and decay branching ratio calculation

In this appendix, the precision of the Higgs boson production cross section and branching ratio calculation is reported.

The ggF Higgs boson production cross section is calculated to NLO [226–228] and NNLO [229–231] in QCD for Run-1, and even to NNNLO [232, 233] for Run-2. For Run-1, the soft-gluon corrections have been calculated in NNLL approximation [234]. For both runs, NLO EW radiative corrections [235, 236] have been applied. The QCD and EW corrections have been joint assuming factorisation [237–239].

The VBF Higgs boson production cross section has been calculated to full QCD and EW NLO [240–242] and approximate NNLO in QCD [243].

The WH and ZH Higgs boson production cross sections have been calculated to NLO [244] and NNLO [245] in QCD. In Run-1, NLO EW radiative corrections [246] have been applied, in Run-2 to NLO EW [247]. For the $gg \to ZH$ calculation, NLO QCD corrections are added [248].

The $t\bar{t}H$ Higgs boson production cross section has been calculated at NLO in QCD [249–252]. In Run-2, the NLO EW corrections [253] have been joint with the NLO QCD corrections according to [214].

The $b\bar{b}H$ Higgs boson production has been calculated in the four-flavour scheme at NLO in QCD [254–256] and in the five-flavour scheme at NNLO in QCD [257]. Both predictions have been combined with the Santander scheme [148, 258].

The Higgs boson decay width for WW and ZZ decays is calculated with

PROPHECY4F [259, 260] including full NLO QCD plus EW corrections [261] and interference effects between fermion final-states that are identical. Other Higgs boson partial decay widths are calculated with HDECAY [262, 263]. Combining the partial decay width calculations, the branching ratio for the $H \to 4\ell$ final state in the SM is 0.0125 %.

Appendix E

$H \to ZZ^* \to 4\ell$ trigger

In this appendix, the trigger items for the Run-1 and Run-2 $H \to ZZ^* \to 4\ell$ analyses are summarised in Tables E.1 and E.2, respectively.

Table E.1: Trigger requirements for the Run-1 $H \to ZZ^* \to 4\ell$ analysis.

Triggered object	Single-lepton trigger	Dilepton trigger
2011 data set		
Muon:	EF_mu18_MG	EF_2mu10_loose
	EF_mu18_MG_medium	—
Electron:	EF_e20_medium	EF_2e12_medium
	EF_e22_medium	EF_2e12T_medium
	EF_e22vh_medium1	EF_2e12Tvh_medium
Electron & muon:	—	EF_e10_medium_mu6
2012 data set		
Muon:	EF_mu24i_tight	EF_2mu13
	EF_mu36_tight	EF_mu18_tight_mu8_EFFS
Electron:	EF_e60_medium1	EF_2e12Tvh_loose1
	EF_e24vhi_medium1	EF_2e12Tvh_loose1_L2StarB
Electron & muon:	—	EF_e12Tvh_medium1_mu8
	—	EF_e24vhi_loose1_mu8

Table E.2: Trigger requirements for the Run-2 $H \to ZZ^* \to 4\ell$ analysis.

Triggered object	Single-lepton trigger	Dilepton trigger	Trilepton trigger
2015 data set			
Muon:	HLT_mu20_iloose_L1MU15	HLT_2mu10	HLT_3mu6
	HLT_mu40	HLT_mu18_mu8noL1	HLT_3mu6_msonly
	HLT_mu60_0eta105_msonly	—	HLT_mu18_2mu4noL1
Electron:	HLT_e24_lhmedium_L1EM18VH	HLT_2e12_lhloose_L12EM10VH	HLT_e17_lhloose_2e9_lhloose
	HLT_e24_lhmedium_L1EM20VH	—	—
	HLT_e60_lhmedium	—	—
	HLT_e120_lhloose	—	—
Electron & muon:	—	HLT_e17_lhloose_mu14	HLT_2e12_lhloose_mu10
	—	HLT_e24_medium_L1EM20VHI_mu8noL1	HLT_e12_lhloose_2mu10
	—	HLT_e7_medium_mu24	—
2016 data set			
Muon:	HLT_mu24_ivarloose_L1MU15	HLT_2mu10	HLT_3mu4
	HLT_mu24_iloose_L1MU15	HLT_2mu10_nomucomb	HLT_3mu6
	HLT_mu24_ivarmedium	HLT_2mu14	HLT_3mu6_msonly
	HLT_mu24_imedium	HLT_2mu14_nomucomb	HLT_mu11_nomucomb_2mu4noL1_nscan03_L1MU11_2MU6
	HLT_mu26_ivarmedium	HLT_mu20_mu8noL1	HLT_mu20_2mu4noL1
	HLT_mu26_imedium	HLT_mu20_nomucomb_mu6noL1_nscan03	HLT_mu20_nomucomb_mu6noL1_nscan03
	HLT_mu40	HLT_mu22_mu8noL1	HLT_mu20_msonly_mu10noL1_msonly_nscan05_noComb
	HLT_mu50	—	—
Electron:	HLT_e24_lhmedium_ivarloose	HLT_2e15_lhvloose_nod0_L12EM13VH	HLT_e17_lhloose_nod0_2e9_lhloose_nod0
	HLT_e26_lhtight_nod0_ivarloose	HLT_2e17_lhvloose_nod0	HLT_e17_lhloose_nod0_2e10_lhloose_nod0_L1EM15VH_3EM8VH
	HLT_e60_lhmedium_nod0		
	HLT_e60_lhmedium		
	HLT_e140_lhloose_nod0		
	HLT_e300_etcut		
Electron & muon:	—	HLT_e17_lhloose_nod0_mu14	HLT_e17_lhloose_nod0_mu14
	—	HLT_e24_lhmedium_nod0_L1EM20VHI_mu8noL1	HLT_e24_lhmedium_nod0_L1EM20VHI_mu8noL1
	—	HLT_e7_lhmedium_nod0_mu24	HLT_e26_lhmedium_nod0_L1EM22VHI_mu8noL1
	—	HLT_e17_lhloose_mu14	HLT_e7_lhmedium_nod0_mu24
	—	HLT_e24_lhmedium_L1EM20VHI_mu8noL1	HLT_e12_lhloose_nod0_2mu10
	—	HLT_e7_lhmedium_mu24	HLT_2e12_lhloose_nod0_mu10

Appendix F

Random variable transformation

Random variables distributed with probability distribution functions can be transformed using the relationship for probability density functions due to the conservation of probability (*change-of-variable* technique [264]).
Let x and y be random variables with probability distribution functions $f(x)$ and $g(y)$. We now want the random variable x to be distributed with distribution function $g(y(x))$, for that the transformation function $y(x)$ needs to be known.
Based on the conservation of probabilities

$$f(x) \cdot \mathrm{d}x = g(y) \cdot \mathrm{d}y\,, \tag{F.1}$$

a differential equation can be formulated:

$$\frac{\mathrm{d}y}{\mathrm{d}x} = \frac{f(x)}{g(y)}. \tag{F.2}$$

By solving the differential equation defined in Equation F.2, the transformation function $y(x) : x \mapsto y$ can be determined if $f(x)$ and $g(y)$ are known and $y(x)$ is invertible. In the following two examples are discussed:

1. Transformation from x with arbitrary probability distribution function to y with uniform distribution:
   Inserting $f(x)$ and $g(y) = 1$ in Equation F.2, the differential equation now reads

$$\frac{\mathrm{d}y}{\mathrm{d}x} = f(x) \tag{F.3}$$

The differential equation can be solved by integration.

$$\implies y(x) = \int_{-\infty}^{x} f(x')\,\mathrm{d}x' = \mathrm{CDF}\,(x) \tag{F.4}$$

The transformation function is the cumulative distribution function of $f(x)$.

2. Transformation from x with uniform probability distribution function to y with Gaussian distribution:
   Inserting $f(x) = 1$ and $g(y) = \frac{1}{\sqrt{2\pi}} \exp\left(-\frac{y^2}{2}\right)$ in Equation F.2, the differential equation now reads

$$\frac{\mathrm{d}y}{\mathrm{d}x} = \frac{f(x)}{g(y)} = \frac{1}{\frac{1}{\sqrt{2\pi}} \exp\left(-\frac{y^2}{2}\right)} \tag{F.5}$$

   This is more challenging to solve. From literature we can obtain the information that the inverse error function erf^{-1} solves this differential equation.

$$\implies y(x) \propto \mathrm{erf}^{-1}(x) \tag{F.6}$$

In Table F.1 the two examples and their respective transformation functions are summarised.

Table F.1: Examples for transformation functions for random variable transformations using the change-of-variable technique.

Example	Probability distribution functions		Transformation
	Start	Target	function
	f(x)	g(y)	y(x)
1.	Arbitrary	Uniform	CDF
2.	Uniform	Gaussian	erf^{-1}

Appendix G

Higgs boson production rate dependence on BSM couplings

The expected dependence of the ggF, VBF, WH and ZH Higgs boson production cross sections on the CP-even and CP-odd BSM coupling parameters $c_\alpha\kappa_{\mathrm{HVV}}$ and $s_\alpha\kappa_{\mathrm{AVV}}$ is shown in Figure G.1. The interference of CP-even SM and BSM couplings leads to a minimum value of the cross section at non-zero $c_\alpha\kappa_{\mathrm{HVV}}$ values. The minimum is at negative $c_\alpha\kappa_{\mathrm{HVV}}$ values for ggF and VBF productions, while it is located at positive coupling values for the VH production.

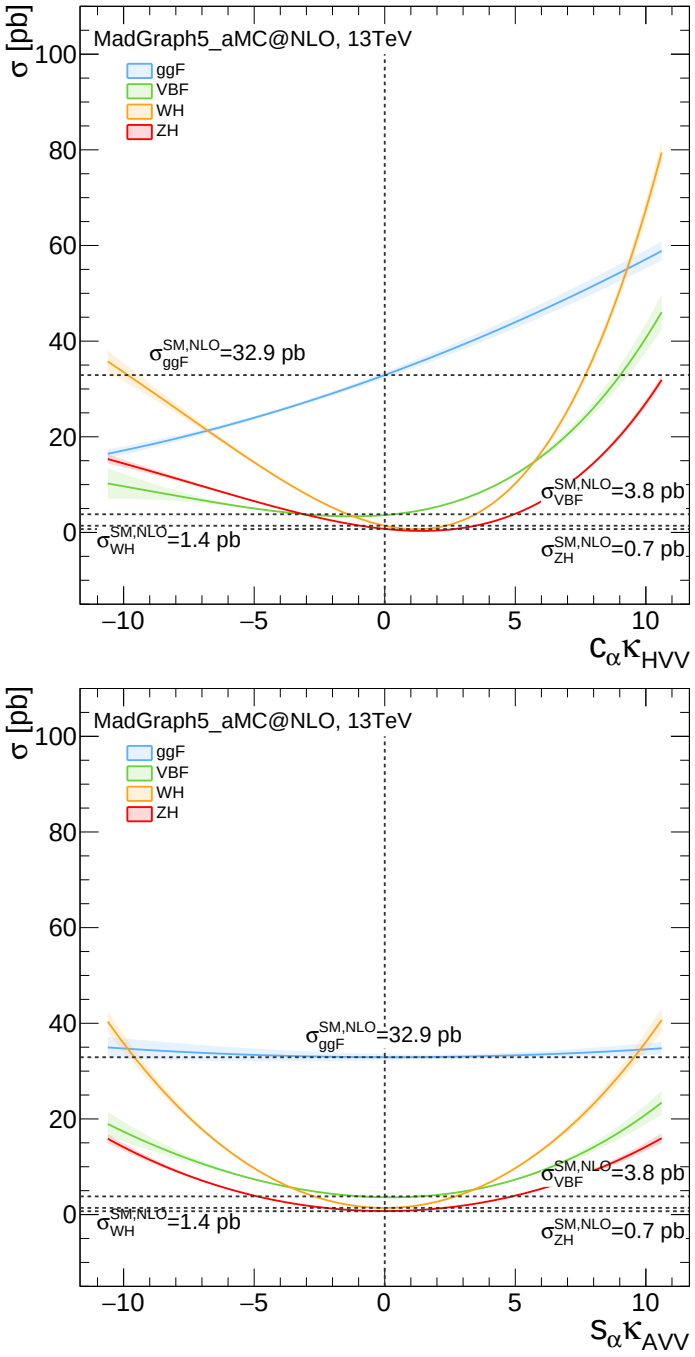

Figure G.1: The ggF (blue), VBF (green), WH (orange) and ZH (red) Higgs boson production cross sections at $\sqrt{s} = 13$ TeV calculated at next-to-leading-order with MadGraph5_aMC@NLO as a function of the CP-even and CP-odd non-SM coupling parameters $c_\alpha \kappa_{\mathrm{HVV}}$ (top) and $s_\alpha \kappa_{\mathrm{AVV}}$ (bottom), respectively.

Appendix H

Input samples for the BSM signal models

H.1 Shape-based tensor structure analysis

The input and reference samples for the shape-based tensor structure analysis are listed in this section. The LO samples have been generated with the JHU [51, 52] generator as described in Section 4.2 and Appendix C. The BSM signal model is constructed with the matrix element reweighting method described in Section 6.1.
For the measurement, the coupling parameters $g_{1/2/4}$ are translated into the Higgs characterisation framework parameters with the translation given in Section 1.4.2.

Table H.1: List of input and reference samples for the signal model of ggF production in the Run-1 rate-based tensor structure analysis describing the BSM contributions, g_2 and g_4, in the HVV vertex.

Description	Data set ID	g_1	g_2	g_4
Input samples				
Mixture	181990	1	$1+i$	$1+i$
Reference samples				
SM	189606	1	0	0
Pure BSM	181992	0	1	0
Pure BSM	181991	0	0	1
Pure BSM	181995	0	1	1
Mixture	181994	1	$1+i$	0
Mixture	181993	1	0	$2+2i$
Mixture	181996	1	1	1

H.2 Rate-based tensor structure analysis

The input and reference samples for the rate-based tensor structure analysis are listed in this section. The samples have been generated with the MadGraph5_aMC@NLO [149, 183]) generator at NLO for ggF production and at LO for VBF and VH productions as described in Section 4.2 and Appendix C. The BSM signal model is constructed with the morphing method described in Section 6.2.

H.2.1 1D CP-odd XVV signal model

The input and reference samples for the 1D CP-odd ggF and combined VBF $+VH$ signal models are listed in Tables H.2 and H.3, respectively.
The pure BSM CP-odd VBF $+VH$ samples with data set numbers 343252 and 344145 can only be combined after scaling the $V(\to \ell\nu/\ell\ell)H$ sample with a factor 4 to account for the different $\cos(\alpha)$ value.

Table H.2: List of input and reference samples for the 1D CP-odd XVV signal model of ggF production in the Run-2 rate-based tensor structure analysis describing the CP-odd BSM contribution, $s_\alpha\kappa_{\text{AVV}}$, in the HVV vertex.

Description	Data set ID	$\cos(\alpha)$	κ_{Hgg}	κ_{SM}	κ_{HVV}	κ_{AVV}	$\sigma \cdot \text{BR}$ [fb]
Input samples							
SM	344158	1	1	1	0	0	4.1
Mixture	344163	$\frac{1}{\sqrt{2}}$	1	1	0	6	1.1
Mixture	344164	$\frac{1}{\sqrt{2}}$	1	1	0	-6	1.1
Reference samples							
Pure BSM	344162	$\frac{1}{\sqrt{2}}$	1	0	0	1	$0.5 \cdot 10^{-3}$

Table H.3: List of input and reference samples for the 1D CP-odd XVV signal model of VBF and VH production in the Run-2 rate-based tensor structure analysis describing the CP-odd BSM contribution, $s_\alpha\kappa_{\text{AVV}}$, in the HVV vertex.

Description	Data set ID		$\cos(\alpha)$	κ_{SM}	κ_{HVV}	κ_{AVV}	$\sigma \cdot \text{BR}$ [fb]	
	VBF and $V(\to qq)H$	$V(\to \ell\nu/\ell\ell)H$					VBF and $V(\to qq)H$	$V(\to \ell\nu/\ell\ell)H$
Input samples								
SM	343247	344135	1	1	0	0	0.55	0.07
Mixture	343256	344144	$\frac{1}{\sqrt{2}}$	1	0	-2.5	0.21	0.04
Mixture	343253	344141	$\frac{1}{\sqrt{2}}$	1	0	5	0.42	0.11
Mixture	343254	344143	$\frac{1}{\sqrt{2}}$	1	0	2.5	0.21	0.04
Mixture	343255	344142	$\frac{1}{\sqrt{2}}$	1	0	-5	0.42	0.11
Reference samples								
Pure BSM	343252		0	0	0	15	1.20	
		344145	$\frac{1}{\sqrt{2}}$	0	0	15		0.09

H.2.2 2D XVV signal model

The input and reference samples for the 2D ggF and combined VBF $+VH$ signal models are listed in Tables H.4 and H.5, respectively.
Again, the pure BSM CP-odd samples, 343252 and 344145, need to be scaled before combination to account for the different $\cos(\alpha)$ value. Either the $V(\to \ell\nu/\ell\ell)H$ sample is scaled up by 4 or the VBF $+V(\to qq)H$ sample is scaled down by $\frac{1}{4}$.

Table H.4: List of input and reference samples for the 2D XVV signal model of ggF production in the Run-2 rate-based tensor structure analysis describing the BSM contributions, $c_\alpha\kappa_{\text{HVV}}$ and $s_\alpha\kappa_{\text{AVV}}$, in the HVV vertex.

Description	Data set ID	$\cos(\alpha)$	κ_{Hgg}	κ_{SM}	κ_{HVV}	κ_{AVV}	$\sigma \cdot \text{BR}$ [fb]
Input samples							
SM	344158	1	1	1	0	0	4.1
Pure BSM	344159	1	1	0	1	0	$5.4 \cdot 10^{-3}$
Pure BSM	344162	$\frac{1}{\sqrt{2}}$	1	0	0	1	$0.5 \cdot 10^{-3}$
Mixture	344161	1	1	1	−6	0	2.8
Mixture	344165	$\frac{1}{\sqrt{2}}$	1	1	6	6	1.5
Mixture	344166	$\frac{1}{\sqrt{2}}$	1	1	−6	−6	0.7
Reference samples							
Mixture	344160	1	1	1	6	0	5.8
Mixture	344163	$\frac{1}{\sqrt{2}}$	1	1	0	6	1.1
Mixture	344164	$\frac{1}{\sqrt{2}}$	1	1	0	−6	1.1

Table H.5: List of input and reference samples for the combined 2D XVV signal model of VBF and VH production in the Run-2 rate-based tensor structure analysis describing the BSM contributions, $c_\alpha\kappa_{\mathrm{HVV}}$ and $s_\alpha\kappa_{\mathrm{AVV}}$, in the HVV vertex.

Description	Data set ID		$\cos(\alpha)$	κ_{SM}	κ_{HVV}	κ_{AVV}	$\sigma \cdot \mathrm{BR}$ [fb]	
	VBF and $V(\to qq)H$	$V(\to \ell\nu/\ell\ell)H$					VBF and $V(\to qq)H$	$V(\to \ell\nu/\ell\ell)H$
Input samples								
SM	343247	344135	1	1	0	0	0.55	0.07
Pure BSM	343249	344140	1	0	10	0	0.83	0.29
Pure BSM	343252		0	0	0	15	1.20	
		344145	$\frac{1}{\sqrt{2}}$	0	0	15		0.09
Mixture	343253	344141	$\frac{1}{\sqrt{2}}$	1	0	5	0.42	0.11
Mixture	343254	344143	$\frac{1}{\sqrt{2}}$	1	0	2.5	0.21	0.04
Mixture	343255	344142	$\frac{1}{\sqrt{2}}$	1	0	−5	0.42	0.11
Mixture	343259	344136	1	1	5	0	2.31	0.45
Mixture	343260	344138	1	1	2.5	0	0.85	0.07
Mixture	343261	344137	1	1	−5	0	1.89	0.68
Mixture	344152	344146	$\frac{1}{\sqrt{2}}$	1	2.5	−5	0.54	0.12
Mixture	344153	344151	$\frac{1}{\sqrt{2}}$	1	5	5	0.96	0.23
Mixture	344154	344150	$\frac{1}{\sqrt{2}}$	1	5	6	1.13	0.29
Mixture	344155	344147	$\frac{1}{\sqrt{2}}$	1	−2.5	−5	0.50	0.15
Mixture	344156	344148	$\frac{1}{\sqrt{2}}$	1	−5	5	0.69	0.24
Mixture	344157	344149	$\frac{1}{\sqrt{2}}$	1	−5	−6	0.78	0.27
Reference samples								
Mixture	343256	344144	$\frac{1}{\sqrt{2}}$	1	0	−2.5	0.21	0.04
Mixture	343262	344139	1	1	−2.5	0	1.00	0.31

H.2.3 Xgg signal model

The input and reference samples for the ggF signal model are listed in Table H.6.

Table H.6: List of input and reference samples for the Xgg signal model of ggF production in the Run-2 rate-based tensor structure analysis describing the CP-odd BSM contribution, $s_\alpha \kappa_{\text{Agg}}$, in the Hgg vertex.

Description	Data set ID	$\cos(\alpha)$	κ_{SM}	κ_{Hgg}	κ_{Agg}	$\sigma \cdot \text{BR}$ [fb]
Input samples						
SM	344158	1	1	0	1	4.1
Mixture	344167	$\frac{1}{\sqrt{2}}$	1	0.5	1	1.6
Mixture	344168	$\frac{1}{\sqrt{2}}$	1	-0.5	1	1.6
Reference samples						
Mixture	344169	$\frac{1}{\sqrt{2}}$	$\sqrt{2}$	$\sqrt{2}$	$\sqrt{2}$	13.4
Pure BSM	344170	$\frac{1}{\sqrt{2}}$	0	1	1	2.3

Appendix I

Signal model of the rate-based analysis

In this appendix the signal model of the rate-based tensor structure measurement in Run-2 is shown. The signal model is the expected event yield in a reconstructed category in dependence on BSM or SM coupling parameters.

The 2D XVV signal model in two-dimensional planes of two coupling parameters is shown in Figures I.1, I.2 and I.3. The total expectation from Higgs boson signal and background processes is shown together with the observed data, if the observed yield is within the boundaries of the expected contours.

The one-dimensional distributions of the XVV and Xgg analyses are shown in Figures I.4, I.5 and I.6. In all figures, the total expectation from Higgs boson signal and background processes is shown together with expected Higgs boson signals that are non-constant functions of the BSM coupling and with the observed data.
The 1D projection of the 2D XVV signal model in dependence on the CP-even BSM coupling, $c_\alpha\kappa_{\mathrm{HVV}}$, in each reconstructed event category is shown in Figure I.4. The 1D projection in dependence on the CP-odd coupling, $s_\alpha\kappa_{\mathrm{AVV}}$, is not shown, since it is identical within the morphing method error to the 1D XVV signal model, which is shown in Figure I.5.
The Xgg signal model in dependence on the CP-odd BSM coupling, $s_\alpha\kappa_{\mathrm{Agg}}$, in each reconstructed event category is shown in Figure I.6.

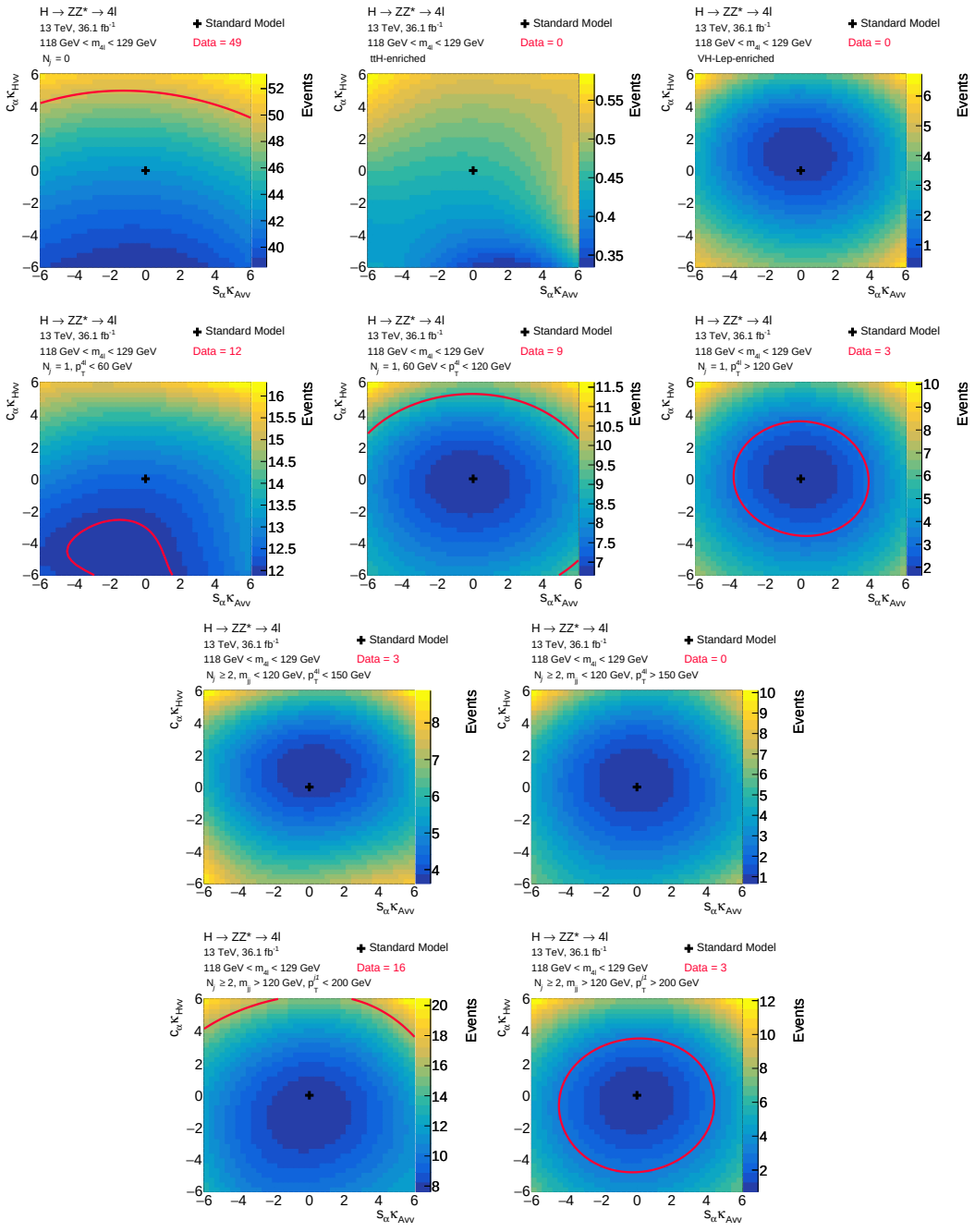

Figure I.1: The contour of expected and observed events in each reconstructed category in Run-2 data for the XVV rate-based tensor structure analysis probing BSM couplings in the HVV vertex in dependence on the BSM CP-odd and even coupling parameters, $s_\alpha\kappa_{\mathrm{AVV}}$ and $c_\alpha\kappa_{\mathrm{HVV}}$. Together with the total signal model expectation, i.e. from Higgs boson signal and background processes, the observed data (red) are shown.

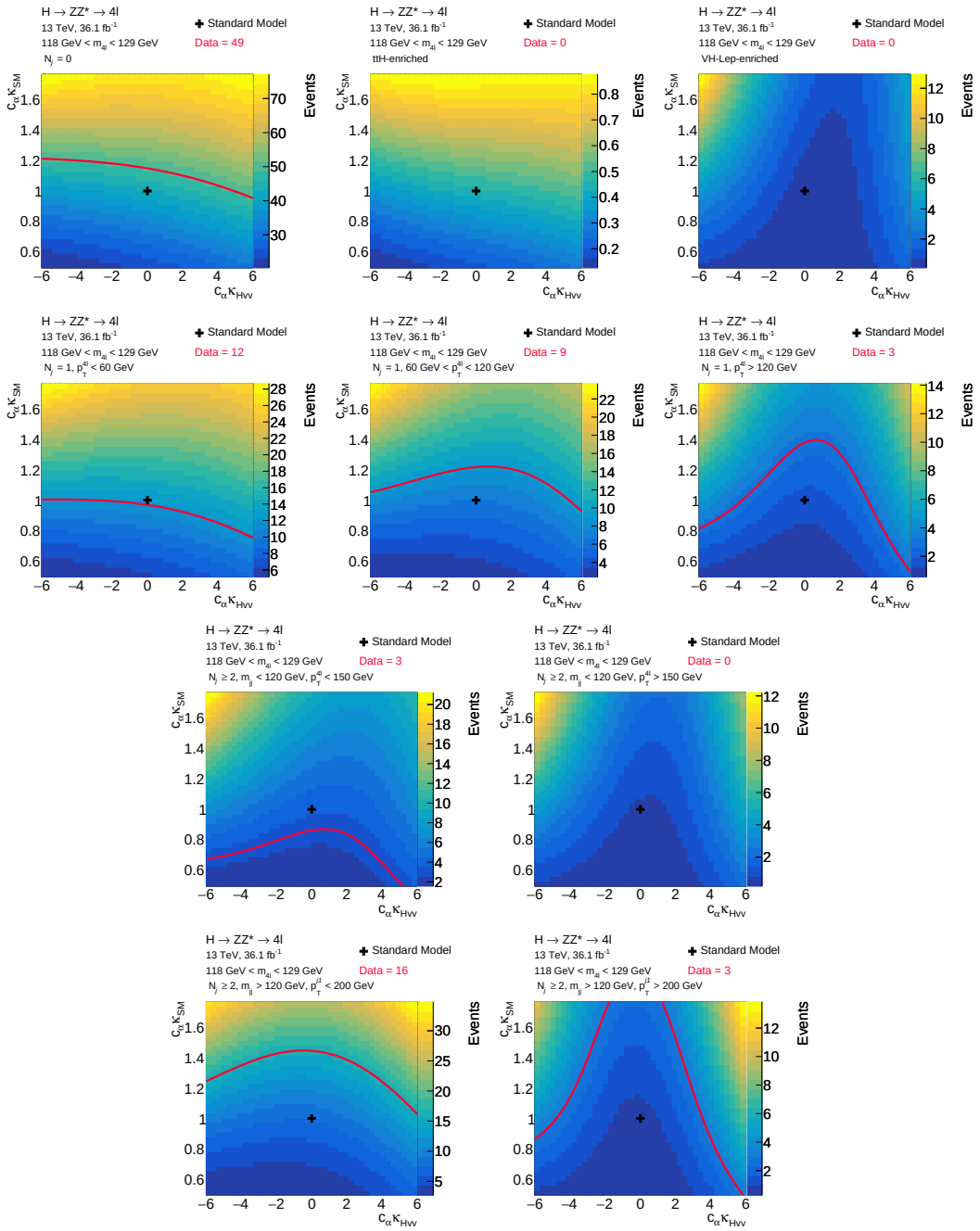

Figure I.2: The contour of expected and observed events in each reconstructed category in Run-2 data for the XVV rate-based tensor structure analysis probing BSM couplings in the HVV vertex in dependence on the BSM CP-even and SM coupling parameters, $c_\alpha\kappa_{\mathrm{HVV}}$ and $c_\alpha\kappa_{\mathrm{SM}}$. Together with the total signal model expectation, i.e. from Higgs boson signal and background processes, the observed data (red) are shown.

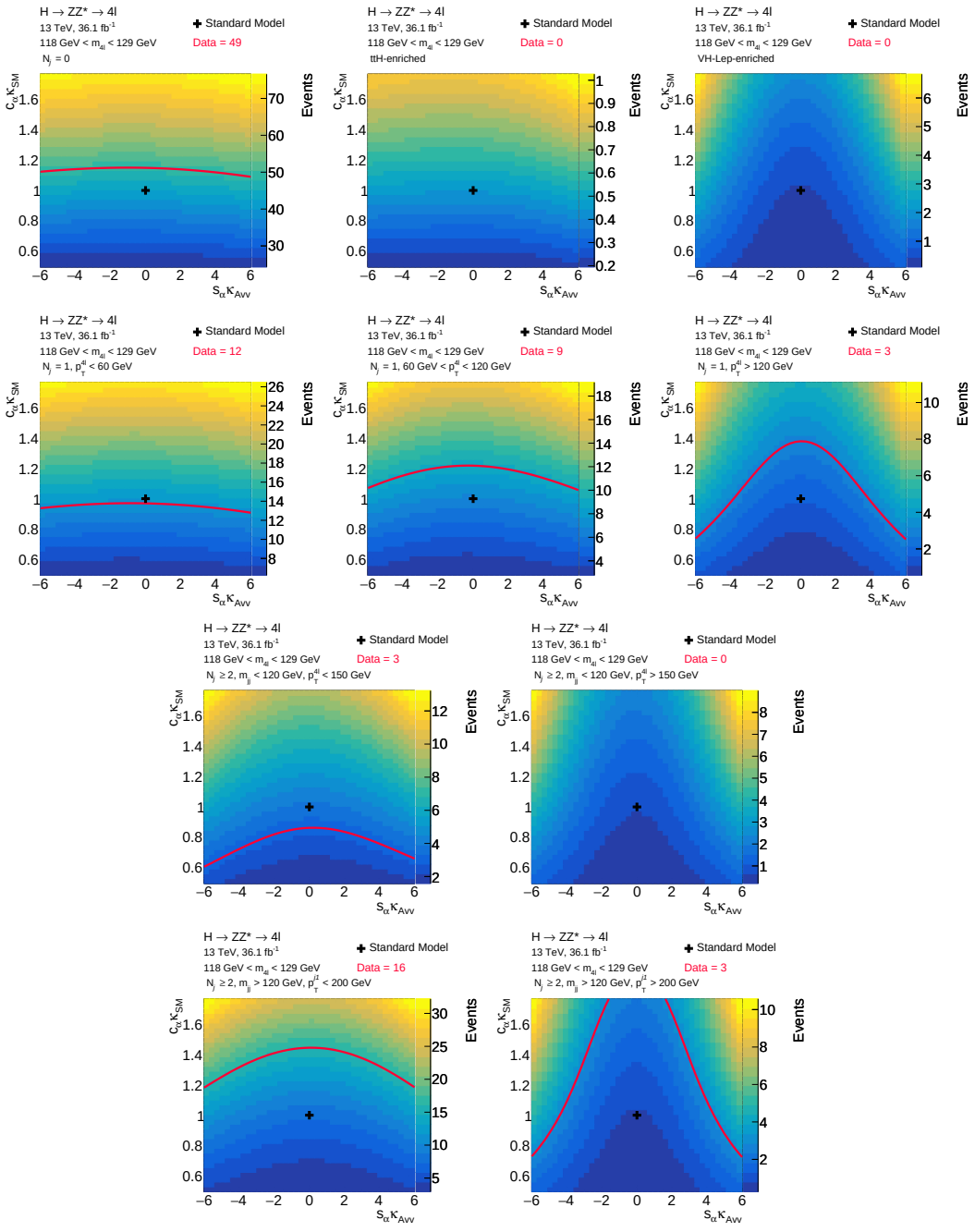

Figure I.3: The contour of expected and observed events in each reconstructed category in Run-2 data for the XVV rate-based tensor structure analysis probing BSM couplings in the HVV vertex in dependence on the BSM CP-odd and SM coupling parameters, $s_\alpha\kappa_{\mathrm{AVV}}$ and $c_\alpha\kappa_{\mathrm{SM}}$. Together with the total signal model expectation, i.e. from Higgs boson signal and background processes, the observed data (red) are shown.

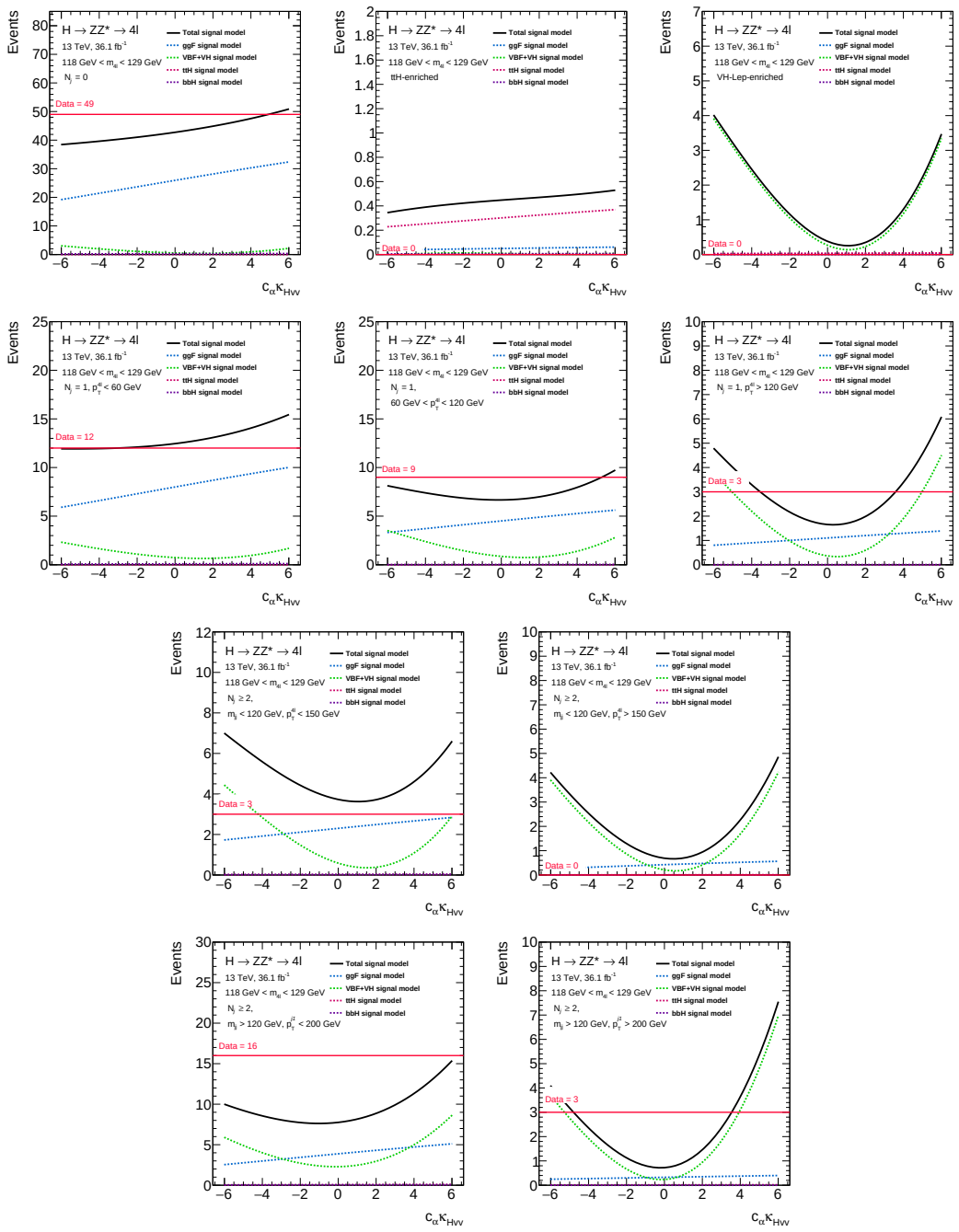

Figure I.4: The expected and observed events in each reconstructed category in Run-2 data for the XVV rate-based tensor structure analysis probing BSM couplings in the HVV vertex in dependence on the BSM CP-even coupling parameter, $c_\alpha\kappa_{\mathrm{HVV}}$. Together with the total (black) signal model expectation, i.e. from Higgs boson signal and background processes, the single expectations from ggF (blue), VBF $+VH$ (green), $t\bar{t}H$ (magenta), $b\bar{b}H$ productions (purple) and the observed data (red) are shown.

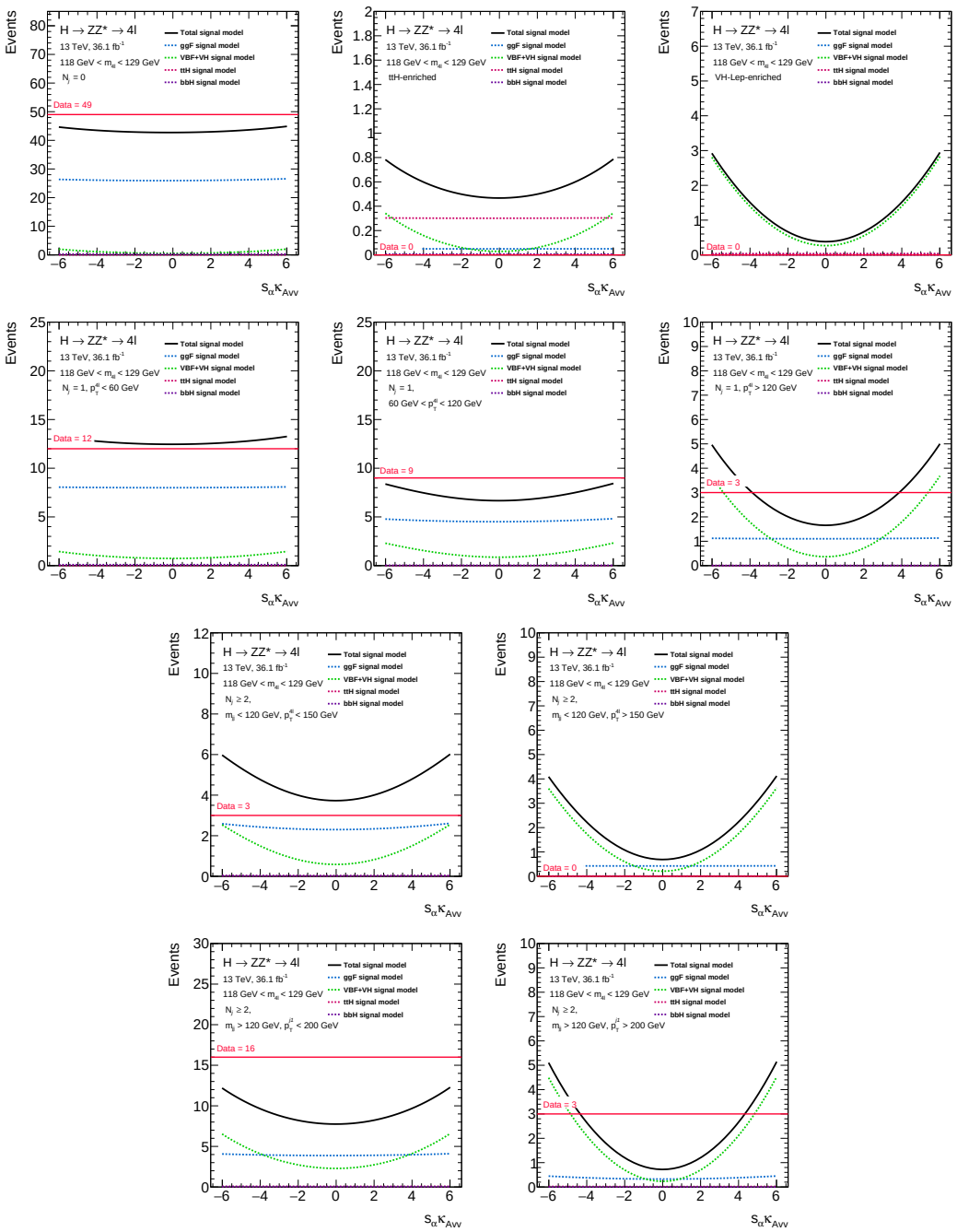

Figure I.5: The expected and observed events in each reconstructed category in Run-2 data for the XVV rate-based tensor structure analysis probing BSM couplings in the HVV vertex in dependence on the BSM CP-odd coupling parameter, $s_\alpha \kappa_{\mathrm{AVV}}$. Together with the total (black) signal model expectation, i.e. from Higgs boson signal and background processes, the single expectations from ggF (blue), VBF $+VH$ (green), $t\bar{t}H$ (magenta), $b\bar{b}H$ productions (purple) and the observed data (red) are shown.

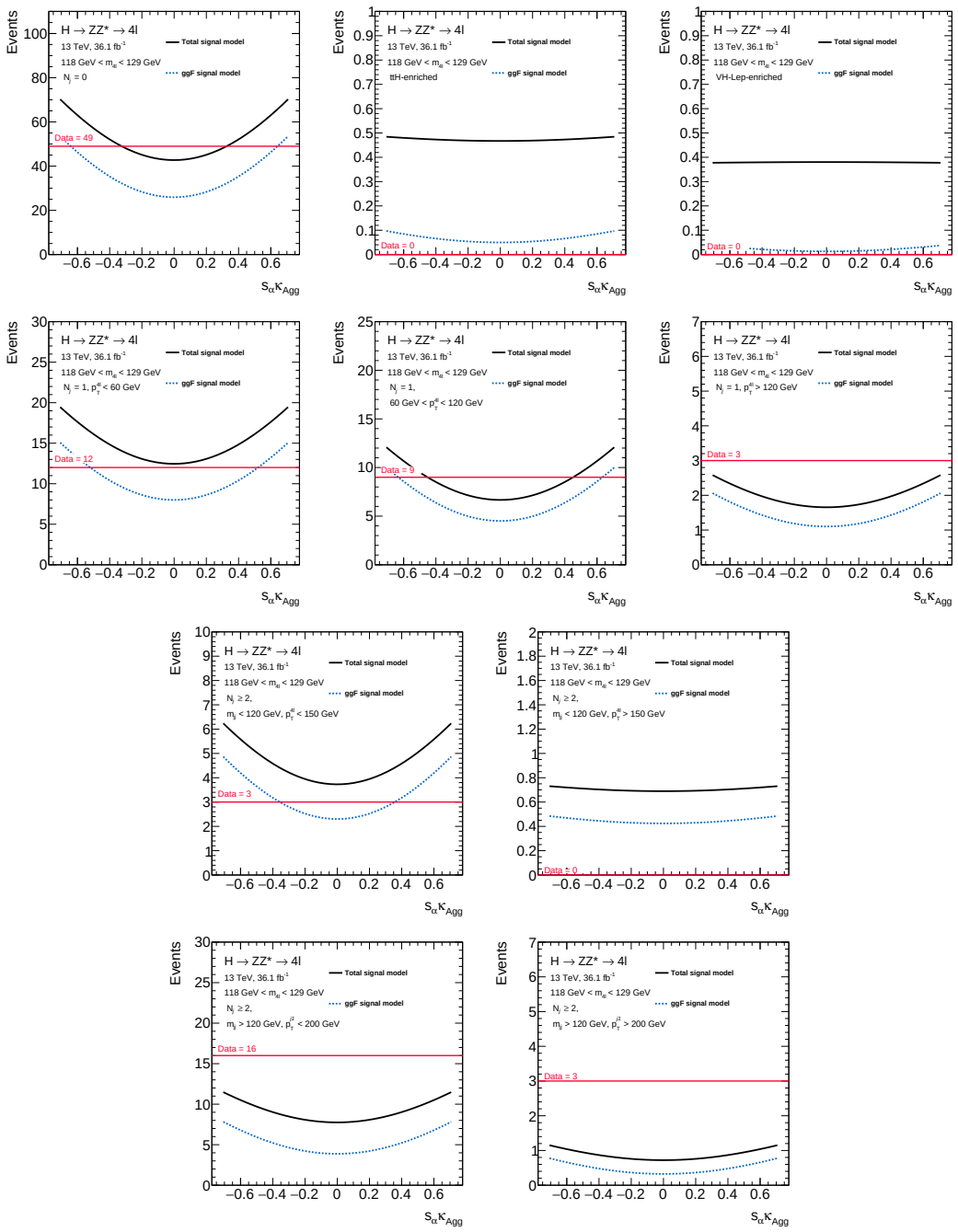

Figure I.6: The expected and observed events in each reconstructed category in Run-2 data for the Xgg rate-based tensor structure analysis probing a BSM CP-odd coupling in the Hgg vertex in dependence on the BSM CP-even coupling parameter, $s_\alpha \kappa_{\mathrm{Agg}}$. Together with the total (black) signal model expectation, i.e. from Higgs boson signal and background processes, the single expectation from ggF (blue) and the observed data (red) are shown.

Appendix J

Validation of the morphing method

In this appendix the error associated with the morphing method used in the signal model of the rate-based tensor structure measurement in Run-2 is estimated. In order to make sure that the error associated to the morphing method is sufficiently low, it is compared to the error expected in Run-2 data. If the morphing error in each reconstructed event category is smaller than the expected data error, it is deemed sufficiently small.

The expected data error is roughly estimated to be $\sqrt{N}$, since the events N counted in data are following a Poisson distribution. The relative error is $\frac{\sqrt{N}}{N}$, it is listed in Table J.1 for each reconstructed event category assuming that the yield given by simulation from Higgs boson signal and background processes is observed in Run-2 data.

The relative morphing error for the ggF and VBF $+VH$ signal models is evaluated for the probed phase space regions (see Section 5.2).
For each signal model a summary table is constructed (Tables J.1, J.2 and J.3), where the maximum morphing error in the studied parameter range in each category is listed. Categories failing the requirement, i.e. morphing errors larger than the expected data error, are indicated in red. In categories, where the morphing method is not reliable, the signal model is built with a polynomial and the morphing error is not reported.
For each scan of each signal model the distribution or contour, in case of two dimensional phase spaces, of the relative morphing error is shown in Figures J.1, J.2, J.3, J.4, J.5, J.6, J.7, J.8 and J.9. The morphing error of the VBF $+VH$ signal model is indicated in green, the ggF one in blue.
All signal models and scans together with the relevant summary tables and morphing error distributions are listed in the following:

1. 2D XVV signal model, see Table J.2:
   a) 1D scan: $|c_\alpha \kappa_{\text{HVV}}| < 6$, see Figure J.1
   b) 2D scan: $|c_\alpha \kappa_{\text{HVV}}| < 6$ and $|s_\alpha \kappa_{\text{AVV}}| < 6$, see ggF and VBF $+VH$ in Figures J.4 and J.5
   c) 2D scan: $|c_\alpha \kappa_{\text{HVV}}| < 6$ and $0.5 < c_\alpha \kappa_{\text{SM}} < 1.7$, see ggF and VBF $+VH$ in Figures J.6 and J.7
2. 1D CP-odd XVV signal model, see Table J.3)
   a) 1D scan: $|s_\alpha \kappa_{\text{AVV}}| < 6$, see Figure J.2
   b) 2D scan: $|s_\alpha \kappa_{\text{AVV}}| < 6$ and $0.5 < c_\alpha \kappa_{\text{SM}} < 1.7$, see ggF and VBF $+VH$ in Figures J.8 and J.9
3. Xgg signal model, see Table J.4 and Figure J.3
   a) 1D scan: $|s_\alpha \kappa_{\text{Agg}}| < 0.7$

All signal models pass the requirement except the VBF $+VH$ 1D CP-odd XVV signal model in the two-dimensional $s_\alpha \kappa_{\text{AVV}}$ and $c_\alpha \kappa_{\text{SM}}$ plane in the $1j$-$p_{\text{T}}^{4\ell}$-Low and $1j$-$p_{\text{T}}^{4\ell}$-Med categories. From Figure J.9 (second row, left and middle) it can be seen that the high morphing error is in corners of the phase space region, while most of the phase space has a morphing error smaller than 20 %. Therefore, the signal model is assumed to be reliable.

Table J.1: The expected total yield from Higgs boson signal and background processes in the four-lepton final state for each event category in Run-2 data together with the relative yield error assuming that the expectation is observed in data.

Category	Yield N	Relative error [%] $\frac{\sqrt{N}}{N}$
$t\bar{t}H$-enriched	0.46	146
VH-Lep-enriched	0.39	162
$0j$	42.80	15
$1j$-$p_{\mathrm{T}}^{4\ell}$-Low	12.35	28
$1j$-$p_{\mathrm{T}}^{4\ell}$-Med	6.73	39
$1j$-$p_{\mathrm{T}}^{4\ell}$-High	1.63	78
VH-Had-enriched-$p_{\mathrm{T}}^{4\ell}$-Low	3.82	52
VH-Had-enriched-$p_{\mathrm{T}}^{4\ell}$-High	0.70	120
VBF-enriched-p_{T}^{j}-Low	7.61	36
VBF-enriched-p_{T}^{j}-High	0.66	118

Table J.2: Summary table of the error associated with the morphing method for the 2D XVV signal model of the rate-based tensor structure measurement in Run-2.

Category	Max. rel. error [%]					
	1D plane $\lvert c_\alpha\kappa_{\mathrm{HVV}}\rvert < 6$		2D plane $\lvert c_\alpha\kappa_{\mathrm{HVV}}\rvert < 6$, $0.5 < \lvert c_\alpha\kappa_{\mathrm{SM}}\rvert < 1.7$		2D plane $\lvert c_\alpha\kappa_{\mathrm{HVV}}\rvert < 6$, $\lvert s_\alpha\kappa_{\mathrm{AVV}}\rvert < 6$,	
	ggF	VBF $+VH$	ggF	VBF $+VH$	ggF	VBF $+VH$
$t\bar{t}H$-enriched	—	—	—	—	—	—
VH-Lep-enriched	—	3.5	—	7	—	7
$0j$	1.5	3	4.5	12	3	12
$1j$-$p_{\mathrm{T}}^{4\ell}$-Low	3.2	4.5	9	19	7	25
$1j$-$p_{\mathrm{T}}^{4\ell}$-Med	4.5	3.5	13	16	9.5	12
$1j$-$p_{\mathrm{T}}^{4\ell}$-High	8	3.5	25	12	18	9
VH-Had-enriched-$p_{\mathrm{T}}^{4\ell}$-Low	7	3.5	19	10	16	12
VH-Had-enriched-$p_{\mathrm{T}}^{4\ell}$-High	12	6	7	10	23	9
VBF-enriched-p_{T}^{j}-Low	5.5	2.2	22	12	13	7
VBF-enriched-p_{T}^{j}-High	—	5.5	—	12	—	9

Table J.3: Summary table of the error associated with the morphing method for the 1D CP-odd XVV signal model of the rate-based tensor structure measurement in Run-2. Categories where the morphing error is larger than the expected error in Run-2 data are indicated in red.

Category	Max. rel. error [%]			
	1D plane $\lvert s_\alpha \kappa_{\text{AVV}} \rvert < 6$		2D plane $\lvert s_\alpha \kappa_{\text{AVV}} \rvert < 6$, $0.5 < \lvert c_\alpha \kappa_{\text{SM}} \rvert < 1.7$	
	ggF	VBF $+VH$	ggF	VBF $+VH$
$t\bar{t}H$-enriched	—	10	—	40
VH-Lep-enriched	—	1.8	—	10
$0j$	1	3	3.5	15
$1j$-$p_{\text{T}}^{4\ell}$-Low	—	5	—	40
$1j$-$p_{\text{T}}^{4\ell}$-Med	2.9	4	9	45
$1j$-$p_{\text{T}}^{4\ell}$-High	5	2.6	17	13
VH-Had-enriched-$p_{\text{T}}^{4\ell}$-Low	4.6	3.4	12	30
VH-Had-enriched-$p_{\text{T}}^{4\ell}$-High	—	2.6	—	15
VBF-enriched-p_{T}^{j}-Low	3.5	2	11	13
VBF-enriched-p_{T}^{j}-High	13	2	21	10

Table J.4: Summary table of the error associated with the morphing method for the Xgg signal model of the rate-based tensor structure measurement in Run-2.

Category	Max. rel. error [%] $\lvert s_\alpha \kappa_{\text{Agg}} \rvert < 0.7$
$t\bar{t}H$-enriched	—
VH-Lep-enriched	75
$0j$	1.3
$1j$-$p_{\text{T}}^{4\ell}$-Low	2.8
$1j$-$p_{\text{T}}^{4\ell}$-Med	3.4
$1j$-$p_{\text{T}}^{4\ell}$-High	7.5
VH-Had-enriched-$p_{\text{T}}^{4\ell}$-Low	4.6
VH-Had-enriched-$p_{\text{T}}^{4\ell}$-High	18
VBF-enriched-p_{T}^{j}-Low	6
VBF-enriched-p_{T}^{j}-High	18

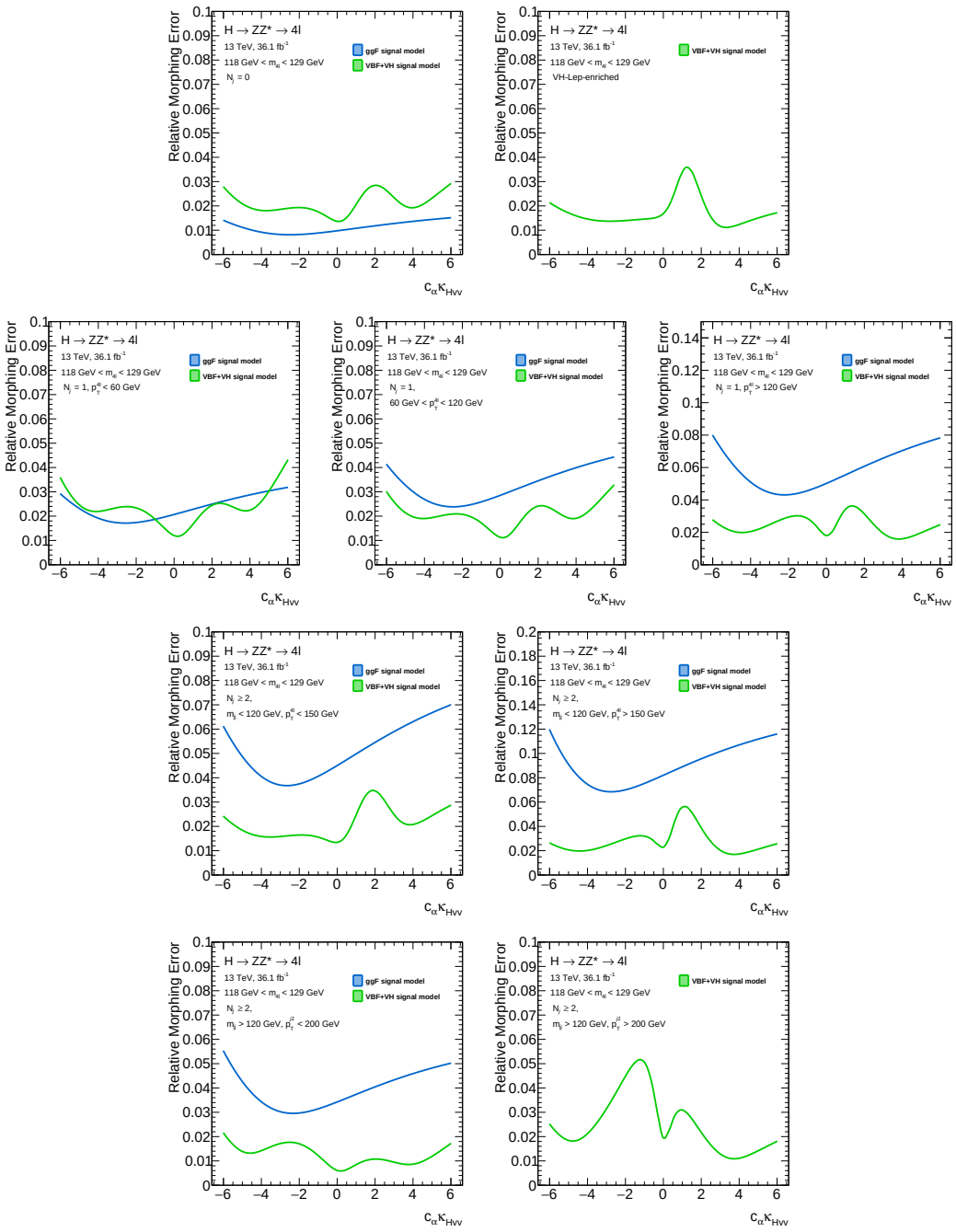

Figure J.1: Distribution of the morphing error as a function of $c_\alpha\kappa_{\mathrm{HVV}}$ for the ggF (blue) and VBF $+VH$ (green) 2D XVV signal model in Run-2 .

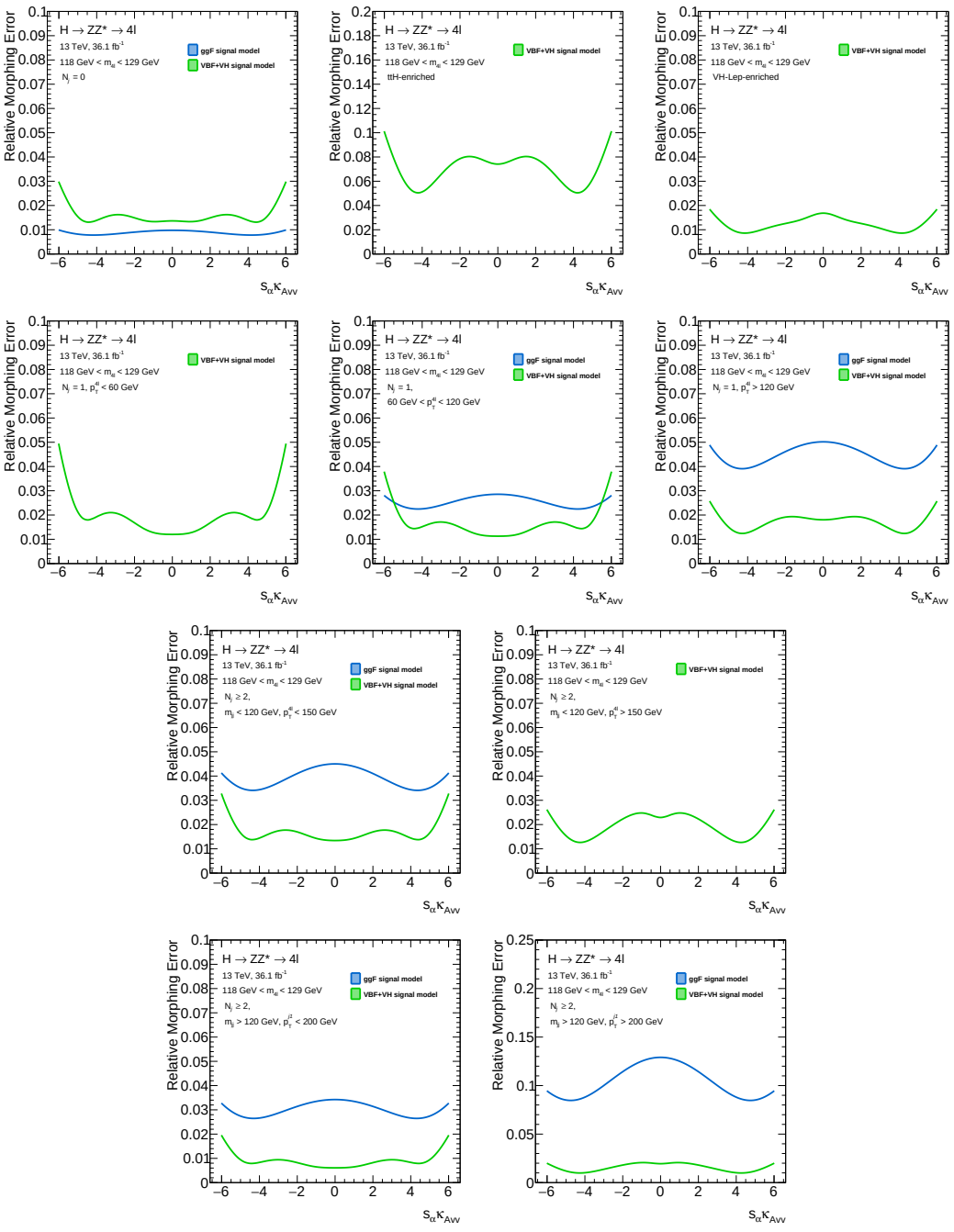

Figure J.2: Distribution of the morphing error as a function of $s_\alpha \kappa_{\mathrm{AVV}}$ for the ggF (blue) and VBF $+VH$ (green) 1D CP-odd XVV signal model in Run-2 .

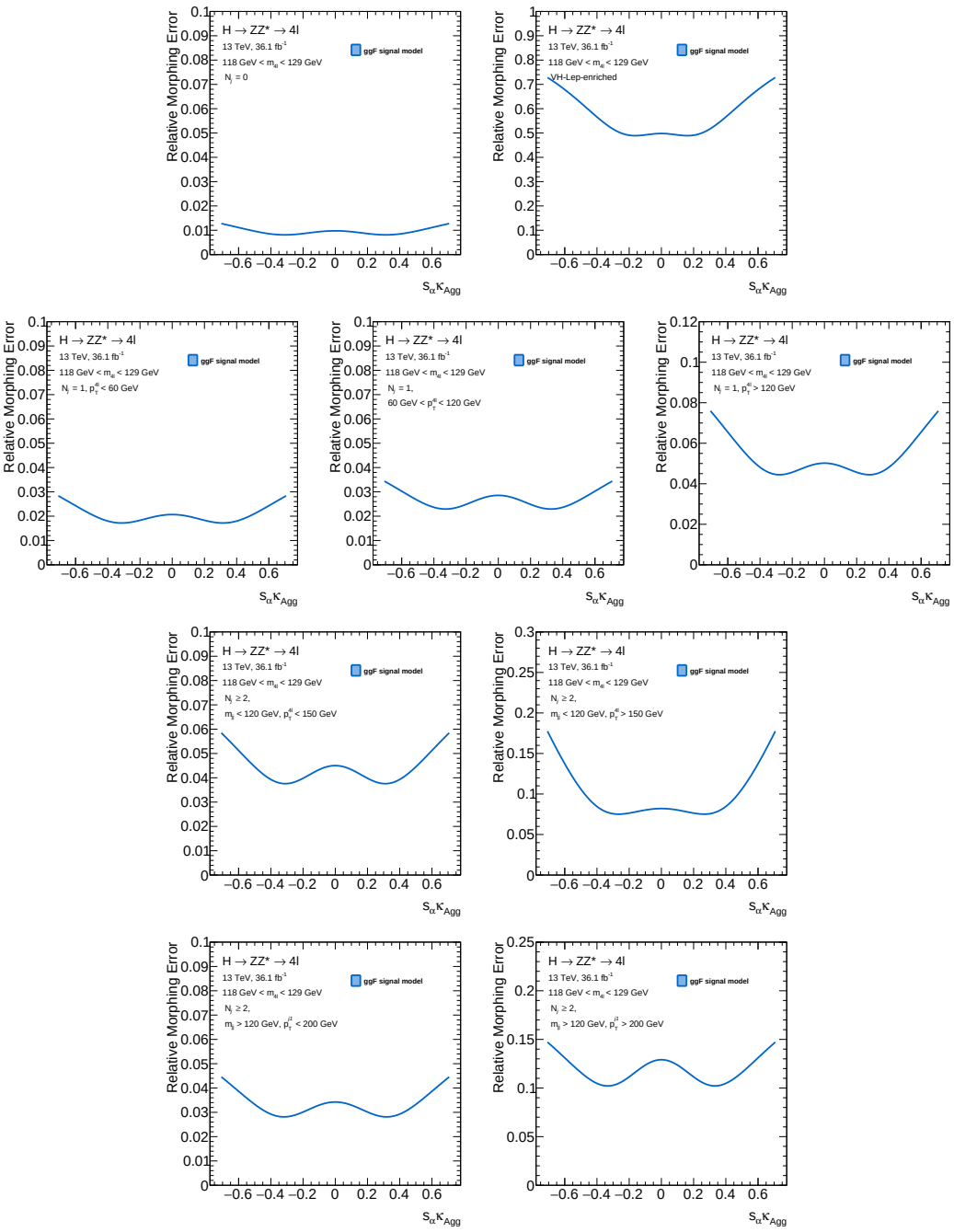

Figure J.3: Distribution of the morphing error as a function of $s_\alpha \kappa_{\mathrm{Agg}}$ for the ggF (blue) Xgg signal model in Run-2 .

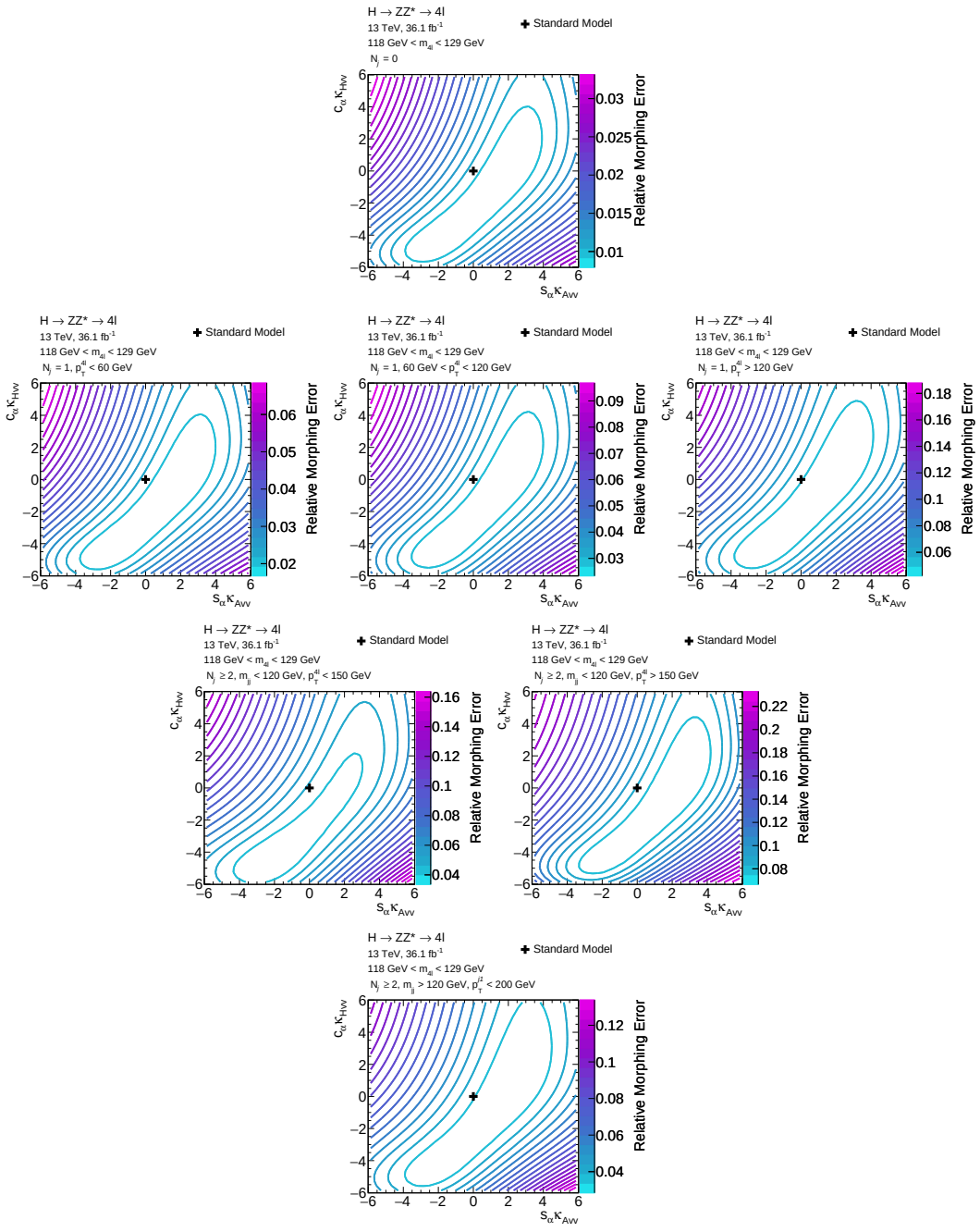

Figure J.4: Contour of the morphing error in the $c_\alpha\kappa_{\mathrm{HVV}}$ and $s_\alpha\kappa_{\mathrm{AVV}}$ plane for the ggF 2D XVV signal model in Run-2 .

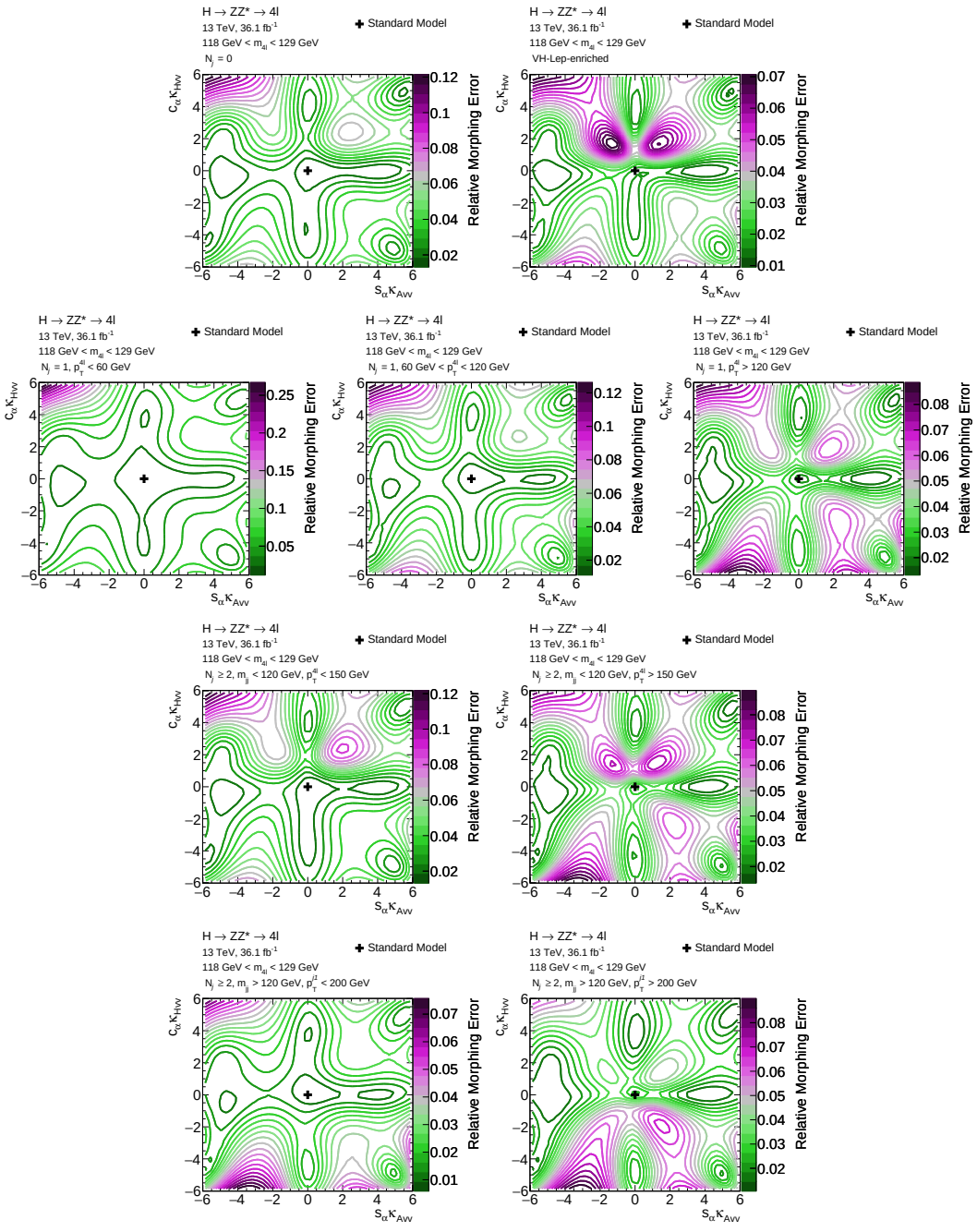

Figure J.5: Contour of the morphing error in the $c_\alpha \kappa_{\mathrm{HVV}}$ and $s_\alpha \kappa_{\mathrm{AVV}}$ plane for the VBF $+VH$ 2D XVV signal model in Run-2 .

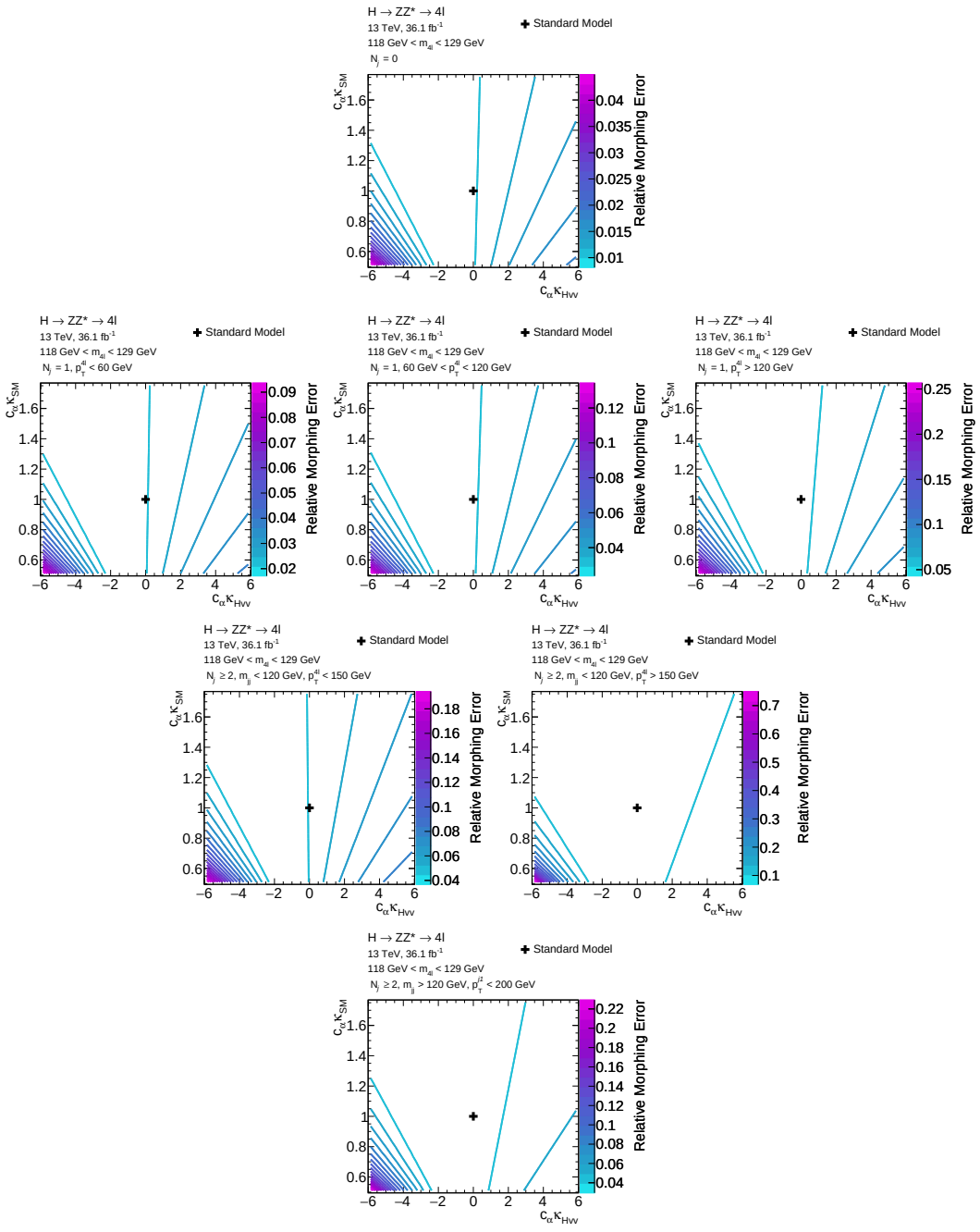

Figure J.6: Contour of the morphing error in the $c_\alpha\kappa_{\mathrm{HVV}}$ and $c_\alpha\kappa_{\mathrm{SM}}$ plane for the ggF 2D XVV signal model in Run-2 .

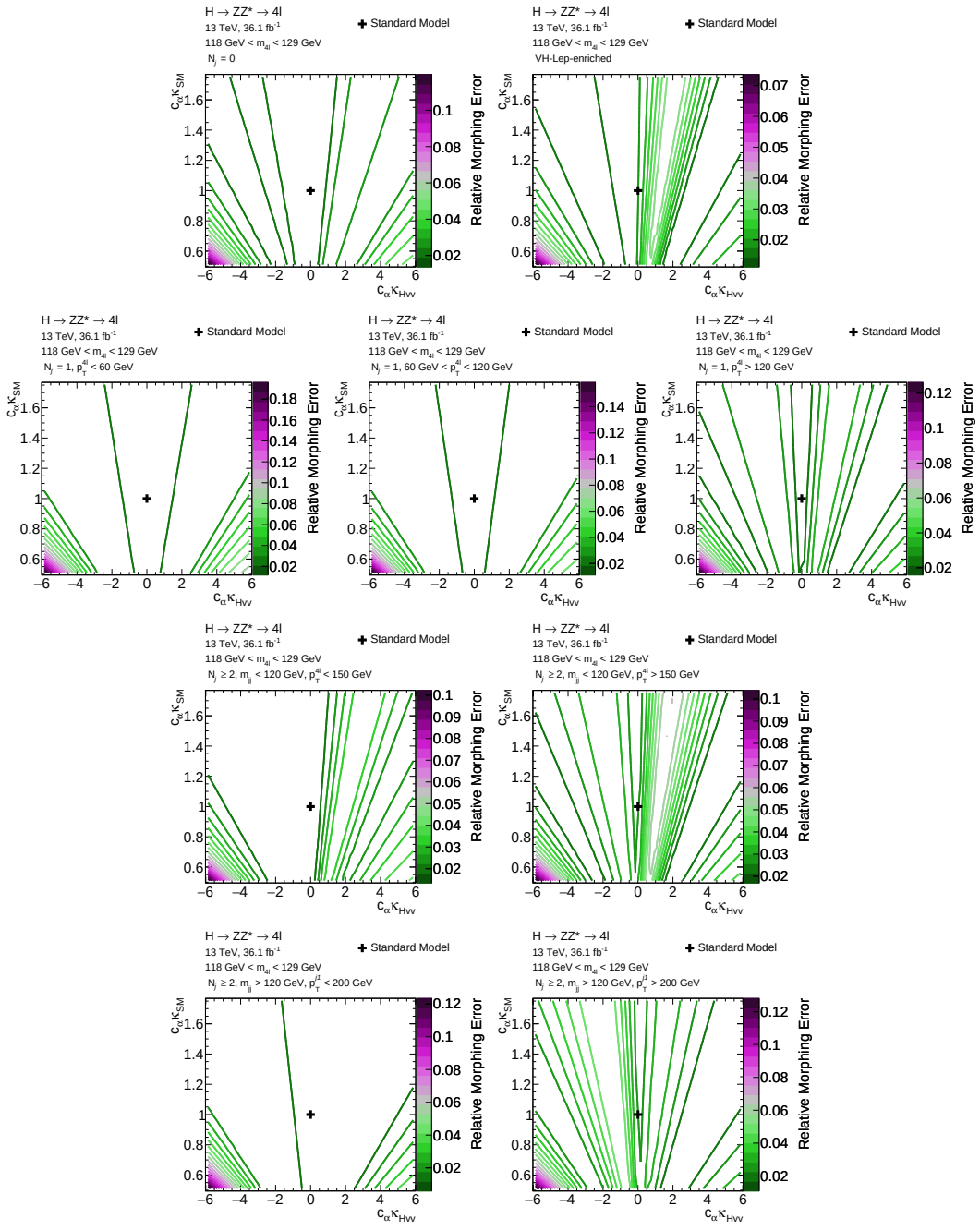

Figure J.7: Contour of the morphing error in the $c_\alpha\kappa_{\mathrm{HVV}}$ and $c_\alpha\kappa_{\mathrm{SM}}$ plane for the VBF $+VH$ 2D XVV signal model in Run-2 .

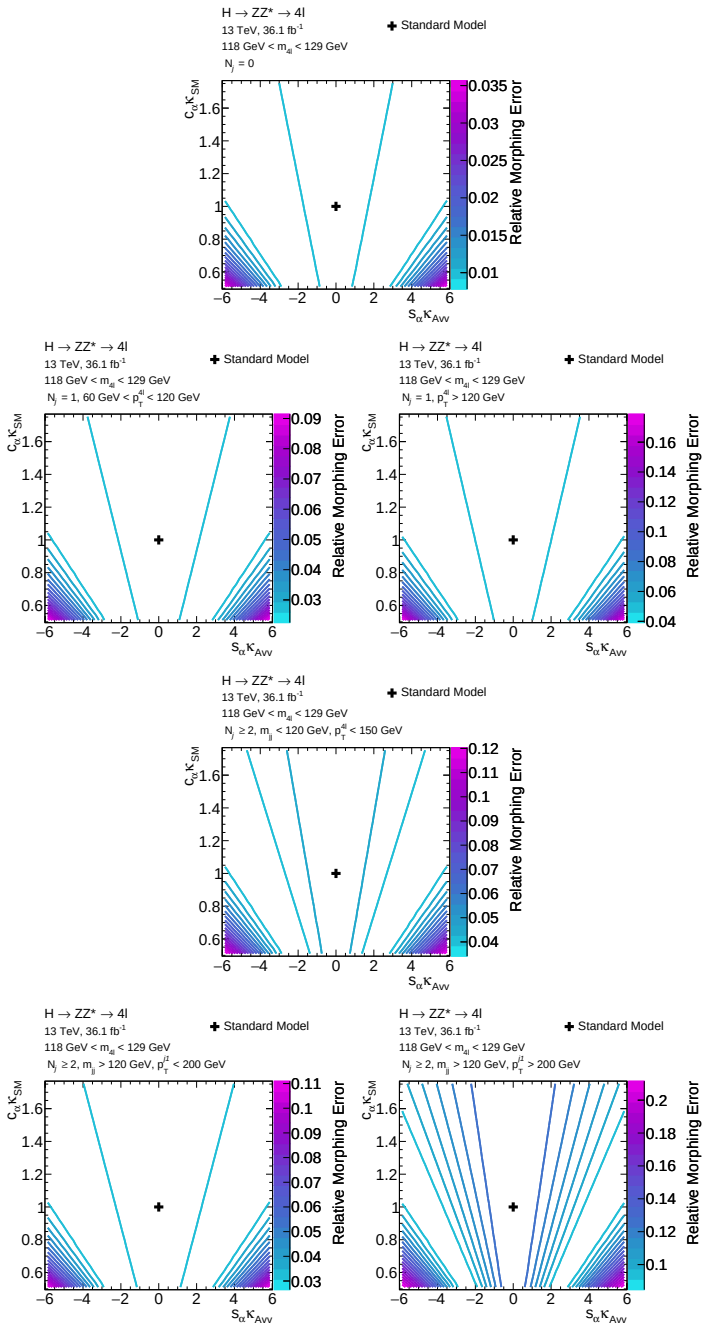

Figure J.8: Contour of the morphing error in the $s_\alpha \kappa_{\mathrm{AVV}}$ and $c_\alpha \kappa_{\mathrm{SM}}$ plane for the ggF 1D CP-odd XVV signal model in Run-2 .

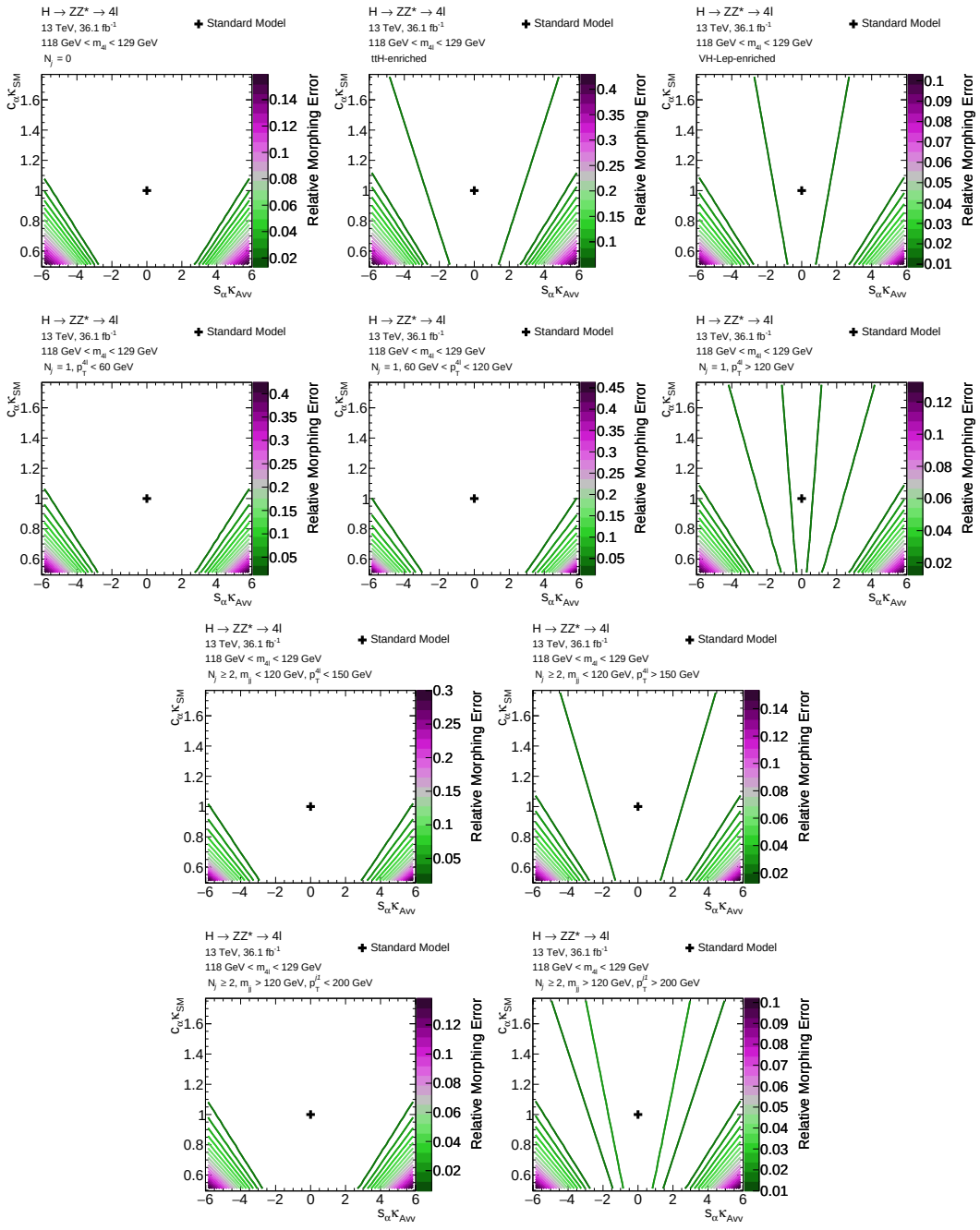

Figure J.9: Contour of the morphing error in the $s_\alpha \kappa_{\mathrm{AVV}}$ and $c_\alpha \kappa_{\mathrm{SM}}$ plane for the VBF $+VH$ 1D CP-odd XVV signal model in Run-2 .

List of Figures

List of Tables

Bibliography

[1] ATLAS Collaboration, G. Aad et al.,
Observation of a new particle in the search for the Standard Model Higgs boson with the ATLAS detector at the LHC, Phys. Lett. B **716** (2012) 1,
arXiv: 1207.7214 [hep-ex].

[2] CMS Collaboration, S. Chatrchyan et al., *Observation of a new boson at a mass of 125 GeV with the CMS experiment at the LHC*,
Phys. Lett. B **716** (2012) 30, arXiv: 1207.7235 [hep-ex].

[3] S. L. Glashow, *Partial Symmetries of Weak Interactions*,
Nucl. Phys. **22** (1961) 579.

[4] S. Weinberg, *A Model of Leptons*, Phys. Rev. Lett. **19** (1967) 1264.

[5] A. Salam, *Weak and Electromagnetic Interactions*,
Conf. Proc. **C680519** (1968) 367.

[6] G. 't Hooft and M. J. G. Veltman,
Regularization and Renormalization of Gauge Fields,
Nucl. Phys. **B44** (1972) 189.

[7] F. Englert and R. Brout,
Broken symmetry and the mass of gauge vector mesons,
Phys. Rev. Lett. **13** (1964) 321.

[8] P. W. Higgs, *Broken symmetries, massless particles and gauge fields*,
Phys. Lett. **12** (1964) 132.

[9] P. W. Higgs, *Broken symmetries and the masses of gauge bosons*,
Phys. Rev. Lett. **13** (1964) 508.

[10] G. Guralnik, C. Hagen and T. Kibble,
Global conservation laws and massless particles,
Phys. Rev. Lett. **13** (1964) 585.

[11] P. W. Higgs, *Spontaneous symmetry breakdown without massless bosons*, Phys. Rev. **145** (1966) 1156.

[12] T. Kibble, *Symmetry breaking in non-Abelian gauge theories*, Phys. Rev. **155** (1967) 1554.

[13] A. D. Sakharov, *Violation of CP Invariance, C asymmetry, and baryon asymmetry of the universe*, Pisma Zh. Eksp. Teor. Fiz. **5** (1967) 32, [Usp. Fiz. Nauk161,no.5,61(1991)].

[14] ATLAS Collaboration, G. Aad et al., *Study of the spin and parity of the Higgs boson in diboson decays with the ATLAS detector*, Eur. Phys. J. C **75** (2015) 476, arXiv: 1506.05669 [hep-ex].

[15] ATLAS Collaboration, G. Aad et al., *Evidence for the spin-0 nature of the Higgs boson using ATLAS data*, Phys. Lett. B **726** (2013) 120, arXiv: 1307.1432 [hep-ex].

[16] CMS Collaboration, V. Khachatryan et al., *Constraints on the spin-parity and anomalous HVV couplings of the Higgs boson in proton collisions at* 7 *and* 8 *TeV*, Phys. Rev. D **92** (2015) 012004, arXiv: 1411.3441 [hep-ex].

[17] S. L. Glashow, *The renormalizability of vector meson interactions*, Nucl. Phys. **10** (1959) 107.

[18] M. E. Peskin and D. V. Schroeder, *An Introduction to quantum field theory*, Reading, USA: Addison-Wesley, 1995.

[19] H. E. Logan, *TASI 2013 lectures on Higgs physics within and beyond the Standard Model*, (2014), arXiv: 1406.1786 [hep-ph].

[20] Patrignani, C. et al. (Particle Data Group), *Review of Particle Physics*, Chin. Phys. **C40** (2016 and 2017 update) 100001.

[21] J. Ellis, *TikZ-Feynman: Feynman diagrams with TikZ*, Comput. Phys. Commun. **210** (2017) 103, arXiv: 1601.05437 [hep-ph].

[22] Super-Kamiokande Collaboration, Y. Fukuda et al., *Evidence for oscillation of atmospheric neutrinos*, Phys. Rev. Lett. **81** (1998) 1562, arXiv: hep-ex/9807003 [hep-ex].

[23] SNO Collaboration, Q. R. Ahmad et al.,
Measurement of the rate of $\nu_e + d \to p + p + e^-$ interactions produced by ^8B solar neutrinos at the Sudbury Neutrino Observatory,
Phys. Rev. Lett. **87** (2001) 071301, arXiv: `nucl-ex/0106015 [nucl-ex]`.

[24] SNO Collaboration, Q. R. Ahmad et al.,
Direct evidence for neutrino flavor transformation from neutral current interactions in the Sudbury Neutrino Observatory,
Phys. Rev. Lett. **89** (2002) 011301, arXiv: `nucl-ex/0204008 [nucl-ex]`.

[25] N. Cabibbo, *Unitary Symmetry and Leptonic Decays*,
Phys. Rev. Lett. **10** (1963) 531, [,648(1963)].

[26] M. Kobayashi and T. Maskawa,
CP Violation in the Renormalizable Theory of Weak Interaction,
Prog. Theor. Phys. **49** (1973) 652.

[27] LHC Higgs Cross Section Working Group, D. de Florian et al., *Handbook of LHC Higgs Cross Sections: 4. Deciphering the Nature of the Higgs Sector*, (2016), arXiv: `1610.07922 [hep-ph]`.

[28] ATLAS and CMS Collaborations, G. Aad et al.,
Measurements of the Higgs boson production and decay rates and constraints on its couplings from a combined ATLAS and CMS analysis of the LHC pp collision data at $\sqrt{s} = 7$ and 8 TeV, JHEP **08** (2016) 045,
arXiv: `1606.02266 [hep-ex]`.

[29] LHC Higgs Cross Section Working Group, S. Heinemeyer et al.,
Handbook of LHC Higgs Cross Sections: 3. Higgs Properties,
CERN-2013-004 (CERN, Geneva, 2013), arXiv: `1307.1347 [hep-ph]`.

[30] P. Artoisenet et al., *A framework for Higgs characterisation*,
JHEP **1311** (2013) 043, arXiv: `1306.6464 [hep-ph]`.

[31] E. Accomando et al.,
Workshop on CP Studies and Non-Standard Higgs Physics, (2006),
arXiv: `hep-ph/0608079 [hep-ph]`.

[32] S. Weinberg, *Implications of Dynamical Symmetry Breaking*,
Phys. Rev. **D13** (1976) 974, [Addendum: Phys. Rev.D19,1277(1979)].

[33] L. Susskind,
Dynamics of Spontaneous Symmetry Breaking in the Weinberg-Salam Theory,
Phys. Rev. **D20** (1979) 2619.

[34] Yu. A. Golfand and E. P. Likhtman, *Extension of the Algebra of Poincare Group Generators and Violation of p Invariance*,
JETP Lett. **13** (1971) 323, [Pisma Zh. Eksp. Teor. Fiz.13,452(1971)].

[35] D. V. Volkov and V. P. Akulov, *Is the Neutrino a Goldstone Particle?*,
Phys. Lett. B **46** (1973) 109.

[36] J. Wess and B. Zumino, *Supergauge Transformations in Four-Dimensions*,
Nucl. Phys. B **70** (1974) 39.

[37] J. Wess and B. Zumino,
Supergauge Invariant Extension of Quantum Electrodynamics,
Nucl. Phys. B **78** (1974) 1.

[38] S. Ferrara and B. Zumino, *Supergauge Invariant Yang-Mills Theories*,
Nucl. Phys. B **79** (1974) 413.

[39] A. Salam and J. A. Strathdee, *Supersymmetry and Nonabelian Gauges*,
Phys. Lett. B **51** (1974) 353.

[40] P. Fayet, *Supersymmetry and weak, electromagnetic and strong interactions*,
Phys. Lett. B **64** (1976) 159.

[41] P. Fayet, *Spontaneously broken supersymmetric theories of weak, electromagnetic and strong interactions*, Phys. Lett. B **69** (1977) 489.

[42] T. D. Lee, *A Theory of Spontaneous T Violation*,
Phys. Rev. **D8** (1973) 1226, [,516(1973)].

[43] W. Bernreuther, P. Gonzalez and M. Wiebusch, *Pseudoscalar Higgs Bosons at the LHC: Production and Decays into Electroweak Gauge Bosons Revisited*,
Eur. Phys. J. **C69** (2010) 31, arXiv: `1003.5585 [hep-ph]`.

[44] T. Figy, S. Palmer and G. Weiglein,
Higgs production via weak boson fusion in the Standard Model and the MSSM,
JHEP **02** (2012) 105, arXiv: `1012.4789 [hep-ph]`.

[45] N. Arkani-Hamed, A. G. Cohen and H. Georgi,
Electroweak symmetry breaking from dimensional deconstruction,
Phys. Lett. **B513** (2001) 232, arXiv: `hep-ph/0105239 [hep-ph]`.

[46] N. Arkani-Hamed et al.,
Phenomenology of electroweak symmetry breaking from theory space,
JHEP **08** (2002) 020, arXiv: `hep-ph/0202089 [hep-ph]`.

[47] N. Arkani-Hamed et al., *The Littlest Higgs*, JHEP **07** (2002) 034,
arXiv: `hep-ph/0206021 [hep-ph]`.

[48] ALEPH, DELPHI, L3, OPAL Collaboration, LEP Working Group for Higgs Boson Searches, S. Schael et al., *Search for neutral MSSM Higgs bosons at LEP*,
Eur. Phys. J. **C47** (2006) 547, arXiv: `hep-ex/0602042 [hep-ex]`.

[49] F. Maltoni, K. Mawatari and M. Zaro, *Higgs characterisation via vector-boson fusion and associated production: NLO and parton-shower effects*,
Eur. Phys. J. **C74** (2014) 2710, arXiv: `1311.1829 [hep-ph]`.

[50] I. Anderson et al.,
Constraining anomalous HVV interactions at proton and lepton colliders,
Phys. Rev. **D89** (2014) 035007, arXiv: `1309.4819 [hep-ph]`.

[51] Y. Gao et al.,
Spin determination of single-produced resonances at hadron colliders,
Phys. Rev. **D81** (2010) 075022, arXiv: `1001.3396 [hep-ph]`.

[52] S. Bolognesi et al.,
On the spin and parity of a single-produced resonance at the LHC,
Phys. Rev. **D86** (2012) 095031, arXiv: `1208.4018 [hep-ph]`.

[53] CMS Collaboration, A. M. Sirunyan et al.,
Constraints on anomalous Higgs boson couplings using production and decay information in the four-lepton final state, Phys. Lett. B **775** (2017) 1,
arXiv: `1707.00541 [hep-ex]`.

[54] CMS Collaboration, S. Chatrchyan et al., *Combined search for anomalous pseudoscalar HVV couplings in $VH(H \to b\bar{b})$ production and $H \to VV$ decay*,
Phys. Lett. B **759** (2016) 672, arXiv: `1602.04305 [hep-ex]`.

[55] CMS Collaboration, S. Chatrchyan et al., *Precise determination of the mass of the Higgs boson and tests of compatibility of its couplings with the standard model predictions using proton collisions at 7 and 8 TeV*,
Eur. Phys. J. C **75** (2015) 212, arXiv: `1412.8662 [hep-ex]`.

[56] ATLAS and CMS Collaborations, G. Aad et al.,
Combined Measurement of the Higgs Boson Mass in pp Collisions at $\sqrt{s} = 7$ and 8 TeV with the ATLAS and CMS Experiments,
Phys. Rev. Lett. **114** (2015) 191803, arXiv: 1503.07589 [hep-ex].

[57] ATLAS Collaboration, G. Aad et al.,
Measurement of the Higgs boson mass in the $H \to ZZ^* \to 4\ell$ and $H \to \gamma\gamma$ channels with $\sqrt{s} = 13$ TeV pp collisions using the ATLAS detector,
ATLAS-CONF-2017-046, 2017, https://cds.cern.ch/record/2273853.

[58] CMS Collaboration, A. M. Sirunyan et al.,
Measurements of properties of the Higgs boson decaying into the four-lepton final state in pp collisions at $\sqrt{s} = 13$ TeV, JHEP **11** (2017) 047,
arXiv: 1706.09936 [hep-ex].

[59] Patrignani, C. et al. (Particle Data Group),
Review of Particle Physics: 11. Status of Higgs Boson Physics,
http://pdg.lbl.gov/2017/reviews/rpp2017-rev-higgs-boson.pdf
(visited on 02/28/2018).

[60] ATLAS Collaboration, G. Aad et al., *Measurement of the Higgs boson mass from the $H \to \gamma\gamma$ and $H \to ZZ^* \to 4\ell$ channels in pp collisions at center-of-mass energies of 7 and 8 TeV with the ATLAS detector*,
Phys. Rev. D **90** (2014) 052004, arXiv: 1406.3827 [hep-ex].

[61] CMS Collaboration, V. Khachatryan et al., *Limits on the Higgs boson lifetime and width from its decay to four charged leptons*,
Phys. Rev. D **92** (2015) 072010, arXiv: 1507.06656 [hep-ex].

[62] L. J. Dixon and M. S. Siu,
Resonance continuum interference in the diphoton Higgs signal at the LHC,
Phys. Rev. Lett. **90** (2003) 252001, arXiv: hep-ph/0302233 [hep-ph].

[63] S. P. Martin,
Shift in the LHC Higgs diphoton mass peak from interference with background,
Phys. Rev. **D86** (2012) 073016, arXiv: 1208.1533 [hep-ph].

[64] L. J. Dixon and Y. Li,
Bounding the Higgs Boson Width Through Interferometry,
Phys. Rev. Lett. **111** (2013) 111802, arXiv: 1305.3854 [hep-ph].

[65] N. Kauer and G. Passarino,
Inadequacy of zero-width approximation for a light Higgs boson signal,
JHEP **08** (2012) 116, arXiv: 1206.4803 [hep-ph].

[66] F. Caola and K. Melnikov,
Constraining the Higgs boson width with ZZ production at the LHC,
Phys. Rev. **D88** (2013) 054024, arXiv: 1307.4935 [hep-ph].

[67] J. M. Campbell, R. K. Ellis and C. Williams, *Bounding the Higgs width at the LHC using full analytic results for $gg \to e^- e^+ \mu^- \mu^+$*, JHEP **04** (2014) 060, arXiv: 1311.3589 [hep-ph].

[68] J. M. Campbell, R. K. Ellis and C. Williams,
Bounding the Higgs width at the LHC: Complementary results from $H \to WW$,
Phys. Rev. **D89** (2014) 053011, arXiv: 1312.1628 [hep-ph].

[69] C. Englert and M. Spannowsky,
Limitations and Opportunities of Off-Shell Coupling Measurements,
Phys. Rev. **D90** (2014) 053003, arXiv: 1405.0285 [hep-ph].

[70] ATLAS Collaboration, G. Aad et al.,
Constraints on the off-shell Higgs boson signal strength in the high-mass ZZ and WW final states with the ATLAS detector, Eur. Phys. J. C **75** (2015) 335, arXiv: 1503.01060 [hep-ex].

[71] CMS Collaboration, V. Khachatryan et al.,
Search for Higgs boson off-shell production in proton–proton collisions at 7 and 8 TeV and derivation of constraints on its total decay width,
JHEP **09** (2016) 051, arXiv: 1605.02329 [hep-ex].

[72] ATLAS Collaboration, G. Aad et al., *Off-shell Higgs boson couplings measurement using $H \to ZZ \to 4\ell$ events at High Luminosity LHC*,
ATL-PHYS-PUB-2015-024, 2015, https://cds.cern.ch/record/2037715.

[73] CMS Collaboration, A. M. Sirunyan et al.,
Observation of the Higgs boson decay to a pair of τ leptons, (2017),
arXiv: 1708.00373 [hep-ex].

[74] ATLAS Collaboration, M. Aaboud et al.,
Evidence for the $H \to b\bar{b}$ decay with the ATLAS detector, JHEP **12** (2017) 024,
arXiv: 1708.03299 [hep-ex].

[75] CMS Collaboration, S. Chatrchyan et al.,
Evidence for the Higgs boson decay to a bottom quark-antiquark pair, (2017), arXiv: 1709.07497 [hep-ex].

[76] ATLAS Collaboration, G. Aad et al., *Evidence for the associated production of the Higgs boson and a top quark pair with the ATLAS detector*, ATLAS-CONF-2017-077, 2017, https://cds.cern.ch/record/2291405.

[77] ATLAS Collaboration, G. Aad et al., *Measurements of the Higgs boson production and decay rates and coupling strengths using pp collision data at $\sqrt{s} = 7$ and 8 TeV in the ATLAS experiment*, Eur. Phys. J. C **76** (2016) 6, arXiv: 1507.04548 [hep-ex].

[78] ATLAS Collaboration, G. Aad et al., *Search for the dimuon decay of the Higgs boson in pp collisions at $\sqrt{s} = 13$ TeV with the ATLAS detector*, ATLAS-CONF-2017-014, 2017, https://cds.cern.ch/record/2257726.

[79] ATLAS Collaboration, G. Aad et al., *Search for Higgs boson decays to a photon and a Z boson in pp collisions at $\sqrt{s} = 7$ and 8 TeV with the ATLAS detector*, Phys. Lett. B **732** (2014) 8, arXiv: 1402.3051 [hep-ex].

[80] CMS Collaboration, V. Khachatryan et al., *Search for a standard model-like Higgs boson in the $\mu^+\mu^-$ and e^+e^- decay channels at the LHC*, Phys. Lett. B **744** (2015) 184, arXiv: 1410.6679 [hep-ex].

[81] CMS Collaboration, S. Chatrchyan et al., *Search for a Higgs boson decaying into a Z and a photon in pp collisions at $\sqrt{s} = 7$ and 8 TeV*, Phys. Lett. B **726** (2013) 587, arXiv: 1307.5515 [hep-ex].

[82] ATLAS Collaboration, G. Aad et al.,
Update of the prospects for the $H \to Z\gamma$ search at the High-Luminosity LHC, ATL-PHYS-PUB-2014-006, 2014, https://cds.cern.ch/record/1703276.

[83] ATLAS Collaboration, G. Aad et al.,
Projections for measurements of Higgs boson cross sections, branching ratios and coupling parameters with the ATLAS detector at a HL-LHC, ATL-PHYS-PUB-2013-014, 2013, https://cds.cern.ch/record/1611186.

[84] ATLAS Collaboration, G. Aad et al., *Higgs Pair Production in the $H(\to \tau\tau)H(\to b\bar{b})$ Channel at the High-Luminosity LHC*, ATL-PHYS-PUB-2015-046, 2015, https://cds.cern.ch/record/2065974.

[85] CMS Collaboration, S. Chatrchyan et al.,
Higgs pair production at the High Luminosity LHC, CMS-PAS-FTR-15-002, 2015, `https://cds.cern.ch/record/2063038`.

[86] CDF and D0 Collaborations, T. Aaltonen et al.,
Tevatron Constraints on Models of the Higgs Boson with Exotic Spin and Parity Using Decays to Bottom-Antibottom Quark Pairs,
Phys. Rev. Lett. **114** (2015) 151802, arXiv: `1502.00967 [hep-ex]`.

[87] L. D. Landau, *On the angular momentum of a system of two photons*,
Dokl. Akad. Nauk Ser. Fiz. **60** (1948) 207.

[88] C.-N. Yang,
Selection Rules for the Dematerialization of a Particle Into Two Photons,
Phys. Rev. **77** (1950) 242.

[89] *About CERN*, (2012), `http://cds.cern.ch/record/1997225`.

[90] J. Haffner,
The CERN accelerator complex. Complexe des accélérateurs du CERN,
(2013), General Photo, `https://cds.cern.ch/record/1621894`.

[91] L. Evans and P. Bryant, *LHC Machine*, JINST **3** (2008) S08001.

[92] O. S. Brüning et al., *LHC Design Report*, CERN Yellow Reports: Monographs, Geneva: CERN, 2004, `https://cds.cern.ch/record/782076`.

[93] ALICE Collaboration, K. Aamodt et al.,
The ALICE experiment at the CERN LHC, JINST **3** (2008) S08002.

[94] ATLAS Collaboration, G. Aad et al.,
The ATLAS Experiment at the CERN Large Hadron Collider,
JINST **3** (2008) S08003.

[95] LHCf Collaboration, O. Adriani et al.,
The LHCf detector at the CERN Large Hadron Collider,
JINST **3** (2008) S08006.

[96] J. Pinfold, *The MoEDAL experiment at the LHC*,
EPJ Web Conf. **145** (2017) 12002.

[97] TOTEM, G. Anelli et al.,
The TOTEM experiment at the CERN Large Hadron Collider,
JINST **3** (2008) S08007.

[98] ATLAS Collaboration, M. Aaboud et al., *Luminosity determination in pp collisions at $\sqrt{s} = 8$ TeV using the ATLAS detector at the LHC*, Eur. Phys. J. C **76** (2016) 653, arXiv: 1608.03953 [hep-ex].

[99] *Luminosity summary plots for 2016 pp data taking with the ATLAS detector*, https://twiki.cern.ch/twiki/bin/view/AtlasPublic/LuminosityPublicResultsRun2 (visited on 03/23/2017).

[100] R. Bruce et al., *LHC Run 2: Results and challenges*, CERN-ACC-2016-0103, 2016, https://cds.cern.ch/record/2201447.

[101] Y. L. Dokshitzer, *Calculation of the Structure Functions for Deep Inelastic Scattering and e^+e^- Annihilation by Perturbation Theory in Quantum Chromodynamics.*, Sov. Phys. JETP **46** (1977) 641, [Zh. Eksp. Teor. Fiz.73,1216(1977)].

[102] V. N. Gribov and L. N. Lipatov, *Deep inelastic e p scattering in perturbation theory*, Sov. J. Nucl. Phys. **15** (1972) 438, [Yad. Fiz.15,781(1972)].

[103] G. Altarelli and G. Parisi, *Asymptotic Freedom in Parton Language*, Nucl. Phys. **B126** (1977) 298.

[104] S. Dulat et al., *New parton distribution functions from a global analysis of quantum chromodynamics*, Phys. Rev. **D93** (2016) 033006, arXiv: 1506.07443 [hep-ph].

[105] L. A. Harland-Lang et al., *Parton distributions in the LHC era: MMHT 2014 PDFs*, Eur. Phys. J. **C75** (2015) 204, arXiv: 1412.3989 [hep-ph].

[106] NNPDF Collaboration, R. D. Ball et al., *Impact of heavy quark masses on parton distributions and LHC phenomenology*, Nucl. Phys. **B849** (2011) 296, arXiv: 1101.1300 [hep-ph].

[107] NNPDF Collaboration, R. D. Ball et al., *Parton distributions for the LHC Run II*, JHEP **04** (2015) 040, arXiv: 1410.8849 [hep-ph].

[108] J. Butterworth et al., *PDF4LHC recommendations for LHC Run II*, J. Phys. **G43** (2016) 023001, arXiv: 1510.03865 [hep-ph].

[109] W. Stirling, *private communication*,
`http://www.hep.ph.ic.ac.uk/~wstirlin/plots/plots.html` (visited on 04/12/2017).

[110] V. M. Walbrecht,
Measurement of the $pp \to H \to ZZ^* \to 4\ell$ Production and HZZ Tensor Coupling with the ATLAS Detector at 13 TeV Centre-of-Mass Energy,
MA thesis: Munich, Tech. U., 2016-09-28,
`https://cds.cern.ch/record/2225970`.

[111] J. Pequenao, *Computer generated image of the whole ATLAS detector*, 2008,
`https://cds.cern.ch/record/1095924`.

[112] M. Brice, *Installing the ATLAS calorimeter. Vue centrale du détecteur ATLAS avec ses huit toroides entourant le calorimètre avant son déplacement au centre du détecteur*, 2005, `http://cds.cern.ch/record/910381`.

[113] ATLAS Collaboration, M. Capeans et al.,
ATLAS Insertable B-Layer Technical Design Report,
CERN-LHCC-2010-013, ATLAS-TDR-19, 2010,
`https://cds.cern.ch/record/1291633`.

[114] ATLAS Collaboration, M. Capeans et al.,
ATLAS Insertable B-Layer Technical Design Report Addendum,
CERN-LHCC-2012-009, ATLAS-TDR-19-ADD-1, 2012,
`https://cds.cern.ch/record/1451888`.

[115] J. Pequenao, *Computer generated image of the ATLAS inner detector*, 2008,
`http://cds.cern.ch/record/1095926`.

[116] J. Pequenao, *Computer Generated image of the ATLAS calorimeter*, 2008,
`http://cds.cern.ch/record/1095927`.

[117] ATLAS collaboration, H. Kroha, R. Fakhrutdinov and A. Kozhin,
New High-Precision Drift-Tube Detectors for the ATLAS Muon Spectrometer,
JINST **12** (2017) C06007, arXiv: `1705.05656 [physics.ins-det]`.

[118] J. Pequenao, *Computer generated image of the ATLAS Muons subsystem*, 2008,
`http://cds.cern.ch/record/1095929`.

[119] ATLAS Collaboration, G. Aad et al.,
Performance of the ATLAS Trigger System in 2010,
Eur. Phys. J. C **72** (2012) 1849, arXiv: `1110.1530 [hep-ex]`.

[120] ATLAS Collaboration, M. Aaboud et al.,
Performance of the ATLAS Trigger System in 2015,
Eur. Phys. J. C **77** (2017) 317, arXiv: 1611.09661 [hep-ex].

[121] *Overview of the ATLAS trigger and data acquisition system in Run-2.*,
https://twiki.cern.ch/twiki/bin/view/AtlasPublic/ApprovedPlotsDAQ
(visited on 02/19/2018).

[122] S. van der Meer, *Calibration of the Effective Beam Height in the ISR*,
CERN-ISR-PO-68-31, 1968, https://cds.cern.ch/record/296752.

[123] ATLAS Collaboration, G. Aad et al., *Improved luminosity determination in pp collisions at $\sqrt{s} = 7$ TeV using the ATLAS detector at the LHC*,
Eur. Phys. J. **C73** (2013) 2518, arXiv: 1302.4393 [hep-ex].

[124] *Integrated luminosity summary plots for 2011-2012 data taking with the ATLAS detector*, https://twiki.cern.ch/twiki/bin/view/AtlasPublic/LuminosityPublicResults (visited on 03/23/2017).

[125] ATLAS Collaboration, G. Aad et al., *The ATLAS simulation Infrastructure*,
Eur. Phys. J. **C 70** (2010) 823, arXiv: 1005.4568 [physics.ins-det].

[126] GEANT4 Collaboration, S. Agostinelli et al., *GEANT4: A Simulation toolkit*,
Nucl. Instrum. Meth. **A506** (2003) 250.

[127] T. Sjöstrand, S. Mrenna and P. Z. Skands,
A Brief Introduction to PYTHIA 8.1,
Comput. Phys. Commun. **178** (2008) 852, arXiv: 0710.3820 [hep-ph].

[128] A. Martin et al., *Parton distributions for the LHC*,
Eur. Phys. J. **C63** (2009) 189, arXiv: 0901.0002 [hep-ph].

[129] ATLAS Collaboration, G. Aad et al., *Summary of ATLAS Pythia 8 tunes*,
ATL-PHYS-PUB-2012-003, 2012, https://cds.cern.ch/record/1474107.

[130] ATLAS Collaboration, M. Aaboud et al., *Electron efficiency measurements with the ATLAS detector using 2012 LHC proton–proton collision data*,
Eur. Phys. J. C **77** (2017) 195, arXiv: 1612.01456 [hep-ex].

[131] ATLAS Collaboration, G. Aad et al., *Electron identification measurements in ATLAS using $\sqrt{s}$ = 13 TeV data with 50 ns bunch spacing*, (2015),
https://cds.cern.ch/record/2048202.

[132] ATLAS Collaboration, G. Aad et al., *Improved electron reconstruction in ATLAS using the Gaussian Sum Filter-based model for bremsstrahlung*, ATLAS-CONF-2012-047, 2012, https://cds.cern.ch/record/1449796.

[133] ATLAS Collaboration, G. Aad et al., *Electron and photon energy calibration with the ATLAS detector using LHC Run 1 data*, Eur. Phys. J. C **74** (2014) 3071, arXiv: 1407.5063 [hep-ex].

[134] ATLAS Collaboration, G. Aad et al., *Measurement of the muon reconstruction performance of the ATLAS detector using 2011 and 2012 LHC proton–proton collision data*, Eur. Phys. J. C **74** (2014) 3130, arXiv: 1407.3935 [hep-ex].

[135] ATLAS Collaboration, G. Aad et al., *Muon reconstruction performance of the ATLAS detector in proton-proton collisions at $\sqrt{s}$ =13 TeV*, Eur. Phys. J. **C76** (2016) 292, arXiv: 1603.05598 [hep-ex].

[136] ATLAS Collaboration, M. Aaboud et al., *Jet energy scale measurements and their systematic uncertainties in proton–proton collisions at $\sqrt{s} = 13$ TeV with the ATLAS detector*, Phys. Rev. D **96** (2017) 072002, arXiv: 1703.09665 [hep-ex].

[137] ATLAS Collaboration, G. Aad et al., *Topological cell clustering in the ATLAS calorimeters and its performance in LHC Run 1*, Eur. Phys. J. C **77** (2017) 490, arXiv: 1603.02934 [hep-ex].

[138] M. Cacciari, G. P. Salam and G. Soyez, *The Anti-k(t) jet clustering algorithm*, JHEP **04** (2008) 063, arXiv: 0802.1189 [hep-ph].

[139] M. Cacciari, G. P. Salam and G. Soyez, *FastJet User Manual*, Eur. Phys. J. **C72** (2012) 1896, arXiv: 1111.6097 [hep-ph].

[140] ATLAS Collaboration, G. Aad et al., *Tagging and suppression of pileup jets with the ATLAS detector*, ATLAS-CONF-2014-018, 2014, https://cds.cern.ch/record/1700870.

[141] ATLAS Collaboration, G. Aad et al., *Performance of pile-up mitigation techniques for jets in pp collisions at $\sqrt{s} = 8$ TeV using the ATLAS detector*, Eur. Phys. J. C **76** (2016) 581, arXiv: 1510.03823 [hep-ex].

[142] ATLAS Collaboration, G. Aad et al., *Performance of b-jet identification in the ATLAS experiment*, JINST **11** (2016) P04008, arXiv: 1512.01094 [hep-ex].

[143] ATLAS Collaboration, G. Aad et al.,
Expected performance of the ATLAS b-tagging algorithms in Run-2,
ATL-PHYS-PUB-2015-022, 2015, `https://cds.cern.ch/record/2037697`.

[144] ATLAS Collaboration, G. Aad et al., *Optimisation and performance studies of the ATLAS b-tagging algorithms for the 2017-18 LHC run*,
ATL-PHYS-PUB-2017-013, 2017, `https://cds.cern.ch/record/2273281`.

[145] ATLAS Collaboration, G. Aad et al., *Measurements of Higgs boson production and couplings in the four-lepton channel in pp collisions at center-of-mass energies of* 7 *and* 8 *TeV with the ATLAS detector*,
Phys. Rev. D **91** (2015) 012006, arXiv: `1408.5191 [hep-ex]`.

[146] ATLAS Collaboration, M. Aaboud et al.,
Measurement of the Higgs boson coupling properties in the $H \to ZZ^* \to 4\ell$ *decay channel at* $\sqrt{s}$ *= 13 TeV with the ATLAS detector*, JHEP **03** (2018) 095,
arXiv: `1712.02304 [hep-ex]`.

[147] LHC Higgs Cross Section Working Group, S. Dittmaier et al.,
Handbook of LHC Higgs Cross Sections: 1. Inclusive Observables,
CERN-2011-002 (CERN, Geneva, 2011), arXiv: `1101.0593 [hep-ph]`.

[148] LHC Higgs Cross Section Working Group, S. Dittmaier et al.,
Handbook of LHC Higgs Cross Sections: 2. Differential Distributions,
CERN-2012-002 (CERN, Geneva, 2012), arXiv: `1201.3084 [hep-ph]`.

[149] J. Alwall et al.,
The automated computation of tree-level and next-to-leading order differential cross sections, and their matching to parton shower simulations,
JHEP **07** (2014) 079, arXiv: `1405.0301 [hep-ph]`.

[150] ATLAS Collaboration, G. Aad et al., *Measurements of Higgs boson production and couplings in the four-lepton channel in pp collisions at center-of-mass energies of 7 and 8 TeV with the ATLAS detector*,
Phys. Rev. **D91** (2015) 012006, arXiv: `1408.5191 [hep-ex]`.

[151] ATLAS Collaboration, M. Aaboud et al.,
Measurement of inclusive and differential cross sections in the $H \to ZZ^* \to 4\ell$ *decay channel in pp collisions at* $\sqrt{s} = 13$ *TeV with the ATLAS detector*,
JHEP **10** (2017) 132, arXiv: `1708.02810 [hep-ex]`.

[152] M. Baak et al., *Interpolation between multi-dimensional histograms using a new non-linear moment morphing method*, Nucl. Instrum. Meth. **A771** (2015) 39, arXiv: 1410.7388 [physics.data-an].

[153] D. Atwood and A. Soni, *Analysis for magnetic moment and electric dipole moment form-factors of the top quark via $e^+e^- \to t\bar{t}$*, Phys. Rev. **D45** (1992) 2405.

[154] M. Davier et al., *The Optimal method for the measurement of tau polarization*, Phys. Lett. **B306** (1993) 411.

[155] M. Diehl, O. Nachtmann and F. Nagel, *Triple gauge couplings in polarized $e^-e^+ \to W^-W^+$ and their measurement using optimal observables*, Eur. Phys. J. **C27** (2003) 375, arXiv: hep-ph/0209229 [hep-ph].

[156] M. Diehl and O. Nachtmann, *Optimal observables for measuring three gauge boson couplings in $e^+e^- \to W^+W^-$*, (1996) 301, arXiv: hep-ph/9603207 [hep-ph].

[157] A. Hoecker et al., *TMVA: Toolkit for Multivariate Data Analysis*, PoS **ACAT** (2007) 040, arXiv: physics/0703039.

[158] K. S. Cranmer, *Kernel estimation in high-energy physics*, Comput. Phys. Commun. **136** (2001) 198, arXiv: hep-ex/0011057.

[159] M. Botje et al., *The PDF4LHC working group interim recommendations*, (2011), arXiv: 1101.0538 [hep-ph].

[160] H.-L. Lai et al., *New parton distributions for collider physics*, Phys. Rev. **D82** (2010) 074024, arXiv: 1007.2241 [hep-ph].

[161] G. Cowan et al., *Asymptotic formulae for likelihood-based tests of new physics*, Eur. Phys. J. **C 71** (2011) 1554, arXiv: 1007.1727 [hep-ex].

[162] S. S. Wilks, *The Large-Sample Distribution of the Likelihood Ratio for Testing Composite Hypotheses*, Annals Math. Statist. **9** (1938) 60.

[163] A. Wald, *Tests of Statistical Hypotheses Concerning Several Parameters When the Number of Observations is Large*, Transactions of the American Mathematical Society **54** (1943) 426.

[164] ATLAS Collaboration, G. Aad et al., *Determination of spin and parity of the Higgs boson in the $WW^* \to e\nu\mu\nu$ decay channel with the ATLAS detector*, Eur. Phys. J. C **75** (2015) 231, arXiv: 1503.03643 [hep-ex].

[165] ATLAS Collaboration, G. Aad et al., *A morphing technique for signal modelling in a multidimensional space of coupling parameters*, ATL-PHYS-PUB-2015-047, 2015, https://cds.cern.ch/record/2066980.

[166] ATLAS Collaboration, M. Aaboud et al., *Measurement of the Inelastic Proton-Proton Cross Section at $\sqrt{s} = 13$ TeV with the ATLAS Detector at the LHC*, Phys. Rev. Lett. **117** (2016) 182002, arXiv: 1606.02625 [hep-ex].

[167] I. W. Stewart and F. J. Tackmann, *Theory uncertainties for Higgs and other searches using jet bins*, Phys. Rev. **D85** (2012) 034011, arXiv: 1107.2117 [hep-ph].

[168] ATLAS Collaboration, G. Aad et al., *Test of CP Invariance in vector-boson fusion production of the Higgs boson using the Optimal Observable method in the ditau decay channel with the ATLAS detector*, Eur. Phys. J. C **76** (2016) 658, arXiv: 1602.04516 [hep-ex].

[169] J. Ellis et al., *A Fast Track towards the 'Higgs' Spin and Parity*, JHEP **11** (2012) 134, arXiv: 1208.6002 [hep-ph].

[170] T. Plehn, D. L. Rainwater and D. Zeppenfeld, *Determining the structure of Higgs couplings at the LHC*, Phys. Rev. Lett. **88** (2002) 051801, arXiv: hep-ph/0105325 [hep-ph].

[171] A. Djouadi et al., *Probing the spin-parity of the Higgs boson via jet kinematics in vector boson fusion*, Phys. Lett. **B723** (2013) 307, arXiv: 1301.4965 [hep-ph].

[172] C. Englert et al., *Higgs Quantum Numbers in Weak Boson Fusion*, JHEP **01** (2013) 148, arXiv: 1212.0843 [hep-ph].

[173] V. Hankele et al., *Anomalous Higgs boson couplings in vector boson fusion at the CERN LHC*, Phys. Rev. **D74** (2006) 095001, arXiv: hep-ph/0609075 [hep-ph].

[174] M. J. Dolan et al., *Constraining CP-violating Higgs Sectors at the LHC using gluon fusion*, Phys. Rev. **D90** (2014) 073008, arXiv: 1406.3322 [hep-ph].

[175] F. E. James, *Statistical Methods in Experimental Physics; 2nd ed.* Singapore: World Scientific, 2006, https://cds.cern.ch/record/1019859.

[176] ROOT Collaboration, K. Cranmer et al., *HistFactory: A tool for creating statistical models for use with RooFit and RooStats*, CERN-OPEN-2012-016, 2012, `https://cds.cern.ch/record/1456844`.

[177] P. Nason, *A New method for combining NLO QCD with shower Monte Carlo algorithms*, JHEP **11** (2004) 040, arXiv: `hep-ph/0409146`.

[178] S. Frixione, P. Nason and C. Oleari, *Matching NLO QCD computations with Parton Shower simulations: the POWHEG method*, JHEP **11** (2007) 070, arXiv: `0709.2092 [hep-ph]`.

[179] S. Alioli et al., *A general framework for implementing NLO calculations in shower Monte Carlo programs: the POWHEG BOX*, JHEP **06** (2010) 043, arXiv: `1002.2581 [hep-ph]`.

[180] S. Alioli et al., *NLO Higgs boson production via gluon fusion matched with shower in POWHEG*, JHEP **04** (2009) 002, arXiv: `0812.0578 [hep-ph]`.

[181] P. Nason and C. Oleari, *NLO Higgs boson production via vector-boson fusion matched with shower in POWHEG*, JHEP **02** (2010) 037, arXiv: `0911.5299 [hep-ph]`.

[182] G. Luisoni et al., *$HW^{\pm}$/HZ + 0 and 1 jet at NLO with the POWHEG BOX interfaced to GoSam and their merging within MiNLO*, JHEP **10** (2013) 083, arXiv: `1306.2542 [hep-ph]`.

[183] M. Wiesemann et al., *Higgs production in association with bottom quarks*, JHEP **02** (2015) 132, arXiv: `1409.5301 [hep-ph]`.

[184] M. L. Mangano et al., *ALPGEN, a generator for hard multiparton processes in hadronic collisions*, JHEP **07** (2003) 001, arXiv: `hep-ph/0206293 [hep-ph]`.

[185] T. Gleisberg et al., *Event generation with SHERPA 1.1*, JHEP **02** (2009) 007, arXiv: `0811.4622 [hep-ph]`.

[186] N. Kauer, C. O'Brien and E. Vryonidou, *Interference effects for $H \to W\,W \to \ell\nu q\bar{q}'$ and $H \to ZZ \to \ell\bar{\ell}q\bar{q}$ searches in gluon fusion at the LHC*, JHEP **10** (2015) 074, arXiv: `1506.01694 [hep-ph]`.

[187] T. Binoth, N. Kauer and P. Mertsch, *Gluon-induced QCD corrections to $pp \to ZZ \to l\bar{l}l'\bar{l}'$*, (2008) 142, arXiv: `0807.0024 [hep-ph]`.

[188] J. Pumplin et al., *New generation of parton distributions with uncertainties from global QCD analysis*, JHEP **07** (2002) 012, arXiv: hep-ph/0201195.

[189] T. Sjöstrand, S. Mrenna and P. Z. Skands, *PYTHIA 6.4 Physics and Manual*, JHEP **05** (2006) 026, arXiv: hep-ph/0603175.

[190] M. Bahr et al., *Herwig++ Physics and Manual*, Eur. Phys. J. **C58** (2008) 639, arXiv: 0803.0883 [hep-ph].

[191] S. Schumann and F. Krauss, *A Parton shower algorithm based on Catani-Seymour dipole factorisation*, JHEP **0803** (2008) 038, arXiv: 0709.1027 [hep-ph].

[192] P. Z. Skands, *Tuning Monte Carlo Generators: The Perugia Tunes*, Phys. Rev. **D82** (2010) 074018, arXiv: 1005.3457 [hep-ph].

[193] ATLAS Collaboration, G. Aad et al., *New ATLAS event generator tunes to 2010 data*, ATL-PHYS-PUB-2011-008, 2011, https://cds.cern.ch/record/1345343.

[194] ATLAS Collaboration, G. Aad et al., *Measurement of the Z/γ^* boson transverse momentum distribution in pp collisions at $\sqrt{s} = 7$ TeV with the ATLAS detector*, JHEP **09** (2014) 145, arXiv: 1406.3660 [hep-ex].

[195] ATLAS Collaboration, G. Aad et al., *ATLAS Run 1 Pythia8 tunes*, ATL-PHYS-PUB-2014-021, 2014, https://cds.cern.ch/record/1966419.

[196] S. Gieseke, C. Rohr and A. Siodmok, *Colour reconnections in Herwig++*, Eur. Phys. J. **C72** (2012) 2225, arXiv: 1206.0041 [hep-ph].

[197] D. de Florian et al., *Transverse-momentum resummation: Higgs boson production at the Tevatron and the LHC*, JHEP **11** (2011) 064, arXiv: 1109.2109 [hep-ph].

[198] M. Grazzini and H. Sargsyan, *Heavy-quark mass effects in Higgs boson production at the LHC*, JHEP **09** (2013) 129, arXiv: 1306.4581 [hep-ph].

[199] K. Hamilton et al., *NNLOPS simulation of Higgs boson production*, JHEP **10** (2013) 222, arXiv: 1309.0017 [hep-ph].

[200] K. Hamilton et al., *Merging H/W/Z + 0 and 1 jet at NLO with no merging scale: a path to parton shower + NNLO matching*, JHEP **05** (2013) 082, arXiv: 1212.4504 [hep-ph].

[201] S. Catani and M. Grazzini, *An NNLO subtraction formalism in hadron collisions and its application to Higgs boson production at the LHC*, Phys. Rev. Lett. **98** (2007) 222002, arXiv: hep-ph/0703012 [hep-ph].

[202] M. Grazzini, *NNLO predictions for the Higgs boson signal in the $H \to WW \to \ell\nu\ell\nu$ and $H \to ZZ \to 4\ell$ decay channels*, JHEP **02** (2008) 043, arXiv: 0801.3232 [hep-ph].

[203] E. Bagnaschi et al., *Higgs production via gluon fusion in the POWHEG approach in the SM and in the MSSM*, JHEP **02** (2012) 088, arXiv: 1111.2854 [hep-ph].

[204] R. Frederix and S. Frixione, *Merging meets matching in MC@NLO*, JHEP **12** (2012) 061, arXiv: 1209.6215 [hep-ph].

[205] M. L. Mangano et al., *Matching matrix elements and shower evolution for top-quark production in hadronic collisions*, JHEP **01** (2007) 013, arXiv: hep-ph/0611129 [hep-ph].

[206] B. Biedermann et al., *Electroweak corrections to $pp \to \mu^+\mu^- e^+ e^- + X$ at the LHC: a Higgs background study*, Phys. Rev. Lett. **116** (2016) 161803, arXiv: 1601.07787 [hep-ph].

[207] B. Biedermann et al., *Next-to-leading-order electroweak corrections to the production of four charged leptons at the LHC*, JHEP **01** (2017) 033, arXiv: 1611.05338 [hep-ph].

[208] F. Caola et al., *QCD corrections to ZZ production in gluon fusion at the LHC*, Phys. Rev. **D92** (2015) 094028, arXiv: 1509.06734 [hep-ph].

[209] F. Caola et al., *QCD corrections to W^+W^- production through gluon fusion*, Phys. Lett. **B754** (2016) 275, arXiv: 1511.08617 [hep-ph].

[210] J. M. Campbell et al., *Two Loop Correction to Interference in $gg \to ZZ$*, (2016), arXiv: 1605.01380 [hep-ph].

[211] K. Melnikov and M. Dowling, *Production of two Z-bosons in gluon fusion in the heavy top quark approximation*, Phys. Lett. **B744** (2015) 43, arXiv: 1503.01274 [hep-ph].

[212] M. Bonvini et al., *Signal-background interference effects for $gg \to H \to W^+W^-$ beyond leading order*, Phys. Rev. **D88** (2013) 034032, arXiv: 1304.3053 [hep-ph].

[213] C. S. Li et al., *Soft gluon resummation in the signal-background interference process of gg(→ h*)→ ZZ*, JHEP **08** (2015) 065, arXiv: 1504.02388 [hep-ph].

[214] S. Frixione et al., *Electroweak and QCD corrections to top-pair hadroproduction in association with heavy bosons*, JHEP **06** (2015) 184, arXiv: 1504.03446 [hep-ph].

[215] K. Melnikov and F. Petriello, *Electroweak gauge boson production at hadron colliders through O(alpha(s)**2)*, Phys. Rev. **D74** (2006) 114017, arXiv: hep-ph/0609070.

[216] C. Anastasiou et al., *High precision QCD at hadron colliders: Electroweak gauge boson rapidity distributions at NNLO*, Phys. Rev. **D69** (2004) 094008, arXiv: hep-ph/0312266.

[217] J. M. Campbell and R. K. Ellis, *MCFM for the Tevatron and the LHC*, Nucl. Phys. Proc. Suppl. **205-206** (2010) 10, arXiv: 1007.3492 [hep-ph].

[218] J. M. Campbell and R. K. Ellis, *Radiative corrections to Z b anti-b production*, Phys. Rev. **D62** (2000) 114012, arXiv: hep-ph/0006304 [hep-ph].

[219] T. Gleisberg and S. Höche, *Comix, a new matrix element generator*, JHEP **0812** (2008) 039, arXiv: 0808.3674 [hep-ph].

[220] F. Cascioli, P. Maierhofer and S. Pozzorini, *Scattering Amplitudes with Open Loops*, Phys. Rev. Lett. **108** (2012) 111601, arXiv: 1111.5206 [hep-ph].

[221] P. Golonka and Z. Was, *PHOTOS Monte Carlo: A Precision tool for QED corrections in Z and W decays*, Eur. Phys. J. **C 45** (2006) 97, arXiv: hep-ph/0506026.

[222] N. Davidson, T. Przedzinski and Z. Was, *PHOTOS Interface in C++: Technical and Physics Documentation*, (2010), arXiv: 1011.0937 [hep-ph].

[223] D. J. Lange, *The EvtGen particle decay simulation package*, Nucl. Instrum. Meth. **A462** (2001) 152.

[224] S. Jadach et al., *The tau decay library TAUOLA: Version 2.4*, Comput. Phys. Commun. **76** (1993) 361.

[225] P. Golonka et al., *The tauola-photos-F environment for the TAUOLA and PHOTOS packages, release II*, Comput. Phys. Commun. **174** (2006) 818.

[226] A. Djouadi, M. Spira and P. Zerwas,
Production of Higgs bosons in proton colliders: QCD corrections,
Phys. Lett. **B264** (1991) 440.

[227] S. Dawson, *Radiative corrections to Higgs boson production*,
Nucl. Phys. **B359** (1991) 283.

[228] M. Spira et al., *Higgs boson production at the LHC*,
Nucl. Phys. **B453** (1995) 17, arXiv: hep-ph/9504378 [hep-ph].

[229] R. V. Harlander and W. B. Kilgore,
Next-to-next-to-leading order Higgs production at hadron colliders,
Phys. Rev. Lett. **88** (2002) 201801, arXiv: hep-ph/0201206 [hep-ph].

[230] C. Anastasiou and K. Melnikov,
Higgs boson production at hadron colliders in NNLO QCD,
Nucl. Phys. **B646** (2002) 220, arXiv: hep-ph/0207004 [hep-ph].

[231] V. Ravindran, J. Smith and W. L. van Neerven, *NNLO corrections to the total cross-section for Higgs boson production in hadron hadron collisions*,
Nucl. Phys. **B665** (2003) 325, arXiv: hep-ph/0302135 [hep-ph].

[232] C. Anastasiou et al.,
Higgs Boson Gluon-Fusion Production in QCD at Three Loops,
Phys. Rev. Lett. **114** (2015) 212001, arXiv: 1503.06056 [hep-ph].

[233] C. Anastasiou et al., *High precision determination of the gluon fusion Higgs boson cross-section at the LHC*, JHEP **05** (2016) 058,
arXiv: 1602.00695 [hep-ph].

[234] S. Catani et al.,
Soft gluon resummation for Higgs boson production at hadron colliders,
JHEP **07** (2003) 028, arXiv: hep-ph/0306211 [hep-ph].

[235] U. Aglietti et al.,
Two loop light fermion contribution to Higgs production and decays,
Phys. Lett. **B595** (2004) 432, arXiv: hep-ph/0404071 [hep-ph].

[236] S. Actis et al.,
NLO electroweak corrections to Higgs boson production at hadron colliders,
Phys. Lett. **B670** (2008) 12, arXiv: 0809.1301 [hep-ph].

[237] C. Anastasiou, R. Boughezal and F. Petriello,
Mixed QCD-electroweak corrections to Higgs boson production in gluon fusion,
JHEP **04** (2009) 003, arXiv: 0811.3458 [hep-ph].

[238] C. Anastasiou et al., *Inclusive Higgs boson cross-section for the LHC at 8 TeV*,
JHEP **04** (2012) 004, arXiv: 1202.3638 [hep-ph].

[239] D. de Florian and M. Grazzini,
Higgs production at the LHC: updated cross sections at $\sqrt{s} = 8$ *TeV*,
Phys. Lett. **B718** (2012) 117, arXiv: 1206.4133 [hep-ph].

[240] M. Ciccolini, A. Denner and S. Dittmaier, *Strong and electroweak corrections to the production of Higgs + 2-jets via weak interactions at the LHC*,
Phys. Rev. Lett. **99** (2007) 161803, arXiv: 0707.0381 [hep-ph].

[241] M. Ciccolini, A. Denner and S. Dittmaier, *Electroweak and QCD corrections to Higgs production via vector-boson fusion at the LHC*,
Phys. Rev. **D77** (2008) 013002, arXiv: 0710.4749 [hep-ph].

[242] K. Arnold et al.,
VBFNLO: A Parton level Monte Carlo for processes with electroweak bosons,
Comput. Phys. Commun. **180** (2009) 1661, arXiv: 0811.4559 [hep-ph].

[243] P. Bolzoni et al., *Higgs production via vector-boson fusion at NNLO in QCD*,
Phys. Rev. Lett. **105** (2010) 011801, arXiv: 1003.4451 [hep-ph].

[244] T. Han and S. Willenbrock,
QCD correction to the $pp \to WH$ *and* ZH *total cross-sections*,
Phys. Lett. **B273** (1991) 167.

[245] O. Brein, A. Djouadi and R. Harlander,
NNLO QCD corrections to the Higgs-strahlung processes at hadron colliders,
Phys. Lett. **B579** (2004) 149, arXiv: hep-ph/0307206.

[246] M. Ciccolini, S. Dittmaier and M. Krämer, *Electroweak radiative corrections to associated* WH *and* ZH *production at hadron colliders*,
Phys. Rev. **D68** (2003) 073003, arXiv: hep-ph/0306234 [hep-ph].

[247] A. Denner et al., *Electroweak corrections to Higgs-strahlung off W/Z bosons at the Tevatron and the LHC with HAWK*, JHEP **03** (2012) 075,
arXiv: 1112.5142 [hep-ph].

[248] L. Altenkamp et al.,
Gluon-induced Higgs-strahlung at next-to-leading order QCD,
JHEP **02** (2013) 078, arXiv: 1211.5015 [hep-ph].

[249] W. Beenakker et al.,
Higgs radiation off top quarks at the Tevatron and the LHC,
Phys. Rev. Lett. **87** (2001) 201805, arXiv: hep-ph/0107081 [hep-ph].

[250] W. Beenakker et al.,
NLO QCD corrections to $t\bar{t}H$ production in hadron collisions,
Nucl. Phys. **B653** (2003) 151, arXiv: hep-ph/0211352.

[251] S. Dawson et al., *Next-to-leading order QCD corrections to $pp \to t\bar{t}h$ at the CERN Large Hadron Collider*, Phys. Rev. **D67** (2003) 071503,
arXiv: hep-ph/0211438 [hep-ph].

[252] S. Dawson et al., *Associated Higgs production with top quarks at the large hadron collider: NLO QCD corrections*, Phys. Rev. **D68** (2003) 034022,
arXiv: hep-ph/0305087.

[253] Y. Zhang et al., *QCD NLO and EW NLO corrections to $t\bar{t}H$ production with top quark decays at hadron collider*, Phys. Lett. **B738** (2014) 1,
arXiv: 1407.1110 [hep-ph].

[254] S. Dawson et al.,
Exclusive Higgs boson production with bottom quarks at hadron colliders,
Phys. Rev. **D69** (2004) 074027, arXiv: hep-ph/0311067.

[255] S. Dittmaier, M. Krämer and M. Spira,
Higgs radiation off bottom quarks at the Tevatron and the CERN LHC,
Phys. Rev. **D70** (2004) 074010, arXiv: hep-ph/0309204.

[256] S. Dawson et al.,
Higgs production in association with bottom quarks at hadron colliders,
Mod. Phys. Lett. **A21** (2006) 89, arXiv: hep-ph/0508293 [hep-ph].

[257] R. V. Harlander and W. B. Kilgore,
Higgs boson production in bottom quark fusion at next-to-next-to leading order,
Phys. Rev. **D68** (2003) 013001, arXiv: hep-ph/0304035.

[258] R. Harlander, M. Krämer and M. Schumacher, *Bottom-quark associated Higgs-boson production: Reconciling the four- and five-flavour scheme approach*,
(2011), arXiv: 1112.3478 [hep-ph].

[259] A. Bredenstein et al.,
Precise predictions for the Higgs-boson decay $H \to WW/ZZ \to 4$ leptons,
Phys. Rev. **D74** (2006) 013004, arXiv: `hep-ph/0604011`.

[260] A. Bredenstein et al., *Radiative corrections to the semileptonic and hadronic Higgs-boson decays $H \to WW/ZZ \to 4$ fermions*, JHEP **02** (2007) 080, arXiv: `hep-ph/0611234`.

[261] S. Boselli et al.,
Higgs boson decay into four leptons at NLOPS electroweak accuracy,
JHEP **06** (2015) 023, arXiv: `1503.07394 [hep-ph]`.

[262] A. Djouadi, J. Kalinowski and M. Spira, *HDECAY: A Program for Higgs boson decays in the Standard Model and its supersymmetric extension*,
Comput. Phys. Commun. **108** (1998) 56, arXiv: `hep-ph/9704448`.

[263] A. Djouadi, M. M. Mühlleitner and M. Spira, *Decays of supersymmetric particles: The Program SUSY-HIT (SUspect-SdecaY-Hdecay-InTerface)*,
Acta Phys. Polon. **B38** (2007) 635, arXiv: `hep-ph/0609292`.

[264] *Change-of-Variable Technique*, PennState Eberly College of Science,
`https://onlinecourses.science.psu.edu/stat414/node/157` (visited on 02/22/2018).

Warum können Piraten keinen Kreis berechnen?
Weil sie Pi-raten.

Acknowledgements

The support of many people made it possible for me to finish my thesis. I am deeply grateful and would like to express my gratitude.

Thank you to Hubert Kroha for accepting me as a PhD student and giving me the opportunity to work in such an interesting research area. I am very grateful, that I could stay a few month at CERN, this was an unique experience, which I will never forget. Thank you for the many hours spent on proof-reading my thesis. Thank you very much to Sandra Kortner for being my supervisor over the years. With her guidance and help my thesis turned into something of which I can be very proud.

Thanks a lot to my colleagues and friends. A special thank goes to Verena, who was the best analysis partner and office mate one could wish for. Thank you to my ex-office mate Sebastian, who has a terrible sense in interior decoration, but a good sense of humour. Thanks for supporting me during my stay at CERN. Thank you Bini for our long talks about everything. Thank you to Adam, Carsten and Lydia for our time in the awesome plots team. Thank you Johannes and my office mate Philipp and the other MPPler, with your special kind of craziness you made my place of work to something where I liked to go.

Thank you to my family and friends. There are not enough words to express my gratitude. Thanks a lot for the support during my thesis, which was at times very trying and difficult. Thanks for always listening and showing me that the centre of the world is not physics and my PhD thesis, but that there are also many other important things in life. You were the foundation, from which I could draw the strength to finish this mammoth project. Thanks to Mat, Susi, Babsi, Stefan, Steffi, Michi and the *stöpsis* Benedikt, Anna and Laura. And of course, thanks to Miro. Thanks for brightening my world and always making me laugh when I needed to laugh. I am very happy to have you in my life.
Thanks a lot to my parents, Anna and Sebastian, you made this thesis possible. It is dedicated to you.